

**Modelling and interpretation of
turbulent fluxes in katabatic flows:
applications to glaciers and the Greenland ice sheet**

Modelleren en interpretatie van turbulente
fluxen in katabatische stromingen:
toepassingen op gletsjers en de Groenlandse ijskap

(met een samenvatting in het Nederlands)

Proefschrift ter verkrijging van de graad van doctor aan
de Universiteit Utrecht op gezag van de Rector Magnifi-
cus, Prof. Dr. H.O. Voorma, ingevolge het besluit van het
College voor Promoties in het openbaar te verdedigen op
maandag 19 maart 2001 des namiddaags om 4:15 uur

door

Bruce Denby

geboren op 11 december 1963 te Sydney, Australia

Promoter: Prof. Dr. J. Oerlemans

Co-promoter: Dr. W. Greuell

Institute for Marine and Atmospheric Research Utrecht (IMAU)
Faculteit Natuur- en Sterrenkunde, Universiteit Utrecht

Dit proefschrift werd mogelijk gemaakt met financiële steun van de
Dutch National Research Programme on Global Air Pollution and
Climate Change (NOP II Project 013 001236.10)

ISBN: 90-393-2664-9

Contents

1	Introduction	3
1.1	Energy balance of glaciers and ice sheets	4
1.2	Turbulent fluxes of heat and momentum	6
1.3	Glacio-meteorology and the atmospheric boundary layer	6
1.4	Observational data	8
1.5	Modelling the atmospheric boundary layer	8
1.6	Contents of this thesis	10
2	Second-Order Modelling of Turbulence in Katabatic Flows	13
2.1	Introduction	14
2.2	Mean and second moment equations	15
2.3	Second-order closures	17
2.4	Determination of constants	19
2.5	Simplification for a homogenous 1-D boundary layer on a tilted surface	21
2.6	Non-dimensional annalysis of the second-order equations: the influ- ence of slope and turbulent transport	22
2.7	Model description	24
2.8	Results from the second-order model	25
2.9	Conclusions	35
	Appendix	37
3	The Use of Bulk and Profile Methods for Determining Surface Heat Fluxes in the Presence of Glacier Winds	43
3.1	Introduction	44
3.2	Observations	45
3.3	The mean and turbulent structure of katabatic flows	45
3.4	Suitability of bulk and profile methods	48
3.5	Conclusion and discussion	53
4	Derivation of Turbulent Flux Profiles and Roughness Lengths from Kata- batic Flow Dynamics	55
4.1	Introduction	56
4.2	The katabatic method for flux determination	57
4.3	Bulk and profile methods	58
4.4	Observations of katabatic flows	59
4.5	The $\overline{w'w'}$ turbulent flux profile	62
4.6	Determination of the surface roughness length for momentum	65
4.7	Discussion	70

5	Observed Roughness Lengths for Momentum and Temperature on a Melting Glacier Surface	73
5.1	Introduction	74
5.2	Observations	74
5.3	Application of the profile method	76
5.4	Results	77
6	Simulating the Greenland Atmospheric Boundary Layer: Model Description and Validation	81
6.1	Introduction	82
6.2	Model description	83
6.3	Comparison with observations	96
6.4	Sensitivity tests	103
6.5	Discussion	114
	Appendix	117
7	Simulating the Greenland Atmospheric Boundary Layer: Energy Balance and Climate Sensitivity	119
7.1	Introduction	120
7.2	Model description and methodology	120
7.3	The 1998 simulation	122
7.4	Climate sensitivity	133
7.5	Simplified parameterisations for energy balance modelling	143
7.6	Summary	148
8	Some final words	151
	Acknowledgments	154
	Curriculum Vitae	155
	References	157

Summary

This thesis is concerned with the turbulent exchange of heat from the atmosphere to glacier surfaces. The motivation behind this interest is driven by the need to estimate sea level changes into the future. Since a major contributor to sea level rise is the changing mass balance of the cryosphere, there is a need to improve our understanding of the processes governing mass loss and gain from ice sheets and glaciers. A large part of this mass loss is due to melt, the result of radiation absorption as well as the exchange of heat between the ice and the overlaying atmosphere, known as the atmospheric boundary layer (ABL).

Though much work has already been carried out in this area for land surfaces the ABL above glaciers is somewhat different to the classical ABL usually studied. Because of the sloping surface of glaciers and ice sheets, their generally high albedo and the limited surface temperature of melting ice, the ABL above glaciers are characterised by a strong temperature inversion and the presence of katabatic winds, caused by the sinking of cold air down a sloping glacier surface.

The aim of this thesis is to improve our understanding of the processes by which heat energy from the atmosphere is transferred through the ABL to glacier surfaces. This is approached from a modelling perspective where appropriate turbulence closure models are developed, interpreted, and applied to both glaciers and the Greenland ice sheet. The first part of this thesis involves the development of such a turbulent closure model which can be used to simulate katabatic flows and the turbulent fluxes associated with them. Knowledge acquired from these simulations is then used to improve the interpretation of meteorological measurements made on glaciers, leading to better estimates of these turbulent fluxes.

The second part of the thesis applies the turbulence closure model to a 3-D boundary layer model of the Greenland ice sheet. This boundary layer model is forced by ECMWF analysis data and simulations are compared to observed meteorological variables of wind, temperature and specific humidity. Experiments with the 3-D model are then carried out to determine the sensitivity of the surface energy flux components to an increase in free atmospheric temperature. The results show that more than half of the increase in the surface energy flux is the result of increases in the turbulent heat fluxes and that albedo feedback can play a significant role in amplifying this increase. In addition, it is pointed out that the climate sensitivity of 2 m temperature is far less than unity as a result of the proximity of the melting ice surface. This is important for other climate sensitivity experiments carried out using 2 m temperature as a forcing parameter.

Samenvatting

Dit proefschrift besteedt aandacht aan de turbulente uitwisseling van warmte tussen atmosfeer en gletsjeroppervlakken. De achterliggende motivatie hiervoor is het voorspellen van de toekomstige zeespiegelstijging. Gezien een groot deel van de zeespiegelstijging wordt bepaald door de massabalans van de cryosfeer, is een verbetering van ons begrip ten aanzien van de fysische processen die de massabalans van gletsjers en ijskappen bepalen nodig. Een groot deel van het massaverlies wordt veroorzaakt door het smelten, het resultaat van stralingsabsorptie en de uitwisseling van turbulente warmte tussen ijs en de bovenliggende atmosfeer, bekend als de atmosferische grenslaag (AG).

Veel aandacht wordt al besteed aan de AG boven landoppervlakken, maar de AG boven gletsjers verschilt van de klassieke grenslaag. Door het hellende oppervlak, de hogere albedo en de beperkende oppervlakte temperatuur van smeltend ijs, wordt de AG boven gletsjers gekenmerkt door een sterke temperatuurinversie en de aanwezigheid van katabatische winden. Deze winden worden veroorzaakt door dalende koude lucht langs het hellende gletsjeroppervlak.

Het doel van dit proefschrift is de verbetering van ons begrip met betrekking op de manier waardoor warmte wordt overgebracht van de AG naar het gletsjeroppervlak. Dit wordt benaderd vanuit een model perspectief waarmee geschikte turbulente sluitingsmethoden worden ontwikkeld, geïnterpreteerd en toegepast op gletsjers en de Groenlandse ijskap. Het eerste deel van dit proefschrift houdt zich bezig met de ontwikkeling van zulke turbulente sluitingsmodellen, die gebruikt kunnen worden voor de simulatie van katabatische stromingen en de bijhorende turbulente fluxen. Kennis verzameld uit deze simulaties wordt vervolgens gebruikt om de interpretatie van meteorologische metingen te verbeteren, wat zal leiden tot betere schattingen van de turbulente flux zelf.

Het tweede deel van dit proefschrift maakt gebruik van het turbulente sluitingsmodel die wordt toegepast op een 3-D atmosferische grenslaagmodel voor de Groenlandse ijskap. Dit model wordt aangedreven door ECMWF analyse data en de simulatie wordt vergeleken met waarnemingen van meteorologische variabelen zoals wind, temperatuur en specifieke vochtigheid. Proeven met het 3-D model worden uitgevoerd om de klimaatgevoeligheid van de oppervlakte energieflexen voor een verandering in atmosferische temperatuur te bepalen. De resultaten hiervan laten zien dat meer dan de helft van de toenamen op oppervlakte energieflexen geweten wordt aan de turbulente warmtefluxen. De albedo terugkoppeling kan ook een belangrijke rol spelen in de versterking hiervan. Verder wordt er op gewezen dat de klimaat gevoeligheid van de 2 m temperatuur veel kleiner is dan één, door de aanwezigheid van een smeltend ijsoppervlak. Dit is belangrijk voor andere klimaatstudies die de 2 m temperatuur als aandrijvende parameter gebruiken.

1

Introduction

The interest in glaciers and ice sheets has for the past decades been fueled by the question of climate change. Ice masses, both large and small, are responsive to climatic variations on differing time scales, and as the result of various physical processes such as precipitation, sublimation, melt, snow drift and calving. The sum of these contributions is known as the mass balance. When mass loss (ablation) is balanced by mass gain (accumulation) then the ice mass is in a steady state with the climate and the total mass balance will be zero.

Variations of the climate system can occur on time scales from decades to hundreds of thousands of years and will lead to changes in glacier mass balance. The current debate on global warming, as the result of anthropological emission of greenhouse gases, has stimulated interest in the response of the cryosphere to climate change, particularly its effect on sea level. A negative mass balance of the various ice masses will contribute to sea level rise, and current estimates (Warrick *et al.*, 1996) indicate a present day global sea level rise of around +1.8 mm per year. This is due to both the thermal expansion of sea water and to the changing mass balance of the cryosphere.

The Antarctic ice sheet, which contains 90% of the worlds grounded ice mass, has a mass balance chiefly dependent on accumulation and calving since, with the exception of the Antarctic peninsula, the grounded ice sheet in Antarctica does not melt. Current estimates indicate a negative mass balance leading to +0.39 mm yr⁻¹ contribution to sea level rise (Huybrechts and de Wolde, 1999). Any increase in temperature in Antarctica will most likely lead to an increase in accumulation and thus a more positive mass balance (Ohmura *et al.*, 1996).

In contrast, the Greenland ice sheet and other small ice caps and glaciers will respond differently to climate change. In Greenland, mass is lost through both calving and melt which are of roughly equal importance in balancing accumulation (Reeh *et al.*, 1999), whilst glaciers and ice caps will loose mass chiefly through melt. Huybrechts and de Wolde (1999) have estimated that the present day mass balance of the Greenland ice sheet is close to zero. However, an atmospheric warming will lead

to a negative mass balance as a result of increased melt. Current estimates suggest that the Greenland ice sheet will contribute from $+0.2$ to $+0.5 \text{ mm yr}^{-1}$ in global sea level rise for just a 1 K atmospheric warming over the coming century (Warrick *et al.*, 1996). Ice caps and glaciers, other than the two main ice sheets, have a mass balance that depends chiefly on accumulation and melt and their contribution to sea level rise is as large as that for Greenland due to their quick response times.

Given the importance of both Greenland and other smaller glaciers to possible sea level change, attention should be given to the physical processes governing their mass balance. The focus of this thesis is on the processes affecting melt. Indeed, one particular aspect will be concentrated on, that being the turbulent exchange of heat between the atmosphere and the ice surface.

1.1 Energy balance of glaciers and ice sheets

The amount of melt that occurs at the surface of a glacier is dependent on the energy flux to the surface. When the surface energy flux is positive the ice or snow will increase in temperature and, once the surface has reached the melting point, melt at a rate proportional to the total energy input. Energy can be transferred to the surface by radiation in the form of short- or longwave radiation fluxes, or via turbulent exchange of latent and sensible heat (Figure 1.1). Processes within the ice or snow pack such as refreezing also affect melt rates.

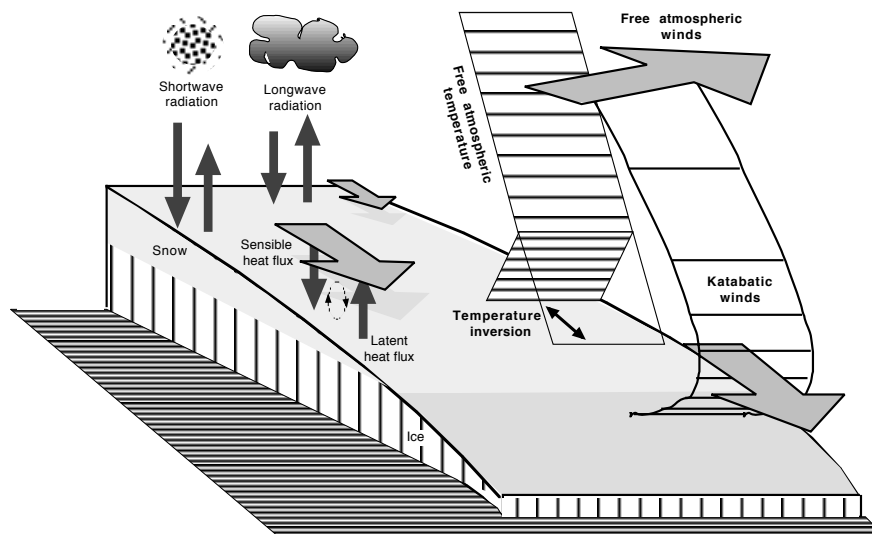


Figure 1.1: Schematic representation of the energy balance and atmospheric boundary layer of a glacier or ice sheet.

The four components of shortwave, longwave, sensible and latent heat make up the surface energy balance. Their influence and sensitivity to atmospheric conditions

varies from glacier to glacier but in general the largest component is the net shortwave radiation flux. In Figure 1.2 a number of sites are listed where observational estimates of the energy balance have been made.

Incoming shortwave radiation originates from the sun and is transmitted through the atmosphere to the surface where it is partially reflected. The ratio of outgoing to incoming solar radiation at the surface is known as the albedo. Incoming longwave radiation is emitted by the atmosphere itself, being primarily dependent on temperature, but also on the constituents of the atmosphere, such as water vapour, CO₂ and ozone. Outgoing longwave radiation is emitted by the surface as a black body, determined by the Stefan-Boltzman equation.

The sensible and latent heat fluxes are the result of turbulent exchange between the surface and the overlying air. Turbulent eddies, created by the inherent non-linearity of atmospheric flow, can transfer heat in the form of temperature (sensible heat) or in the form of water vapour (latent heat). This transfer mechanism is the link between the free atmosphere and the surface. The lower region of the atmosphere where this occurs is known as the atmospheric boundary layer (ABL).

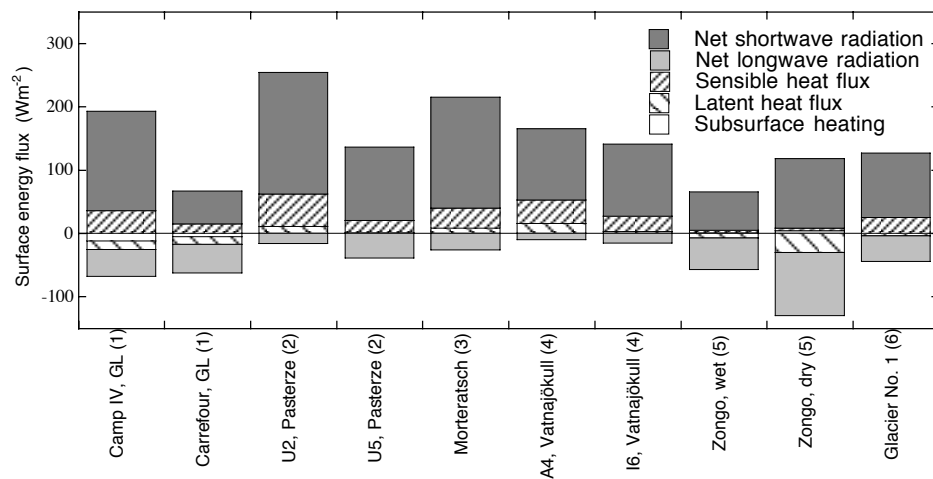


Figure 1.2: Observed energy balance components for a number of glacier sites. (1) Greenland ice sheet, Camp IV at 1013 m a.s.l. and Carrefour at 1850 m a.s.l. (Ambach, 1979); (2) Pasterze glacier Austria, U2 at 2310 m a.s.l. and U5 at m a.s.l. (Greuell and Smeets, 2000); (3) Morteratsch glacier, Switzerland at 2300 m a.s.l. (Oerlemans, 2000); (4) Vatnajökull ice cap, Iceland, A4 at 265 m a.s.l. and I6 at 715 m a.s.l. (de Ruyter de Wildt et al., 2000); (5) Zongo glacier, Bolivia, during wet and dry seasons at 5200 m a.s.l. (Wagnon et al., 1999). (6) Glacier No. 1, China at 3895 m a.s.l. (Ohata, 1989).

The surface energy flux and melt depends on many factors, of which the most important are albedo, temperature and cloud cover. Because incoming shortwave radiation is high during summer, the surface albedo has a strong influence on the absorbed shortwave radiation. The albedo of snow and ice is dependent on such factors as water content, impurity content, grain size and shape, density, debris cov-

erage, and dust (Warren, 1982). Albedo is significantly influenced by the melt process, which alters the grain size and water content, and is sensitive to changes in the total energy balance. This sensitivity is known as the albedo feedback mechanism and can amplify changes in the other energy balance components (van de Wal, 1996).

This is one of the reasons why improved estimates of sensible and latent heat fluxes are necessary. The turbulent heat fluxes as well as the incoming longwave radiation react directly to changes in atmospheric conditions, and so any increase in atmospheric temperature will be transmitted to the surface via these components. Not only do they directly affect the surface energy balance but their effect can be amplified by the albedo feedback mechanism.

1.2 Turbulent fluxes of heat and momentum

Turbulent exchange of momentum, temperature and water vapour with the surface is often described using Monin-Obukhov (M-O) similarity theory (Monin and Obukhov, 1954). This theory uses a number of assumptions concerning homogeneity and the structure of the surface layer in order to develop scaling parameters that can describe the turbulent flow. The surface layer is the turbulent layer close to the surface where fluxes are assumed to vary by less than 10%. This theory gives us the well known logarithmic profiles for wind and scalars (temperature and specific humidity). A necessary parameter in this theory is the concept of a roughness length. This is the height at which the extrapolated logarithmic profile reaches its surface value. Roughness lengths are a necessary parameterisation of the interfacial-sublayer, a transition layer close to the surface where assumptions made in M-O theory no longer hold.

M-O theory is popular because it is relatively simple and it works under many conditions. If profile measurements at two or more levels of wind, temperature and humidity are made in the surface-layer, then the surface fluxes of momentum and sensible and latent heat can be determined. Alternatively measurements made at a single level can also be used if the surface roughness lengths for momentum, temperature and water vapour, as well as their surface values, are known. These two methods are known respectively as the profile and bulk methods. M-O theory is not only useful for interpreting observations but forms the basis for describing the lower boundary layer in atmospheric models.

Though M-O theory is effective in determining turbulent fluxes when the conditions on which it is based are met, it does not necessarily hold on sloping glacier surfaces where katabatic wind maxima are located just above the surface. This inhibits the determination of the turbulent fluxes from observations and the derivation of surface roughness lengths. Both these questions are addressed in this thesis.

1.3 Glacio-meteorology and the atmospheric boundary layer

The atmospheric boundary layer above an ice sheet or glacier is characterized by a strong temperature inversion and the presence of katabatic flows, also known as

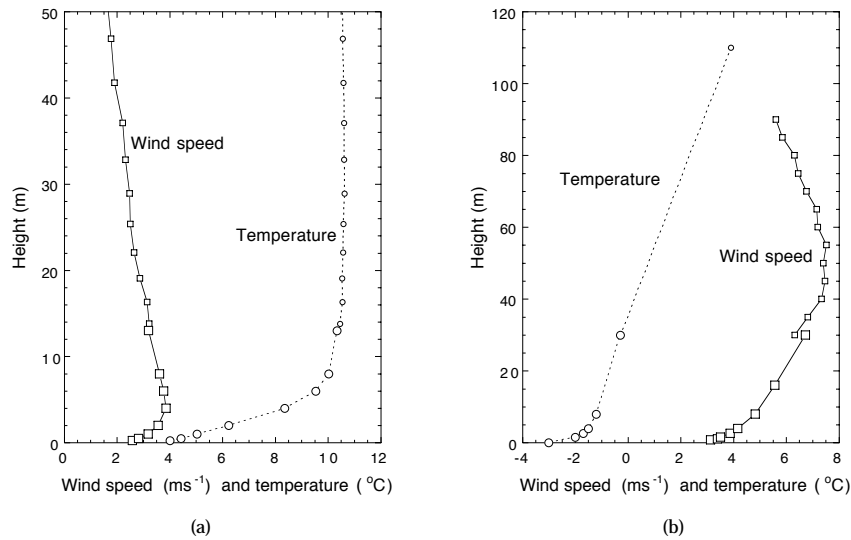


Figure 1.3: (a) Two day average wind and temperature profiles observed on the Pasterze glacier, Austria during the PASTEX campaign in 1994. Observations were made with a 13 m meteorological mast from the Free University of Amsterdam, large circles and squares, and with tethered balloon soundings made by Utrecht University, small circles and squares. (b) Three hour average wind and temperature profiles observed during a strong katabatic period on the Greenland ice sheet during the GIMEX-91 campaign in 1991. Observations were made with a 30 m meteorological mast, large circles and squares, and by sodar, small circles and squares. All observations were made by the Free University of Amsterdam.

glacier winds. The temperature inversion, meaning that temperatures increase with height within the ABL, is the result of either the surface energy balance of the glacier or the limiting temperature of a melting ice surface. In regions where the surface is not melting the radiative energy balance is often negative, which means that more radiation is emitted than absorbed. This is largely due to the high albedo associated with ice or snow surfaces. As a result of the radiative surface cooling, a temperature inversion is created. When the ice surface is melting, a temperature inversion is also created by the limiting melt temperature of 0 °C.

The existence of a temperature inversion on a sloping glacier surface is directly linked to the production of katabatic flows. Colder denser air, created by the inversion, will flow down the inclined glacier surface creating the katabatic wind. This flow will warm the surface as the result of increased turbulent heat fluxes and allow the energy budget to balance in non-melt regions.

Processes other than katabatic forcing can also affect the state of the ABL. Large scale forcing by synoptic pressure gradients produce synoptic winds that can enhance or diminish the katabatic flow. Mesoscale pressure gradients, also known as thermal winds, which are created by horizontal pressure gradients in response to differential cooling of the glacier or the proximity of land or sea masses, can also influence the development of the ABL. However, on glaciers with slopes of 2° or more katabatic forcing will be the dominant forcing mechanism near the surface.

The major characteristic of katabatic flow is the wind speed maximum. This can

be as low as a meter or two above the surface, as on steeper valley glaciers, or several hundred meters high, as on the Greenland ice sheet. The height of the wind speed maximum is dependent on slope, temperature, surface roughness and other forcing mechanisms. The height will depend to a large extent on the turbulent structure of the boundary layer since it is the turbulent transport of momentum down to the surface that retards the katabatic flow. Two examples of observed katabatic flow, the Pasterze glacier in Austria with a local slope of 3.5° and the Greenland ice sheet with a local slope of 0.4° , are shown in Figure 1.3. Both show the general characteristics of katabatic flows, namely the wind speed maxima and temperature inversion.

The ability of the ABL above glaciers to dynamically respond to temperature changes through katabatic forcing is one of the features that differentiates it from the nocturnal ABL, the stable boundary layer that occurs over flat surfaces as a result of night time radiative cooling. Another important feature of the katabatic ABL is that it is forced from beneath and so turbulence is created at the surface, unlike the nocturnal ABL where turbulence is often created at the top of the ABL as the result of flow instabilities. The nature of katabatic flow, its involvement in the surface energy balance and how best to interpret measurements made in katabatic flows are some of the problems addressed in this thesis.

1.4 Observational data

Within this thesis use is made of observational data gathered during various glacio-meteorological campaigns and from automatic weather stations (AWS). These experiments have been carried out by Utrecht University in conjunction with other institutes such as The Free University of Amsterdam, The University of Innsbruck and The University of Iceland. Data used in this thesis was collected during the Greenland Ice Margin Experiment in 1991 (GIMEX-91) (Oerlemans and Vugts, 1993), the Pasterze Experiment (PASTEX) Austria in 1994 (Smeets *et al.*, 1998), the Glacio-meteorological campaign on the Vatnajökull ice cap Iceland in 1996 (Oerlemans *et al.*, 1999) and AWS data from Greenland collected along the GIMEX K-transect in 1998. Data from the PARCA AWS network in Greenland, University of Colorado, have also been used in the comparisons (Steffen *et al.*, 1996).

The 13 m meteorological mast from the Free University of Amsterdam used during the PASTEX campaign and one of the Greenland AWS from Utrecht University are shown in Figure 1.4. The observational data collected from such stations are essential for understanding boundary layer processes as well as for model verification. The usefulness of such experimental campaigns cannot be underestimated and much of the work presented in this thesis is dependent on the availability of these observational data.

1.5 Modelling the atmospheric boundary layer

One of the major tools used for interpretation and understanding of the ABL is numerical simulation. Many simulation studies of katabatic flows have been carried out, ranging from 1-D bulk models to 3-D mesoscale models. An overview of some

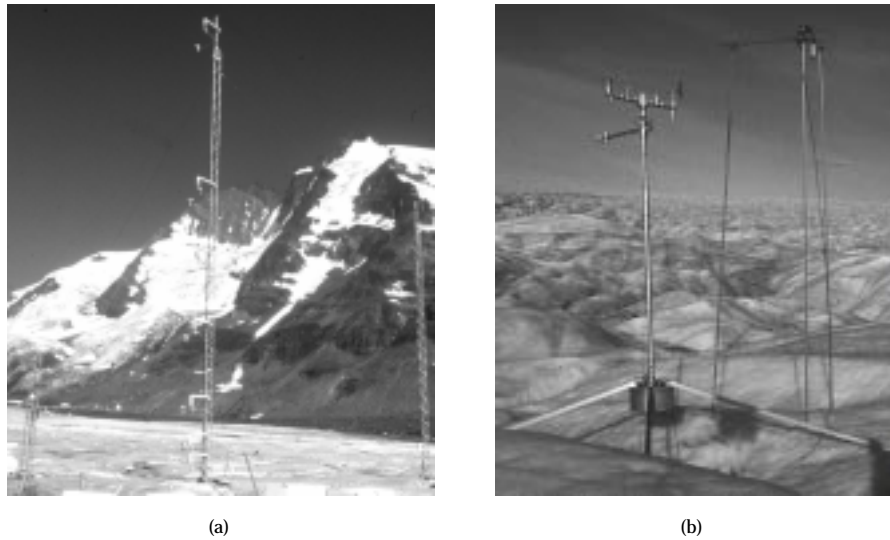


Figure 1.4: (a) 13 m meteorological mast from the Free University of Amsterdam during the PASTEX campaign, Pasterze glacier Austria in 1994. (b) Automatic weather station S5 and sonic height sensor in West Greenland from Utrecht University in 1998.

of the papers concerned directly with modelling katabatic flows is given in Chapter 2. There are fewer model studies directly concerned with the ABL above glaciers and the Greenland ice sheet, which are the focus of this thesis.

For the Greenland ice sheet, 2-D modelling studies of GIMEX data along the K-transect have been carried out by Meesters *et al.* (1994) and Gallée and Duynkerke (1997) as well as bulk model studies by van den Broeke (1997a). All these models use horizontal resolutions of less than 20 km in order to resolve surface topography near the ice margin, but are limited to two dimensional simulations for short periods.

Other modelling studies concerned with the mass and energy balance of Greenland have used low resolution GCMs, e.g. Thompson and Pollard (1997) or Glover (1999), to simulate precipitation and melt. The horizontal resolution of these models is larger than 2.8° (300 km). As such they fail to resolve the topography of the narrow ablation region of Greenland to a sufficient accuracy. To overcome this problem, downscaling techniques are applied so that coarse GCM data is interpolated to a higher resolution topography and the GCM fields of wind, temperature and humidity are extrapolated using assumed lapse rates. These models, even when downscaling is applied, have been shown by the authors to overestimate ablation by a factor of 2 to 6. The GCM simulation from Ohmura *et al.* (1996) using a model resolution of 1° (125 km) gave improved estimates for precipitation and ablation without downscaling.

Despite the improvement with increased resolution these GCM models still fail to resolve the narrow ablation region of the Greenland ice sheet. Incorrect topography, resulting from the low resolution, will affect not just extrapolated temperatures but also katabatically induced winds near the ice margin. To improve estimates of the turbulent heat fluxes in the ablation region of the Greenland ice sheet, a 3-D

boundary layer model is developed in the second part of this thesis with a maximum horizontal resolution of 10 km, sufficient to resolve much of the ablation region.

1.6 Contents of this thesis

The major aim of the research described here is to improve our understanding of the role turbulent fluxes play in the energy balance of glaciers and ice sheets. To do this, models are developed that can describe the dynamic processes of the ABL under conditions of katabatic flow. Methods for determining turbulent fluxes and surface roughness lengths from observational data are also discussed. The thesis is essentially divided into two parts. The first part, Chapters 2 to 5, is concerned with the interpretation of measurements made on sloping glacier surfaces with the help of a 1-D turbulence model which is developed in Chapter 2. The second part, Chapters 6 and 7, involves the development, verification and application of a 3-D boundary layer model to the Greenland ice sheet. This allows estimates of the surface energy fluxes and their sensitivity to climate change to be made.

The basis of this thesis is laid in **Chapter 2**. In this paper a 1-D turbulent closure model is developed which is suitable for simulating katabatic flows under stable conditions. This model is based on second-order closure schemes developed by Hanjalić and Launder (1972) and Shir (1973) more than two decades ago. Such a model is needed because many of the assumptions made in more popular formulations, based on M-O similarity theory (Monin and Obukhov, 1954) or local scaling arguments (Nieuwstadt, 1984), are not valid under conditions of katabatic flow. This point is highlighted in the first four chapters of this thesis. The closure scheme is tested for the classical stable ABL and on sloping surfaces where katabatic flows develop. The model results are compared to observations of mean and turbulent quantities for both cases.

In **Chapter 3** the 1-D turbulent closure model is used to help interpret measurements made under conditions of katabatic flow on glaciers. It is shown that profile methods cannot be used in order to determine turbulent fluxes or surface roughness lengths due to the presence of the wind speed maximum. Furthermore, it is shown that the best estimate will come from the bulk method if surface roughness lengths are known.

The problem of determining surface roughness lengths is addressed in **Chapter 4** and **Chapter 5**. In the first of these two papers, use is made of the dynamics of katabatic flows in order to determine the surface momentum flux. This can be done by integrating the temperature profile up to the height of the wind speed maximum. Having determined the momentum flux in this way, katabatic profile fits are made to the data to derive the roughness length for momentum. Comparison is made with bulk derived fluxes, direct eddy correlation measurements and with profile derived roughness lengths determined when the wind speed maximum was not present.

The roughness lengths for temperature and water vapour are physically different to that of momentum since they do not involve pressure fluctuations or ‘form drag’. In **Chapter 5** data from the Vatnajökull experiment are used to determine the surface roughness length for temperature. With the newly acquired knowledge of the turbulent structure of katabatic flows described in the foregoing chapters, an appropriate

selection criteria is applied to these data in order to determine the roughness lengths of the ice surface. Standard profile methods are applied to determine the surface roughness lengths for momentum and temperature. It is shown that surface renewal theories, often used to determine roughness lengths for scalars, are valid.

The second part of the thesis is contained in the last two chapters, **Chapter 6** and **Chapter 7**, where the previously developed 1-D turbulence model is applied to the Greenland ice sheet. To accomplish this a 3-D hydrostatic boundary layer model, essentially a form of dynamic downscaling, is developed and applied to the entire Greenland ice sheet with a horizontal resolution of 10 to 20 km. The aim of this model is to simulate the spatial and temporal distribution of the various energy balance components on the ice sheet and their response to changes in free atmospheric temperature. The high resolution is necessary to resolve the thin ablation region of the ice sheet where energy fluxes lead to melt.

The Greenland Atmospheric Boundary Layer Model (GABLM) is forced by ECMWF analysis fields of synoptic pressure, temperature and humidity from above the boundary layer, as well as cloud cover and sea surface temperature. In this way, free atmospheric meteorological fields are taken from the coarser ECMWF fields, with a horizontal resolution of approximately 70 – 125 km, and dynamically down-scaled to determine surface energy fluxes and near surface meteorological parameters.

The simulations are compared with observations at several sites on the ice sheet. In **Chapter 6** use is made of GIMEX observational data from 1991 for verification. In **Chapter 7** the entire ablation season is simulated for the year 1998 when more AWS data are available, allowing a more comprehensive comparison with observations. The model simulations compare quite well with observations and are seen in most cases to improve on ECMWF analysis of near surface meteorological variables.

Lastly the model is used for a climate sensitivity run where the sensitivity of the energy balance to an increase in atmospheric temperature is tested. From this, simplified parameterisations linking turbulent heat and longwave radiation fluxes to free atmospheric temperature are developed for application in energy balance models.

Three of the Chapters presented here are already accepted or published articles and one is undergoing the review process. They are presented in this thesis in almost the exact form, apart from typesetters eccentricities, in which they are published.

Chapter 2: Denby B. (1999). Second-order modelling of turbulence in katabatic flows. *Boundary-Layer Meteorol.*, **92**, 67–100.

Chapter 3: Denby, B. and Greuell, W. (2000). The use of bulk and profile methods for determining the surface heat fluxes in the presence of glacier winds. *J. Glaciol.* **46**, 445–452.

Chapter 4: Denby, B. and Smeets, P. (2000). Derivation of turbulent flux profiles and roughness lengths from katabatic flow dynamics. *J. Appl. Meteorol.*, **39**, 1601–1612.

Chapter 5: Denby, B. and Snellen, H. (2000). Observed roughness lengths for momentum and temperature on a melting glacier surface. *Submitted to J. Geophys. Res.*

2

Second-Order Modelling of Turbulence in Katabatic Flows

A complete one-dimensional second-order closure model is used to simulate katabatic flows observed on glaciers and ice caps. The model is tested with two different closure assumptions for the viscous dissipation, one based on a prognostic equation for ϵ and the other on a diagnostic buoyant length scale. Both formulations give quite similar results. Model simulations are compared to observations made over sloping ice surfaces during periods dominated by katabatic flow. In general good agreement is found for both mean wind and temperature profiles as well as eddy correlation measurements. It is also found that the turbulent transport terms play an important role in katabatic flows as opposed to the classical stable boundary layer where these terms are usually ignored. Even the turbulent transport of temperature variance, which leads to the well known countergradient term in unstable boundary layers, is relatively important for modelling the observed temperature profiles. The effect of these terms on the flux-profile relationships, using observed and simulated profiles, is also discussed.

2.1 Introduction

Katabatic flows, also known as drainage or gravity flows, are generated by vertical density gradients on sloping surfaces. Air cooled by turbulent exchange with a colder surface will 'sink' downslope, being forced by the effect of buoyancy. Unlike boundary layers on flat surfaces the dynamics of the flow is intrinsically determined by the temperature field, the so called katabatic forcing term.

In the atmospheric boundary layer these flows can occur on any sloping surface but the katabatic forcing is generally smaller than other terms in the momentum budget, such as the synoptic pressure gradient. It is therefore usually only possible to observe drainage flows during clear sky conditions when night time radiative cooling of the land surface is at its strongest. Several papers have been published concerning this phenomenon, e.g. Yamada (1983) and Horst and Doran (1986), but the observational data have been quite limited. Recent measurements made above glaciers and ice caps, e.g. Oerlemans *et al.* (1999) and Smeets *et al.* (1998), have provided a new and much more continuous source of data on katabatic flows.

The modelling of katabatic flows has been, to varying degrees of success, carried out by several authors. Table 2.1 gives a list of these papers and the closure schemes used by each author. These closure schemes all require a velocity and length scale to calculate turbulent exchange coefficients. Most authors use the so called 1.5-order closure from Delage (1974), which uses a prognostic equation for the turbulent kinetic energy (TKE) to determine the velocity scale and a length scale calculated using local Monin-Obukhov theory (M-O). These models are thus dependent on parameterisations determined for horizontally homogenous and vertically monotonous stable boundary layers (SBL). Some authors, e.g. Yamada (1983) and Gallée *et al.* (1995), have used prognostic equations for the dissipation to determine the dissipative length scale.

Conditions in katabatic flows are, however, incompatible with some of these parameterisations. In particular, consider the existence of a wind maximum close to the surface, which is one of the most prominent features of katabatic flows. Generation of turbulence by shear at this maximum is zero, as is the vertical exchange of momentum. The local scaling velocity u_* will thus be zero as will the local Obukhov length (Λ), by definition. According to parameterisations using M-O theory turbulent exchange across the wind maximum would cease and a total de-coupling of the flow would occur.

This sort of problem is often overcome by placing limits on flux-profile relationships or on length scales, which are generally ad-hoc and not always specified. It is the aim of this paper to shed some light on the type of turbulent closure necessary to realistically simulate katabatic flows. As a starting point we turn to second-order closures of the type that have been effectively applied to near-wall jets. These flows have a similar vertical velocity structure to katabatic flows (Irwin, 1974). We will limit ourselves to a quasi one-dimensional case where two-dimensional influences will be parameterised. This is meant to simplify interpretation of the vertical structure of katabatic flows with which we are concerned in this study.

We begin by discussing the equations and closures used in the second-order model as well as a short discussion concerning the derivation of the closure constants. Using the approximation for a 1-D homogenous boundary layer on a tilted

surface, equations are derived for the mean and second-order terms. These equations are firstly solved analytically, using standard assumptions of steady state and the neglect of transport terms, giving non-dimensional solutions for the stable boundary layer on a sloping surface. Numerical solutions of the complete set of equations are then carried out for three case studies, consisting of a standard SBL and two katabatic cases of differing slope, and then for three different observational periods taken from recent measurement campaigns on sloping ice surfaces.

Using these results we investigate the sensitivity of the model to several closure assumptions, including two different viscous dissipation closures, and to the effect of slope on the second moment equations. The role of the turbulent transport terms in the TKE budget and on the flux-profile relationships will also be discussed and their importance highlighted. Lastly, the model will be compared with a simplified version with a view to determining the most efficient method necessary to effectively simulate these types of flows.

Table 2.1: List of authors and closures used in modelling katabatic flows.

Paper	Closure scheme
Rao and Snodgrass (1981)	Prognostic TKE using M-O length scale.
Yamada (1983)	Prognostic TKE and prognostic $q^2 l$.
Doran and Horst (1983)	Prognostic TKE with limited M-O length scale.
Arritt and Pielke (1986)	Prognostic TKE using M-O length scale.
Nappo and Shankar Rao (1987)	Prognostic TKE using M-O length scale.
Wong <i>et al.</i> (1987)	First-order with Richardson number.
Økland <i>et al.</i> (1988)	Prognostic TKE with BL depth length scale.
Meesters <i>et al.</i> (1994)	First-order with limited Richardson number.
Gallée <i>et al.</i> (1995)	Prognostic TKE and prognostic ϵ .
Davies <i>et al.</i> (1995)	Prognostic TKE using M-O length scale.

2.2 Mean and second moment equations

The mean Navier-Stokes equations for dry air after Reynolds decomposition, see e.g. Garratt (1992), are given by:

$$\frac{DU_i}{Dt} = -\frac{\partial \overline{u_i u_j}}{\partial x_j} - \frac{1}{\rho} \frac{\partial P}{\partial x_i} - g_i + f \epsilon_{i3k} U_k \quad (2.1)$$

$$\frac{D\Theta}{Dt} = -\frac{\partial \overline{u_j \theta}}{\partial x_j} \quad (2.2)$$

The variables have been separated into their mean (U_i, Θ, P) and fluctuating (u_i, θ, p) components and we have ignored adiabatic heating terms. In the above equations we have assumed incompressibility and have neglected the effect of viscosity. The other terms have their usual meaning.

The second moment equations, neglecting the effects of rotation and radiation and having related density fluctuations to temperature fluctuations via the equation

of state, are written as follows, e.g. Launder (1975):

$$\begin{aligned}
\frac{D\overline{u_i u_j}}{Dt} = & - \underbrace{\left(\overline{u_i u_k} \frac{\partial U_j}{\partial x_k} + \overline{u_j u_k} \frac{\partial U_i}{\partial x_k} \right)}_{MP_{ij}} - \underbrace{\frac{1}{\Theta} (g_j \overline{u_i \theta} + g_i \overline{u_j \theta})}_{BP_{ij}} \\
& - \underbrace{2\nu \frac{\partial u_i}{\partial x_k} \frac{\partial u_j}{\partial x_k}}_{DIS_{ij}} + \underbrace{\frac{p}{\rho} \left(\frac{\partial u_i}{\partial x_j} + \frac{\partial u_j}{\partial x_i} \right)}_{PS_{ij}} \\
& - \underbrace{\frac{\partial \overline{u_i u_j u_k}}{\partial x_k} - \frac{\partial}{\partial x_k} \left(\delta_{ik} \frac{\overline{u_j p}}{\rho} + \delta_{jk} \frac{\overline{u_i p}}{\rho} \right)}_{TR_{ij}} \quad (2.3)
\end{aligned}$$

$$\begin{aligned}
\frac{D\overline{u_i \theta}}{Dt} = & - \underbrace{\left(\overline{u_i u_k} \frac{\partial \Theta}{\partial x_k} + \overline{u_k \theta} \frac{\partial U_i}{\partial x_k} \right)}_{MP_{i\theta}} - \underbrace{\frac{g_i}{\Theta} \overline{\theta^2}}_{BP_{i\theta}} \\
& - \underbrace{(\kappa_T + \nu) \frac{\partial \theta}{\partial x_k} \frac{\partial u_i}{\partial x_k}}_{DIS_{i\theta}} - \underbrace{\frac{1}{\rho} \frac{\partial p}{\partial x_i}}_{PS_{i\theta}} - \underbrace{\frac{\partial \overline{u_i \theta u_k}}{\partial x_k}}_{TR_{i\theta}} \quad (2.4)
\end{aligned}$$

$$\begin{aligned}
\frac{D\overline{\theta^2}}{Dt} = & - \underbrace{2\overline{u_k \theta} \frac{\partial \Theta}{\partial x_k}}_{MP_{\theta\theta}} - \underbrace{2\kappa_T \left(\frac{\partial \theta}{\partial x_k} \right)^2}_{DIS_{\theta\theta}} - \underbrace{\frac{\partial \overline{\theta^2 u_k}}{\partial x_k}}_{TR_{\theta\theta}} \quad (2.5)
\end{aligned}$$

Here, MP represents terms due to mean field generation (for momentum this is mechanical production), BP represents buoyancy generation, DIS the viscous dissipation, PS the pressure-strain/temperature correlations and TR the turbulent transport terms.

Contained in the above Reynolds stress equations are a number of terms requiring closure. Various authors have used different techniques in order to close the above set of equations in terms of the mean flow and second moment components. The closure schemes to be used here are based on the work of Hanjalić and Launder (1972), Shir (1973), Irwin (1974), Launder (1975) and Gibson and Launder (1978). These closure schemes have been tested under varying laboratory conditions and have proved successful for thin shear flows and plane wall jets. More recently the same schemes have been applied to the atmospheric boundary layer (ABL) by Andrén (1990) and Koo and Reible (1995).

The closures are slightly different to those more commonly used in the ABL, e.g. Mellor and Yamada (1982), and make use of wall effects in the pressure-strain correlations to account for the observed turbulent anisotropy that results from the proximity of a wall.

2.3 Second-order closures

In this section we briefly describe the approaches used to close Equations (2.3–2.5). Three different terms need to be closed at this level. They are the viscous dissipation terms, the turbulent transport terms and the pressure-strain/temperature correlations.

2.3.1 Viscous dissipation of momentum and heat (DIS)

Here, two approaches are used for the closure of the viscous dissipation term in Equation 2.3. Both of these assume the turbulence to be isotropic at the dissipative length scale so that DIS_{ij} can be written as

$$2\nu \frac{\partial u_i}{\partial x_k} \frac{\partial u_j}{\partial x_k} = \delta_{ij} \frac{2}{3} \epsilon \quad (2.6)$$

The first closure, initially proposed by Kolmogorov (1941), relates the viscous dissipation ϵ to a length and velocity scale according to

$$\epsilon = c_\epsilon \frac{E^{3/2}}{l} \quad (2.7)$$

where $E = 1/2 \overline{u_i u_i}$ is the turbulent kinetic energy (TKE), l is the dissipative length scale and c_ϵ is a constant.

The above length scale is usually specified for boundary layers by writing it in terms of the height z and an asymptotic length scale. We use the local buoyant length scale l_b (Brost and Wyngaard, 1978; Nieuwstadt, 1984) as the appropriate asymptotic length scale, which is based on the balance between inertial and buoyant forces. The asymptotic form used here is written as

$$\frac{1}{l^2} = \frac{1}{(\kappa z)^2} + \frac{1}{l_b^2} \quad (2.8)$$

where,

$$l_b = \kappa C_B \left(\frac{\overline{w^2}}{N^2} \right)^{1/2} \quad (2.9)$$

and where N is the Brunt Väisällä frequency and C_B a constant. Note that the exact form of the asymptotic length scale (Equation 2.8) is quite arbitrary, most authors using a first power equation. We have chosen a second power form because of its faster approach to the asymptotic limits.

The alternative to the above closure is to develop a prognostic equation for the viscous dissipation ϵ . This has been done by several authors in various forms such as the ‘k- ϵ ’ closure from Hanjalić and Launder (1972), ‘E- ϵ ’ closures from Detering and Etling (1985) and Duynkerke (1988), a prognostic equation for ‘ l ’ from Shir (1973) or the ‘ $q^2 l$ ’ equation used by Yamada (1983).

The formulation used here is the one suggested by Duynkerke (1988), which not only takes into account the production of turbulence through mechanical production

(MP_E) but also includes the effect of transport (TR_E) and buoyancy (BP_E) terms when they are positive. Basically the rate of dissipation is assumed to be linked, via the energy cascade, to the production of turbulence in the TKE equation, its dissipation and a transport term.

$$\begin{aligned} \frac{D\epsilon}{Dt} = & c_{\epsilon 1} \frac{\epsilon}{E} (MP_E + \max(0, BP_E) + \max(0, TR_E)) - c_{\epsilon 2} \frac{\epsilon^2}{E} \\ & + c_{\epsilon s} \frac{\partial}{\partial x_k} \left\{ \frac{E}{\epsilon} \overline{u_k u_l} \frac{\partial \epsilon}{\partial x_l} \right\} \end{aligned} \quad (2.10)$$

It is worth noting that the above equation, though based on reasonable arguments (Hanjalić and Launder, 1972), is built entirely on parameterised terms and must be considered a highly ‘engineered’ solution.

Under isotropic conditions the viscous dissipation term in the temperature covariance Equation 2.4 is zero. Assuming near isotropic turbulence on the dissipative scale then we can ignore this term. The viscous dissipation of the temperature variance (Equation 2.5), on the other hand, is considered to be directly related to the viscous dissipation of momentum (Launder, 1975) by

$$2\kappa_T \theta \frac{\partial^2 \theta}{\partial x_k^2} = 2\epsilon_\theta = 2d_\epsilon \frac{\epsilon}{E} \theta^2 \quad (2.11)$$

2.3.2 Turbulent transport (TR)

The transport terms, which include both turbulent and pressure transport, are generally ignored in most SBL models since they would appear to play a minor role in a layer with monotonically decreasing flux. Only in the upper region of the boundary layer does this term appear to be of any relative importance (Delage, 1974). However, these terms are very important in flows associated with jets where the transport terms allow exchange of momentum and energy across the jet.

It is possible to derive prognostic equations for the third moment terms in the turbulent transport equations. From these equations the following closure form can be derived, e.g. Nieuwstadt and van Dop (1981), where the buoyant terms have been ignored.

$$\overline{u_i u_j u_k} = -c_s \frac{E}{\epsilon} \left(\overline{u_i u_l} \frac{\partial \overline{u_j u_k}}{\partial x_l} + \overline{u_j u_l} \frac{\partial \overline{u_k u_i}}{\partial x_l} + \overline{u_k u_l} \frac{\partial \overline{u_i u_j}}{\partial x_l} \right) \quad (2.12)$$

Irwin (1974) has used the above form for his model of a plane wall jet and found the calculated triple correlations to agree quite well with observations.

The turbulent transport terms for heat have been defined by Mellor and Yamada (1982) using the following form, which is similar to the transport closure for momentum.

$$\overline{u_i \theta u_k} = -d_{s1} \frac{E^2}{\epsilon} \left(\frac{\partial \overline{u_k \theta}}{\partial x_i} + \frac{\partial \overline{u_i \theta}}{\partial x_k} \right) \quad (2.13)$$

$$\overline{u_k \theta^2} = -d_{s2} \frac{E^2}{\epsilon} \frac{\partial \overline{\theta^2}}{\partial x_k} \quad (2.14)$$

Little is known concerning the pressure transport terms. They are difficult to measure directly in the ABL and are usually only deduced from budget residuals, e.g. Brost *et al.* (1982). We simply ignore them or assume them to have parameterised forms similar to the turbulent transport terms. In this way they are absorbed into the constants for turbulent transport.

2.3.3 Pressure-strain/temperature correlations (PS)

In shear flows the pressure-strain correlations lead to a redistribution of turbulence from the direction of production into the other components, what Rotta (1951) calls the return to isotropy. Its total contribution to the turbulent kinetic energy is zero. From laboratory experiments (Gibson and Launder, 1978) it has been confirmed that the proximity of a wall profoundly influences this redistribution, limiting the contribution to the variance component normal to the wall surface.

The pressure-strain correlations are closed by assuming them to consist of three components representing: 1- turbulent interactions, 2- mean strain effects, and 3- buoyant terms. Using the same notation as Gibson and Launder (1978) this may be written as

$$PS_{ij} = \phi_{ij} = \phi_{ij,1} + \phi_{ij,2} + \phi_{ij,3} + (\phi'_{ij,1} + \phi'_{ij,2} + \phi'_{ij,3}) F(n, l) \quad (2.15)$$

where the primes indicate the anisotropic terms and the subscripts 1, 2 and 3 represent the three components previously mentioned. The proximity of the wall is reflected by the factor F , which is a function of the distance to the wall (n) and the turbulent length scale (l). It is defined as being equal to unity close to the wall and approaches zero for free-shear flows. The pressure-temperature correlations in Equation 2.4 are treated analogously to those for momentum. The complete set of equations describing these correlations are listed in Appendix 2.A.

2.4 Determination of constants

Contained in the above closures are a number of constants that need to be determined. Their values are chiefly calculated from the results of simplified laboratory experiments or atmospheric observations under near-neutral conditions. One of the assumptions associated with second-order closures is that these constants remain relatively unchanged for different flow regimes and stabilities. The following is a short description of the methods used to determine the set of constants for the above closures. The full set of equations needed to calculate these constants is listed in Appendix 2.B.

Before determining these constants we define the non-dimensional ratio of Reynolds stresses and variances to the turbulent kinetic energy as $a_{ij} = \overline{u_i u_j} / E$ for both near-wall (designated with a prime) and free-shear flows under neutral conditions. A set of these ratios taken from various papers is listed in Appendix 2.B, Table 2.B.1. Note that atmospheric boundary layer measurements are also considered to be near-wall.

To start with, the constants c_2 , c_3 , and d_3 can be determined from isotropic turbulence conditions and are given by $c_2 = 0.6$ (Crow, 1968), $c_3 = 0.3$ and $d_3 = 0.33$ (Gibson and Launder, 1978). Furthermore, under idealised conditions, it is possible to use the near-wall and free-shear ratios a_{ii} to determine the pressure correlation constants c_1 , c'_1 , d_1 and d'_1 . By solving Equation 2.3, using the closure assumptions under steady state and neutral free-shear conditions, a relationship between the constants c_1 and c_2 can be found, which gives $c_1 = 1.82$. The near wall constants $c'_1 = 0.98$ and $c'_2 = 0.05$ are also determined in a similar fashion using appropriate near-wall values. The values $d_1 = 3.0$ and $d'_1 = 3.8$ are determined for near-neutral conditions using the ratios a_{ii} and the near neutral turbulent Prandtl number (σ_{To}).

In order to determine c_ϵ in Equation 2.7 we turn to the neutral boundary layer where the following definition is applied.

$$\phi_m(\text{neutral}) = 1 = \frac{\kappa z}{u_*} \frac{\partial U}{\partial z} \quad (2.16)$$

Combining this with Equation 2.7, assuming $l = \kappa z$ where $\kappa = 0.4$, gives $c_\epsilon = a'_{13}{}^{3/2} = 0.076$.

We also define the following non-dimensional ratios which can be used to determine the remaining buoyancy related constants.

$$b_1 = \frac{\overline{u\theta}}{w\theta} \quad b_2 = \frac{\overline{\theta^2 \overline{uw}}}{\overline{w\theta}^2} = - \left(\frac{\sigma_\theta}{\theta_*} \right)^2 \quad b_3 = \frac{\epsilon}{E} \frac{\overline{\theta^2}}{\epsilon_\theta} \quad (2.17)$$

The ratios b_2 and b_3 are actually manifestations of the same constant, however b_2 is more commonly referred to in the ABL. They both represent the ratio of the decay time of velocity to temperature fluctuations (Gibson and Launder, 1978). Using these ratios d_ϵ can be determined from Equation 2.11 and a value of $d_\epsilon = 0.77$ is reasonably consistent for both laboratory and atmospheric data. Using Equation 2.4 under near neutral conditions, and the previously mentioned non-dimensional ratios, gives $d_2 = 0.78$. The constants c'_3 and d'_3 have been set to zero for lack of information and the constant d'_2 has not been determined since it does not appear in the equations after simplification for a flat wall.

The transport constants c_s and $d_{s1,2}$ can, in principle, only be determined by detailed comparison of observed second- and third-order velocity correlations with modelled flows. As previously mentioned Irwin (1974) found a reasonably good comparison for wall jets using a value of $c_s = 0.08$. Launder (1975) found a value of $c_s = 0.11$ by optimising their simulations. Measurements made directly in the neutral marine ABL by Brost *et al.* (1982) and Grant (1990) give values for c_s of 0.14 and 0.28 respectively. We choose to use a value of $c_s = 0.20$, which lies somewhere between the two atmospheric values. Still less clear are the appropriate values for

$d_{s1,2}$. When these are specified, e.g. Mellor and Yamada (1982), they are generally given the same effective coefficient as c_s . For lack of any other information we will use the formulation $d_{s1,2} = a_{33}c_s$.

There remains one more buoyancy related constant, that is C_B , used to determine the buoyant length scale. A value of 1.69 has been used by Brost and Wyngaard (1978) and Nieuwstadt (1984). This is based on computer simulations that match the constant to desired critical Richardson numbers. For the moment we will retain the value of 1.69.

The constants used in the prognostic dissipation equation have been taken from Duynkerke (1988) and Duynkerke and Nieuwstadt (1989) who give a thorough account of their derivation. Their values are listed below, with all the other constants, in Table 2.2.

Table 2.2: Closure constants used in this paper based on atmospheric and laboratory data. For details of their derivation see Appendix 2.B

c_1	c_2	c_3	c'_1	c'_2	d_1	d_2	d_3	d'_1	
1.82	0.6	0.3	0.98	0.05	3.01	0.78	0.33	3.8	
c_ϵ	d_ϵ	c_s	d_{s1}	d_{s2}	C_B	$c_{\epsilon1}$	$c_{\epsilon2}$	$c_{\epsilon s}$	κ
.076	0.77	0.2	0.05	0.05	1.69	1.46	1.83	0.027	0.4

2.5 Simplification for a homogenous 1-D boundary layer on a tilted surface

Since we are primarily interested in the vertical structure of katabatic flows we wish to simplify Equations 2.1–2.5 to their one-dimensional form. To do this we assume a horizontally homogenous boundary layer rotated around the x_2 axis. This implies that all derivatives in the $x_{1,2}$ directions are zero. Furthermore the equations are split into an ambient part in which the pressure gradients are in hydrostatic and geostrophic balance, marked by the subscript zero, and a perturbation from this hydrostatic state, marked by a prime. This allows the effect of density variations to be translated to temperature perturbations following the equation of state. i.e. $P = P_o + P'$, $\Theta = \Theta_o + \Theta'$, $\rho = \rho_o + \rho'$ and $\rho'/\rho_o = -\Theta'/\Theta_o$ where $\Theta_o(x_3) = \Theta_o(x_{3r}) + \gamma_\theta(x_r - x_{3r})$ and γ_θ is the ambient potential temperature gradient and x_{3r} is a reference height.

The transformation from one set of co-ordinates x_i to another \tilde{x}_i can be accomplished by use of the metric tensor (Anderson *et al.*, 1984). The metric tensor and the vector gravity field under rotation around the x_2 axis through an angle α , that is defined to be positive in the anti-clockwise direction, is given by:

$$\frac{\partial \tilde{x}_i}{\partial x_j} = \begin{bmatrix} \cos \alpha & 0 & \sin \alpha \\ 0 & 1 & 0 \\ -\sin \alpha & 0 & \cos \alpha \end{bmatrix} \quad \mathbf{g} = g \begin{bmatrix} \sin \alpha \\ 0 \\ \cos \alpha \end{bmatrix} \quad (2.18)$$

Rewriting Equation 2.1 and 2.2 in their transformed form, after application of the

above 1-D approximations, gives the following set of equations for the mean flow values, where the primes for the perturbation quantities have been dropped. The transformed co-ordinate system is now indicated by $\tilde{x}_i = (x, y, z)$ and the velocity vectors by $\tilde{U}_i = (U, V, W)$ and $\tilde{u}_i = (u, v, w)$.

$$\frac{\partial U}{\partial t} = -\frac{\partial \overline{uw}}{\partial z} + (\sin \alpha) \frac{g}{\Theta_o} \Theta + (\cos \alpha) f(V - V_g) \quad (2.19)$$

$$\frac{\partial V}{\partial t} = -\frac{\partial \overline{vw}}{\partial z} - f(U - U_g) \quad (2.20)$$

$$\frac{\partial \Theta}{\partial t} = -(\sin \alpha) \gamma_\theta \overline{U} - \frac{\partial \overline{w\theta}}{\partial z} \quad (2.21)$$

In the above equations the katabatic forcing term is given by the temperature perturbation term in Equation 2.19 and is always largest near the surface for katabatic flows. Though radiative cooling can be important in the temperature budget it has been left out of the following analysis for simplicity.

The second moment equations under the above rotation, and using the homogeneous boundary layer approximation, are given in Appendix 2.C. These Equations (2.C.12–2.C.22) differ from similar forms derived by other authors, e.g. Koo and Reible (1995) and Shir (1973), by the presence of the turbulent transport terms and slope dependence.

As an example we show the TKE equation (2.C.18) based on these second-order closures below.

$$\begin{aligned} \frac{\partial E}{\partial t} = & - \left(\overline{uw} \frac{\partial U}{\partial z} + \overline{vw} \frac{\partial V}{\partial z} \right) + \frac{g}{\Theta_o} (\sin \alpha \overline{u\theta} + \cos \alpha \overline{w\theta}) - \epsilon \\ & + \frac{\partial}{\partial z} \left\{ c_s \frac{E}{\epsilon} \left(\overline{uw} \frac{\partial \overline{uw}}{\partial z} + \overline{vw} \frac{\partial \overline{vw}}{\partial z} + \overline{ww} \frac{\partial (E + \overline{ww})}{\partial z} \right) \right\} \end{aligned}$$

The turbulent transport term, though it contains some extra components, is still basically a diffusion type term. The buoyancy term, however, is slightly different due to the influence of the slope. Through the rotation of the gravity vector, buoyancy effects can now occur in the direction of the flow. In fact if the ratio $\overline{u\theta}/\overline{w\theta} < -\cot \alpha$ then buoyancy effects, even under extremely stable stratifications, can lead to positive buoyant production in the flow. This will be discussed further in the following section.

2.6 Non-dimensional analysis of the second-order equations: the influence of slope and turbulent transport

Before numerically solving the complete set of second moment equations it is worthwhile checking the results obtained from a non-dimensional analysis of these equations. This can be done if we assume steady state conditions, ignore the transport

terms and use the buoyant length scale to determine the dissipation. The results should be similar to other analyses that have been carried out along similar lines, e.g. Nieuwstadt (1984) and Shir (1973).

The solutions to these equations over flat terrain give critical gradient and flux Richardson numbers of $Ri_c = 0.25$ and $Rf_c = 0.23$ respectively. This corresponds to values for the flux-profile relationship constants of $\alpha_m = 4.3$ and $\alpha_h = 4.8$, assuming a linear relationship of $\phi_{m,h} = 1 + \alpha_{m,h}\zeta$ where $\zeta = z/\Lambda$. These values are, of course, dependent on the choice of constants however the results obtained are quite realistic given the experimental scatter always associated with observations. Other non-dimensional turbulent quantities, such as σ_w/u_* , also agree quite well with published observational results.

Since we are interested in the effects of slope and turbulent transport on the local turbulence we retain the slope related terms in Equations 2.C.12–2.C.22 and include a parameterisation for the transport term. This involves prescribing the transport of TKE as a ratio, $A_E = TR_E/MP_E$, which indicates the importance of the turbulent transport to the mechanical production. Temperature related transport terms are ignored in this analysis and the $\overline{w\theta}$ transport term is assumed to be related to the TKE transport by $TR_{w\theta} = 3 TR_E/(1 + \alpha'_{33})$. This assumption is based on Equations 2.C.17–2.C.18 assuming the ratio $\overline{w\theta}/E$ to be relatively constant.

Firstly, let us look at the effect of turbulent transport on the critical Richardson numbers. The addition of this term in the TKE budget can enhance or suppress turbulence by transporting it from other regions and is thus dependent on the structure of the flow. When it enhances production, $A_E > 0$, stability effects must be greater in order to suppress turbulence and thus Ri_c is also larger. Similarly, when $A_E < 0$, turbulent production is suppressed and the flow is far more sensitive to the effects of stability, leading to a decrease in the critical Richardson number. This tendency can be clearly seen in Figure 2.1, which shows the variation in Ri_c and Rf_c as a function of A_E for the non-dimensional model.

We mention this point now, concerning the transport term, since it plays an important role in katabatic flow. Indeed, as shear production approaches zero at the height of the wind maximum the ratio A_E approaches ∞ as will Ri_c . Thus, local length scales, based on M-O theory, become invalid and any attempt to apply them in this region is bound to lead to failure.

The dependence of the second-order equations on slope has previously been studied by Horst and Doran (1988) using the equations from Nieuwstadt (1984). Their results for Rf_c are quite similar to those presented here but are quite different for Ri_c , which shows an opposite trend in their work. Their results thus suggest a strong slope dependence for the turbulent Prandtl number, which we do not find using this closure scheme. The basic reason for the slope dependence of Rf_c is to be seen in the buoyant term of the TKE equation (2.C.18). The critical, or limiting, Richardson number occurs when z/Λ approaches ∞ . This can occur when $\overline{u\theta}/w\theta = -\cot\alpha$ and implies that for a ratio of horizontal to vertical heat fluxes of -2.1, as used here for neutral near-wall conditions, a critical angle of 25° exists whereby the destructive effect of vertical buoyancy is completely cancelled by the generation due to the tilted horizontal buoyancy. In other words the effective heat flux vector is perpendicular to the gravity vector and so no gains or losses of turbu-

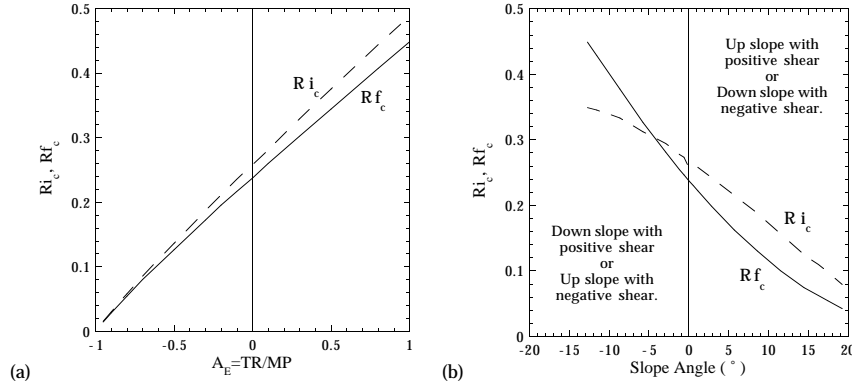


Figure 2.1: (a) Sensitivity of the critical gradient (Ri_c) and flux (Rf_c) Richardson numbers for the non-dimensional turbulent transport parameter A_E using the non-dimensional model described in the text. (b) Sensitivity of the critical gradient (Ri_c) and flux (Rf_c) Richardson numbers for the slope angle using the non-dimensional model.

lent potential energy will occur.

For downslope flow in the positive x direction with positive wind shear, i.e. under the wind maximum, this limit is never reached. However, above the wind maximum, where shear is negative, it is possible to generate positive buoyant fluxes in spite of the strong stability.

From these two results it would appear that conditions in katabatic flows do not conform to the standard local scaling approaches used by most authors. To investigate this thoroughly, however, we need to solve the complete set of mean and second moment equations. This is the topic of the following sections.

2.7 Model description

The entire set of 12 prognostic second-order equations (Appendix 2.C) and the three mean flow equations (2.19–2.21) are numerically solved and integrated in time using standard finite difference techniques. The model is a straightforward 1-D model where turbulent and mean quantities have been placed on a staggered grid such that temperature and momentum fluxes are placed on the even (boundary) grid points and mean velocity and temperature related fluxes have been placed on the odd grid points. In general the lowest grid level used in the simulations was 0.2 m and the highest 1000 m using 50 grid points on a logarithmic scale.

The lower boundary conditions are based on bulk similarity theory, where the roughness lengths for momentum and temperature (z_o and z_h) are constant. The upper boundary condition for all variables is zero except for the wind speed, which is equal to its geostrophic value. The second moment equations are solved semi-implicitly and the mean flow equations are solved using a simple forward time step. This meant that time steps needed to be quite small, around 0.5 seconds, for most runs.

2.8 Results from the second-order model

In this section we wish to discuss a number of results concerning the second-order closure as described in the previous sections. To begin with the model will be applied to a standard SBL and two katabatic case studies of differing slope angle. This is done firstly to compare the different flow regimes and secondly to compare the two different dissipation closures used, i.e. the buoyant length scale closure ($E-l_b$) and the prognostic dissipation closure ($E-\epsilon$). The model will then be used to simulate observed katabatic wind and temperature profiles and eddy correlation fluxes over melting ice surfaces, including a comparison of simulated and observed flux-profile relationships. Finally, the importance of the various terms in the second-order closure scheme will be discussed in relation to the most effective means of modelling katabatic flows.

2.8.1 Comparison of $E-\epsilon$ and $E-l_b$ closures for the stable boundary layer on a horizontal surface

Using the complete second-order closure model we can simulate the SBL with a similar case study to that used by Duynkerke (1988) and Andr en (1990). This involves initiating the model with a well developed near-neutral case, geostrophic wind $U_g=10\text{ ms}^{-1}$ and an ambient stratification of 3 K km^{-1} , and cooling the surface at a rate of 0.5 K hr^{-1} for 10 hours. The resulting wind and temperature profiles, Figure 2.2a, are very similar for both the $E-\epsilon$ and $E-l_b$ closures. The flux-profile relations derived using the $E-\epsilon$ closure also give very similar values for α_m and α_h to those derived using the non-dimensional analysis in Section 2.6.

To demonstrate the role played by turbulent transport in the SBL we have plotted the TKE budget, using the $E-l_b$ closure, as a function of height in Figure 2.2b. Throughout most of the boundary-layer transport is negligible. It is only near the top of the SBL, where production by shear becomes quite small, that it plays a relatively important role though in absolute terms it remains of minor importance.

2.8.2 Comparison of $E-\epsilon$ and $E-l_b$ closures for pure katabatic flows

We saw in the previous section that both dissipation closures produce very similar profiles for a standard SBL run. Since the vertical structure of katabatic flow is somewhat more complicated than a standard SBL the two closures may not give similar results under conditions of katabatic forcing. To investigate the two closures we will use two separate case studies. One with a slope angle of 6° (Case I), typical of many glaciers, and one with an angle of 0.6° (Case II) typical of slopes near the equilibrium line on the Greenland ice sheet. Both examples use a background stratification of 5 K km^{-1} and a constant surface temperature deficit of -10 K , which is realistic for summer conditions in both cases.

The results of these two runs for both dissipative closure schemes are also shown in Figure 2.2. The model has been run to equilibrium for Case I, which took approximately 4 hours, whilst Case II was stopped after 40 hours of integration though the boundary layer was still developing slowly. The difference between the two schemes

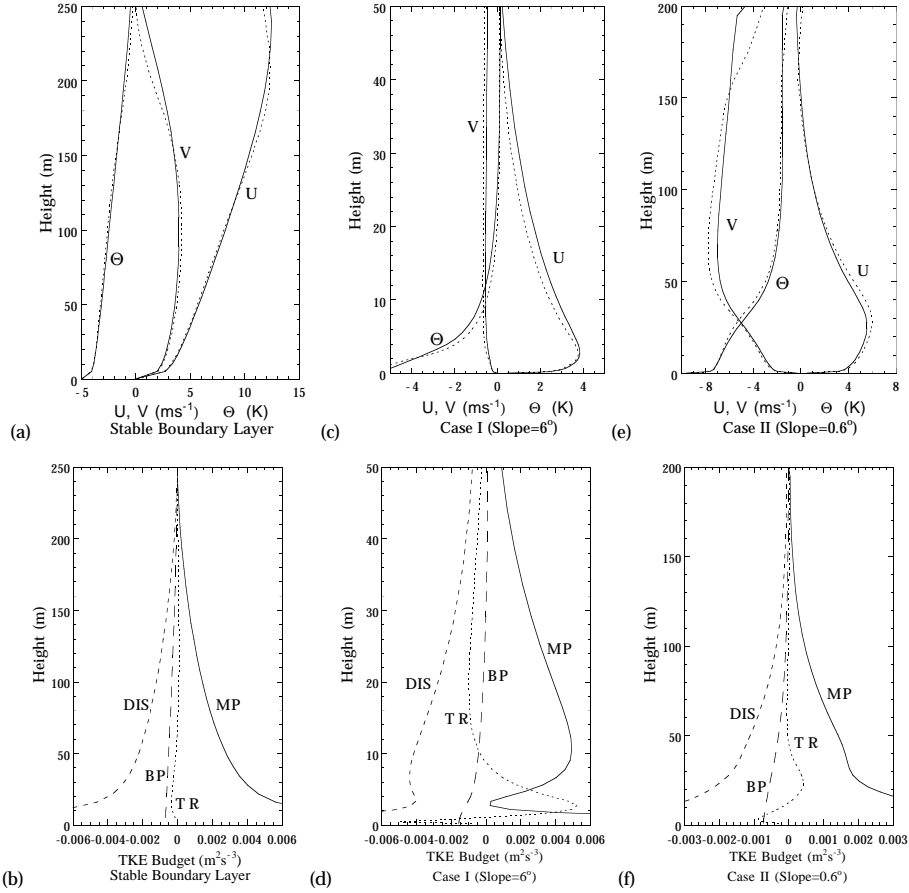


Figure 2.2: Upper: Model runs showing downslope wind speed (U), cross slope wind speed (V) and temperature deficit (Θ) for (a): the stable boundary layer, (c): Case I for katabatic flow and (e): Case II for katabatic flow as described in the text. Solid lines are the results from the $E-l_b$ scheme and dotted lines from the $E-\epsilon$ scheme. Lower: TKE budgets using the $E-l_b$ scheme for the same model runs, i.e. (b): Stable boundary layer, (d): Case I and (f): Case II. MP is the mechanical production, BP the buoyant production, TR the diffusive transport and DIS the viscous dissipation. Note: Horizontal and vertical scales are not the same for all three cases.

appears once more quite small. The largest difference occurs in Case II where the inversion that develops at the top of the boundary layer is much stronger for the $E-l_b$ closure. This is the result of a greater reduction in the buoyant length scale at the boundary-layer top.

Clearly, Cases I and II represent two different flow regimes that reflect the relative ratios of the forcing terms in the momentum budgets (Mahrt, 1982). In Case I the Coriolis forcing term remains significantly less than the katabatic forcing term throughout most of the boundary layer and the downslope momentum budget is balanced by negative flux divergence and positive buoyant forcing. This balance also exists for Case II, but only beneath the wind maximum. Above this height the

Coriolis term balances chiefly with the buoyant forcing. So downslope winds, generated by katabatic forcing, continue to accelerate the air mass until Coriolis effects are significant enough to retard the motion.

Let us examine, as we did for the stable boundary layer, the TKE budget for the two cases. For simplicity we will limit our analysis again to the $E-l_b$ scheme. Case II resembles quite strongly, apart from the increased transport (TR) at the wind maximum, the stable boundary layer already described. In this case turbulent transport plays a minor role in the TKE budget and so local closure theories, which ignore this term, will probably work quite adequately.

Case I shows a much more complicated character. Firstly, since katabatic forcing dominates this flow the wind direction is almost exclusively in the downslope direction. This means that mechanical production through shear will cease at the height of the wind maximum (≈ 4 m) and production of TKE will be entirely due to the turbulent transport terms. We cannot expect local closure theories which ignore the transport terms to be valid in this region.

Secondly, in spite of the assured stability of this boundary-layer, the buoyancy term, which normally retards production of turbulence, slightly enhances it throughout a large part of the boundary layer (30 m - 100 m). This is the result of two effects, the first of which is the turbulent transport in the temperature variance equation. This leads to a significant countergradient term in the upper part of the boundary layer sufficient to cause a positive vertical heat flux. The second is the slope, which allows positive buoyant production along the tilted flow lines as previously described. However, in this case, the ratio $\overline{u\theta}/\overline{w\theta}$ is not constant throughout the katabatic flow, as implied in the simplified non-dimensional model, but varies from zero (at the wind maximum) to ∞ (at the height where $\overline{w\theta} = 0$, in this case $z \approx 50$ m). Though this is an interesting point it should be noted that the above effects are quite small in regard to their influence on the flow itself. As we will see later, removal of the slope dependence actually has little effect on the mean profiles.

Table 2.3: Model input for the three case studies described in this paper.

MODEL PARAMETER	SBL	Case I	Case II
Surface temperature deficit (K) or cooling rate (K hr ⁻¹)	-0.5	-10.0	-10.0
Stratification (K km ⁻¹)	-3.0	-5.0	-5.0
Slope (°)	0	-6.0	-0.6
Geostrophic wind (U_g, V_g) (ms ⁻¹)	(10, 0)	(0, 0)	(0, 0)
z_o, z_h (mm)	2, 0.04	2, 0.04	2, 0.04
Integration time (hr)	10	4	40
Lowest grid level (m)	4.0	0.2	0.2

2.8.3 Comparison with observations

It is important to compare the model with measured flows to see if it is capable of reproducing not just observed mean profiles but also observed fluxes. To this end we have selected average eddy flux and profile measurements from three different mea-

surement campaigns made on the Pasterze glacier in 1994 (van den Broeke, 1997b, c; Smeets *et al.*, 1998), the Vatnajökull ice cap in 1996 (Oerlemans *et al.*, 1999; van der Avoird and Duynkerke, 1999) and the Greenland ice sheet in 1991 (Meesters *et al.*, 1997a, b). It is not the aim here to describe in detail these observations, suffice to say that they consisted of profile mast, balloon sounding, sonic anemometer and sodar measurements. The periods selected for use here are based on the need for reasonably good coverage by all instruments and weak synoptic forcing, allowing a distinctive katabatic layer to develop. Some details of these observations are given in Table 2.4.

In order to make a comparison between observation and simulation it is important to note that the model in use is strictly one-dimensional and that it also neglects the effects of water vapour and diabatic heating through radiation divergence, which can be important, on the mean equations. Since observed profiles will be influenced to some degree by these effects we cannot expect modelled profiles to be accurate in an absolute sense. We thus introduce an entrainment velocity, which reaches its maximum at the top of the boundary layer and reduces linearly to zero at the surface, which is adjusted so that the simulated maximum wind speed is similar to that which is observed.

The value of the entrainment velocity will depend on whether the katabatic layer is shrinking '+' or growing '-'. For the Pasterze, for example, van den Broeke (1997b) calculated the average entrainment velocity along the glacier for a similar 12 day period to be -2.4 cms^{-1} at the top of the boundary layer. For cases where slope is increasing the mass flux of a katabatic layer tends to decrease (Figure 2.2c and 2.2e) leading to a positive entrainment velocity. The largest effect of negative entrainment on these flows is the downward advection of warm air across the strong temperature inversion at the height of the wind maximum. This will retard the flow since warming decreases the katabatic forcing term. It is not implied in this study that entrainment is the only mechanism present to alter the flow dynamics, we use it solely as a means to match absolute wind speeds in a physically realistic manner. In this way a better comparison between simulated and observed data can be obtained.

In Figures 2.3, 2.4 and 2.5 we compare observed average profiles of wind and temperature as well as various eddy correlation terms, measured using sonic anemometers, with results from the $E-l_b$ model for the three different sites. In all cases the model is run to near equilibrium and adjusted using an entrainment velocity so that the maximum wind speed is approximately the same as that observed. Input parameters are thus surface temperature, surface slope, ambient temperature stratification, entrainment velocity and in the Greenland case, the geostrophic wind. These values are listed in Table 2.4.

The mean profiles for wind and temperature for two of these sites are quite well reproduced. Only the Pasterze glacier shows a significant difference in the mean wind profile. This is perhaps not surprising since there are several effects present on the Pasterze that are not represented by the model. These include the valley wind that transports warm air from the lower valley up and over the glacier wind, the pooling of cold air in the glacier valley at night due to the inflow from radiatively cooled valley walls and the nearby presence of a convective boundary layer. These effects, which cannot be represented by the model, also lead to a significant diurnal cycle in the glacier wind so one cannot speak of a steady state.

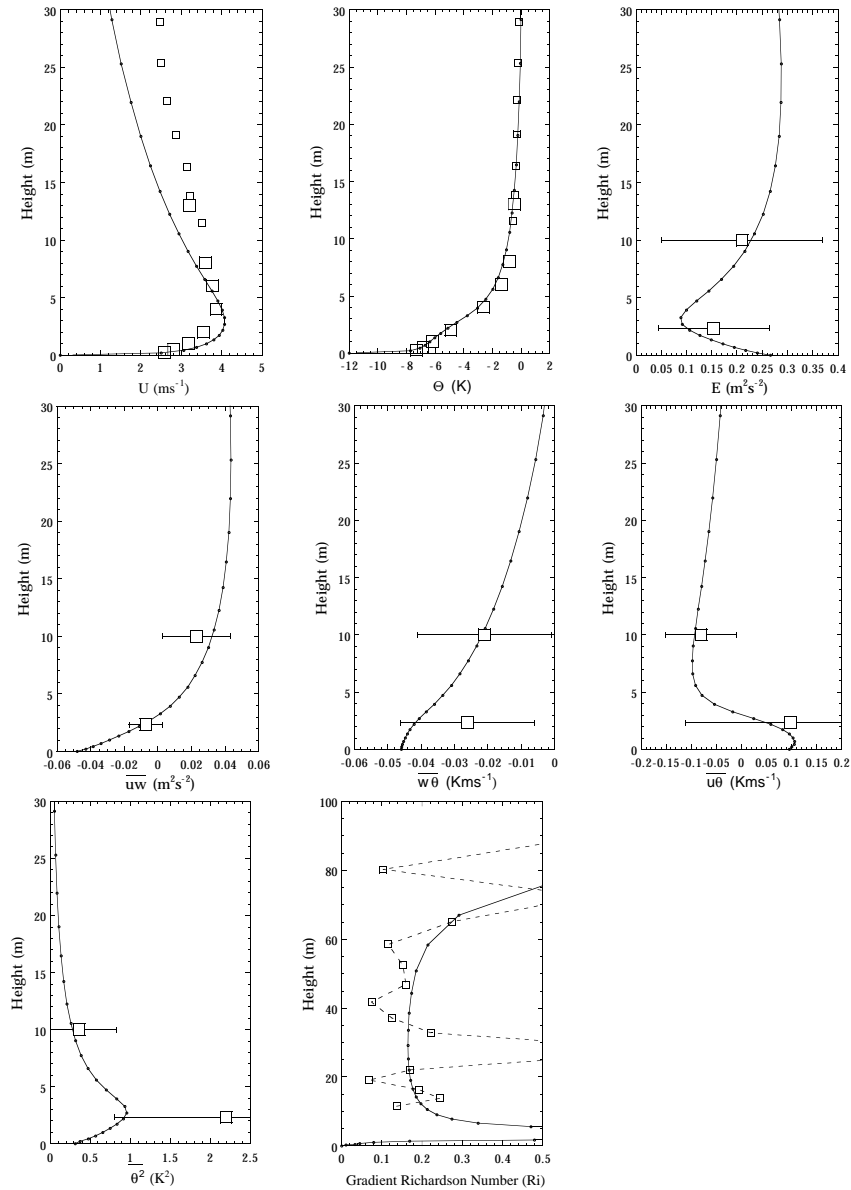


Figure 2.3: Comparison of modelled and observed mean profiles and turbulent quantities for the Pasterze glacier. Solid lines indicate the model simulation with dots indicating the model resolution. Large squares indicate profile mast measurements, small squares balloon sounding measurements and large squares with error bars, representing the standard deviation over the observational period, indicate eddy correlation measurements. The dotted line and squares in the last figure represent the gradient Richardson number from the average wind and temperature balloon soundings. Observational data from Smeets et al. (1998).

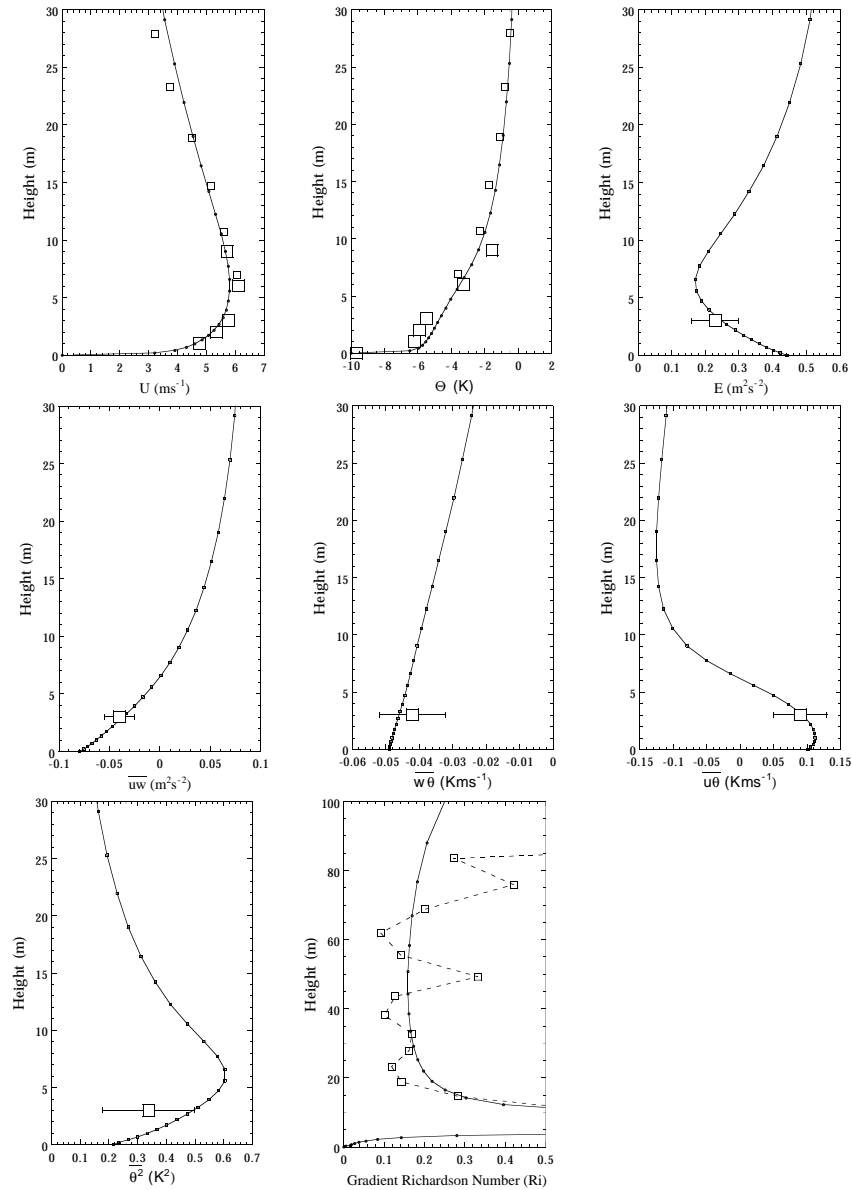


Figure 2.4: As in Figure 2.3 but for Vatnajökull. Observational data from van der Avoird and Duyenkerke (1999).

In regard to the turbulent fluxes, only the results from Vatnajökull give consistent results for all fluxes and variances. Once more it is the Pasterze glacier that shows the greatest discrepancy between observed and simulated values, in particular the large difference in the vertical heat flux at the 2 m level. It is possible that the measurements themselves are strongly influenced by the presence of gravity waves,

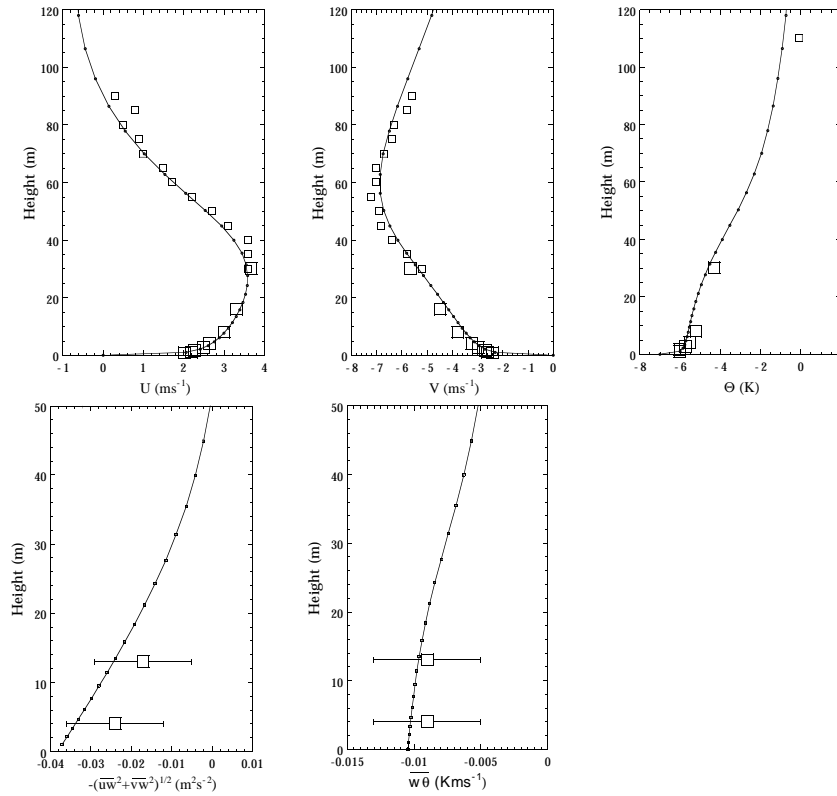


Figure 2.5: As in Figure 2.3 but for Greenland. In this case small squares indicate sodar measurements. Observational data from Meesters *et al.* (1997a).

since low frequency filtering was not carried out with this set of data, or due to the path muddling process performed by the sonic making it impossible to properly resolve eddies smaller than the distance between the sonic sensors. Under the very stable conditions found in katabatic flows, especially in the region around the wind maximum and close to the surface, these eddies are expected to be quite small. The other problem with the boundary layer observed at the Pasterze is that it is strongly influenced by non-local fluxes that occur as a result of the surrounding topography and the presence of a convective boundary layer during the day (Smeets *et al.*, 1998).

Included in Figures 2.3 and 2.4 are comparisons of modelled and observed gradient Richardson numbers (Ri) in the upper region of the katabatic layer. Both figures indicate a fairly constant value for the modelled Ri throughout this region of slightly less than 0.2, giving reasonable agreement with the observed values. The consistency of Ri is indicative of a region where z-less scaling would apply. This supposition is confirmed by the model results, which show that the length scale in this region, defined in Equations 2.8 and 2.9, is determined solely by the buoyant length scale. The implication of this is that turbulent eddies above the wind maximum do not 'feel' the surface and are determined completely by the local stability.

Table 2.4: Model input and observational data for the three simulations described in this paper.

MODEL PARAMETER	Pasterze	Vatnajökull	Greenland
Surface temperature deficit (K)	-12.0	-10.0	-7.0
Stratification (K km^{-1})	-3.0	-4.5	-5.0
Slope ($^\circ$)	-4.0	-4.5	-0.4
Geostrophic wind (U_g, V_g) (ms^{-1})	(0, 0)	(0, 0)	(0, -3)
Entrainment velocity (cms^{-1})	-3.5	+1.0	0
z_o, z_h (mm)	2, 0.04	2, 0.04	2, 0.04
Integration time (hr)	4	4	20
Lowest grid level (m)	0.2	0.2	1.0
OBSERVATIONS			
Description of ice mass	Glacier	Ice cap	Ice sheet
Approximate length (km)	10	100	500
Profile mast height (m)	13	9	30
Balloon sounding height (m)	600	600	-
Sodar maximum height (m)	-	-	100
Sonic heights (m)	2, 10	3	4, 13
Averaging period (hr)	48	24	3

2.8.4 Flux-profile relations in katabatic flow

Eddy correlation measurements are used to determine the non-dimensional flux-profile relationships for boundary-layer flows. Studies of these relationships have already been carried out for ice surfaces such as Antarctica (King, 1990), Greenland (Forrer and Rotach, 1997), Pasterze (Smeets *et al.*, 1998) and Vatnajökull (van der Avoird and Duynkerke, 1999).

In Figure 2.6 we compare measured and modelled flux-profile relationships made at Cabauw (over flat terrain in The Netherlands), Pasterze and Vatnajökull. The flux measurements were all made at a single height, which for Cabauw and Vatnajökull was 3 m and for the Pasterze 2.25 m. In fact, the measurements made at Cabauw and Vatnajökull were made with exactly the same experimental set up (Larsson, 1997). The data from Vatnajökull and the Pasterze were selected on the basis of the presence of a wind maximum beneath the profile mast height and above the sonic height. The modelled data are from the runs shown in Figures 2.3 and 2.4, taken from beneath the wind maximum. Apart from the normal scatter associated with these plots ϕ appears to be relatively independent of stability for the two cases of katabatic flow. This is the direct result of the increased influence of the transport terms in the TKE budget. As previously mentioned the critical Richardson number should approach infinity at the wind maximum and so ϕ should also approach 1 at this point.

Close to the surface, where the transport term becomes less important, the modelled flux-profile relationships behave in a familiar linear fashion and it is only in this region that M-O theory is applicable. This point has been observed by Munro and Davies (1978) and Smeets *et al.* (1998) who both found M-O theory to be valid only up to heights of around 10 – 20% of the height of the wind speed maximum.

From Figures 2.3 and 2.4 it is also clear that there is little support for the concept of a constant flux layer, at least in the case of momentum, when dealing with the low-level jet of a katabatic flow. Though this is of little consequence when applying local closure schemes it does imply that surface-layer theories, which assume constant

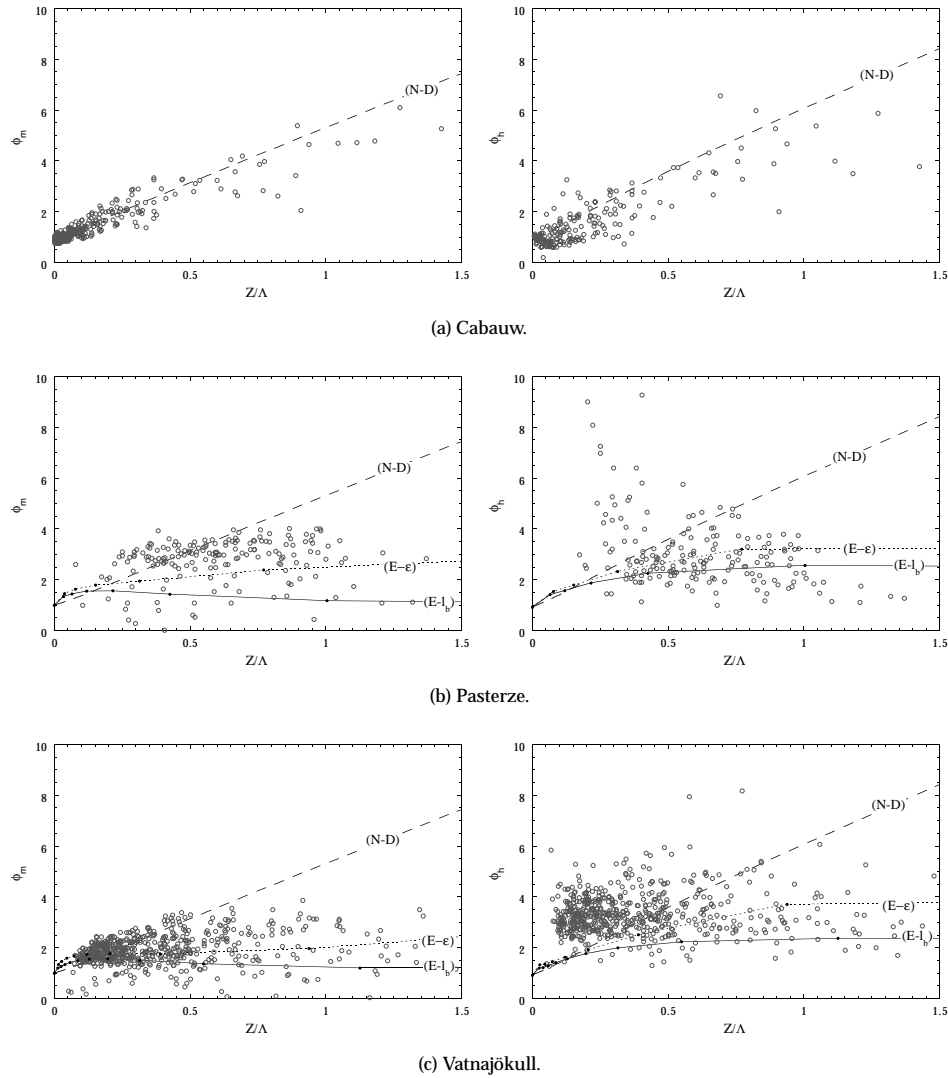


Figure 2.6: Flux-profile relationships for (a) Cabauw, (b) Pasterze and (c) Vatnajökull. Observational points for Cabauw and Vatnajökull are filtered hourly averages sampled at 20 Hz whilst those for the Pasterze are unfiltered half-hourly averages sampled at 1 Hz. For these last two, only observations made during periods of katabatic flow, when the wind speed maximum is detectable beneath the mast, are selected. (N-D) represents the results of the non-dimensional analysis and (E-l_b) and (E-ε) represent the two different dissipative closure schemes.

surface fluxes, are not suitable for use in this region. This will lead to discrepancies in flux calculations when using profile methods such as those normally applied to the SBL, e.g. Munro and Davies (1978).

2.8.5 Model simplification and sensitivity

The model as it now stands is quite complex. It is useful to produce a simplified model that will lead to the same results. Sensitivity runs are made with the case studies to see which terms in the second-order closure are of significant influence. In particular we are interested in reducing the number of prognostic equations to as few as possible. This can be achieved if the non-local transport terms can be excluded from the model. It turns out that only the diffusive transport terms associated with the variances have significant influence on the flow and this mainly in cases with strong katabatic forcing, e.g. Case I. This includes the temperature variance term and should thus preclude the use of standard K-type theory closures that assume the transport term for temperature variance to be negligible.

By way of example the model has been rewritten in the so called 1.5-order closure form, similar to the level 2.5 scheme used by Andr en (1990), which uses only the prognostic equation for TKE. The other fluxes in Appendix 2.C are diagnostically determined using the assumption of steady state and neglect of the transport terms. In this way a K-theory type closure is achieved where $K_{m,h} = C_{m,h} E^2 / \epsilon$. The dimensionless constant $C_{m,h}$ then becomes a function of stability and is calculated from the shear and temperature gradient.

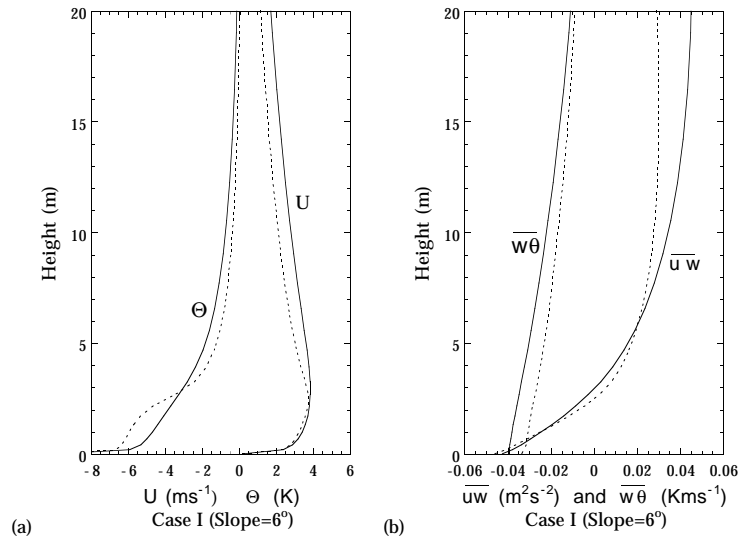


Figure 2.7: Comparison of the simplified 1.5-order model, dashed lines, with the complete $E-l_b$ model, solid lines. Shown in (a) are the downslope wind speed U and the temperature deficit Θ . In (b) the vertical momentum flux \overline{uw} and the vertical heat flux $\overline{w\theta}$ are shown.

A comparison, using Case I, between the complete second-order and the 1.5-order closure schemes is given in Figure 2.7. There is a significant difference in both the temperature and wind profiles due to this simplification. There are two reasons for this, the first is the absence of the turbulent transport of $\overline{\theta^2}$ across the wind max-

imum, and its absence leads to a strengthening of the inversion at this height. The second is the assumption inherent in the 1.5-order closure simplification that transport of $\overline{w\theta}$ can be ignored. This implies that the ratio $\overline{w\theta}/E$ is zero at the height of the wind maximum and leads to an inaccurate and inconsistent representation of the stability constants ($C_{m,h}$) at this point. As a result, almost identical fluxes and profiles can only be achieved for strong katabatic flows by the inclusion of the three variance prognostic equations, i.e. equations for E , $\overline{w\theta}$ and $\overline{\theta^2}$. For katabatic flows similar to Case II, not shown, the influence of $\overline{\theta^2}$ and $\overline{w\theta}$ transport is less marked and does not seriously affect the flow though the inversion at the top of the boundary layer becomes slightly stronger in their absence.

The slope related terms in the second-order equations are also removed to check their influence on the general flow. For slope angles which we are dealing with, up to around 20° , the influence of slope is barely perceptible on the mean flow and fluxes. This is chiefly due to the fact that at the wind maximum the horizontal heat flux goes to zero, so around this region the slope induced buoyancy is not important. Higher up where it could become important the fluxes are too small to have any significant effect on the flow below.

The sensitivity of the model to the diffusive transport constants c_s and $d_{s1,2}$ is also tested since these are not well known quantities. For Case I a reduction in the magnitude of these constants by a factor of 50% leads to a strengthening of the temperature inversion at the height of the wind speed maximum similar to the results shown in Figure 2.7. This is the direct result of a reduction in the turbulent transport across the wind maximum, which leads to a reduction in TKE at this height. Increasing the value of c_s by 50% has very little effect on the mean flow.

2.9 Conclusions

A complete 1-D second-order model is used to simulate pure katabatic flows under a variety of conditions. The model is based on closures that take into account the proximity of the surface in determining the turbulent anisotropy and includes surface slope in the second moment equations. The constants needed for this closure scheme are chiefly determined from measurements made in the laboratory and in neutral boundary layers. The resultant model, which is run with two different closures for the viscous dissipation (either a diagnostic buoyant length scale or a prognostic dissipation equation), agrees well with other models of the stable boundary layer, e.g. Nieuwstadt (1984).

Simulations carried out with the model of observed katabatic flows show that the model is capable of reproducing both mean profile and flux measurements when the flow is almost one dimensional and turbulence is locally determined. However, when the flow is not one-dimensional and turbulence may be influenced by non-local effects, such as on the Pasterze, the model does not adequately simulate the observed profiles. Some improvement could be made by increasing the model dimensions, to take advection into account, however it is difficult to see how non-local features caused by wave induced turbulence or local topography can be incorporated in such a model.

Two case studies are used to investigate the various terms in the TKE budget for

katabatic flows. For steeper slopes, such as found on glaciers, the turbulent transport term is an essential part of the TKE budget. It is the sole means of turbulence production at the height of the wind maximum and also plays an important role in the upward transport of turbulence in the higher regions of the boundary layer where wind shear does not play a significant role. For these cases katabatic forcing dominates throughout the boundary layer. For lesser slopes, such as those encountered on large ice sheets, the katabatic forcing is dominant only in the lowest part of the boundary layer beneath the wind maximum. Above this height the Coriolis term becomes important and even allows a further deepening of the katabatic layer, due to the increased shear caused by the turning of the wind with height. The length scale in both cases appears to be locally determined by the buoyant length scale throughout most of the boundary layer.

Analysis of the modelled flux-profile relationships for katabatic flows on steep slopes, Case I type, shows that the tendency for these functions to deviate from their normal near-linear dependence on stability, as has been observed on various glaciers, is due to the influence of the turbulent transport terms. These terms are not included in non-dimensional analyses or similarity relationships but need to be taken into account when dealing with this type of flow. Both observations and model results show that the flux-profile relationships are probably better described as being independent of stability for measurements made under the wind maximum. For katabatic flows on lesser slopes, Case II type, the lower boundary layer closely resembles that of a standard SBL and here local M-O theory is still valid.

The inclusion of slope in the second moment terms is investigated using a non-dimensional analysis. It is shown that slope could have a significant influence on the critical Richardson numbers. Sensitivity tests, however, with the model showed that these effects had little influence on the mean profiles and fluxes under katabatic flow conditions encountered on glaciers and ice sheets.

As a result of the various simplifications made to the model it is clear that the minimum prerequisite for a successful katabatic flow simulation is the inclusion of the turbulent transport term in a prognostic TKE equation, and preferably also in the $\overline{w'w'}$ equation, since it is these terms that couple the boundary layer above and below the wind maximum. In addition to this, if a diagnostic length scale is used, then it cannot be based on a velocity scale such as u_* , as in M-O theory, since this will also lead to a de-coupling at the height of the wind maximum. A prognostic equation for viscous dissipation, which also includes a diffusive term, is also suitable for this form of modelling.

Of additional, though lesser, importance is the inclusion of a prognostic equation, with transport, of the temperature variance term. Since this term peaks at the height of the wind maximum, transport across the maximum will cool the air above and warm the air below the wind maximum, reducing the temperature gradient and thus stability at this height. Though neglect of this term noticeably alters the temperature profile the vertical heat flux remains relatively unchanged.

By using a second-order closure model we have been able to avoid the usual assumptions made by most authors concerning local closures based on M-O theory. The use of these closure assumptions leads to a total de-coupling of the katabatic layer above and below the wind maximum for steep slopes unless various numerical 'tricks' are used to avoid this. In this regard one of the weakest links in the present

model is perhaps the closure used for the viscous dissipation, or length scale, though it is heartening to see that both closures give quite similar results. The ϵ equation is a highly engineered solution and the buoyant length scale closure, based on a fairly simple physical principle, assumes the dominance of the buoyant length scale in determining the viscous dissipation. It would be useful if more observational evidence for dominant length scales was available.

Acknowledgements

I would like to thank those people who provided the observational data for this paper. From the IMAU, University of Utrecht, Ernst van der Avoird, Lisalot Larsson and Peter Duynkerke and from the VU, Free University of Amsterdam, Niek-Jan Bink, Paul Smeets and Anton Meesters. This research was funded by the Dutch National Research Programme on Global Air Pollution and Climate Change (NOP II Project 013 001236.10).

Appendix

2.A Pressure correlation closure

The closure used here is based on the work from Gibson and Launder (1978) and includes terms that represent the anisotropy that develops in turbulence in the proximity of a wall. Using their notation the individual terms in the pressure-strain correlations, given in Equation 2.15 are as follows:

$$\begin{aligned}
 \phi_{ij,1} &= -c_1 \frac{\epsilon}{E} \left(\overline{u_i u_j} - \frac{2}{3} \delta_{ij} E \right) \\
 \phi_{ij,2} &= -c_2 \left(M P_{ij} - \frac{2}{3} \delta_{ij} M P_E \right) \\
 \phi_{ij,3} &= -c_3 \left(B P_{ij} - \frac{2}{3} \delta_{ij} B P_E \right) \\
 \phi'_{ij,1} &= c'_1 \frac{\epsilon}{E} \left(\overline{u_k u_m n_k n_m} \delta_{ij} - \frac{3}{2} \overline{u_k u_i n_k n_j} - \frac{3}{2} \overline{u_k u_j n_k n_i} \right) \\
 \phi'_{ij,2} &= c'_2 \left(\phi_{km,2} n_k n_m \delta_{ij} - \frac{3}{2} \phi_{ik,2} n_k n_j - \frac{3}{2} \phi_{jk,2} n_k n_i \right) \\
 \phi'_{ij,3} &= c'_3 \left(\phi_{km,3} n_k n_m \delta_{ij} - \frac{3}{2} \phi_{ik,3} n_k n_j - \frac{3}{2} \phi_{jk,3} n_k n_i \right) \quad (2.A.1)
 \end{aligned}$$

where the terms $M P_{ij}$ and $B P_{ij}$ are defined in Equation 2.3.

The function F , in Equation 2.15, indicates the proximity of the wall in terms of the turbulent length scale and the distance to the wall and is defined simply as $F = l/(n_i r_i)$ where \mathbf{n} is the unit vector normal to a surface, \mathbf{r} the position vector and l is a turbulent length scale. It is defined as being equal to unity close to the wall and approaches zero for free turbulent flows. The above general forms were

originally developed to cope with flows on curved surfaces but are much simpler when applied to flat surfaces.

The pressure-temperature correlations in Equation 2.4, $PS_{i\theta}$, are treated analogously to those for momentum so that:

$$\phi_{i\theta} = \phi_{i\theta,1} + \phi_{i\theta,2} + \phi_{i\theta,3} + (\phi'_{i\theta,1} + \phi'_{i\theta,2} + \phi'_{i\theta,3}) F(n,l) \quad (2.A.2)$$

and the individual terms are:

$$\begin{aligned} \phi_{i\theta,1} &= -d_1 \frac{\epsilon}{E} \overline{u_i \theta} \\ \phi_{i\theta,2} &= -d_2 M P_{i\theta} \\ \phi_{i\theta,3} &= -d_3 B P_{i\theta} \\ \phi'_{i\theta,1} &= -d'_1 \frac{\epsilon}{E} \overline{u_k \theta} n_i n_k \\ \phi'_{i\theta,2} &= d'_2 d_2 M P_{k\theta} n_i n_k \\ \phi'_{i\theta,3} &= d'_3 d_3 B P_{k\theta} n_i n_k \end{aligned} \quad (2.A.3)$$

2.B Algebraic equations for determining closure constants

The constants c_2 , c_3 , and d_3 can all be determined on the basis of calculations of isotropic turbulence, the results of which are given in Section 2.4. To determine most of the other constants the non-dimensional ratio of Reynolds stresses and variances to the turbulent kinetic energy ($a_{ij} = \overline{u_i u_j} / E$) for both near-wall (designated with a prime) and free-shear flows under neutral conditions are used.

Firstly, solving Equation 2.3 using the closure assumptions in Equation 2.A.1 under neutral free-shear conditions and assuming steady state turbulence such that the mechanical production is equal to the dissipation, will lead to the following relationship for c_1 and c_2

$$c_1 = \frac{(1 - c_2)}{(1 - 1.5a_{33})} \quad (2.B.4)$$

as well as an equality that can be used to test the consistency of the closure assumptions under these conditions.

$$a_{13}^2 = a_{33}(1 - 1.5a_{33}) \quad (2.B.5)$$

The chosen values for a_{33} and a_{13} (Table 2.B.1) agree exactly with Equation 2.B.5.

The near-wall constants can also be algebraically solved in a similar fashion using appropriate near-wall values for a'_{33} and a'_{13} .

$$c'_1 = \frac{1 - c_2 + c_1(3 - 4a'_{13}{}^2/a'_{33} - 4.5a'_{33})}{6a'_{13}{}^2/a'_{33} + 9a'_{33}} \quad (2.B.6)$$

$$c'_2 = \frac{c_1(1 + 0.5a'_{33}) + (c_2 - 1)(1 + 2a'_{33}{}^2/a'_{13}{}^2)}{c_2(2 + 3a'_{33}{}^2/a'_{13}{}^2)} \quad (2.B.7)$$

The values d_1 and d'_1 can also be determined for near-neutral conditions using the following relationship derived from Equations 2.3–2.4 and Equations 2.A.1–2.A.3:

$$d_1 = \sigma_{T_o} \frac{a_{33}}{a_{13}^2} \quad (2.B.8)$$

$$d'_1 = \sigma'_{T_o} \frac{a'_{33}}{a'_{13}{}^2} - d_1 \quad (2.B.9)$$

where σ_{T_o} is the turbulent Prandtl number under near neutral conditions.

Using the defined non-dimensional ratios (Equation 2.17) we find that d_ϵ can be determined by either

$$d_\epsilon = \frac{1}{b_3} \text{ or } d_\epsilon = \frac{\sigma_{T_o}}{b_2 a_{13}} \quad (2.B.10)$$

depending on whether b_2 or b_3 is used.

The following relation can also be derived from Equation 2.3 under near neutral conditions to determine d_2

$$d_2 = (1 + \sigma_{T_o}) - d_1 b_1 a_{13} \quad (2.B.11)$$

where in this case we have used atmospheric, thus near-wall, values for σ_{T_o} , b_1 and a_{13} to obtain the correct neutral limit for the temperature related flux-profile relationships.

Table 2.B.1: The various measured momentum and buoyancy related turbulent ratios used in the text and their sources (REF). '*' indicates an implied value for b_3 taken from atmospheric measurements of b_2 . The references are as follows {1}:Gibson and Launder (1978), {2}: Launder et al. (1975), {3}:King (1990), {4}:Grant (1990), {5}:Nieuwstadt (1984) and {6}:Constants used in this paper.

REF	NEUTRAL CONSTANTS						STABILITY CONSTANTS				
	Free-Shear			Near-Wall			Free-Shear		Near-Wall		
	a_{11}	a_{33}	a_{13}	a'_{11}	a'_{33}	a'_{13}	b_1	σ_{T_o}	b'_1	σ'_{T_o}	b_3
{1}	.96	.52	-.34	1.1	.25	-.26	-1.3	.67	-2.1	.92	1.6
{2}	.96	.50	-.32	1.2	.24	-.24					
{3}				1.1	.28	-.16					.7*
{4}				1.1	.28	-.22					
{5}					.4	-.25			-2.3		1.5*
{6}	.96	.52	-.34	1.1	.24	-.18	-1.3	.67	-2.1	.92	1.3

2.C Second-order equations for a homogenous 1-D boundary layer on a tilted surface

The following is the complete set of second-order equations used in the model.

$$\begin{aligned} \frac{\partial \overline{uv}}{\partial t} &= - \left(\overline{vw} \frac{\partial U}{\partial z} + \overline{uw} \frac{\partial V}{\partial z} \right) + (1 - c_3) \frac{g}{\Theta_o} \sin \alpha \overline{v\theta} - c_1 \frac{\epsilon}{E} \overline{uv} \\ &\quad + \frac{\partial}{\partial z} \left\{ c_s \frac{E}{\epsilon} \left(\overline{vw} \frac{\partial \overline{uw}}{\partial z} + \overline{uw} \frac{\partial \overline{vw}}{\partial z} + \overline{ww} \frac{\partial \overline{uv}}{\partial z} \right) \right\} \end{aligned} \quad (2.C.12)$$

$$\begin{aligned} \frac{\partial \overline{uw}}{\partial t} &= - (1 - c_2(1 - 1.5c_2'F)) \overline{ww} \frac{\partial U}{\partial z} + (1 - c_3) \frac{g}{\Theta_o} (\cos \alpha \overline{u\theta} + \sin \alpha \overline{w\theta}) \\ &\quad - (c_1 + 1.5c_1'F) \frac{\epsilon}{E} \overline{uw} + \frac{\partial}{\partial z} \left\{ c_s \frac{E}{\epsilon} \left(\overline{uw} \frac{\partial \overline{ww}}{\partial z} + 2\overline{ww} \frac{\partial \overline{uw}}{\partial z} \right) \right\} \end{aligned} \quad (2.C.13)$$

$$\begin{aligned} \frac{\partial \overline{vw}}{\partial t} &= - (1 - c_2(1 - 1.5c_2'F)) \overline{ww} \frac{\partial V}{\partial z} + (1 - c_3) \frac{g}{\Theta_o} \cos \alpha \overline{v\theta} \\ &\quad - (c_1 + 1.5c_1'F) \frac{\epsilon}{E} \overline{vw} + \frac{\partial}{\partial z} \left\{ c_s \frac{E}{\epsilon} \left(\overline{vw} \frac{\partial \overline{ww}}{\partial z} + 2\overline{ww} \frac{\partial \overline{vw}}{\partial z} \right) \right\} \end{aligned} \quad (2.C.14)$$

$$\begin{aligned} \frac{\partial \overline{uu}}{\partial t} &= -2(1 - c_2) \overline{uw} \frac{\partial U}{\partial z} + 2(1 - c_3) \frac{g}{\Theta_o} \sin \alpha \overline{u\theta} - \frac{2}{3}(1 - c_1)\epsilon \\ &\quad - (c_1 \overline{uu} - c_1'F \overline{ww}) \frac{\epsilon}{E} + \frac{2}{3}c_2(1 + c_2'F)MP_E + \frac{2}{3}c_3BP_E \\ &\quad + \frac{\partial}{\partial z} \left\{ c_s \frac{E}{\epsilon} \left(2\overline{uw} \frac{\partial \overline{uw}}{\partial z} + \overline{ww} \frac{\partial \overline{uu}}{\partial z} \right) \right\} \end{aligned} \quad (2.C.15)$$

$$\begin{aligned} \frac{\partial \overline{vv}}{\partial t} &= -2(1 - c_2) \overline{vw} \frac{\partial V}{\partial z} - \frac{2}{3}(1 - c_1)\epsilon \\ &\quad - (c_1 \overline{vv} - c_1'F \overline{ww}) \frac{\epsilon}{E} + \frac{2}{3}c_2(1 + c_2'F)MP_E + \frac{2}{3}c_3BP_E \\ &\quad + \frac{\partial}{\partial z} \left\{ c_s \frac{E}{\epsilon} \left(2\overline{vw} \frac{\partial \overline{vw}}{\partial z} + \overline{ww} \frac{\partial \overline{vv}}{\partial z} \right) \right\} \end{aligned} \quad (2.C.16)$$

$$\begin{aligned} \frac{\partial \overline{ww}}{\partial t} &= +2(1 - c_3) \frac{g}{\Theta_o} \cos \alpha \overline{w\theta} - \frac{2}{3}(1 - c_1)\epsilon - \overline{ww}(c_1 + 2c_1'F) \frac{\epsilon}{E} \\ &\quad + \frac{2}{3}c_2(1 - 2c_2'F)MP_E + \frac{2}{3}c_3BP_E + \frac{\partial}{\partial z} \left\{ 3c_s \frac{E}{\epsilon} \overline{ww} \frac{\partial \overline{ww}}{\partial z} \right\} \end{aligned} \quad (2.C.17)$$

$$\begin{aligned} \frac{\partial E}{\partial t} &= MP_E + BP_E - \epsilon \\ &\quad + \frac{\partial}{\partial z} \left\{ c_s \frac{E}{\epsilon} \left(\overline{uw} \frac{\partial \overline{uw}}{\partial z} + \overline{vw} \frac{\partial \overline{vw}}{\partial z} + \overline{ww} \frac{\partial (E + \overline{ww})}{\partial z} \right) \right\} \end{aligned} \quad (2.C.18)$$

$$\begin{aligned} \frac{\partial \overline{u\theta}}{\partial t} &= - \left(\overline{uw} \frac{\partial \overline{\theta}}{\partial z} + \overline{uw} \gamma_\theta \sin \alpha + (1 - d_2) \overline{w\theta} \frac{\partial U}{\partial z} \right) + (1 - d_3) \frac{g}{\Theta_o} \sin \alpha \overline{\theta^2} \\ &\quad - d_1 \frac{\epsilon}{E} \overline{u\theta} + \frac{\partial}{\partial z} \left\{ d_{s1} \frac{E^2}{\epsilon} \frac{\partial \overline{u\theta}}{\partial z} \right\} \end{aligned} \quad (2.C.19)$$

$$\begin{aligned} \frac{\partial \overline{v\theta}}{\partial t} &= - \left(\overline{vw} \frac{\partial \overline{\theta}}{\partial z} + \overline{vw} \gamma_\theta \sin \alpha + (1 - d_2) \overline{w\theta} \frac{\partial V}{\partial z} \right) - d_1 \frac{\epsilon}{E} \overline{v\theta} \\ &\quad + \frac{\partial}{\partial z} \left\{ d_{s1} \frac{E^2}{\epsilon} \frac{\partial \overline{v\theta}}{\partial z} \right\} \end{aligned} \quad (2.C.20)$$

$$\begin{aligned} \frac{\partial \overline{w\theta}}{\partial t} &= - \left(\overline{w\theta} \frac{\partial \overline{\Theta}}{\partial z} + \overline{uw} \gamma_\theta \sin \alpha \right) + (1 - d_3) \frac{g}{\Theta_o} \cos \alpha \overline{\theta^2} \\ &\quad - (d_1 + d'_1 F) \frac{\epsilon}{E} \overline{w\theta} + \frac{\partial}{\partial z} \left\{ 2d_{s1} \frac{E^2}{\epsilon} \frac{\partial \overline{w\theta}}{\partial z} \right\} \end{aligned} \quad (2.C.21)$$

$$\frac{\partial \overline{\theta^2}}{\partial t} = -2 \left(\overline{w\theta} \frac{\partial \overline{\Theta}}{\partial z} + \overline{u\theta} \gamma_\theta \sin \alpha \right) - 2d_\epsilon \frac{\epsilon}{E} \overline{\theta^2} + \frac{\partial}{\partial z} \left\{ d_{s2} \frac{E^2}{\epsilon} \frac{\partial \overline{\theta^2}}{\partial z} \right\} \quad (2.C.22)$$

where,

$$MP_E = - \left(\overline{uw} \frac{\partial U}{\partial z} + \overline{vw} \frac{\partial V}{\partial z} \right) \quad (2.C.23)$$

$$BP_E = \frac{g}{\Theta_o} (\sin \alpha \overline{u\theta} + \cos \alpha \overline{w\theta}) \quad (2.C.24)$$

$$\frac{\partial \overline{\Theta}}{\partial z} = \frac{\partial \Theta}{\partial z} + \gamma_\theta \cos \alpha \quad (2.C.25)$$

The prognostic equation for dissipation is given as:

$$\begin{aligned} \frac{\partial \epsilon}{\partial t} &= c_{\epsilon 1} \frac{\epsilon}{E} (MP_E + \max(0, BP_E) + \max(0, TR_E)) - c_{\epsilon 2} \frac{\epsilon^2}{E} \\ &\quad + \frac{c_{\epsilon s}}{2} \frac{\partial}{\partial z} \left\{ \frac{E^2}{\epsilon} \frac{\partial \epsilon}{\partial z} \right\} \end{aligned} \quad (2.C.26)$$

and the diagnostic form is described in the text (Equations 2.7–2.9).

3

The Use of Bulk and Profile Methods for Determining Surface Heat Fluxes in the Presence of Glacier Winds

A 1-D second-order closure model and in situ observations on a melting glacier surface are used to investigate the suitability of bulk and profile methods for determining turbulent fluxes in the presence of the katabatic wind speed maximum associated with glacier winds. The results show that profile methods severely underestimate turbulent fluxes when a wind speed maximum is present. The bulk method, on the other hand, only slightly overestimates the turbulent heat flux in the entire region below the wind speed maximum and is thus much more appropriate for use on sloping glacier surfaces where katabatic winds dominate and wind speed maximums are just a few meters above the surface.

3.1 Introduction

The mass and energy balance of glaciers and ice caps are to varying degrees determined by the turbulent sensible and latent heat fluxes. Measurements made on glacier surfaces show that turbulent fluxes contribute from 20% to 40% of the total energy balance, see for example Kuhn (1979), Ohata (1989), van den Broeke (1996), Oerlemans *et al.* (1999) and Wagnon *et al.* (1999). They are thus an important component especially in relation to the climate sensitivity of the mass balance since it is these energy fluxes, along with longwave radiation, which are directly affected by temperature changes. It is therefore important in energy balance studies to correctly measure and model these fluxes.

Determining turbulent fluxes in the field can be done in several ways. The first is by direct eddy correlation methods made with sonic anemometers. Measurements using these instruments are the most direct, but also the most difficult to carry out chiefly due to the fragility of the instruments, the continuous maintenance and the problem involved with interpretation. The various attempts to directly measure turbulent fluxes on glacier surfaces, e.g. Munro (1989), Smeets *et al.* (1998) and van der Avoird and Duynkerke (1999), are generally only for short periods of time and do not always agree with other methods for determining the fluxes. The second, and most widely used method is to make use of mean wind, temperature and humidity measurements (made with robust instruments) and convert these mean values to surface fluxes by way of Monin-Obukhov (M-O) similarity theory. The third method, and most inaccurate, is the residual method whereby all the other components of the energy balance are measured, along with the mass balance, and the remaining melt must be explained by way of the turbulent heat fluxes. This is a useful check but errors in radiation measurements are generally so large that it cannot be used to determine these fluxes to any sufficient accuracy.

The second method described above, using mean values and M-O similarity theory, is the subject of this paper. Recent work with second-order models (Denby, 1999), which describe in more detail the turbulent structure of the atmospheric boundary layer (ABL) above sloping terrain has shown that assumptions made in M-O theory are often invalid on sloping glacier surfaces. This is the result of katabatic forcing in the ABL, which produces the katabatic, or glacier, wind. Katabatic winds are gravity flows caused by the turbulent cooling of air close to the surface. This cooler denser air sinks downslope producing the well known glacier wind, which is characterized by a low level wind speed maximum. The wind speed maximum found on glaciers with slopes of around 5° can be as low as 2 m above the surface and are thus close to or even below standard measuring heights. As is pointed out in Section 3.2, measurements made on the Pasterze glacier show wind maxima below 13 m for more than 75% of the time.

The presence of the wind speed maximum alters the turbulent scaling laws, used in M-O similarity theory, for two reasons. The first is the non-negligible turbulent transport term in the turbulent kinetic energy (TKE) budget. Since mechanical production of turbulence by shear is zero at the height of the wind speed maximum ($\partial U / \partial z = 0$) turbulent transport, a second-order term in the TKE budget, will dominate in this region and thus similarity arguments, which assume this term to be negligible, cannot be used. The second reason is that M-O similarity theory assumes

a constant turbulent flux layer, the so called surface layer where fluxes change in the vertical by less than 10%. This layer can be very thin when a katabatic wind speed maximum is present. As mentioned above, wind shear reduces to zero at the height of the wind speed maximum as will the vertical flux of horizontal momentum (\overline{uw}). This indicates a strong divergence in \overline{uw} and thus a very thin surface-layer. For a wind speed maximum of 5 m M-O theory would then only be valid in the lowest 0.5 m.

In spite of this, M-O theory is still used to calculate turbulent fluxes under these conditions. The question posed here is what sort of influence the presence of a wind speed maximum has on the bulk and profile methods commonly used to determine these fluxes. By making use of observations and second-order modelling results it will be shown that profile methods will always severely underestimate turbulent fluxes when a wind speed maximum is present but that the bulk method still gives quite good estimates of these fluxes up to at least the height of the wind speed maximum.

3.2 Observations

In this paper use is made of experimental data from the PASTEX glacio-meteorological experiment carried out on the Pasterze glacier in Austria during the summer of 1994 (Greuell *et al.*, 1997). Six weather stations for determining the energy balance of the glacier were stationed along the central flow line. Most of these consisted of just two measurement heights, 0.5 m and 2 m, but at one site, known as A1, a 13 m profile mast with 8 measurement heights (0.4, 0.7, 1, 2, 4, 6, 8 and 13 m) and a balloon sounder were placed at a point roughly 1 km from the end of the glacier tongue at an elevation of 2200 m a.s.l.. Smeets *et al.* (1998) provides more information concerning the measurements made using this mast. The local slope at this site was approximately 3.5° .

During the observational period from 16 June to 11 August over 2600 half-hourly average observations were made. Of these 77% showed the existence of a wind speed maximum below the highest profile level when wind direction was downslope, indicative of katabatic flows. Air temperatures were well above 0°C during the observational period and the surface was almost always melting. Figure 3.1b shows the average downslope wind speed and temperature profiles during a two day fair weather period at this site. During this period a wind speed maximum was present more than 90% of the time.

3.3 The mean and turbulent structure of katabatic flows

Katabatic flows on glaciers are driven from beneath by buoyancy, or katabatic, forcing. Warm air overlaying the glacier is cooled by turbulent exchange with the ice or snow surface, becoming denser and resulting in the downslope flow of cool air. This katabatic flow, often referred to as glacier wind, is a dominant feature of the ABL above most temperate glaciers. The low level forcing combined with the turbulent exchange of momentum will intrinsically lead to the development of a wind speed

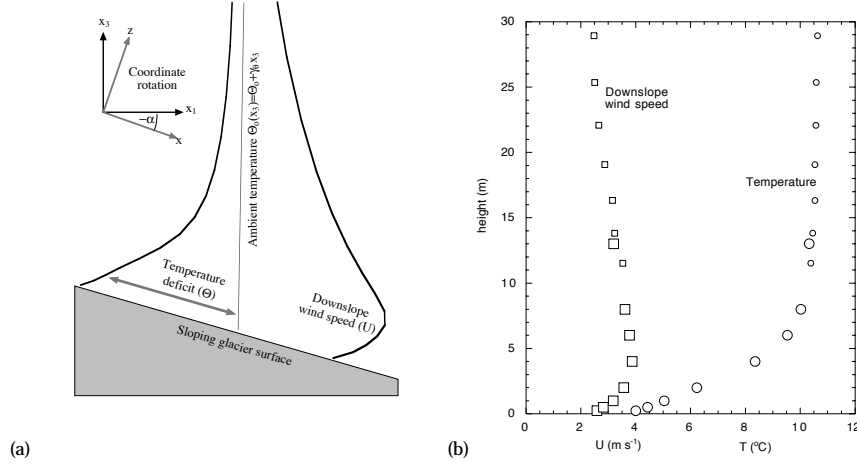


Figure 3.1: a) Schematic diagram of the glacier wind showing terms described in the text. b) Average observed downslope wind speed (squares) and temperature (circles) at site A1 on the Pasterze glacier during a 2 day fair weather period. Most profile measurements are indicated by large shapes whilst balloon soundings, made approximately every 3 hours, are indicated by the smaller shapes.

maximum at some level. It is the nature of the turbulence that determines the form the mean wind and temperature profiles adopt.

A 1-D second-order turbulence closure model, which simulates the vertical profile of the ABL, is used here to help describe the turbulent structure of katabatic flows. The 1-D model is discussed in detail in Denby (1999) where it has been shown to describe the mean and turbulent structure of katabatic flows quite well. It makes use of second-order closures, including closures for the turbulent transport of TKE, thus M-O similarity is not assumed in order to calculate the katabatic profiles. Only at the lowest level of the model, $z = 0.2$ m, is the assumption of similarity used to calculate lowest level fluxes. The roughness length for momentum in the model is predefined and the roughness length for temperature is based on the surface renewal model from Andreas (1987). The flux profile relationships, as defined in Section 3.4, are used for the stability correction at this lowest level.

Equations 3.1 and 3.2 show the simplified 1-D equation for downslope momentum U and temperature perturbation Θ .

$$\frac{\partial U}{\partial t} = - \frac{\partial \overline{uw}}{\partial z} + \sin(\alpha) \frac{g}{\Theta_o} \Theta + \cos(\alpha) f(V - V_g) \quad (3.1)$$

Flux divergence Katabatic forcing Coriolis forcing

$$\frac{\partial \Theta}{\partial t} = \sin(\alpha) \gamma_\theta U - \frac{\partial \overline{w\theta}}{\partial z} \quad (3.2)$$

Ambient advection Flux divergence

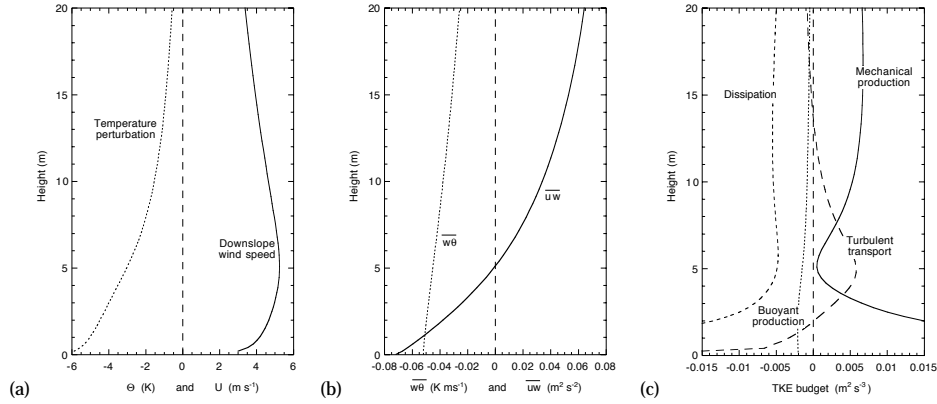


Figure 3.2: a) Simulated downslope wind speed (U) and temperature deficit (Θ) profiles for the 1-D katabatic case described in the text. The wind speed maximum is at a height of 5 m. b) Simulated \overline{uw} and $\overline{w\theta}$ profiles. c) Simulated TKE budget profile.

Θ is defined as the potential temperature difference from a pre-defined ambient temperature profile given as $\Theta_o(x_3) = \Theta_o + \gamma_\theta x_3$, where x_3 is the true vertical component, i.e. parallel with the gravitational vector, and where the co-ordinate system (x, z) is defined as a cartesian co-ordinate system orthogonal to the sloping surface with slope angle α . V_g is the geostrophic wind component and the over bar indicates the turbulent flux terms, as defined by Reynolds decomposition. These are the vertical flux of horizontal momentum \overline{uw} and the vertical flux of potential temperature $\overline{w\theta}$, which is directly converted to the turbulent flux of sensible heat $H = \rho c_p \overline{w\theta}$ where ρ is the density and c_p the specific heat of air. A schematic representation of the glacier wind is given in Figure 3.1a indicating the terms mentioned above.

In Figure 3.2a the simulated downslope wind and temperature profiles are shown for a typical case of katabatic forcing on a sloping glacier with surface temperature perturbation $\Theta_s = -10$ K, surface roughness length $z_o = 2$ mm, temperature lapse rate $\gamma_\theta = 3$ K km^{-1} and slope $\sin(\alpha) = -0.1$ (6°). The major features of the mean flow are of course the wind speed maximum, in this case at a height of around 5 m, and the strong temperature inversion beneath the wind speed maximum of approximately 0.5 K m^{-1} .

On typical temperate glaciers katabatic forcing is the dominant driving force in the momentum budget close to the surface (Denby and Smeets, 2000). This is balanced by the flux divergence of horizontal momentum in Equation 3.1 resulting in the strong gradient in \overline{uw} seen in Figure 3.2b. \overline{uw} will pass through zero at, or at least close to, the height of the wind maximum. Though there is a steep gradient in \overline{uw} , the vertical profile for sensible heat flux ($\overline{w\theta}$) is almost constant in the region below the wind speed maximum, varying in this case by just 15% (Figure 3.2b). Though this is a 1-D simulation and other terms in the temperature budget are also important in a 2- or 3-dimensional case, such as horizontal advection of temperature perturbation, the basic turbulence structure remains the same.

In order to indicate the role played by turbulent transport in katabatic flow the TKE budget is also shown in Figure 3.2c. As the height of the wind speed maximum

is approached the mechanical production through shear approaches zero and the turbulent transport term transports TKE into this region. This is where M-O theory, as well as local scaling arguments, break down since they do not take into account the transport terms. Above the wind speed maximum, where shear dominates the TKE budget, local scaling arguments such as those described by Nieuwstadt (1984) become applicable again.

3.4 Suitability of bulk and profile methods

Before comparing the bulk and profile methods with observations and model results it is useful to give a brief description of these two methods. Both the bulk and profile methods use Monin-Obukhov similarity theory, which is based on scaling arguments using the turbulent velocity and temperature scales, u_* and θ_* , and the length scales z (height), L (Obukhov length), and z_o and z_h (surface roughness lengths of momentum and temperature). These turbulent scales define completely, under idealized horizontally homogeneous and quasi steady-state conditions, the turbulent structure of the surface layer, the lowest region of the atmospheric boundary layer (ABL).

The flux-profile relationships, Equations 3.3 and 3.4, are definitions relating the vertical gradients of mean wind and temperature to these turbulent scales:

$$\phi_m \equiv \frac{\kappa z}{u_*} \frac{\partial U}{\partial z} \quad (3.3)$$

$$\phi_h \equiv \frac{\kappa z}{\theta_*} \frac{\partial \Theta}{\partial z} \quad (3.4)$$

where $u_* = |\overline{uw}|^{1/2}$ and $\theta_* = \frac{-\overline{w\theta}}{u_*}$.

Under neutral conditions ϕ_m is defined as being equal to unity and the von Karman constant ($\kappa=0.4$) is determined from observations to fulfill this definition. Integration of these relationships, under stable conditions and the assumption of a constant flux layer, leads to the well known log-linear wind and temperature profiles if a linear relationship is assumed for $\phi_{m,h}$ of the following form (Garratt, 1992):

$$\phi_m = 1 + \alpha_m \frac{z}{L} \quad (3.5)$$

$$\phi_h = Pr + \alpha_h \frac{z}{L} \quad (3.6)$$

where $L = \frac{u_*^2}{\kappa(g/\Theta_o)\theta_*}$.

The constants in Equation 3.5 and 3.6 are determined solely from observations and vary to some extent in the literature. We use here a value of 5 for both α_m and α_h and a near-neutral turbulent Prandtl number $Pr=1$. Integrating Equations 3.3 and 3.4 from level z_1 to z_2 leads to the following log-linear profile equations:

$$(U(z_2) - U(z_1)) \frac{\kappa}{u_*} = \ln \left[\frac{z_2}{z_1} \right] + \alpha_m \frac{z_2 - z_1}{L} \quad (3.7)$$

$$(\Theta(z_2) - \Theta(z_1)) \frac{\kappa}{\theta_*} = Pr \ln \left[\frac{z_2}{z_1} \right] + \alpha_h \frac{z_2 - z_1}{L} \quad (3.8)$$

and integrating these equations from the roughness length heights of z_o and z_h to z gives the log-linear bulk equations:

$$U(z) \frac{\kappa}{u_*} = \ln \left[\frac{z}{z_o} \right] + \alpha_m \frac{z}{L} \quad (3.9)$$

$$(\Theta(z) - \Theta_s) \frac{\kappa}{\theta_*} = Pr \ln \left[\frac{z}{z_h} \right] + \alpha_h \frac{z}{L} \quad (3.10)$$

It should be noted that the roughness lengths are the height at which the extrapolated wind and temperature profiles would reach their surface values.

Equations 3.7 and 3.8 require a minimum of two profile heights for wind and temperature to derive the four unknowns u_* , θ_* , z_o and z_h assuming the surface temperature Θ_s to be known. The accuracy of the profile method will increase when more profile levels are used and these are fitted using least-squares techniques. For simplicity in this paper we will limit ourselves to the case where only two profile heights are available, this defines the profile method for determining surface fluxes. The bulk method on the other hand makes use of only one height to derive u_* and θ_* assuming the roughness lengths (z_o, z_h) and the surface temperature Θ_s to be known. The application of these methods has been quite successful in the stable ABL, which is the reason for its popularity under most conditions.

We will now take bulk and profile derived fluxes calculated from the profile mast data and compare these to model simulations. The results are presented in Figures 3.3 and 3.4 for both \overline{uw} and $\overline{w\theta}$ where we have used the non-dimensional height z/H , H is the height of the wind speed maximum, as the scaled vertical axis. In these figures all mast levels are used to calculate the bulk and profile derived fluxes. For the profile method each point represents the profile derived flux taken from two adjoining mast levels at a height determined by their average. For the bulk method each point indicates the bulk derived fluxes for a particular mast level. Both sets of data are normalized by the bulk derived value taken from the 0.7 m mast level using previously derived roughness lengths (Denby and Smeets, 2000). This is considered to give the best estimate of the surface flux since it is expected that when $H \gg z \gg z_o$, M-O theory will still be valid. The normalized fluxes should approach unity in this range.

The model results are calculated by a continuous run of the 1-D model where the surface temperature perturbation is allowed to slowly decrease by -0.1 K hr^{-1} from 0 to -20 K . In this way a continuous range of simulated katabatic profiles are generated by varying the katabatic forcing. Fixed heights of 2 and 0.5 m within the model are then used to calculate the profile derived fluxes and a height of 2 m is used to calculate the bulk derived fluxes. Both the bulk and profile derived model fluxes are normalized by the model generated surface flux value. The local slope, $\alpha = 3.5^\circ$, is used as well as the average lapse rate of $\gamma_\theta = 3.5 \text{ K km}^{-1}$.

It is worth noting at this point that even though the simulations are one dimensional the basic turbulent structure of the katabatic flow remains the same, even with the introduction of advection terms in Equations 3.1 and 3.2. As previously mentioned, Section 3.3, the momentum budget is dominated by the katabatic forcing

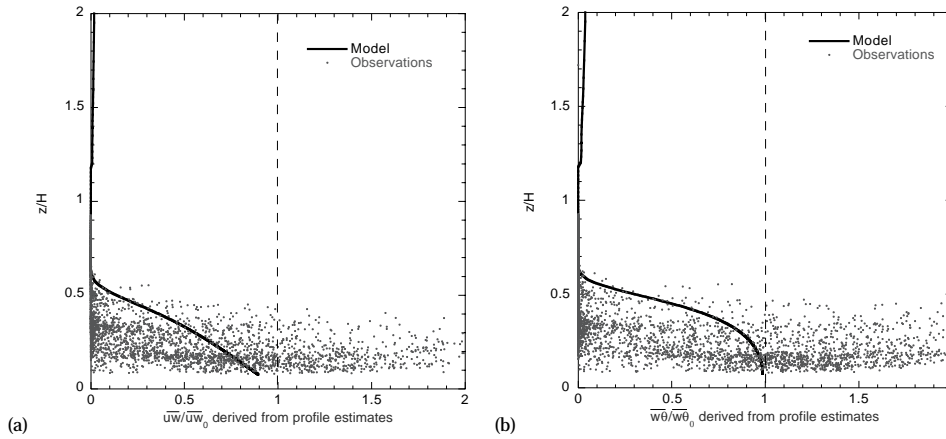


Figure 3.3: Profile derived normalized vertical momentum flux (a) and sensible heat flux (b) as function of the non-dimensional height z/H (H =height of the wind speed maximum) derived from observations, dots, and from 1-D model simulations, continuous line. Both the heat and momentum fluxes are normalized by the bulk derived surface flux determined at a height of 0.7 m. See text for details.

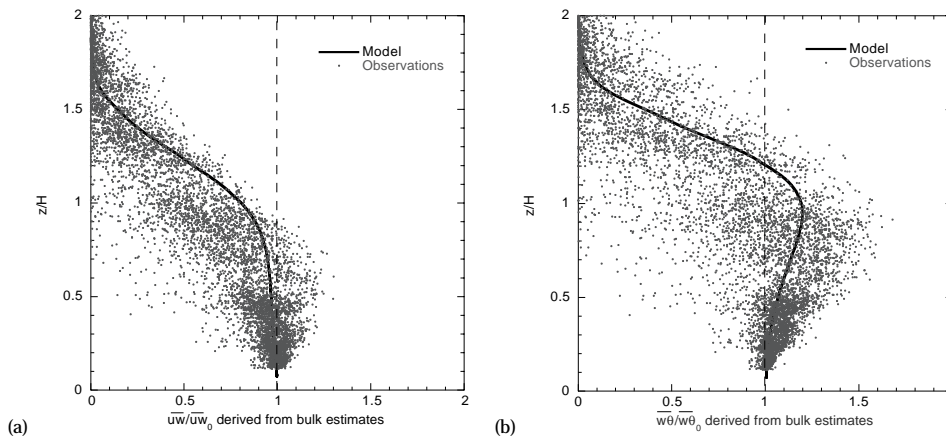


Figure 3.4: Bulk derived normalized vertical momentum flux (a) and sensible heat flux (b) as function of the non-dimensional height z/H (H =height of the wind speed maximum) derived from observations, dots, and from 1-D model simulations, continuous line. Both the heat and momentum fluxes are normalized by the bulk derived surface flux determined at a height of 0.7 m. See text for details.

and flux divergence terms even when horizontal and vertical advection are present. The temperature budget, on the other hand, is more strongly affected by the horizontal and vertical advection of temperature perturbation. To test the sensitivity of the results to temperature advection an entrainment velocity is introduced to the temperature budget, as was carried out in Denby (1999), which allows the representation of vertical advection within the 1-D model. Even under conditions of strong entrainment the normalized profiles shown in Figures 3.3 and 3.4 remain essentially

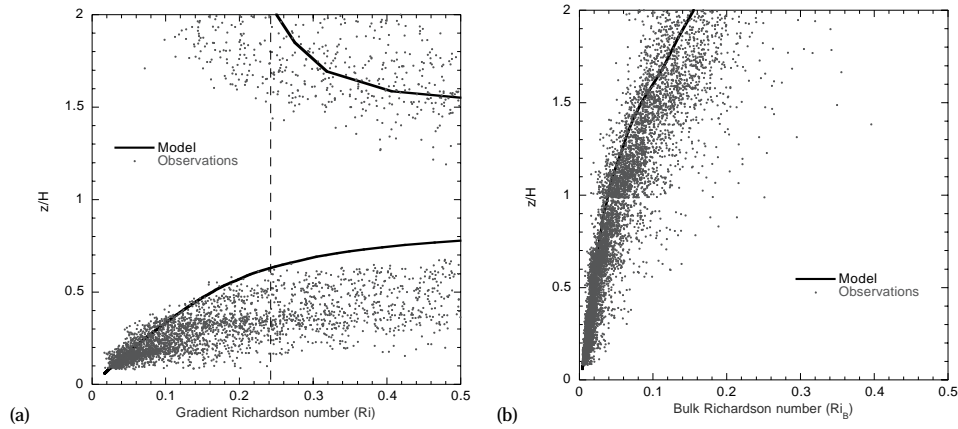


Figure 3.5: Gradient Richardson number (a) and Bulk Richardson number (b) as function of the non-dimensional height z/H (H =height of the wind speed maximum) derived from observations, dots, and from 1-D model simulations, continuous line. The dotted line in (a) indicates the models critical gradient Richardson number of 0.23. The bulk Richardson number is defined as $Ri_B = \frac{g/\Theta_o(\Theta(z)-\Theta_s)z}{U(z)^2+V(z)^2}$

unaltered. In this regard the 1-D results obtained here are quite robust.

The profile derived fluxes show a large amount of scatter in the observations, which results from the sensitivity of this method to measurement errors and variability. What is clear though is that turbulent fluxes are severely underestimated throughout the region below the wind speed maximum. This is the result of reduced shear and increasing temperature gradients as the wind speed maximum is approached. This ensures that the local gradient Richardson number ($Ri = \frac{g/\Theta_o \partial \Theta / \partial z}{(\partial U / \partial z)^2 + (\partial V / \partial z)^2}$) approaches its critical value ($Ri_c = 0.23$ in this model), above which all turbulence is suppressed according to M-O theory. This occurs at around half the height of the wind speed maximum (Figure 3.5a).

The bulk method, on the other hand, shows far less scatter since gradients need not be determined. Though \overline{uw}_o is underestimated when measurements are made above the height of the wind maximum this is not as severe as in the profile case. $\overline{w\theta}_o$ on the other hand is slightly overestimated when measurements are made below the wind speed maximum but reduce quickly as the measurement height increases above the wind speed maximum. Generally wind maxima are above a normal measuring height of 2 m so we are not usually concerned with this region.

How can we explain the ability of the the bulk method to estimate the surface fluxes even in the region of the wind speed maximum? The bulk method is essentially an integrated form of the profile method and, as such, is less sensitive to variations in gradients brought about by the presence of a wind speed maximum. As turbulence decreases with decreasing shear near the wind maximum, wind speeds reduce relative to their log-linear form (Equation 3.9). This effect is shown in Figure 3.6, where the katabatic wind and temperature profiles from Figure 3.2 are plotted against logarithmic and log-linear profiles with equivalent surface flux values. This then leads to a reduction in the bulk derived \overline{uw}_o values in Figure 3.4a. How-

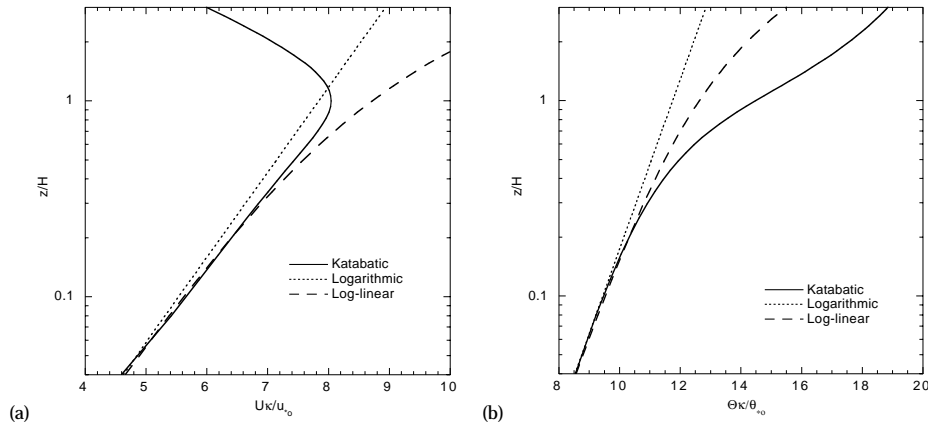


Figure 3.6: Comparison of simulated katabatic wind (a) and temperature (b) profiles with the logarithmic and log-linear profile forms. The logarithmic and log-linear profiles are calculated assuming surface fluxes equivalent to the katabatic surface value.

ever, this same reduction in turbulence will increase the temperature gradient, and therefore the temperature, as the wind speed maximum is approached (Figure 3.6b). These two effects tend to cancel each other out, reducing u_* and increasing θ_* , and the resulting bulk determined heat flux remains fairly constant until the diminishing wind speed above the wind maximum leads to stability corrections severely reducing the apparent turbulence.

For the 1-D katabatic case the normalized model profiles generated for Figure 3.6 are not universal. The height of the katabatic wind speed maximum (H) is not the only scaling length that determines the form of the normalized curves since the turbulent M-O scaling length L is of a similar order. The dependence on slope for the bulk derived heat flux is illustrated in Figure 3.7a where three model runs with differing slopes are shown. From a pragmatic point of view the slope dependence is of little consequence since the largest deviations from unity occur by weaker slopes where wind maxima are higher and so measurements will always be made well below the wind speed maximum. It is therefore relieving to see that even for steep slopes, where the wind speed maximum can be quite low, that the bulk derived heat flux appears to be quite representative of the surface value.

To illustrate this point further, the height of the wind speed maximum is plotted as a function of maximum wind speed for the three differing slope angles in Figure 3.7b. As in all the simulations the surface temperature deficit is allowed to slowly decrease from 0 to -20 K and the closed circles in Figure 3.7b indicate 2 K steps. For wind speed maxima under 2 m the temperature perturbation and wind speed are quite low, corresponding to small surface turbulent heat fluxes, especially for lesser slopes. Any errors introduced due to the proximity of the wind speed maximum will be, on an absolute scale, negligible.

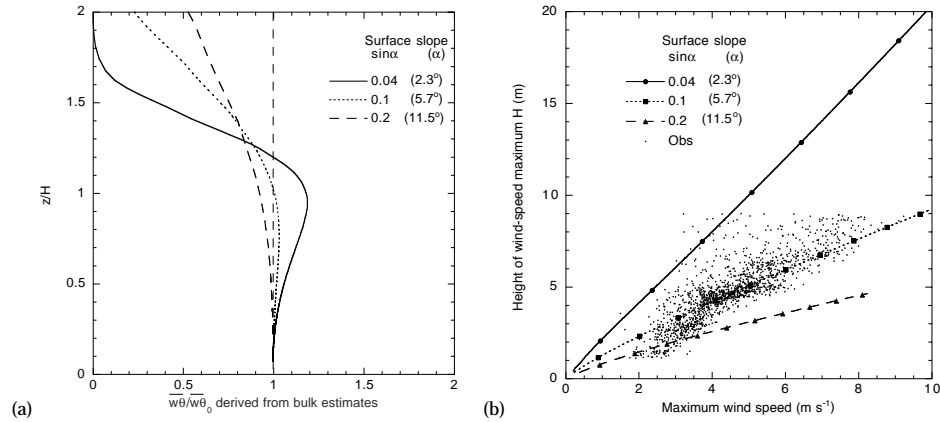


Figure 3.7: (a) Variation in the normalized bulk derived heat flux for three different surface slopes taken from 1-D simulations. (b) Maximum wind speed height as a function of maximum wind speed for the same simulations. Points indicate observations from the profile mast A1 on the Pasterze glacier. Local slope is approximately 3.5° .

3.5 Conclusion and discussion

The suitability of Monin-Obukhov similarity theory under conditions of katabatic flow where a low level wind speed maximum is present is discussed. Though assumptions made in M-O theory are not valid in the presence of a wind speed maximum it is shown that bulk estimates of turbulent heat fluxes give quite reasonable results in the entire region below the wind maximum whereas profile derived fluxes underestimate the surface fluxes severely. Only in the lowest region, $z/H < 0.5$, does the profile method give any value for the surface flux at all, due to stability corrections, and only in a narrower region, $z/H < 0.3$, do we find values comparable to low level bulk estimates. For a wind speed maximum at 5 m this would infer that profile measurements would need to be made below a height of approximately 1.5 m. However, profile fits need to be made well above the average surface roughness element size which can easily be of the same order on some melting ice surfaces.

That bulk methods are effective in determining turbulent fluxes, even under conditions of katabatic flow, is good news for energy balance studies since measurements of mean wind and temperature at one level are far easier to carry out than profile or eddy correlation measurements. There remains, however, two problems in using the bulk method to determine turbulent heat fluxes. The first is the determination of the surface temperature. Though this can be an important point for non-melting surfaces it is inconsequential when studying melting ice surfaces, as is done here, since the surface is permanently at the melting point.

The second problem is the determination of surface roughness lengths for momentum, temperature and water vapour, which are essential parameters when using the bulk method. Normally roughness lengths are determined using profile methods since this is how they are defined, being the height at which the extrapolated

profiles in the surface layer reach their surface value. In essence roughness lengths are a parameterisation for the inertial-sublayer, a region affected by both viscous and inertial forces, close to the surface. The depth of this layer, and also z_o , is correlated with the surface roughness element form, height and spacing (Garratt, 1992).

In practise the determination of roughness lengths for momentum requires near neutral conditions of long fetch and a well developed deep quasi steady-state boundary layer. These conditions are seldom met on a melting glacier where the strong temperature inversions and katabatic winds prohibit the use of profiles to determine z_o due to stability considerations and the presence of the low-level wind speed maximum, as is shown in Section 3.4. For instance Smeets *et al.* (1998) could use just 38 of the 2600 half-hourly mean measured profiles from the same PASTEX data set in order to estimate surface roughness lengths. An alternative possibility for determining z_o is that proposed by Denby and Smeets (2000), which makes use of the dynamics of katabatic forcing to determine the vertical profile of momentum flux from wind and temperature profile data. This method, though having been shown to give quite good results, also requires high resolution profile masts in order to determine the height of the wind speed maximum.

This is why various attempts have been made, both in the field and in laboratories, to relate surface roughness element height and form with the aerodynamic roughness length, at least for momentum (Lettau, 1969). The use of microtopographical surveys, e.g. Munro (1989), to determine roughness lengths for momentum and surface renewal theories, e.g. Brutsaert (1975b) and Andreas (1987), to determine the roughness lengths for temperature and water vapour are much easier and appealing methods. Though these methods are promising, since measuring microtopography is much simpler than directly measuring aerodynamic roughness lengths, estimates based on roughness element data must be considered with care, as pointed out by Smeets *et al.* (1999), and should be seen as reasonable approximations when aerodynamical data is not available. Once more, confirmation of these methods on glacier surfaces is difficult due to the presence of katabatic flows.

This remains a problem and so best estimates will still have to be used with the available data. Luckily an order of magnitude error in z_o will only lead, when the bulk method is used, to roughly a 25% error in surface heat fluxes. This is still a far better alternative than the use of profile methods to determine the same fluxes under conditions of katabatic flow.

Acknowledgments

We would like to thank Paul Smeets from the Vrije Universiteit Amsterdam for the observational data used in this paper and also all those who participated in the PASTEX measurement campaign. This research was funded by the Dutch National Research Programme on Global Air Pollution and Climate Change (NOP II Project 013 001236.10).

4

Derivation of Turbulent Flux Profiles and Roughness Lengths from Katabatic Flow Dynamics

The dynamics of katabatic flows are used to determine the vertical momentum flux profiles and surface roughness lengths under stable conditions on glacier surfaces. By assuming a momentum budget balance between katabatic forcing and vertical flux divergence of horizontal momentum in the region beneath the wind speed maximum, it is possible to derive the vertical momentum flux profile by integrating the temperature deficit. By use of the surface flux determined in this way and appropriate profile fits, the roughness length for momentum can be derived. The roughness length obtained in this way agrees well with estimates made under nonkatabatic conditions using standard log-linear fits. The katabatically determined fluxes are compared with eddy correlation measurements and with bulk methods. The eddy correlation measurements are not always in agreement with the katabatic fluxes, however the comparison with bulk derived fluxes is particularly good.

4.1 Introduction

A number of glacio-meteorological experiments have been made in the past few years to better understand the surface energy balance of glaciers and ice caps, see e.g. Greuell *et al.* (1997) and Oerlemans *et al.* (1999). These experiments have attempted to quantify the various components of the surface energy balance, which consists of long- and shortwave radiation fluxes as well as turbulent sensible and latent heat fluxes. The components of the surface energy balance can be measured either directly, such as radiation, or indirectly, as is usually the case with turbulent fluxes. Unless eddy correlation techniques are employed, the surface sensible and latent heat fluxes must be derived from the mean variables of wind, temperature and humidity. These variables are almost always converted to turbulent flux values by way of classical Monin-Obukhov similarity (M-O) theory utilizing either bulk or profile methods.

The atmospheric boundary layer (ABL) above glaciers has been found to be dominated by katabatic winds, see e.g. Munro and Davies (1978), Oerlemans *et al.* (1999) and Smeets *et al.* (1998), which are characterized by a low-level wind speed maximum just a few meters above the surface. Similarity arguments based on the dominance of vertical wind shear in the production of turbulent kinetic energy (TKE) will not be valid in the region of the wind maximum because shear production approaches zero at this height and turbulent transport will dominate the TKE budget (Denby, 1999). Only when $z_o \ll z \ll H$, where H is the height of the wind speed maximum and z_o is the surface roughness length for momentum, would one expect similarity theory to be valid. Unfortunately, the low level of the wind speed maximum, commonly just a few meters, often brings it in the proximity of the profile measurement heights. This makes determination of turbulent fluxes and, in particular, surface roughness lengths difficult if not impossible when using standard profile methods because the profiles do not conform to the assumed log-linear form.

In this paper, an alternative method for determining the surface roughness length for momentum, essential for the bulk determination of turbulent fluxes, is proposed and takes advantage of the nature of katabatic forcing to determine the vertical profile of the vertical momentum flux and then, through profile fitting, the surface roughness length z_o . The argument for this method is put forward in Section 4.2. The basic assumption is that a dynamic balance exists in the momentum budget between katabatic forcing and the vertical flux divergence of horizontal momentum in the region below the wind speed maximum of a katabatic flow. This balance allows the determination of the momentum flux by direct integration of the temperature profile when the height of the wind speed maximum is known.

This method is applied to two sites (Section 4.4) at which observations have been made during the summer melt period. Flux values derived using this katabatic method are compared with direct eddy correlation measurements made with sonic anemometers as well as with bulk-method calculations. The katabatically derived roughness lengths for momentum are also compared to more standard profile derived values, which can be determined when the wind speed maximum is located well above the observational mast.

4.2 The katabatic method for flux determination

The 2-D mean equations for downslope momentum and heat on an inclined surface of constant slope α with co-ordinates (x, z) orthogonal to the surface, positive x directed down slope, can be written as follows (Nappo and Shankar Rao, 1987):

$$\begin{aligned} \frac{\partial U}{\partial t} = & \underbrace{-U \frac{\partial U}{\partial x} - W \frac{\partial U}{\partial z}}_{\text{Advection}} \underbrace{-\frac{\partial \overline{uw}}{\partial z}}_{\text{Flux divergence}} + \underbrace{(\sin \alpha) \frac{g}{\Theta_o} \Theta}_{\text{Katabatic}} \\ & + \underbrace{(\cos \alpha) \frac{g}{\Theta_o} \frac{\partial \hat{\Theta}}{\partial x}}_{\text{Thermal wind}} + \underbrace{(\cos \alpha) f (V - V_g)}_{\text{Coriolis}} \end{aligned} \quad (4.1)$$

$$\begin{aligned} \frac{\partial \Theta}{\partial t} = & \underbrace{-U \frac{\partial \Theta}{\partial x} - W \frac{\partial \Theta}{\partial z}}_{\text{Perturbation advection}} \underbrace{-(\sin \alpha) U \gamma_\theta - (\cos \alpha) W \gamma_\theta}_{\text{Ambient advection}} \\ & - \underbrace{\frac{\partial \overline{w\theta}}{\partial z}}_{\text{Flux divergence}} - \underbrace{\frac{1}{\rho c_p} \frac{\partial R_n}{\partial z}}_{\text{Radiation}} \end{aligned} \quad (4.2)$$

where $\hat{\Theta} = \int_z^\infty \Theta(z') dz'$

These equations are derived from the conservation of momentum and entropy after splitting the potential temperature field into a mean ambient component $\Theta_o(\tilde{z})$, where \tilde{z} is the true vertical co-ordinate, and a mean perturbation $\Theta(\hat{x}, \tilde{z})$. The ambient part is assumed to have a constant lapse rate γ_θ and to be in hydrostatic equilibrium. In this way, density perturbations from the hydrostatic state can be translated to temperature fluctuations via the equation of state. The equations are then rotated through an angle α transforming the co-ordinates from a vertically oriented Cartesian co-ordinate system to a surface orthogonal Cartesian system with mean wind components (U, V, W) . Geostrophic balance and the hydrostatic approximation are assumed, so the synoptic scale horizontal pressure gradient is represented by the geostrophic wind terms U_g and V_g , f is the Coriolis parameter, and the horizontal perturbation pressure gradient (thermal wind) is determined by $\hat{\Theta}$. Here, g is gravitational acceleration, ρ is air density, c_p is the heat capacity of air and R_n is net radiation. The turbulent components are derived by Reynolds decomposition and are represented by small type, the overbar indicating time averages, and mean values are represented by capitals.

We start by investigating the conservation of momentum equation and describing typical scales expected on glaciers. The driving force behind glacier winds is the temperature perturbation or deficit term in Equation 4.1, also known as the katabatic forcing term. Given a typical summer temperature deficit of -10°C and a slope of 5° , then this forcing term is $\approx 3 \times 10^{-2} \text{ ms}^{-2}$ close to the surface. Assuming a horizontal length scale of 10 km (length of a glacier) and a typical wind speed of 5 ms^{-1} gives advection tendencies of $\approx 2 \times 10^{-3} \text{ ms}^{-2}$, Coriolis forcing of $\approx 5 \times 10^{-4} \text{ ms}^{-2}$ and horizontal pressure gradients (thermal wind) of $\approx 1 \times 10^{-3} \text{ ms}^{-2}$.

The above scale analysis clearly indicates that katabatic forcing on glacier surfaces is approximately an order of magnitude greater than the other terms in regions where the temperature deficit is large. This condition occurs chiefly close to the surface below the wind speed maximum where a strong temperature inversion exists, see Figure 4.1. Clearly the only term capable of balancing this forcing is the flux divergence term in Equation 4.1.

This fact is the basis of the forthcoming analysis. Having assumed a balance between flux divergence and temperature deficit, a simple integration of the temperature profile will give the vertical profile of the momentum flux. However, since the integration is limited in height because profile data are only available up to about 10 m, and katabatic forcing will be most dominant in the region below the wind maximum where the temperature deficit is greatest, it is necessary to fix the \overline{uw} profile at some height and value. This can be done if we assume that $\overline{uw} \rightarrow 0$ as $\partial U/\partial z \rightarrow 0$. This assumption is certainly the case when a K-theory relationship between the two is valid. It is possible however, as Irwin (1974) has shown for near wall jets, that transport terms in the \overline{uw} budget are important enough to shift the \overline{uw} zero point away from the height of the wind maximum. We will assume in this paper that this is not the case and that we can set \overline{uw} to zero at the wind maximum height (H) and thus write the integration as

$$\overline{uw}(z) = -\sin \alpha \frac{g}{\Theta_o} \int_z^H \Theta(z') dz' \quad (4.3)$$

If a similar scale analysis is carried out for the heat budget, then temperature perturbation advection terms of $\approx 5 \times 10^{-3} \text{ K s}^{-1}$, ambient advection of $\approx 2 \times 10^{-3} \text{ K s}^{-1}$ and typical radiation cooling of $\approx 1 \times 10^{-3} \text{ K s}^{-1}$ are found. In this case, advection terms on glaciers dominate. These terms are impossible to determine from a single profile analysis, so one cannot deduce the turbulent heat flux profile from budget analysis.

4.3 Bulk and profile methods

In the coming sections, use will be made of the bulk and profile methods for determining turbulent fluxes and roughness lengths so for completeness a quick summary is made here. Both of these methods make use of M-O similarity using the turbulent velocity and temperature scales u_* and θ_* respectively, which also determine the stability correction M-O length scale L . The flux-profile relationship for momentum, Equation 4.4, is a definition that relates the vertical gradient of mean wind to u_* and is applicable in the surface layer in which fluxes are assumed to be vertically constant, horizontally homogeneous and in equilibrium.

$$\phi_m \equiv \frac{\kappa z}{u_*} \frac{\partial U}{\partial z} \quad (4.4)$$

$$\phi_h \equiv \frac{\kappa z}{\theta_*} \frac{\partial \Theta}{\partial z} \quad (4.5)$$

where $u_* = |\overline{uw}|^{1/2}$ and $\theta_* = \frac{-\overline{w\theta}}{u_*}$. A similar definition exists for ϕ_h , the flux-profile relationship for temperature, Equation 4.5.

Under neutral conditions ϕ_m is defined as being equal to unity and the von Karman constant ($\kappa = 0.4$) is determined from observations to fulfill this definition. Integration of these relationships, under stable conditions, leads to the well known log-linear wind profile when a linear relationship is assumed for ϕ_m of the following form (Garratt, 1992)

$$\phi_m = 1 + \alpha_m \frac{z}{L} \quad (4.6)$$

$$\phi_h = Pr + \alpha_h \frac{z}{L} \quad (4.7)$$

where $L = \frac{u_*^2}{\kappa(g/\Theta_o)\theta_*}$. The constants α_m and α_h in Equations 4.6 and 4.7 are determined solely from observations and vary to some extent in the literature. In this paper a value of 5.0 for both α_m and α_h is used. The log-linear form is written as:

$$U(z) \frac{\kappa}{u_*} = \ln \left[\frac{z}{z_o} \right] + \alpha_m \frac{z}{L} \quad (4.8)$$

$$(\Theta(z) - \Theta_s) \frac{\kappa}{\theta_*} = Pr \ln \left[\frac{z}{z_h} \right] + \alpha_h \frac{z}{L} \quad (4.9)$$

where Pr is the turbulent Prandtl number, and z_o and z_h are the roughness lengths for momentum and temperature respectively (Garratt, 1992).

Equations 4.8 and 4.9 require a minimum of two profile heights to derive the four unknowns u_* , θ_* , z_o and z_h , however accuracy increases when more levels are used and these levels are fitted using least square techniques. The bulk method makes use of only one height to derive u_* and θ_* , assuming the roughness lengths and the surface temperature Θ_s are known. The bulk method tends to be less sensitive to sensor errors than the profile method when surface parameters are reasonably well known. This difference in sensitivity is due to the uncertainty in small gradients that must often be measured when making profile fits.

These equations should be applied only to the surface layer where turbulent scales completely determine the characteristics of this layer and the turbulent fluxes are assumed to be constant.

4.4 Observations of katabatic flows

In this paper two sets of profile data gathered during two different meteorological experiments will be used. The first of these experiments, called PASTEX, was carried out on the Pasterze glacier in Austria during the summer of 1994 (Greuell *et al.*, 1997). Six weather stations for determining the energy balance of the glacier were stationed along the central flow line. Most of these stations consisted of just two measurement heights, 0.5 and 2 m, but at one site, known as A1, a 13 m profile mast with eight measurement heights, two sonic anemometers, and a balloon sounder were placed at a point roughly 1 km from the end of the glacier tongue.

During the observational period from 16 June to 11 August, over 2600 half-hourly average observations were made. Of these observations 77% showed the existence of a wind speed maximum below the highest profile level when wind direction was downslope, indicative of katabatic flows. This is a clear indication that the local ABL is strongly influenced by katabatic forcing.

The second experiment, TEMBA, was an observational campaign on the Vatnajökull ice cap in Iceland (Oerlemans *et al.*, 1999). Seventeen weather stations were placed on the ice cap in the summer of 1996. In particular three masts, of height 9 m and five measurement heights, each with an accompanying sonic anemometer at 3 m, were placed along the flow line of the Breidamerkurjökull, one of the larger outlet glaciers of Vatnajökull. Only one of these sites, known as U3, will be analyzed in this paper. The other sites, positioned higher on the glacier, were not deemed to be appropriate because the surface melt during the observation period lead to the development of large hummocks, on the order of 1 to 2 m in height, which complicated the analysis. These hummocks created a zero plane displacement and strong local wind anomalies in the lower profile level (Smeets *et al.*, 1999). Due to the limited number of profile levels these conditions made interpretation of these sites difficult. Also available at site U3 were balloon soundings, made when conditions allowed. A general description of this site and the instrumentation can be found in van der Avoird and Duynderke (1999).

The observational period on the Breidamerkurjökull was somewhat longer than on the Pasterze, running from 22 May to 31 August, with almost 5000 half-hourly averages being recorded. Of these observations 65% showed wind maxima under the 9 m profile level. More details concerning these two sites are listed in Table 4.1.

To indicate the kind of profiles measured under katabatic conditions, Figure 4.1 shows average profiles of wind and temperature for different wind maximum heights at site A1. That is, all profiles with a wind maximum at a height of $H \pm 1$ m are averaged to give the profiles indicated. Profiles for U3 are very similar to these and so have not been included. There is a clear relationship between maximum wind speed and maximum wind speed height, however the temperature profile is not as clearly delimited. Though increasing wind maximum heights correlate with increasing 13 m temperatures, the temperatures at 4 m are very similar for all cases.

The half-hourly average profiles from both sites are split into two categories depending on whether a wind maximum is present or not. From the observed profiles with detectable wind maxima, a fairly loose selection criterion is employed. For the Pasterze those profiles with wind maxima between 1 and 9 m and wind directions within 30° of the glacier fall line are selected for further analysis. Because we also prefer a melting ice surface, to be sure of the surface temperature, profiles with lowest level temperatures $< 2^\circ\text{C}$ are discarded. This leaves approximately 1500 data sets or 57% of the total collected. Data from Breidamerkurjökull are selected in a similar fashion except that the maximum allowable height of the wind maximum is set to 7 m. This procedure left just 40% of the collected data. Wind maximum heights and velocities are obtained by a quadratic fit around the maximum-wind sensor height.

In the coming sections, analytical functions are fitted to the wind profile beneath the wind maximum to determine roughness lengths. When fitting the data in this way, a minimum of three levels below the wind maximum are needed, further limiting the number of available profiles. Only fits with a regression coefficient $R > 0.99$

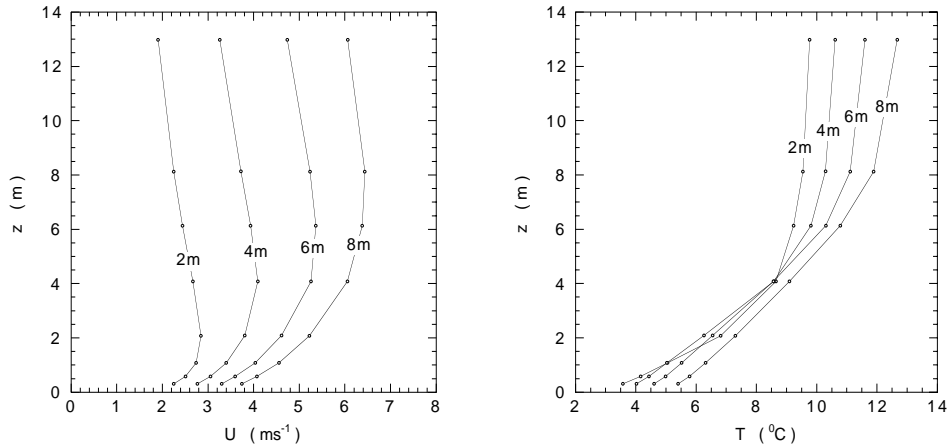


Figure 4.1: (left) Downslope wind speed U and (right) temperature T profiles at site A1. These are average profiles from the complete data set for the indicated wind maximum heights ± 1 m. The number of samples for each height division is 270, 668, 414 and 152 for 2, 4, 6 and 8 m respectively.

are used.

Observed profiles without wind maxima are candidates for log-linear profile fits. These are applied to levels 2 to 5 for A1 and levels 1 to 3 for U3. The number of levels is limited to try to ensure that profile levels remain within a reasonably constant flux layer because balloon soundings showed that wind maxima were frequently present above the highest mast level during these periods. To help avoid this problem, as well as that of buoyancy correction, profiles with values of $L < 50$ m are eliminated from the selection since almost all katabatic cases showed values below this. Level 1 wind data from A1 are not used in the analysis because this level showed systematic deviations from the log-linear form.

The eddy correlation measurements and their selection processes have been described in detail in the papers from van der Avoird and Duynkerke (1999) and Smeets *et al.* (1998) and will not be discussed again here. After allowance for these selection processes and technical problems encountered on site, the number of available flux

Table 4.1: Important quantities for the two observational sites.

Site	A1	U3
Glacier name	Pasterze	Breidamerkurjökull
Country	Austria	Iceland
Glacier length (km)	9	30
Distance from terminus (km)	1.0	0.75
Elevation (m a.s.l.)	2200	165
Local slope	$3.5^\circ \pm 0.5$	$5.1^\circ \pm 0.5$
Profile heights (m)	0.25, 0.5, 1, 2, 4, 6, 8, 13	1, 2, 3, 6, 9
Sonic anemometer heights (m)	2, 10	3
Period of observation	16 Jun - 11 Aug 1994	22 May - 31 Aug 1996

measurements are reduced to 36% of the total data set for A1 and 43% for U3.

4.5 The \overline{uw} turbulent flux profile

The method used to obtain \overline{uw} profiles and roughness lengths for momentum from the mean profile data under conditions of katabatic forcing uses two important assumptions: first, that the momentum budget is determined chiefly by the balance between katabatic forcing and the vertical divergence of horizontal momentum flux, and second that \overline{uw} goes to zero at the height of the wind maximum. To apply this method one must first determine the temperature deficit profile and then integrate this profile up to the height of the wind speed maximum.

To calculate the temperature deficit it is necessary to know what the ambient temperature at the surface would be in the absence of cooling. To a first approximation, the temperature of the highest mast level can be used, because the deficit approaches zero as height increases. However, irregular balloon observations clearly show the temperature to be increasing slightly above this height.

Figure 4.2 shows the relationship between the highest level temperature and the ambient temperature taken from balloon soundings for both sites. The ambient temperature is derived by extrapolating the air temperature between 50 and 100 m down to the surface. The solid line in Figure 4.2 indicates a quadratic fit of the form $T_{amb} = a_1 T_{mast} + a_2 T_{mast}^2$. The constants found using this fit are listed in Figure 4.2. As can be seen from the scatter in the diagram, the calculation of ambient temperature from the top mast level will introduce an error of at least ± 1 °C in the temperature deficit.

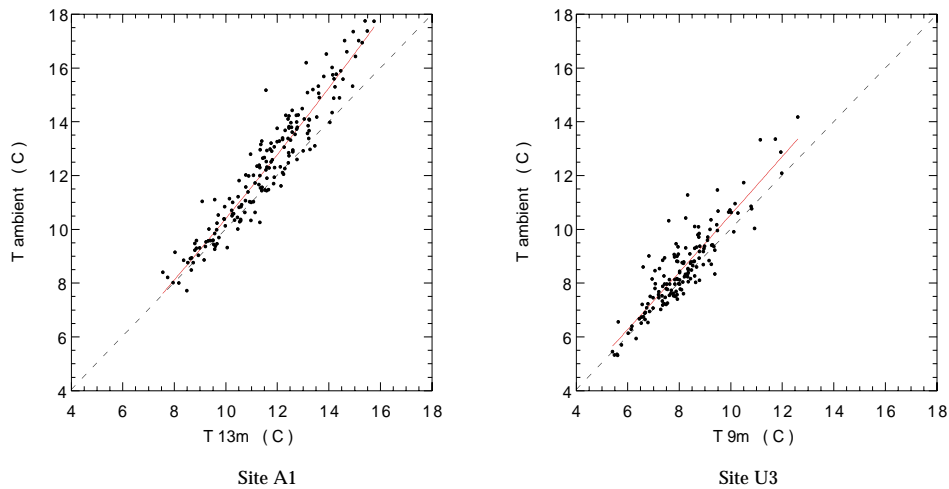


Figure 4.2: The relationship between uppermost mast temperature and the background ambient temperature as measured by balloon soundings for site A1 (left) and site U3 (right). The 1:1 line is indicated by a dashed line, and the quadratic fit is indicated by the solid line. Constants to the fit, described in the text, for A1 are $a_1 = 0.92$ and $a_2 = 0.012$, and for U3 $a_1 = 1.03$ and $a_2 = 0.002$.

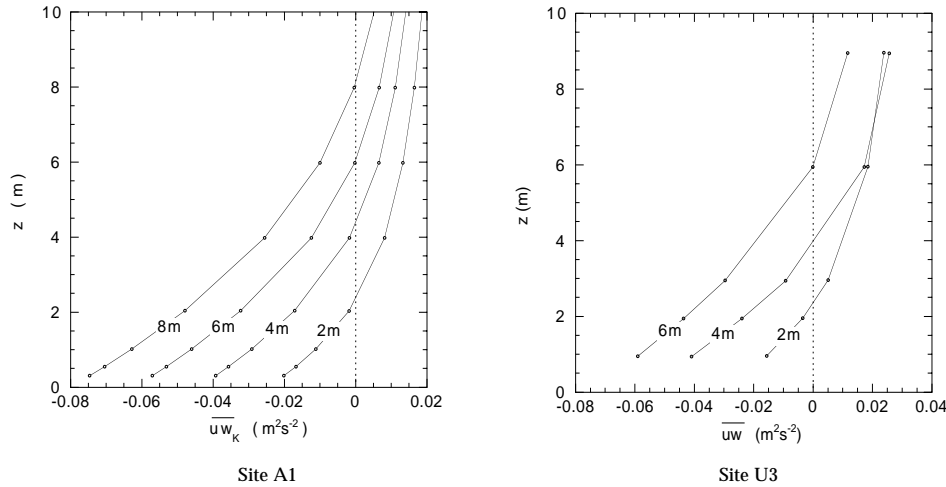


Figure 4.3: Katabatically derived \overline{uw}_K profiles for site A1 (left) and U3 (right) derived from the height averaged profiles given in Figure 4.1.

Using the above relationship for the ambient temperature one can integrate the temperature deficit for all the available profile sets and apply Equation 4.3 to directly derive the \overline{uw} profile. The result is shown for both sites in Figure 4.3 in which, by way of example, the height averaged wind and temperature profiles from both sites, as in Figure 4.1, are used and the integration is applied to these profiles.

There are two methods available to validate the katabatically derived vertical momentum flux. The first of these methods is the direct eddy correlation measurements made at heights of between 2 and 3 m and the second method is to compare the katabatically derived values with surface values estimated using the bulk method. Because of the large divergence in the \overline{uw} profile (Figure 4.3) these two values will be very different from each other and so cannot be compared directly.

In Figure 4.4 the sonic measurements are compared (\overline{uw}_S) with the katabatically determined values (\overline{uw}_K) at the anemometer height. Clearly there is a large amount of scatter in both cases, and neither result lies on the 1:1 line.

For A1 there is reasonably good correlation ($R = 0.87$) between katabatically determined fluxes and sonic measurements, however there is a bias of approximately 20% in the slope of the linear fit and an offset from the zero point of $0.005 \text{ m}^2\text{s}^{-2}$. This last result would be equivalent to a shift in the height of \overline{uw} with respect to the wind maximum H of approximately -0.5 m implying that the measured sonic value for \overline{uw} does not go to zero at H but rather at a point approximately 0.5 m below the maximum wind height. It should be noted here, and is discussed later in Section 4.7, that the accuracy in determining H at this site is no better than $\pm 0.5 \text{ m}$ in any case.

Apart from the large scatter for site U3, the katabatically determined vertical momentum flux is much less than that determined by eddy correlation measurements, by a factor of around 50%. This result is clearly an unsatisfactory one that would indicate that the katabatic method is not successful in determining the \overline{uw} profile.

As an alternative test to the validity of the katabatically derived \overline{uw}_K profiles,

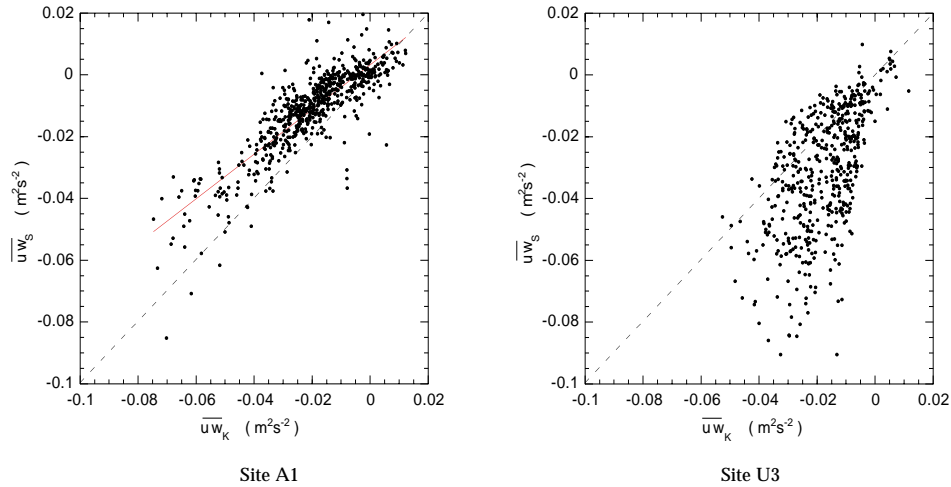


Figure 4.4: Comparison of katabatically calculated turbulent vertical momentum flux ($\overline{u w_K}$) with sonic eddy correlation measurements ($\overline{u w_S}$) for the two sites A1 (left) and U3 (right). Sonic anemometers were situated at 2.25 (A1) and 3 m (U3). The 1:1 line is indicated (dash line), as is the line of best fit (solid line). Correlation coefficient $R = 0.87$ for A1 with a slope of 0.73. No line of best fit is shown for U3.

the surface values for $\overline{u w_K}$ will now be compared with those derived using the bulk method ($\overline{u w_B}$). Though the wind and temperature profiles do not fit the standard log-linear form it is expected that close to the surface, where changes in fluxes are less than 10%, this form will become valid. The surface value of $\overline{u w_o}$ can be calculated using the bulk equations and by assuming a surface roughness length. In Section 4.6 surface roughness lengths are determined with both standard log-linear profile-fitting techniques and katabatic profile fits. These values are used here to compare katabatically determined values for $\overline{u w_o}$ with bulk method determinations.

The results for the bulk method are shown in Figure 4.5 in which a height of 0.5 m and a fixed value of $z_o = 1.6$ mm for A1 is used. For U3 a measurement height of 1 m with $z_o = 1.4$ mm is used. The correlation is clearly much better than the sonic anemometer results in Figure 4.4 with $R \approx 0.9$ in both cases.

This result is an interesting one, contradicting the poor correlation observed with the sonic anemometers, and indicates that the katabatically derived fluxes do indeed give good estimates of the surface momentum flux. The assumptions used to derive the momentum flux would thus appear to be valid. The derivation of $\overline{u w_K}$ is dependent only on the observed temperature profile and on the height of the wind speed maximum so there is no ‘hidden’ correlation between these two values. It is not clear, except for the possible errors in determining the height of the wind maximum, why the correlation with sonic data is so poor.

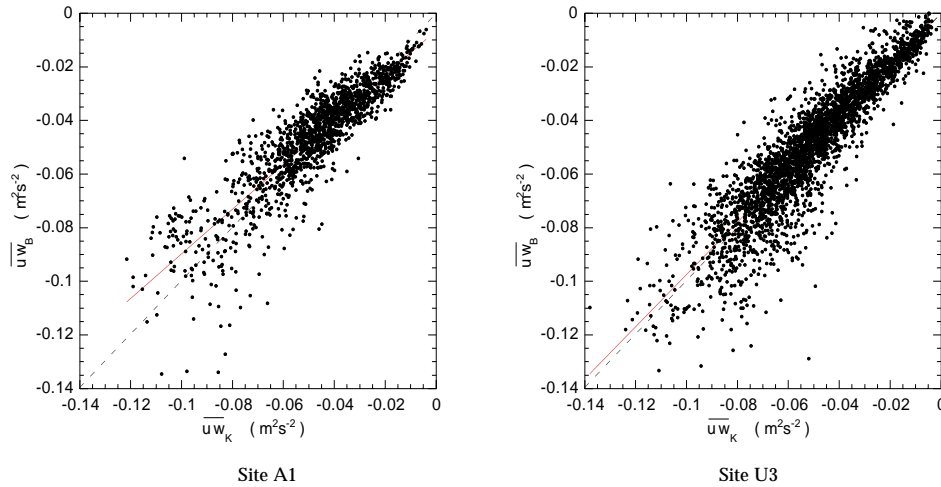


Figure 4.5: Comparison of katabatically calculated surface turbulent vertical momentum flux (\overline{uw}_K) with bulk method calculations (\overline{uw}_B) for the two sites A1 (left) and U3 (right). The 1:1 line is indicated (dash line), as is the line of best fit (solid line). Correlation coefficient $R = 0.89$ for A1 with a slope of 0.84, and for U3 $R = 0.91$ with a slope of 0.97.

4.6 Determination of the surface roughness length for momentum

The surface roughness length for momentum is defined as the height at which $U = 0$ when integrating the flux-profile relationship, Equation 4.4. Usually, z_o is determined under near-neutral conditions by assuming u_* to be constant and fitting the wind and temperature profiles with a log-linear fit, Equation 4.8. We also apply this method (Figure 4.8) but fits of this type can only be made during high wind periods when stability corrections are small and the katabatic wind maximum, if it is present, is much higher. These periods are also infrequent, so we wish to determine z_o by making use of the katabatically derived \overline{uw} profiles.

The simplest method to estimate z_o would be to apply the bulk method to the lowest level using the katabatically derived value for u_* in Equation 4.8 and to neglect stability corrections, assuming them to be small close to the surface. However, a more accurate method would be to fit the profile data that are available, which include the katabatically derived profile data for \overline{uw} . From the wind and \overline{uw} profiles, the flux-profile relationship in the region below the wind speed maximum can be determined using Equation 4.4. Integration of this function, if it is represented by suitable functions, would allow the determination of z_o by profile fitting techniques. To carry out this integration analytical formulas for ϕ_m and u_* as a function of some dimensionless height are required that can be fitted to the data. The most obvious vertical scaling length is the height of the wind maximum H , because it is the one well defined length scale available to us that is characteristic of katabatic flows. The scaled height can thus be written as $\mu = z/H$.

These functions are intended solely as a means for fitting the measured wind

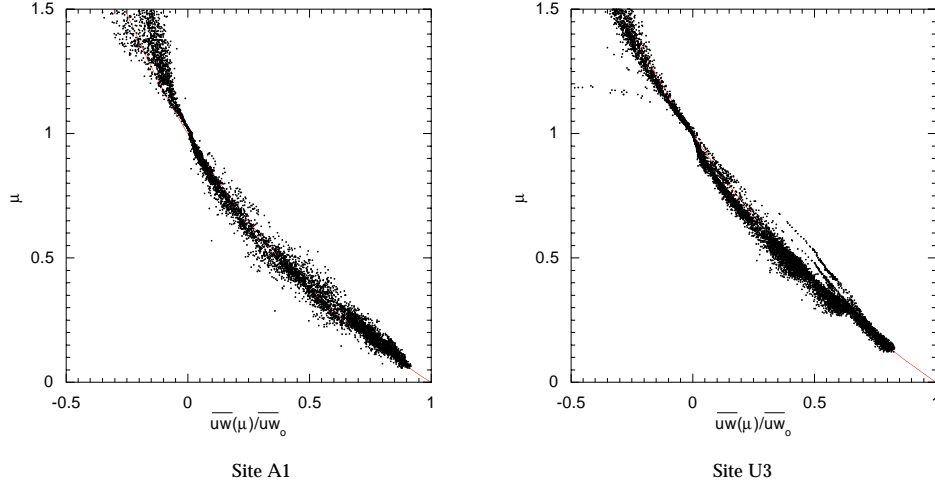


Figure 4.6: Normalized \overline{uw}_K profile as a function of the dimensionless height $\mu = z/H$ where H is the height of the wind maximum at site A1 (left) and site U3 (right). Also shown is the analytical fit (solid line) defined in the text (Equation 4.10).

profiles to determine z_o . It is not implied that they have a universal character, though the two sites do show very similar characteristics. In this regard, the functions will be kept as simple as possible, provided they can represent the measured profiles.

4.6.1 Normalized function for $u_*(\mu)$

The shape of $u_*(\mu)$ can be ascertained from the katabatically derived \overline{uw}_K profiles, normalized by the surface value. The normalized function $\overline{uw}(\mu)$ is shown for both sites in Figure 4.6. A function that fits these curves quite well and is suitable for analytical integration is given by

$$\frac{\overline{uw}(\mu)}{\overline{uw}_o} = \frac{1 - \mu}{(1 + \alpha_2 \mu)^2} \quad (4.10)$$

The constant α_2 is found to be 0.28 for A1 and 0.22 for U3. The fits are not very sensitive to this parameter, so a single value of $\alpha_2 = 0.25$ will be taken to be valid always.

4.6.2 The flux-profile relationship $\phi_m(\mu)$

Having made this choice for \overline{uw} we need now to define $\phi_m(\mu)$. Given both profile wind data and derived \overline{uw}_K data, ϕ_m can be determined directly. In Figure 4.7 ϕ_m is plotted as a function of the dimensionless height μ . The data have been separated into two parts representing $Ri_g < 1$ and $Ri_g > 1$ where Ri_g is the local gradient Richardson number. This separation is done to delineate between the less accurate values of ϕ_m ($Ri_g = 1$ is equivalent to $\Delta U < 0.2 \text{ ms}^{-1}$ in most cases) and the more

accurate ones. Gradients are determined directly from the data using finite differences.

In Figure 4.7 $\phi_m \rightarrow 1$ as $\mu \rightarrow 0$. This is the expected result because far from the wind maximum and close to the surface where stability corrections are small the wind profile should approach a simple logarithmic form. As $\mu \rightarrow 1$ we find $\phi_m \rightarrow 0$. This result is the necessary consequence of nonzero turbulent diffusion at the wind maximum where production from shear is zero. It is known from eddy correlation measurements and from model studies (Denby, 1999) that the turbulent kinetic energy is nonzero at the height of the wind maximum. If this is the case then the turbulent diffusion coefficient, $K_m = -\overline{uw}(\partial U/\partial \mu)^{-1}$ should also be nonzero. If one substitutes the definition for ϕ_m (Equation 4.4) and the analytical function for \overline{uw} (Equation 4.10) into this definition then $\phi_m \rightarrow (1 - \mu)^{1/2}$ as $\mu \rightarrow 1$.

Figure 4.7 shows that a simple linear relationship may be appropriate for values of $\mu < 0.5$. Thus ϕ_m must be written in a form that is linear as $\mu \rightarrow 0$ and that approaches $(1 - \mu)^{1/2}$ as $\mu \rightarrow 1$. Though several fits are tried, the eventual fitting procedure applied in the following section is fairly insensitive to their exact form, and so a simple combination of linear and $\mu \rightarrow 1$ limit is used as given below.

$$\phi_m(\mu) = (1 + \alpha_1 \mu)(1 - \mu)^{1/2} \quad (4.11)$$

The best fit to all the data with $Ri_g < 1$ using this equation is also shown in Figure 4.7, giving values of $\alpha_1(\text{A1}) = 4.4$ and $\alpha_1(\text{U3}) = 4.2$. These values are quite close to those derived by Munro and Davies (1978) who applied more standard profile fitting techniques to their set of katabatic wind profiles. By replacing L with H as a length scale in the linear flux-profile relationships they determined an average value for $\alpha_1 = 4.5$ when $\mu < 0.25$. Above this height, the linear flux-profile relationship ceased to hold.

The derived shape of the flux-profile relationship as a function of μ is due to both buoyancy effects and turbulent transport. For lower values of μ , buoyancy retards the production of turbulence and reduces the dissipative length scale, leading to the initial increase of ϕ_m with height. Turbulent transport, on the other hand, which dominates the turbulent kinetic energy budget in the region close to the wind maximum, leads to the observed decrease in ϕ_m as production by shear starts to play a far less important role in determining this budget (Denby, 1999).

Because of the large scatter in ϕ_m and its possible dependence on other variables, the constant α_1 will be used as a fitting parameter.

4.6.3 Analytical function for $U(\mu)$

Inserting the equations for $u_*(\mu)$ and $\phi_m(\mu)$ (Equations 4.10 and 4.11) into the flux-profile relationship (Equation 4.4) gives the following formula:

$$\frac{\partial U}{\partial \mu} \frac{\kappa}{u_{*o}} = \frac{(1 - \mu)(1 + \alpha_1 \mu)}{\mu(1 + \alpha_2 \mu)} \quad (4.12)$$

Integrating this relationship from $\mu_o = z_o/H$ to μ gives :

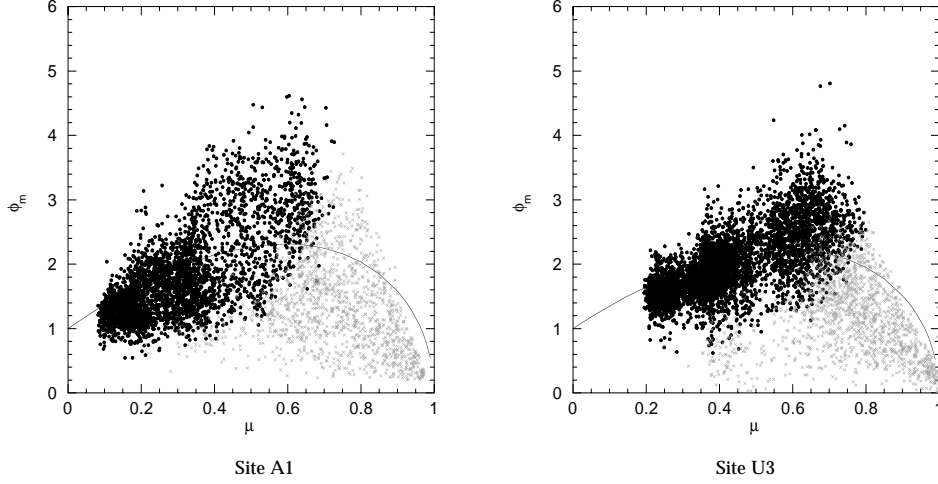


Figure 4.7: Flux-profile relationship $\phi_m(\mu)$ as a function of the dimensionless height $\mu = z/H$ where H is the height of the wind maximum at site A1 (left) and site U3 (right). Dark dots indicate $Ri_g < 1$ and grey crosses are $Ri_g > 1$. Also shown is the analytical fit defined in the text (Equation 4.11) to the $Ri_g < 1$ data.

$$U(\mu) \frac{\kappa}{u_{*o}} = \ln \left[\frac{\mu}{\mu_o} \right] + \frac{(\alpha_1 - \alpha_2)(1 + \alpha_2)}{\alpha_2^2} \ln [1 + \alpha_2 \mu] - \frac{\alpha_1}{\alpha_2} \mu \quad (4.13)$$

In the limit as $H \rightarrow \infty$ this function approaches the simple neutral logarithmic wind profile.

4.6.4 The surface roughness length for momentum

By least squares fitting the wind profile with Equation 4.13 up to the height of the wind maximum, and using the katabatically determined value for u_{*o} the two unknown parameters z_o and α_1 can be determined. Of the already selected katabatic cases 90% of these could be fitted with this equation to a sufficiently high accuracy ($R > 0.99$).

In Figure 4.8 the resulting katabatically and log-linear profile derived roughness lengths for A1 and U3 are plotted as a function of time to see whether the roughness length has varied during the measurement period as a result of differential melting of the surface. Both sites show no noticeable change in roughness length during the observational period, which is the expected result, because visually there was little change at these sites during the melt season.

As can be seen, the profile-derived roughness length estimates do not fall simultaneously with the katabatic estimates because they are mutually exclusive. However, both methods give very similar results. The average roughness length at A1 determined using the katabatic method over the entire period is found to be 1.6 mm, with a range of 1.0 to 2.8 mm, taken from the standard deviation. The profile method

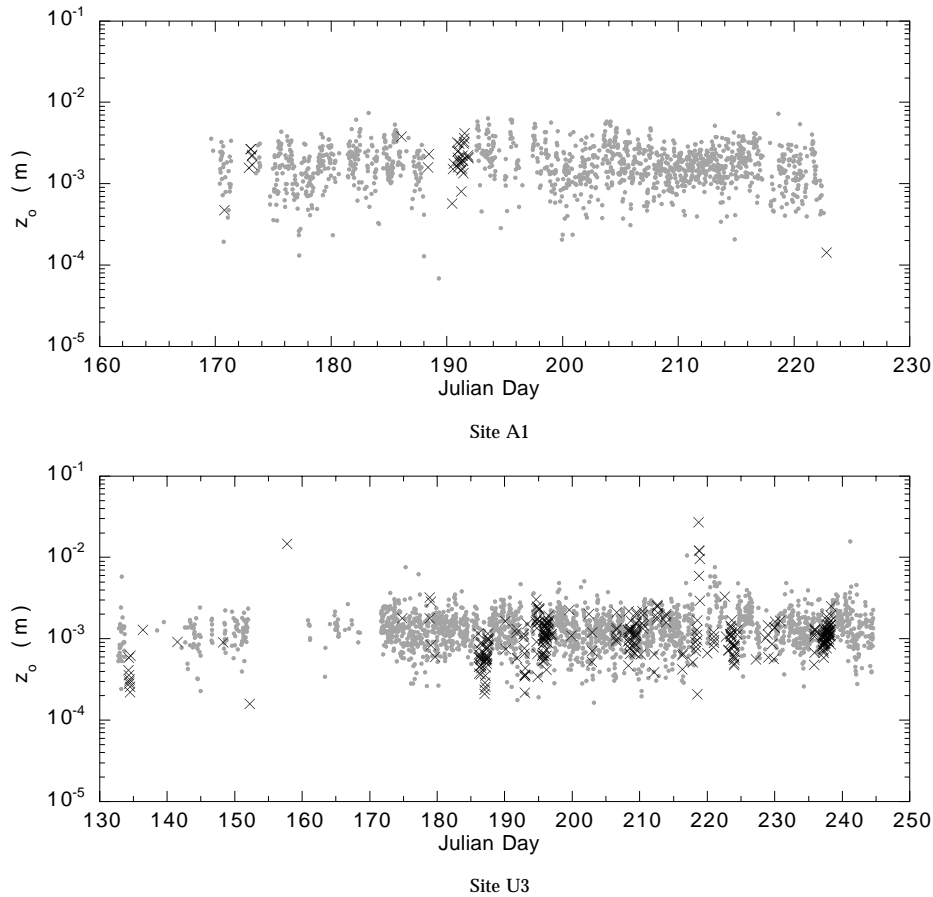


Figure 4.8: Surface roughness length for momentum as function of time for the two sites A1 (top) and U3 (bottom). Katabatically derived roughness lengths are given by grey dots and log-linear fitted values are indicated by black crosses.

gives an average $z_o = 1.8$ mm with roughly the same range but far fewer data points. A similar result is obtained at U3, where $z_o = 1.4$ mm, ranging once more from 1.0 to 2.2 mm. In this case the average profile derived roughness length is slightly lower, $z_o = 1.0$ mm, with a slightly larger standard deviation.

It is interesting to note that over 50% (1350 in total) of all the collected profile data during the measurement campaign on the Pasterze glacier can be used to determine the roughness length of the ice surface at A1 when using the katabatic method. In contrast to this, just 38 samples, or 1.5% of the total observations, are deemed to be suitable for use with the profile method. On Breidamerkurjökull, 38% (2064 in total) of all half-hourly means are used to determine z_o using the katabatic method as opposed to the profile method that made use of just 6%. That both profile and katabatic methods arrive at almost the same roughness lengths adds strength to the argument that \overline{uw}_K is well determined by the integration of the temperature deficit.

4.7 Discussion

In the previous sections, turbulent fluxes are derived using the katabatic profile method, which assumes a dynamic balance between katabatic forcing and vertical flux divergence in the momentum budget for the region beneath the wind maximum of a katabatic flow. The derived flux values are then compared with other measurements and methods, namely, direct eddy correlation measurements from sonics anemometers and with bulk method calculations given assumed roughness lengths. The katabatically derived roughness lengths are also compared with roughness lengths derived using the profile method, which could be applied only when the katabatic method could not.

The results of these comparisons are not always consistent. At site A1 there is reasonable agreement between katabatic and sonic values for \overline{uw} , yet at site U3 the correlation is very poor. However when these katabatically derived fluxes are compared with bulk method calculations, using profile and katabatically determined roughness lengths, the correlation is very good.

A comparison of katabatic and profile derived surface roughness lengths indicates that the katabatic method is at least as good as the profile method in determining roughness lengths for momentum. The katabatic method has the added advantage that it can be applied far more frequently than the profile method because of the dominance of katabatic forcing.

It is worthwhile to discuss some of the errors and uncertainties in regard to the derivation of the quantities mentioned above. In Table 4.2 possible sources of these uncertainties and their influence on the katabatically derived fluxes and roughness lengths are listed for typical katabatic conditions.

That sonic derived fluxes in general compare poorly with katabatically derived fluxes may have several causes. First, the katabatic method may not be applicable, either because of its method of derivation or because the momentum budget is strongly influenced by other, perhaps local, terms. The fact that bulk method calculations agree well with the katabatically derived values tends to discount this idea. Second, it may be that the local influence of topography in terms of slope or fetch is significant enough to create the differences observed between the two masts situated just 30 m apart. Comparison of the mean sonic and profile mast wind speeds and temperatures under katabatic conditions does not indicate any significant differences between the two instruments, though simultaneous profile measurements at both positions would be necessary to check this possibility properly. The third possibility is that errors made in determining the height of the wind maximum at U3 (± 1 m), which are significantly larger than those at A1 (± 0.5 m), make estimates of the zero point for \overline{uw} sufficiently inaccurate to render the comparison with the sonic measurements meaningless. This possibility is quite important given that the wind maximum often lies in the 4 - 6 m range. A 1 m error in determining the height of the wind maximum at 5 m would lead to relative errors in \overline{uw} of between +30% and -50% at the 3 m sonic height. The relative error is smaller, approximately 20%, at the surface. The fourth possibility is that sonic derived fluxes are unreliable under conditions of katabatic flow, in which eddies tend to be small and the influence of gravity waves may be large.

Though the results of this study are not always consistent with eddy correla-

tion measurements, they are consistent with other profile and bulk methods that use mean values to calculate turbulent fluxes and roughness lengths. For a more thorough test of the methods used here, higher resolution profile masts, including a number of well calibrated sonic anemometers within close proximity, would be necessary to help to establish the relationships properly. Application of this method during the winter period, which is also dominated by katabatic forcing, would help to improve roughness estimates over snow surfaces.

Table 4.2: Possible sources of errors and uncertainties in the derivation of turbulent fluxes and roughness lengths when using the katabatic method.

Source of error or uncertainty	$\pm X$ (unit)	\overline{uw}_o (m^2s^{-2})	$\ln(z_o)$ (m)	H (m)
Typical values		-0.05	-6.5	5
Instrumental error temperature	± 0.2 °C	4%	2%	-
Instrumental error wind speed	± 0.2 ms^{-1}	10%	5%	10%
Inaccuracy in maximum wind height	± 1.0 m	20%	10%	20%
Inaccuracy in ambient temperature	± 1 °C	20%	10%	-
Inaccuracy in slope	$\pm 15\%$	15%	7%	-

Acknowledgments

We would like to thank Ernst van der Avoird and Jan de Wolde from Utrecht University, IMAU for providing the observational data for this paper and also all those who participated in the two measurement campaigns. This research was funded by the Dutch National Research Programme on Global Air Pollution and Climate Change (NOP II Project 013 001236.10).

5

Observed Roughness Lengths for Momentum and Temperature on a Melting Glacier Surface

The roughness lengths for momentum and temperature are calculated on a melting glacier surface. Data from a five level 9 m meteorological mast positioned near the edge of Breidamerkurjökull, an outlet glacier of the Vatnajökull ice cap in Iceland, are used for the calculations. The surface roughness length for momentum is determined to be ≈ 1.0 mm, similar to other estimates made on flat melting ice surfaces. The surface roughness length for temperature is found to be in good agreement with previously proposed surface renewal theories for the observed roughness Reynolds number range of $20 < Re_* < 70$.

5.1 Introduction

The surface roughness lengths for momentum, temperature and water vapour are essential parameters for calculating and modelling turbulent heat fluxes on ice and snow surfaces. When bulk methods are used to calculate turbulent heat fluxes in energy balance models, e.g. Greuell and Konzelmann (1994), reliable estimates for these roughness lengths are needed. Almost all meteorological models include surface roughness lengths as an essential boundary condition for determining both the turbulent fluxes and the lowest level values for wind, temperature and water vapour. Many publications have been made concerning roughness length calculations for momentum but there are still very few published data available for scalar roughness lengths.

Surface renewal theories can be used to calculate scalar roughness lengths over non-vegetated surfaces. The scalar roughness lengths of ice and non-drifting snow surfaces are often calculated using the formulations from Brutsaert (1975b) or Andreas (1987), both of which give very similar results. There is little verification in the literature for these relationships in spite of their importance in calculating turbulent heat fluxes, particularly for higher roughness Reynolds numbers ($Re_* > 10$), on which scalar roughness lengths are dependent. Previous work by Joffre (1982) over sea ice and King (1994) over the Brunt ice shelf in Antarctica do not show a convincing correlation between surface renewal theories and observations. Measurements from Munro (1989) and Smeets *et al.* (1998), over melting glaciers, and Kondo and Yamazawa (1986) over a snow covered field do indicate that surface renewal methods give at least correct estimates for temperature roughness lengths inspite of a large scatter and a limited roughness Reynolds number range.

In 1996 a glacio-meteorological experiment was conducted on the Vatnajökull ice cap. One of the masts positioned on the ice cap was operated by Utrecht University where profile data was collected for a 100 day summer period. The data is analyzed in this paper in order to determine the surface roughness lengths for momentum and temperature. In a previous paper (van der Avoird and Duyenkerke, 1999) estimates of surface roughness lengths for both momentum and temperature were hampered by the presence of the katabatic wind speed maximum. Since then further investigations (Denby and Greuell, 2000) have shown that the presence of the wind speed maximum, within or close to the profile measurement heights, will give poor results when using profile techniques. With this new knowledge the data is re-analyzed and the roughness lengths once more determined.

Inspite of the almost continual presence of the katabatic wind speed maximum, which inhibits the use of profile methods for determining roughness lengths, more than 300 half-hourly average profile measurements are analyzed, after appropriate selection, to calculate the roughness lengths for momentum and temperature. Results agree quite well with the previously mentioned surface renewal theories.

5.2 Observations

Observational data was obtained during the Vatnajökull glacio-meteorological experiment in the summer of 1996 (Oerlemans *et al.*, 1999). During the period from

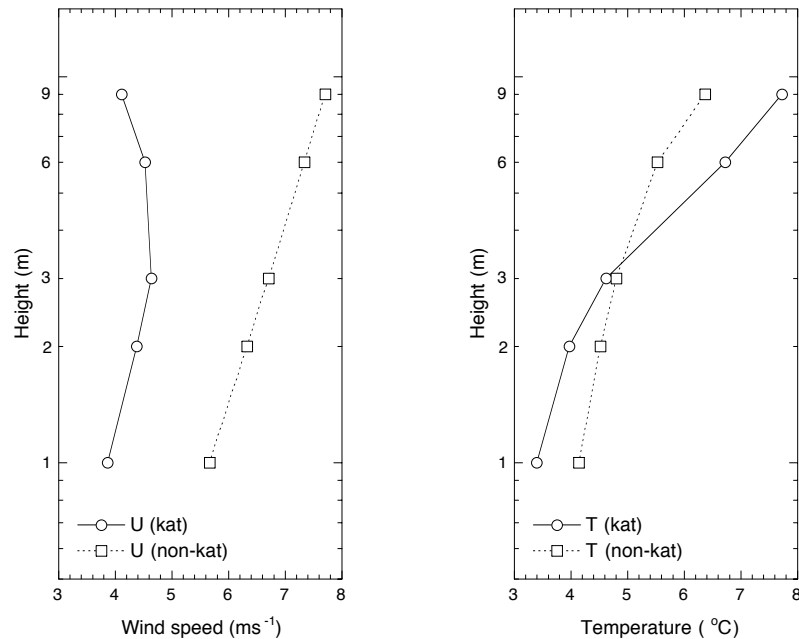


Figure 5.1: Average down slope wind speed U (left) and temperature T (right) profiles at site U3. These are average profiles over the entire observational period selected on the basis of the presence of the wind speed maximum. “kat” indicates average profiles where the wind speed maximum is present (2638 half-hourly average samples), “non-kat” when it is not (1390 samples). The vertical scale is shown logarithmically.

22 May to 31 August 1996 sixteen weather stations were placed close to or on the Vatnajökull ice cap. Along Breidamerkurjökull, an outlet glacier on the south east side of Vatnajökull, four profile masts were deployed. In this paper data from the site known as U3 is used which was situated just 0.75 km from the ice edge at an elevation of 165 m a.s.l. and with a surface slope of $\approx 5^\circ$. This mast consisted of five measurement heights at 1, 2, 3, 5 and 9 m at which temperature, wind speed and humidity were measured. For a detailed description of this mast one is referred to van der Avoird and Duynkerke (1999).

In total 5000 half-hourly averages were recorded at U3. During this period the katabatic, or glacier wind, was quite dominant. Of all the measured profiles, 60% show the presence of the katabatic wind speed maximum below the maximum profile height of 9 m and 80% of all observed winds were found to be directed within 30° of the downslope glacier fall line. In Figure 5.1 the average wind and temperature profiles for both katabatic and non-katabatic cases over the entire observational period are shown. In this figure katabatic and non-katabatic periods are separated on the basis of the presence or absence of a downslope wind speed maximum below 9 m. Clearly visible, in the katabatic case, is the wind speed maximum at a height of around 4 m and the strong temperature inversion associated with the katabatic flow. It should be noted that the above separation into katabatic and non-katabatic cases

is arbitrarily determined by the height of the profile mast since wind speed maxima will also occur above 9 m.

Non-katabatic periods are often connected with downslope wind storms which occur when synoptic conditions lead to northerly flows over the ice cap and down the southern slope. During these events wind speeds are quite high, resulting in damage to masts and instruments on two occasions. The periods with synoptically forced down slope winds are appropriate for calculating surface fluxes and roughness lengths from profile data since the wind speed maximum, if it exists, is much higher than the profile mast itself.

During almost the entire observational period the surface ice was observed to be melting. The micro-structure of the surface consisted chiefly of ice crystals ≈ 1 cm in height. On a larger horizontal scale, of around 10 m, the surface undulated slightly, of the order of decimeters, and was crossed regularly by melt grooves. The fetch at U3 was quite homogeneous for several kilometers in the up glacier direction which is the dominant wind direction due to the katabatic forcing.

5.3 Application of the profile method

Descriptions of Monin-Obukhov (M-O) similarity theory and the derived log-linear equations for wind and temperature under stable conditions can be found in many texts, e.g. Garratt (1992), and are reiterated below

$$U(z) \frac{\kappa}{u_*} = \ln \left[\frac{z}{z_o} \right] + \alpha_m \frac{z}{L} \quad (5.1)$$

$$(\Theta(z) - \Theta_s) \frac{\kappa}{\theta_*} = Pr \ln \left[\frac{z}{z_h} \right] + \alpha_h \frac{z}{L} \quad (5.2)$$

In the above equations Pr is the turbulent Prandtl number (assumed to be equal to unity in this paper), κ the von Karman constant (0.4), u_* the surface layer velocity scale, θ_* the surface layer temperature scale, z_o the surface roughness length for momentum, z_h the surface roughness length for temperature, z the height above the surface and $L = \frac{u_*^2}{\kappa(g/\Theta_s)\theta_*}$ is the M-O length scale. The constants α_m and α_h are determined empirically and vary to some extent in the literature. In this paper values of 5 for both α_m and α_h are used. The above log-linear form is assumed to be applicable in a horizontally homogeneous stable surface layer where the turbulent fluxes, u_* and θ_* , are constant with height.

The surface roughness length for momentum is determined mainly by roughness element shape and distribution since momentum is most efficiently transferred to the surface through pressure fluctuation gradients across roughness elements, the so called 'form drag'. Scalar roughness lengths, on the other hand, will differ greatly from that of momentum since these roughness lengths are dependent on viscous scales related to molecular diffusion processes. According to the surface renewal theories described in Brutsaert (1975b) and Andreas (1987) the surface roughness lengths of scalars, such as temperature and water vapour, can be expressed as a function of roughness Reynolds number, $Re_* = u_* z_o / \nu$ where ν is the viscosity of air

($1.35 \times 10^{-5} \text{ m}^2\text{s}^{-1}$). The relationship between z_o and z_h , as determined by Andreas (1987), differs only slightly from that of Brutsaert (1975b) and is shown below.

$$\ln\left(\frac{z_h}{z_o}\right) = 0.317 - 0.565 \ln(Re_*) - 0.183 \ln(Re_*)^2 \quad (5.3)$$

By least squares fitting profile measurements with Equations 5.1 and 5.2 the turbulent velocity and temperature scales, u_* and θ_* , as well as the roughness lengths z_o and z_h can be determined, assuming the surface temperature is known. One of the problems often encountered when trying to determine surface roughness lengths for temperature is that the surface temperature is not well determined. This is possibly the only advantage of measuring on a melting ice surface since the surface temperature over a large region is known to be at a constant 0°C .

When making least squares fits, selection criteria are needed to guarantee appropriate conditions and goodness of fit. As discussed in Denby and Greuell (2000), the katabatic profiles, shown in Figure 5.1, do not fit the log-linear form since turbulent fluxes are not constant in the lowest few meters. It was also pointed out in that paper that profile fits of any worth can only be made at heights $< 30\%$ of the wind speed maximum height. As a result, the first selection criteria is that the wind speed maximum be positioned above the highest profile mast level. This selection reduces the number of usable half-hourly average profiles to 40% of the total observed. However, it is not clear how far above the profile mast the wind speed maximum actually is and so to ensure that the profile measurements are carried out low enough only the lowest three levels, up to 3 m, are used for the fitting procedure. Profiles are also selected for fetch, so that only observations made when the wind direction is within $\pm 45^\circ$ of the glacier fall line are used. This reduces the number of usable profiles to 31% of the total.

Both wind and temperature profiles are fitted simultaneously and iteratively in order to calculate the M-O length scale in the stability correction factor. Only least square fits of these profiles, where both the wind and temperature coefficients of correlation (Press *et al.*, 1992) is greater than 0.995 are used. Around 40% of the usable profile results are discarded on the basis of this criterion leaving 17% of the total number of measured profiles.

Lastly the resulting roughness lengths are selected on the basis of a stability criterion. To reduce possible errors introduced by the stability correction factor in Equations 5.1 and 5.2 only fits where $z/L < 0.1$ are used, using $z = 3$ m. The final number of half-hourly average profiles used to determine the surface roughness lengths is 340, or 6% , of all measurements made.

5.4 Results

By applying the selection criterion and the fitting procedure described in Section 5.3 the roughness lengths for momentum and temperature are determined. The roughness length for momentum is shown in Figure 5.2 as a function of roughness Reynolds number. The roughness length for momentum is not expected to show any dependence on Reynolds number, being independent of viscous scaling laws,

and does not indicate any discernable dependence. On a melting ice surface z_o may vary with time due to differential melt of the surface and changing ice crystal structure. However, in this case the data show that there is very little temporal variation with time for this particular site. An average value of $z_o = 1.0 \pm 0.4$ mm is determined for the roughness length of momentum, the range being taken from the standard deviation. Also included in Figure 5.2 are the results from Smeets *et al.* (1998), who uses a similar method to the one described above to determine roughness lengths on the melting Pasterze glacier, which had similar surface conditions.

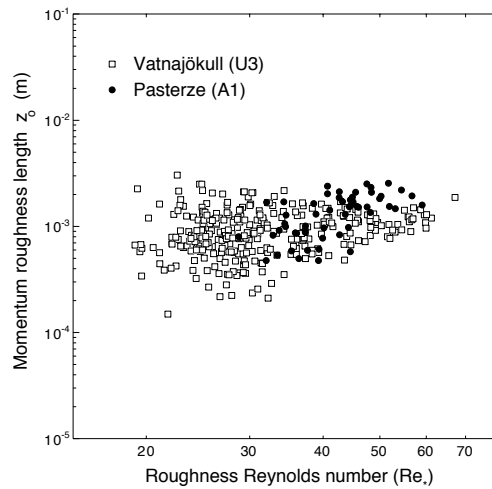


Figure 5.2: Surface roughness length for momentum (z_o) as function of roughness Reynolds number (Re_*) calculated using the profile method described in the text. Also included is the data from Smeets *et al.* (1998).

The ratio of z_h/z_o is shown in Figure 5.3 along with the results from Smeets *et al.* (1998) for the Pasterze glacier and the formulation from Andreas (1987), Equation 5.3. For $Re_* > 30$ there is good agreement between both sets of data and Equation 5.3. For $Re_* < 30$ the Vatnajökull data shows slightly higher values for z_h/z_o than Equation 5.3.

When the wind speed maximum is present estimated surface roughness lengths for temperature will tend to be higher. For example, when a logarithmic fit is made to the lowest three levels of the katabatic temperature curve in Figure 5.1 the increased stratification, which is present during strong katabatic periods, will tend to lead to an overestimation of z_h . This effect can be seen in Figure 5.3 for $Re_* < 30$ since lower roughness Reynolds numbers are associated with lower wind speeds and thus decreased wind speed maximum heights.

Error analysis of the equations used to determine z_o and z_h show that assumed instrumental errors in the anemometer readings of $\pm 0.2 \text{ ms}^{-1}$ and of $\pm 0.2 \text{ }^\circ\text{C}$ in the thermistors would account for approximately half the scatter seen in Figures 5.2 and 5.3. Other effects, such as non-stationarity of the half-hourly mean wind and tem-

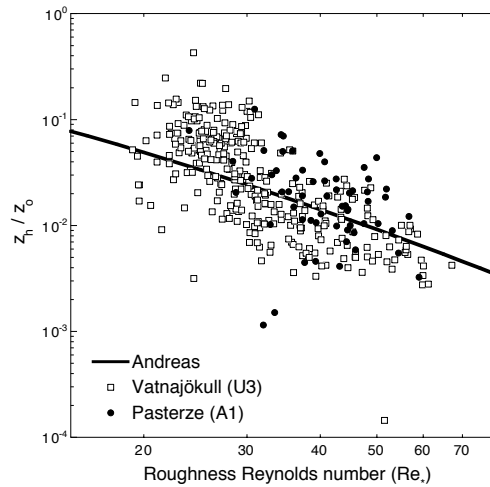


Figure 5.3: The ratio of surface roughness length for temperature and momentum (z_h / z_o) as function of roughness Reynolds number (Re_*) calculated using the profile method described in the text. Also included is the data from Smeets et al. (1998) and the formulation from Andreas, Equation 5.3.

perature profiles and statistical sampling errors will also contribute to the observed scatter.

In spite of this, the measurements presented here validate the surface renewal theories currently being used to calculate the temperature roughness length of a relatively flat melting ice surface.

Acknowledgments

We would like to thank Ernst van der Avoird from Utrecht University and Paul Smeets from the Free University of Amsterdam for providing the observational data for this paper. Also, all those who participated in the Vatnajökull field experiment. This research was funded by the Dutch National Research Programme on Global Air Pollution and Climate Change (NOP II Project 013 001236.10).

6

Simulating the Greenland Atmospheric Boundary Layer: Model Description and Validation

A three-dimensional atmospheric boundary-layer model of the Greenland ice sheet, with a maximum horizontal resolution of 10 km is described, verified by observations and tested for its sensitivity to a number of model parameters. The model is developed to improve calculations of the ice sheet energy balance, particularly the turbulent heat flux, during the ablation season. A case study is carried out where the model is forced by ECMWF re-analysis data for a 20 day period in the summer of 1991 and compared to observations made during the Greenland Ice Margin Experiment. The simulation agrees quite well with observations made during this period on both tundra and ice sheet. Sensitivity runs are also carried out with the model to test the dependence of the turbulent heat flux on various dynamic, numeric and prescribed surface parameters. Though surface albedo is an important factor in the total surface energy balance of the ice sheet, it does not strongly affect the turbulent heat flux during the ablation season. The most important surface parameter is shown to be the roughness length for temperature. It is also found that increasing the horizontal resolution of the model from 20 to 10 km does not significantly improve estimates of the turbulent heat fluxes.

6.1 Introduction

The surface mass balance of ice sheets and glaciers, excluding calving, is determined by accumulation and ablation. On the Greenland ice sheet it is estimated that half of all mass loss is via calving at the ice-sea interface, the other half is the result of ablation via surface melt. Changes in climatic conditions will lead to a shift in the mass balance of these ice masses with a resulting change in ice flow. In order to quantify the mass balance of the Greenland ice sheet it is necessary to determine these ablation rates and their sensitivity to climatic variations.

The ablation rate is directly determined by the surface energy balance (SEB) which consists of short- and longwave radiation fluxes as well as sensible and latent turbulent heat fluxes. The most important component of the SEB during summer is the absorbed shortwave radiation. This is dependent chiefly on surface albedo and secondly on cloud type and distribution. However, changes in atmospheric conditions, such as temperature and circulation patterns, have a more important influence on the three other components of the SEB. Atmospheric temperature, humidity and wind speed are determinant for the turbulent heat fluxes at the surface. Likewise atmospheric temperature, humidity and cloud cover are important for determining the incoming longwave radiation.

Currently the ablation components of mass balance models vary in their sophistication ranging from simple degree day models to complete energy balance models driven by observed wind, temperature and radiation fluxes (Greuell and Konzelmann, 1994). Energy balance models represent as completely as possible the physics behind ablation and are thus more appropriate for extrapolation into unknown climate scenarios than degree day models which are empirically based on present day observations. Even so, energy balance models are often based on simplified assumptions. In particular, and the subject of this study, the turbulent sensible and latent heat fluxes are often prescribed as a linear function of atmospheric temperature at some predefined height, usually 2 m. This simplification excludes variations in wind even though turbulent exchange varies directly with wind speed. Climatic changes in free atmospheric temperatures are also often assumed to be equivalent to changes in 2 m temperatures (van de Wal, 1994). Above a melting ice surface this is not the case since the 2 m temperature is strongly influenced by the surface temperature, which remains constant during melt.

Incoming longwave radiation can be determined from parameterisations based on single height values of temperature and water vapour, when available, as well as cloud cover estimates (Konzelmann *et al.*, 1994). These parameterisations are empirically fitted to existing data which, above ice sheets, is still quite scarce. Near surface conditions and boundary layer structure will vary spatially with the resulting variations in the empirically fitted constants.

The state of the free atmosphere is translated down to the surface through the atmospheric boundary layer (ABL). Conditions within the ABL are the result of both surface conditions, such as roughness and temperature, as well as free atmospheric conditions. Determination of the turbulent flux and incoming longwave radiation at the surface will require some physical description of the ABL itself.

The Greenland atmospheric boundary layer model (GABLM) is developed to improve estimates of the surface energy flux, particularly the turbulent heat fluxes and

longwave radiation fluxes, on the Greenland ice sheet. The model uses prescribed boundary and initial conditions such as synoptic pressure gradients, temperature and humidity fields, cloud cover and height, and various surface parameters in order to force the ABL above the Greenland ice sheet. The atmospheric input fields are taken from ECMWF analyses or re-analyses data. The aim is to take these fields and to translate them directly into surface energy fluxes which can be used in mass balance modelling.

Since ablation occurs in a narrow region near the ice margin, no more than 100 km wide at its greatest extent, normal atmospheric models cannot resolve this region to a sufficient degree of accuracy. As such, any mesoscale model used to simulate the surface energy fluxes would require a resolution much higher than 100 km. ECMWF re-analysis data, for instance, is available on a 1.125° roster, approximately 125 km, and is not capable of resolving the ablation region of Greenland. The model developed here has a maximum horizontal resolution of 10 km which allows it to resolve the ablation region to a sufficient level.

In this, and the following, chapter use is made of the GABLM to determine the energy balance and near surface meteorological variables on the Greenland ice sheet. In this chapter the GABLM is described, verified with observations and tested for its sensitivity to many of the input parameters. Use is made of observations made during the Greenland Ice Margin Experiment in the summer of 1991 (GIMEX-91). During this experiment several weather stations were positioned along a transect in the ablation region of the west Greenland ice sheet near Kangerlussuaq, known as the K-transect. After comparing model results with observations a series of sensitivity tests are carried out in order to identify parameterisations and variables for which the surface energy fluxes are most sensitive.

In Chapter 7 the model is run for the entire 1998 ablation season. Observational data from six automatic weather stations on the ice sheet are available during this period and use is made of these to verify the simulation. The surface energy balance and ABL dynamics are discussed and a climate sensitivity run is carried out in order to determine the sensitivity of the surface energy fluxes, particularly the turbulent heat fluxes, to a change in free atmospheric temperature.

6.2 Model description

The GABLM is a 3-D hydrostatic atmospheric boundary layer model based on the basic dynamic and thermo-dynamic equations. It incorporates a second-order closure turbulence scheme, a longwave emissivity scheme to determine longwave radiation in the boundary layer and a subsurface temperature diffusion model. Surface parameters and cloud cover are prescribed and the model is forced at the top and lateral boundaries by ECMWF re-analysis data. The maximum horizontal resolution used is 10 km.

6.2.1 Dynamics

The boundary layer model is based on the basic conservation laws as can be found in many texts, e.g. Pielke (1984). The equations describing conservation of momentum

are written in their scaled pressure form as follows:

$$\frac{DU_i}{Dt} = -\frac{\partial \overline{u_i u_j}}{\partial x_j} - \overline{\Theta} \frac{\partial \overline{\Pi}}{\partial x_i} - g_i + f \epsilon_{i3k} U_k \quad (6.1)$$

The velocity components in the above equation are separated into their turbulent (lower case) and mean (upper case) values by way of Reynolds decomposition. This equation can be simplified and transformed for use in mesoscale models over inclined terrain. The total Exner function $\overline{\Pi}$ and potential temperature $\overline{\Theta}$ are split into their synoptic (Π_o, Θ_o) and mesoscale, or perturbation, components (Π, Θ) and the hydrostatic assumption for the synoptic components, i.e. $\Theta_o \frac{\partial \Pi_o}{\partial z} = -g$ where g is gravitational acceleration, is also applied.

It is then useful to transform the co-ordinate system to a terrain-following system. This is done by way of the transformation matrix as described in Anderson *et al.* (1984), Gal-Chen and Somerville (1975) or Pielke (1984). The simplest and most suitable co-ordinate transformation for the present model is that of equidistant orthogonal horizontal co-ordinates (x, y) and stretched terrain-following vertical co-ordinates. Vertical stretching is logarithmic so that the grid spacing is smallest near the surface where gradients of meteorological variables are largest. The model grid is then transformed to follow the surface terrain. The resulting transformation metrics which transform the real Cartesian co-ordinate system (x_i) to the equidistant computational co-ordinate system (\tilde{x}_i) can be written as follows.

$$J^{ij} = \frac{\partial x_i}{\partial \tilde{x}_j} = \begin{bmatrix} 1 & 0 & 0 \\ 0 & 1 & 0 \\ \frac{\partial z}{\partial x} & \frac{\partial z}{\partial y} & \frac{\partial z}{\partial z} \end{bmatrix} \quad (6.2)$$

where $U_i = J^{ij} \tilde{U}_j$ and $\frac{\partial}{\partial x_i} = J_{ij} \frac{\partial}{\partial \tilde{x}_j}$. The two transformation metrics are related to each other by their inverse, i.e. $J_{ij} = J^{ij-1}$

With the grid transformation made here, only three terms in the transformation metric need be determined, i.e. J_{zz} which defines the vertical stretching of the grid, and J_{zx} and J_{zy} which define the slope of the grid in the x and y directions. At the surface these last two terms are equivalent to the surface slope. Application of these metrics and the simplifications described above give the following two equations for the horizontal wind components (U, V) where the tilde is dropped from the horizontal components since these are unaltered by the co-ordinate transformation.

$$\frac{dU}{dt} = -J_{zz} \frac{\partial \overline{u w}}{\partial \tilde{z}} - \Theta_o \frac{\partial \Pi}{\partial x} + J_{zx} \frac{g}{\Theta_o} \Theta + f(V - V_g) \quad (6.3)$$

$$\frac{dV}{dt} = -J_{zz} \frac{\partial \overline{v w}}{\partial \tilde{z}} - \Theta_o \frac{\partial \Pi}{\partial y} + J_{zy} \frac{g}{\Theta_o} \Theta - f(U - U_g) \quad (6.4)$$

where

$$\frac{d}{dt} = \frac{\partial}{\partial t} + U \frac{\partial}{\partial x} + V \frac{\partial}{\partial y} + \tilde{W} \frac{\partial}{\partial \tilde{z}} \quad (6.5)$$

and where the geostrophic wind fields are given by

$$U_g = -\frac{\Theta_o}{f} \frac{\partial \Pi_o}{\partial y} \quad \text{and} \quad V_g = \frac{\Theta_o}{f} \frac{\partial \Pi_o}{\partial x} \quad (6.6)$$

and f is the Coriolis parameter. In the above equations the flux divergence terms are simplified by including only the vertical gradient terms since horizontal gradients are generally much smaller.

The transformed vertical component of motion \tilde{W} is deduced from the continuity equation

$$\frac{\partial \tilde{W}}{\partial \tilde{z}} = -\left(\frac{\partial U}{\partial x} + \frac{\partial V}{\partial y}\right) \quad (6.7)$$

and is assumed to be in hydrostatic equilibrium so that the scaled pressure perturbation can be determined by integrating

$$J_{zz} \frac{\partial \Pi}{\partial \tilde{z}} = \frac{g}{\Theta_o^2} \Theta \quad (6.8)$$

with the assumption that Π at the top of the model domain is equal to zero. The hydrostatic assumption applied in this fashion on terrain following co-ordinates is applicable only for slopes $< 5^\circ$ (Pielke, 1984).

Conservation of entropy, which leads to the prognostic equation for potential temperature, is written as follows:

$$\frac{D\bar{\Theta}}{Dt} = -\frac{\partial \overline{u_j \theta}}{\partial x_j} - \frac{1}{c_p \rho} \frac{\partial R_j}{\partial x_j} \quad (6.9)$$

where $\overline{u_j \theta}$ is the turbulent temperature flux and R_j is the net radiation flux, both oriented in the j direction. As previously mentioned the total potential temperature $\bar{\Theta}$ is split into a synoptic component $\Theta_o(x, y, z)$ and a perturbation component $\Theta(x, y, z)$. By assuming vertical gradients to be much larger than horizontal gradients the transformed equations for potential temperature perturbation (Θ) and water vapour (Q) become

$$\frac{d\Theta}{dt} = -\frac{d\Theta_o}{dt} - J_{zz} \frac{\partial \overline{w\theta}}{\partial \tilde{z}} - \frac{J_{zz}}{c_p \rho} \frac{\partial R_z}{\partial \tilde{z}} \quad (6.10)$$

$$\frac{dQ}{dt} = -J_{zz} \frac{\partial \overline{wq}}{\partial \tilde{z}} \quad (6.11)$$

where

$$\frac{d\Theta_o}{dt} = \frac{\partial \Theta_o}{\partial t} + U \frac{\partial \Theta_o}{\partial x} + V \frac{\partial \Theta_o}{\partial y} + \tilde{W} \frac{\partial \Theta_o}{\partial \tilde{z}} \quad (6.12)$$

Since Θ_o is prescribed in the model the time dependent term in Equation 6.12 is also prescribed. No attempt is made to include diabatic processes such as cloud formation in this model.

6.2.2 Turbulence scheme

The turbulence scheme is based on previous work from Denby (1999) which describes the application of a complete second-order closure model for katabatic flows. This scheme, based on earlier work from Hanjalić and Launder (1972) and Shir (1973), involves the use of 11 turbulent prognostic equations. In Denby (1999) it was shown that one could simplify the turbulence model down to a prognostic equation for turbulent kinetic energy (E) and vertical velocity variation ($\overline{w\overline{w}}$) for the type of atmospheric flow present on the Greenland ice sheet. This simplification allows the turbulent fluxes to be described in terms of K-theory where the diffusion coefficient K is diagnosed from the prognostic equations for E and $\overline{w\overline{w}}$. These equations are listed in Appendix 6.A.

6.2.3 Surface layer

Monin-Obukhov theory is used at the bottom level of the model to describe the boundary conditions for the mean variables and turbulent fluxes. The surface fluxes are thus related to the stability parameter Ψ and the mean components of wind, temperature and water vapour at the lowest model level z_1 in the following way

$$\overline{uw}_o = -\frac{\kappa^2 U(z_1) |U(z_1)|}{(\ln(z_1/z_o) - \Psi_m)^2} \quad (6.13)$$

$$\overline{vw}_o = -\frac{\kappa^2 V(z_1) |U(z_1)|}{(\ln(z_1/z_o) - \Psi_m)^2} \quad (6.14)$$

$$\overline{w\theta}_o = -\frac{\kappa^2 (\Theta(z_1) - \Theta_s) |U(z_1)|}{(P_r \ln(z_1/z_h) - \Psi_h) (\ln(z_1/z_o) - \Psi_m)} \quad (6.15)$$

$$\overline{wq}_o = -\frac{\kappa^2 (Q(z_1) - Q_s) |U(z_1)|}{(P_r \ln(z_1/z_q) - \Psi_q) (\ln(z_1/z_o) - \Psi_m)} \quad (6.16)$$

In the above equations the subscript s denotes surface values, κ is the von Karman constant (0.4) and z_o , z_h and z_q are the roughness lengths for momentum, temperature and water vapour respectively. The stability parameters Ψ are the integrated form of the flux-profile relationships ϕ and are listed in Garratt (1992) for both stable and unstable conditions. The turbulent Prandtl number is given as $P_r = 0.92$ as is used for near-neutral conditions in Denby (1999).

6.2.4 Longwave radiation scheme

The incoming and outgoing longwave fluxes are calculated using the emissivity approximation from Garratt and Brost (1982) given by

$$\begin{aligned} L \downarrow (z) &= \int_z^\infty \sigma T(z')^4 \frac{\partial \varepsilon(z', z)}{\partial z'} dz' \\ L \uparrow (z) &= \int_z^0 \sigma T(z')^4 \frac{\partial \varepsilon(z', z)}{\partial z'} dz' + \varepsilon_s \sigma T_s^4 (1 - \varepsilon(z, z_s)) \end{aligned} \quad (6.17)$$

where the Stefan-Boltzman constant $\sigma = 5.67 \times 10^{-8} \text{ Wm}^{-2} \text{ K}^{-4}$, T is the temperature in Kelvin and the subscript s denotes surface values. The emissivity ε is calculated for water vapour using the scheme from Welch and Zdunkowski (1976) and for CO_2 using a scheme from Rodgers (1967). Liquid water is also included at levels where clouds are specified and the emissivity is calculated as a fraction of cloud coverage. The total emissivity ε is thus written as:

$$(1 - \varepsilon) = (1 - \varepsilon_{wv})(1 - \varepsilon_{\text{CO}_2})(1 - n \varepsilon_{lw}) \quad (6.18)$$

where n is the fractional cloud cover. The net vertical radiation is calculated at any height from

$$R_z = L \uparrow (z) - L \downarrow (z). \quad (6.19)$$

6.2.5 Shortwave parameterisation

The incoming short wave radiation at the surface is calculated in the following way

$$S_s = S_o \tau_{cs} \tau_{cl} \quad (6.20)$$

where S_o is the incoming short wave radiation at the top of the atmosphere using the formulation found in Iqbal (1983). τ_{cs} and τ_{cl} are the clear and cloudy sky attenuations which are calculated using the parameterisation from van de Wal (1994) and Konzelmann *et al.* (1994), respectively, based on measurements made along the K-transect during GIMEX. These are given as

$$\tau_{cs} = (0.75 + 6.8 \times 10^{-5} h + 7.1 \times 10^{-9} h^2) (1 - 9.0 \times 10^{-4} Z) \quad (6.21)$$

$$\tau_{cl} = 1 - 0.78 n^2 e^{-0.00085 h} \quad (6.22)$$

where h is the elevation in meters a.s.l., Z the zenith angle in degrees and n the cloud cover (0-1).

6.2.6 Surface and subsurface parameters

In the model most surface parameters are prescribed and not diagnosed from the model itself. The prescribed surface parameters are albedo, surface roughness lengths, sea surface temperature, deep soil and ice temperatures and the subsurface parameters of density, specific heat and thermal conductivity. These parameters

are in general coupled to a parameterised surface temperature field, Equation 6.23, since there is a direct physical relationship between the state of the surface and temperature. Use of this temperature field, which is adopted from Ohmura (1987), is limited to the determination of these surface parameters and to the initialization of the model surface temperature.

6.2.6.1 Initial surface temperature parameterisation

A surface climatological temperature field is used to determine the spatial distribution of several of the surface parameters and to initialize subsurface temperatures. This is based on the parameterisation from Ohmura (1987) taken from surface observations made in the period 1953 to 1981. This temperature field uses measurements made both on tundra and ice surfaces and is the same parameterisation used by van de Wal (1994) to drive his energy balance model of the Greenland ice sheet. The daily average surface temperature field, in $^{\circ}\text{C}$, is described by

$$T(\phi, z, day) = T_{an} - T_{amp} \cos\left(\frac{2\pi(day - 3)}{365}\right) \quad (6.23)$$

where the average annual temperature is given by

$$T_{an} = 49.13 - 0.7576\phi - 0.007992h$$

and h is the elevation above sea level, ϕ the latitude in degrees and day the Julian day. The amplitude of the variation throughout the year is given by

$$T_{amp} = -18.35 + 0.4314\phi + 0.00172h$$

6.2.6.2 Albedo

Surface albedo is a complicated function of mass balance, snow depth, accumulation, time and temperature. Because of the short simulation period of the present study (20 days), albedo must be specified and this is done on the basis of yearly and daily temperature isotherms determined from the surface temperature parameterisation, Equation 6.23. The parameterisation developed here is derived from satellite observations along the K-transect and is coupled to the daily and yearly surface temperatures for applicability to the whole of the ice sheet. In Chapter 7, albedo is internally generated by the model, since the simulation period will cover the entire ablation season, and is based on a two layer snow model. The internally generated scheme will be described in that Chapter.

Figure 6.1a indicates schematically the parameterisation used for the ice sheet surface albedo in this study. Three heights are prescribed which are associated with three different isotherms. h_{ice} indicates the height below which it is assumed ice is always present with an albedo α_{ice} and h_{snow} indicates the height above which it is assumed that fresh snow lies with the maximum albedo $\alpha_{snow} = 0.85$. Both these heights are determined by the yearly average temperature isotherms of $T_{ice} = -5.7^{\circ}\text{C}$ and $T_{snow} = -19.0^{\circ}\text{C}$. The third level, h_{slush} , is the variable slush line height

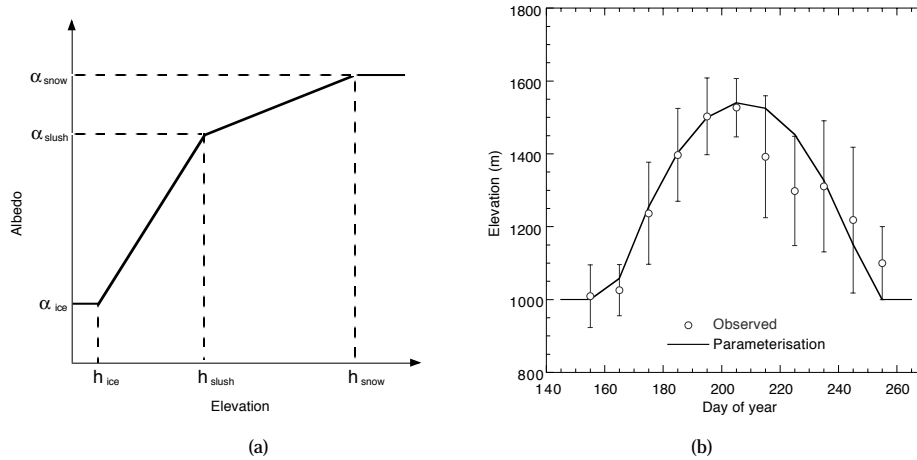


Figure 6.1: a) Schematic representation of the albedo parameterisation used in the model. b) Comparison of 10 year average observed (circles with error bars equal to the standard deviation over the 10 year period) height of the slush line at the K transect with the parameterisation used in the model. See text for details.

as derived by Greuell and Knap (2000), indicating the height at which wet snow changes to dry snow and a transition in albedo occurs.

The position of the slush line varies throughout the melt season. In order to couple this height to Equation 6.23 10 years of satellite observations (1990-1999) are evaluated and compared to Equation 6.23. It is found, as shown in Figure 6.1b, that a reasonable fit to the observations can be made by choosing the height with a daily average temperature of $T_{slush} = -0.8^{\circ}\text{C}$ and allowing this to lag behind the temperature parameterisation by 7 days. The minimum height for h_{slush} is set by the yearly average isotherm of -9.7°C , which is approximately 1000 m at the latitude of the K-transect.

The albedo at heights h_{slush} and h_{ice} are also allowed to vary with time during the melt season reflecting the aging and wetting of the snow and ice. α_{slush} and α_{ice} decrease linearly as a function of time by a total of 0.1 from day 150 to day 240. Outside this period the maximum values for ice and snow are assumed, i.e. 0.5 and 0.85. Having defined the three levels and three associated albedos, the albedo profile is calculated as a linear function between them.

The isotherms chosen to represent the three different heights in the parameterisation are derived from albedo observations along the K-transect over a 10 year period. In Figure 6.2, satellite derived and parameterised albedo profiles are compared. The parameterisation gives a reasonable fit to the 1992 data but not in 1995 when a dark zone has developed near the ice margin (Knap and Oerlemans, 1996). The sensitivity of the model to albedo will be discussed later in Section 6.4.2.

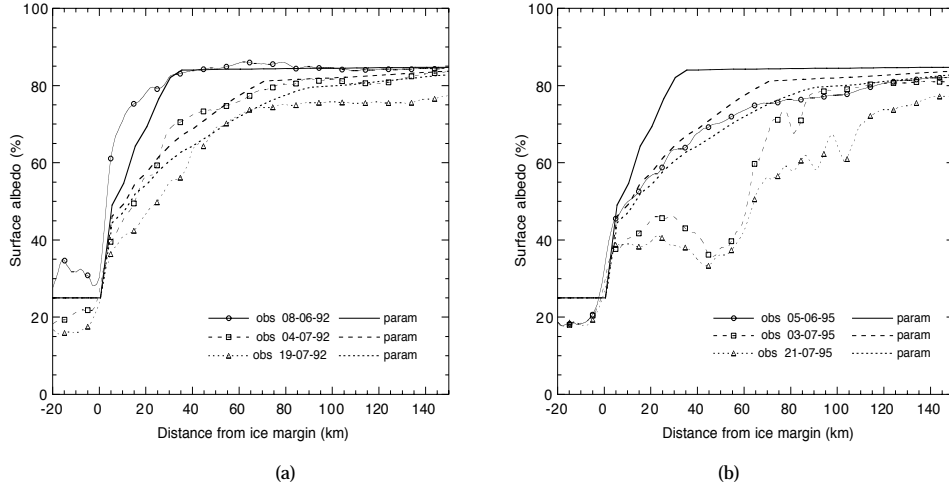


Figure 6.2: Comparison of model parameterised surface albedo with satellite derived albedos along the K transect during the melt seasons of 1992 (a) and 1995 (b).

6.2.6.3 Roughness lengths

The aerodynamic surface roughness length of momentum (z_o) is simply prescribed in the model. Four different surface types are defined (water, tundra, ice and snow, see Table 6.1) and z_o is specified for each of these. On the ice sheet $\ln(z_o)$ is interpolated as a linear function of height going from the ice isotherm at level h_{ice} with a value of $z_o = 50$ mm to the snow isotherm at level h_{snow} of $z_o = 1$ mm.

The aerodynamic surface roughness length for water is derived from the equations given by Garratt (1977) for smooth and rough surfaces as below

$$\begin{aligned}
 z_o &= 0.11 \frac{\nu}{u_*} & \text{for } u_* < \left(\frac{0.11g\nu}{\alpha_c} \right)^{1/3} \\
 z_o &= \frac{\alpha_c}{g} u_* & \text{for } u_* > \left(\frac{0.11g\nu}{\alpha_c} \right)^{1/3}
 \end{aligned} \tag{6.24}$$

where ν is the viscosity of air, g gravitational acceleration, u_* the friction velocity and Charnocks constant is $\alpha_c = 0.016$.

The scalar surface roughness lengths for temperature and water vapour on ice and snow surfaces are specified using the formulation from Andreas (1987) which is based on surface renewal theory. In this formulation the temperature roughness length is expressed as a function of roughness Reynolds number, $Re_* = u_* z_o / \nu$ where ν is the viscosity of air. The roughness length for temperature (z_h) is determined by:

$$\ln \left(\frac{z_h}{z_o} \right) = 0.317 - 0.565 \ln(Re_*) - 0.183 \ln(Re_*)^2 \tag{6.25}$$

Though Andreas also gives a separate formulation for the water vapour roughness length this differs only slightly from that of temperature and so these two roughness lengths are assumed to be equivalent in the simulations.

The above formulation is slightly modified in the model according to Smeets and Vugts (2000) who suggest that the most appropriate length scale for momentum in Equation 6.25 is determined by the micro-scale crystal structure and not by the large-scale ice hummocks. This would appear to be a more appropriate length scale for the molecular diffusion processes associated with surface renewal theory. As such, a constant $z_{o,flat} = 1$ mm is used to calculate z_h on both ice and snow, representing the micro-scale structure of the surface, throughout the model.

The scalar roughness lengths for tundra surfaces are determined from the relationship

$$\ln \left(\frac{z_{h,q}}{z_o} \right) = -2 \quad (6.26)$$

and above water by

$$\ln \left(\frac{z_{h,q}}{z_o} \right) = 2.5 Re_*^{1/4} - 2 \quad (6.27)$$

Both these relationships are taken from Garratt (1992).

6.2.6.4 Subsurface model

The subsurface model is a simple 10 layer temperature diffusion model where englacial and deep soil processes such as absorption of shortwave radiation, refreezing and soil moisture content variations are ignored. Density, thermal diffusivity and heat capacity are taken as constant with depth and are specified according to the four surface types given in Table 6.1. Ice and snow subsurface parameters are specified in a similar fashion to the surface roughness lengths. That is, a linear function of height bounded at the maximum height h_{snow} by the snow parameters and at the minimum height h_{ice} by the ice parameters.

The deepest layer in the subsurface model is 5 m for all surface types and the temperature at this level is held constant according to the yearly average value calculated with Equation 6.23. The shallowest level is set at a depth of 5 mm and the grid points are logarithmically stretched in between. The top boundary condition is the net surface energy flux as calculated from the surface energy budget, Equation 6.29. The numerical scheme uses a fully implicit time step to solve the diffusion equation. The equation solved is:

$$\frac{\partial T_{ss}}{\partial t} = \frac{\partial}{\partial z_s} \left(\kappa_s \frac{\partial T_{ss}}{\partial z_s} \right) \quad (6.28)$$

where the subscript ss stands for subsurface and the thermal conductivity $k_s = \kappa_s \rho_s c_s$, where κ_s is the thermal diffusivity, ρ_s the density and c_s the specific heat.

The surface boundary condition is given by $GFL = -k_s \frac{\partial T_{ss}(z_s=0)}{\partial z_s}$, where GFL is the net surface energy flux, and the bottom boundary condition as $T_{ss}(z_s = z_{bot})$, i.e. the annual average temperature according to Equation 6.23.

The surface specific humidity of ice, snow and water is set to the saturated value based on surface temperature and the Clausius-Clapeyron equation. For tundra surfaces a surface relative humidity of 50% is assumed.

Table 6.1: Surface parameters for the 4 different surface types specified in the model.

Parameter	water	tundra	ice	snow
Roughness length z_o (mm)	Eq. 6.24	20	50	1
Albedo α (0 - 1)	0.1	0.25	0.5-0.4	0.85-0.75
Density ρ (kg m^{-3})	1000	1600	910	200
Thermal conductivity k_s ($\text{Wm}^{-1}\text{K}^{-1}$)	∞	0.3	2.0	0.2
Specific heat c_s ($\text{Jkg}^{-1}\text{K}^{-1}$)	4186	800	2100	2100

6.2.7 The energy balance model

The surface energy flux is calculated directly from the model according to

$$GFL = NSW + NLW + HFL + EFL \quad (6.29)$$

and is defined as positive downwards. Each term is described below.

$NSW = S_s(1 - \alpha)$: The net shortwave radiation where S_s is the surface global radiation calculated from Equation 6.20.

$NLW = L \downarrow_s - L \uparrow_s$: The net longwave radiation at the surface where both the upward and downward longwave radiation fluxes are calculated using the emissivity scheme described in Section 6.2.4.

$HFL = -\rho_a c_p \overline{w\theta}$: The sensible heat flux calculated from the turbulent vertical temperature flux where ρ_a is the density of air and $c_p = 1006 \text{ Jkg}^{-1}\text{K}^{-1}$.

$EFL = -\rho_a L_e \overline{wq}$: The latent heat flux calculated from the turbulent vertical water vapour flux where $L_e = 2.5 \times 10^6 \text{ Jkg}^{-1}$ is the latent heat of vapourisation of water.

GFL : The total net energy flux which is used as the upper boundary condition for the subsurface model, Section 6.2.6.4.

6.2.8 Synoptic pressure and wind field

The synoptic wind field, $U_g(x, y)$ and $V_g(x, y)$, is prescribed from ECMWF re-analysis data which is available with a horizontal resolution of roughly 125 km. The 700 hPa geo-potential pressure level is used to determine the synoptic pressure gradient, and

from this geostrophic winds. This pressure level has an approximate elevation of 3000 m a.s.l. and as such intersects the surface where the ice sheet rises above this elevation. Though errors are expected when the ECMWF pressure level is extrapolated below the surface in this region, the 700 hPa level has been chosen because it is representative of the geostrophic flow above the ABL in the ablation zone, the region of most interest in this study. The synoptic pressure field is assumed to be barotropic and so geostrophic winds are constant with height. It is updated every 6 hours and linearly interpolated between these periods. The velocity field at the top of the model is set to the geostrophic values.

6.2.9 Synoptic temperature and humidity fields

The synoptic, or ambient, temperature field $\Theta_o(x, y, z)$ is also specified using ECMWF re-analysis data. As with the synoptic wind fields, Θ_o is updated and linearly interpolated every 6 hours. The Θ_o field is determined by linearly fitting the vertical temperature profiles from the re-analysis data at every second model level from 27 to 19, which corresponds to elevations of 900 to 4000 m a.s.l. respectively when the surface elevation is at sea level. In this way a surface reference value $\Theta_{o\ ref}(x, y)$ and a lapse rate $\gamma_{o\ ref}(x, y)$ is determined for each grid point.

Specific humidity is similarly specified from ECMWF re-analysis data using the average relative humidity field from the three levels 27, 25 and 23. Specific humidity is determined by taking the relative humidity field to be constant with height. Relative humidity is updated during the simulation at the top and lateral boundaries only.

6.2.10 Cloud cover

The total cloud cover is taken from ECMWF re-analysis data and inserted at a constant height of approximately 3500 m a.s.l. Cloud cover is used for the attenuation of shortwave radiation (Equation 6.22) and for the longwave radiation scheme (Section 6.2.4). The liquid water content of the clouds is calculated from Albrecht *et al.* (1990) and the cloud depth is taken to be 500 m in order to determine the liquid water emissivity ε_{lw} at cloud height. ε_{lw} , calculated in this fashion, is very close to unity and so the insertion of clouds is effectively the same as the placement of a black body at the height of the cloud base.

6.2.11 Sea surface temperature

The sea surface temperature is held constant throughout the model runs and is specified as the monthly mean ECMWF re-analyses skin temperature in all areas not associated with the Greenland topography.

6.2.12 Topography

The Greenland topography and land/ice/sea mask is taken from the EKHOLM 0.02° data set (Ekholm, 1996). This data set is converted to an equidistant 5 km grid using a general stereographic projection centered at 72 °N, 42 °W. When using model

resolutions larger than 5 km grid points are simply stepped over, no interpolation of data points is employed. Smoothing of the data is carried out over the rough tundra region.

Topographical features not associated with Greenland are not represented in the model. This means that Ellesmere Island, to the North-west of Greenland, is not represented topographically. However the monthly mean surface temperature of this region is retained in the sea surface temperatures.

6.2.13 Numerics

The model grid is a terrain following vertically stretched grid, extending from the surface up to an elevation of 5000 m a.s.l.. The lowest grid level at sea level is 2 m but decreases slightly with elevation to 1.5 m on top of the ice sheet. In this study vertical resolutions of both 10 and 20 levels, and horizontal resolutions of 10, 20 and 40 km are used. The 20×20 km horizontal grid is shown in Figure 6.3 superimposed on the surface topography.

The computational grid used in the model is an equidistant grid $(\tilde{x}, \tilde{y}, \tilde{z})$. In order to determine the transformation metrics necessary for converting to the actual spatial co-ordinates, Section 6.2.1, this grid is first stretched logarithmically in the vertical, with the lowest grid level at 2 m, and then transformed to a terrain following co-ordinate system. The transformation metrics J_{zz} , J_{zx} and J_{zy} are numerically determined from the transformed grid itself. The various prognostic and diagnostic fields are defined on a staggered grid as shown in Figure 6.4.

The lateral boundaries are all above sea. Wind and perturbation temperature fields are solved at the boundaries as 2-D solutions, along the boundaries, to the top boundary conditions. Specific humidity is determined at the top and side boundaries using the synoptic temperature profile, Θ_o , and the ECMWF relative humidity field. The top boundary conditions are fixed perturbation temperature ($\Theta = 0$), humidity and wind which are set to their ECMWF analysis values as defined in Sections 6.2.8 and 6.2.9.

The numeric scheme is a simple forward in time scheme where the turbulent diffusion equation is implicitly solved and advection is treated with a first-order upwind scheme. A time step of 6 minutes is used for the 20 km grid and is reduced or increased appropriately with grid size. Longwave radiation is calculated every fifth time step.

A Laplacian filter is employed to introduce numerical diffusion into the numerical solution to avoid instabilities. This is applied to all prognostic variables in the horizontal direction. The simulated fields for wind, perturbation temperature and specific humidity are relaxed into their ECMWF values at the top of the model domain using a relaxation scheme in the following form:

$$\frac{\partial \Phi}{\partial t} = -C_r(z) \frac{\Phi - \Phi_o}{\tau_r} \quad (6.30)$$

where Φ is the parameter being relaxed, Φ_o the ambient field it is relaxed to and τ_r is the relaxation time, which has a value of 4 hours. $C_r(z)$ is a height dependent

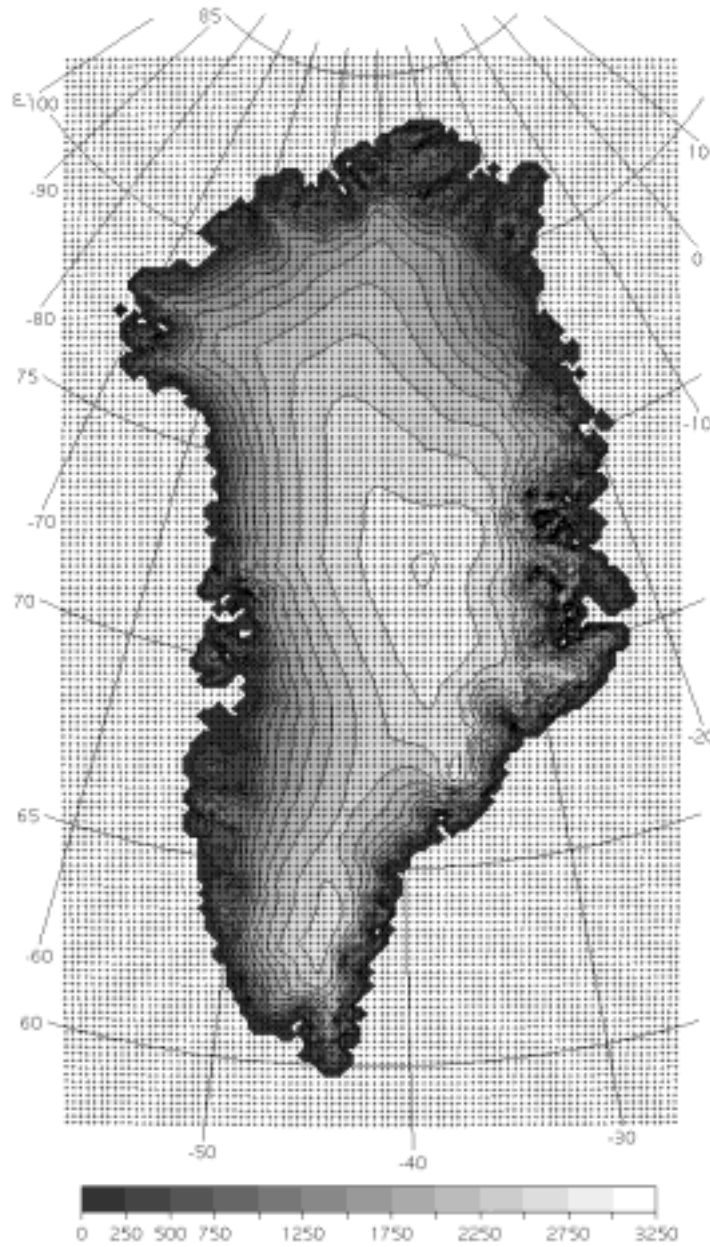


Figure 6.3: The extent of the model domain used in the simulations. Grid positions are shown every 20 km. Shading indicates height above sea level in meters with contour intervals every 250 m.

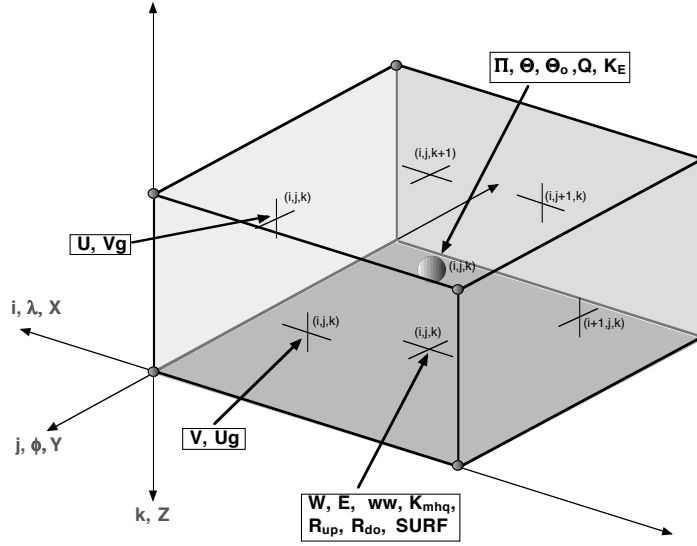


Figure 6.4: Staggered grid used in the GABLM showing the positions of the variables. (i, λ, X) , (j, ϕ, Y) and (k, Z) indicate the model co-ordinates for the grid position (i, j, k) , the geographical position of longitude and latitude (λ, ϕ) , and the grid distance (X, Y, Z) . (U, V, W) are the three wind components, (U_g, V_g) the geostrophic wind components, E the turbulent kinetic energy, ww the vertical velocity variance, K_{mhq} the turbulent diffusivity, R_{up} and R_{do} the longwave radiation components and $SURF$ indicates the position in the grid of the surface variables. Π is the perturbation Exner function, Θ the perturbation potential temperature, Θ_o the ambient potential temperature, Q the specific humidity and K_E the turbulent transport diffusivity.

function that increases from 0 at the surface to 1 at the top of the model domain and is specified by:

$$C_r(z) = \frac{1}{2} + \frac{1}{2} \sin \left(\frac{\pi}{2} \left(2 \frac{z}{z_d} - 1 \right) \right) \quad (6.31)$$

where z is the model height above the surface and z_d is the depth of the model domain.

Advection of the ambient temperature field Θ_o , radiative divergence and the partial time derivative of Θ_o (Equation 6.12) are assumed to be accounted for in the ECMWF model above the boundary layer. These terms are only calculated at grid points within the boundary layer itself, defined as the height at which the turbulent kinetic energy goes to zero.

6.3 Comparison with observations

In order to verify the models ability to simulate the ABL above the Greenland ice sheet a case study is employed. Observational data on the ice sheet itself is quite limited and so use is made of the GIMEX experiment from 1991 in West Greenland.

During this experiment 7 weather stations, 3 on the tundra and 4 on the ice sheet, were positioned along a transect up to 110 km East of Kangerlussuaq. This is referred to as the K-transect and is situated at a latitude of approximately 67°N , Figure 6.5. See for example van den Broeke (1994) for more details concerning this experiment. The positions of the stations are shown, along with the 5 km model topography, for the K-transect in Figure 6.6. Other data available come from an automatic weather station (AWS) from the University of Wisconsin nearby Summit at an elevation of 3010 m a.s.l. and the Kangerlussuaq weather station (K-WS) 20 km from the ice edge.

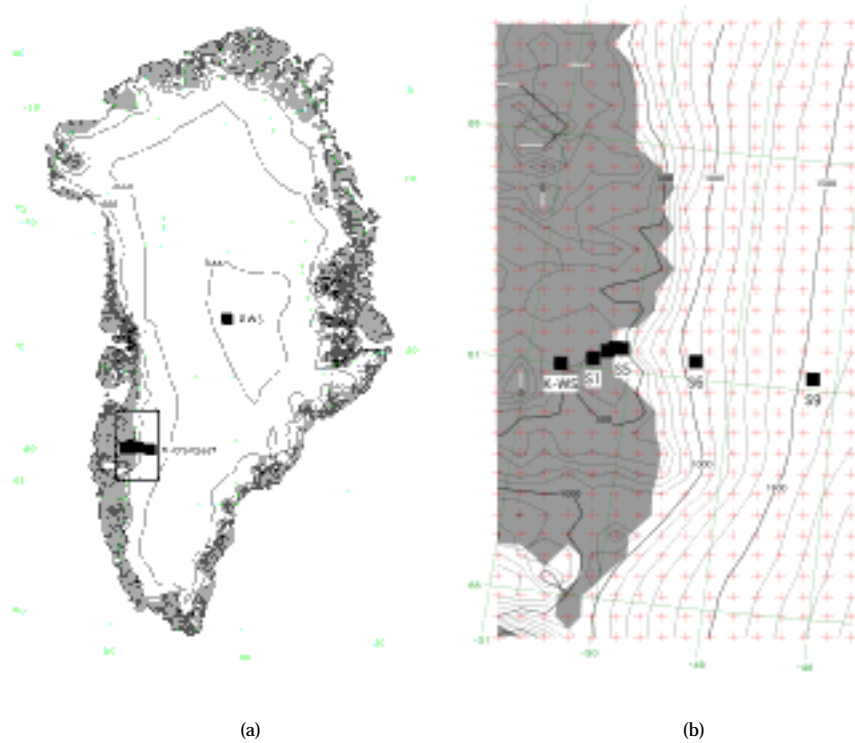


Figure 6.5: (a) Greenland model topography with the position of weather stations used in the comparison. Shaded areas indicate tundra. (b) Close up of the rectangular region surrounding the K-transect showing station positions and the 10 km model grid.

The 10 km resolution model with 20 vertical levels is used to simulate a selected 20 day period during GIMEX, from 5 to 24 July (day 186 to 205) in 1991. The model is initialized from rest using the ECMWF temperature field from day 186 and the monthly average sea surface temperature. After a two day spin up time, six hourly ambient temperature fields (Θ_o), relative humidity fields, geo-potential height (U_g and V_g) and total cloud cover from ECMWF re-analysis data are used to force the

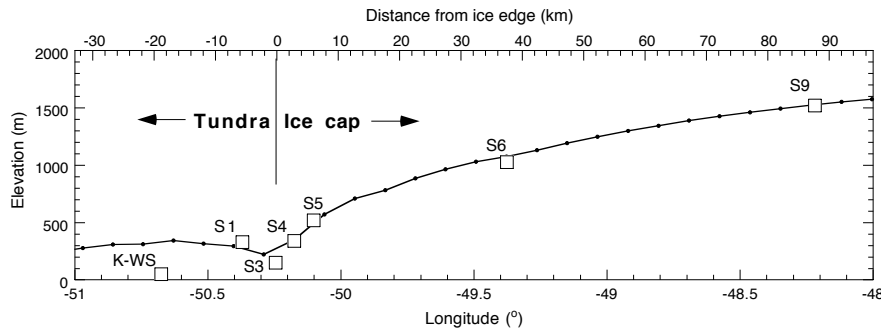


Figure 6.6: Longitudinal positions and elevations of the various GIMEX stations superimposed on the model 5 km topography at the same latitude (67°). The distance from the ice edge is shown on the top axis.

model.

Results are shown as a function of time in Figures 6.7 to 6.10 for the stations K-WS, S5, S9 and AWS in which simulated and observed wind, temperature, specific humidity, cloud cover and net short wave radiation are compared. Also included for the ice sheet sites are the simulated surface energy fluxes.

In general the simulation is quite good, however there are a number of features that warrant attention. Kangerlussuaq (K-WS) is strongly influenced by the local topography and land use, silt and asphalt, because the weather station is situated near the local airport. This site is positioned at the end of Søndre Strømfjord and bounded by hills in the East-West direction. Simulated temperatures on the tundra at Kangerlussuaq, Figure 6.7, show a slightly smaller amplitude than those observed, and observed wind direction is dominated by the local topography at this site. However, daily average temperatures and wind speeds agree quite well with the simulations. Improvement of the simulated temperatures and winds would require a much more detailed simulation using local surface parameters, such as albedo and surface type. ECMWF cloud cover at this site agrees fairly well with observations.

Simulated temperatures and specific humidity at the two K-transect ice sheet sites, S5 and S9, also agree quite well with observations except in the period from day 194 to 197. During this period the ECMWF atmospheric temperature drops in this area by around 5°C but more importantly ECMWF cloud cover reduces to 0.1. This is in contrast to observations at site S9 that show cloudy conditions from day 195 onwards. This indicates the importance of cloud cover in determining the surface energy balance and temperature.

Wind speed and direction are also well represented by the model at these two sites. The directional consistency indicates the dominance of katabatic forcing in determining near surface winds. At site S5 the simulated and observed winds are almost continually directed 35° to the north of the downslope direction, in spite of varying geostrophic wind directions. The most significant difference in wind speed occurs during the previously mentioned cool period where wind speeds at S9 are 2 to 3 ms^{-1} higher. This is due to the extra katabatic forcing which results from the lower surface temperatures.

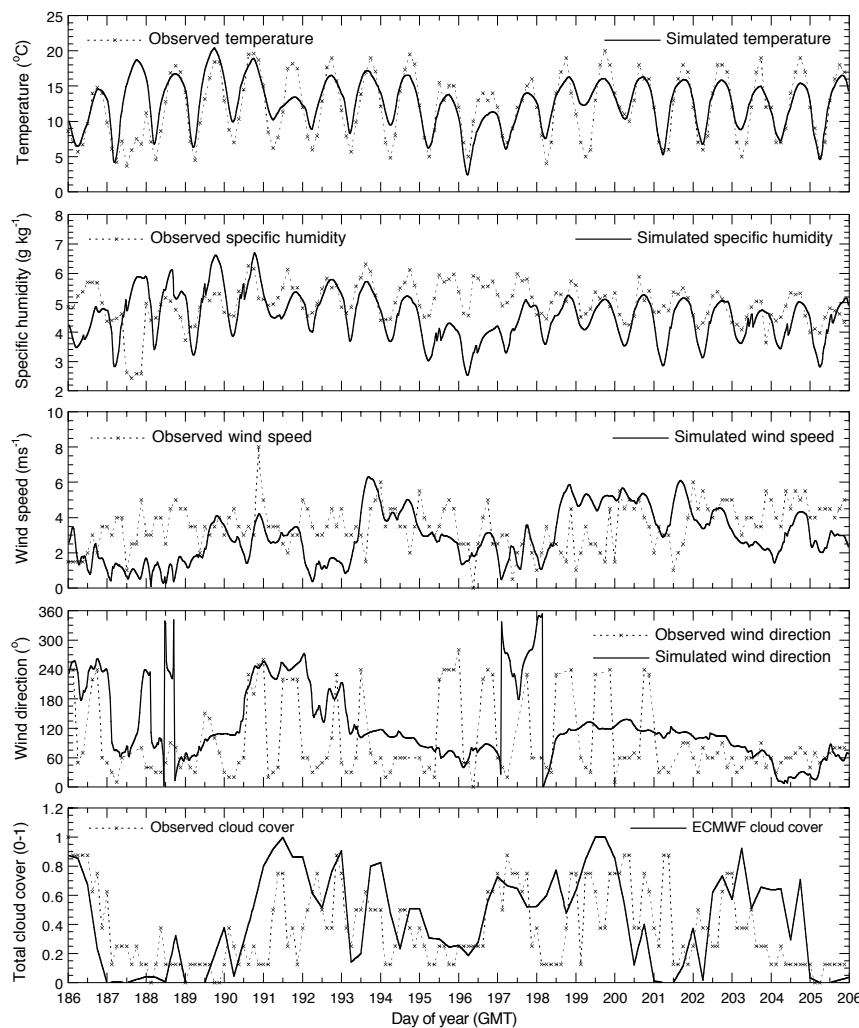


Figure 6.7: Comparison of observed and simulated 2 m temperature, specific humidity, wind speed, wind direction, and total cloud cover at the tundra site K-WS for the period 5 to 24 July (Day 186 to 205) 1991.

Temperatures at AWS, positioned at an elevation of 3010 m a.s.l. near Summit, are in the first 10 day period well represented but in the second generally too low. In non-melt regions the radiation components of the energy balance strongly determine the surface and near surface temperature. Correct cloud cover data in this region is thus important in order to accurately determine surface temperatures. It is unfortunate that no cloud cover observations are available from the AWS. During the second half of the case study period, where temperatures are too low, ECMWF re-analysis data give mainly clear skies, as opposed to the first half where cloud cover is high.

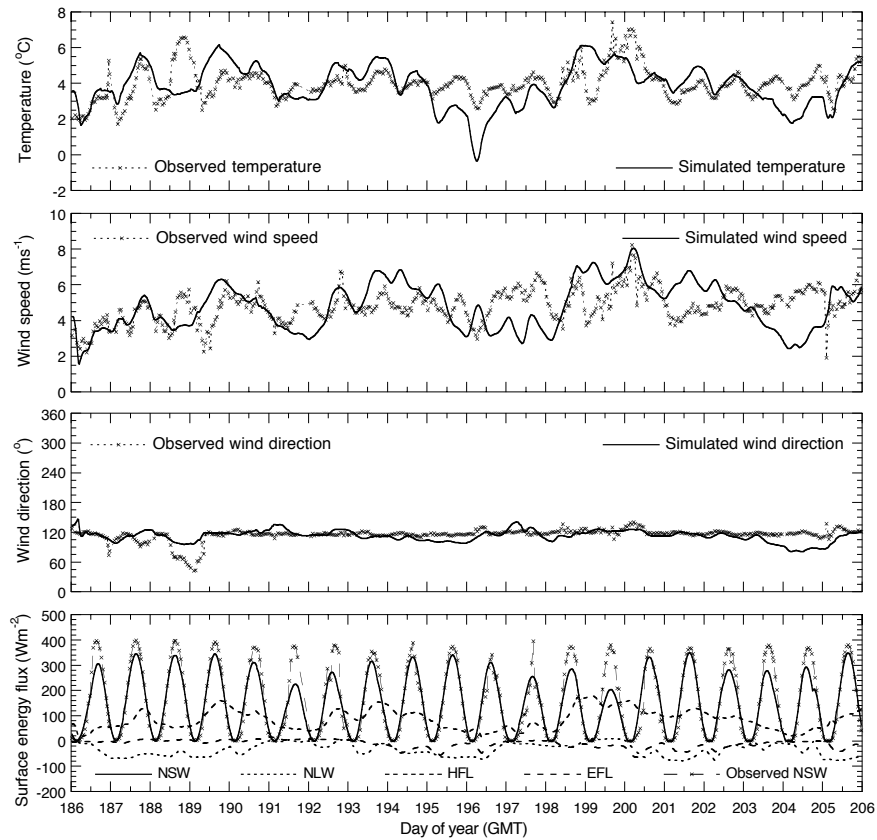


Figure 6.8: Comparison of observed and simulated 2 m temperature, wind speed, wind direction and net shortwave radiation at site S5 for the period 5 to 24 July (Day 186 to 205) 1991. The simulated surface energy fluxes are also shown.

In Section 6.4.7 the sensitivity of the model to changes in cloud cover is tested. This test shows that increasing the cloud cover by a factor of 0.1 leads to an average 2 m temperature increase of approximately 3 °C at site AWS, once more pointing to the importance of clouds in determining the surface energy balance.

Since slopes are smaller near the Greenland summit, winds are mainly driven by the synoptic pressure gradients. Simulated wind speeds and directions agree quite well with observations which indicates that the use of the 700 hPa pressure level to force synoptic winds does not introduce serious errors into the model wind fields.

Average values for the simulated and observed 2 m temperature and wind speed along the K-transect are shown in Figure 6.11. Temperatures agree very well with observed averages at all measurement sites whilst wind speeds tend to be too low near the ice edge and slightly too high ice inwards.

A very similar GIMEX period (10 to 24 July) has also been studied by Gallée and Duyenkerke (1997) using a 2-D meso- γ -scale model with a horizontal resolution of

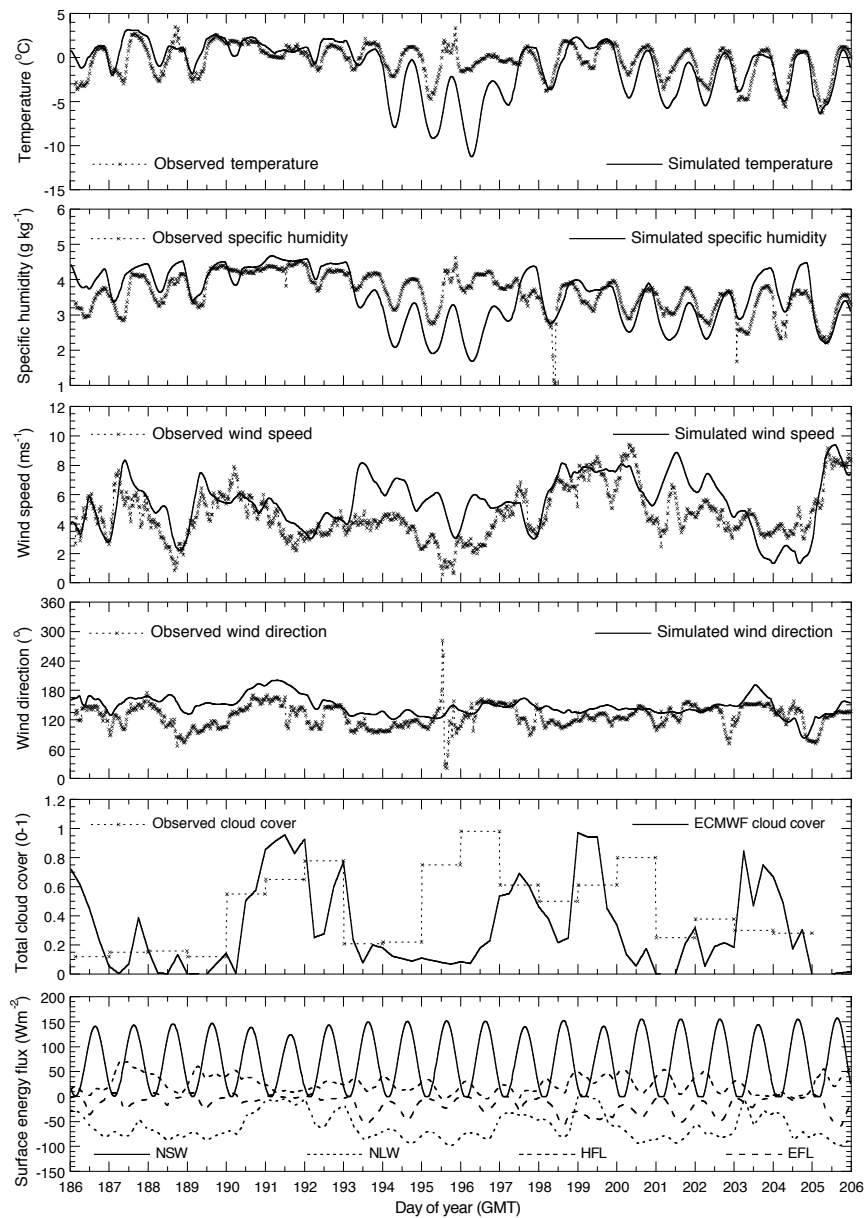


Figure 6.9: Comparison of observed and simulated 2 m temperature, specific humidity, wind speed, wind direction and total cloud cover at site S9 for the period 5 to 24 July (Day 186 to 205) 1991. The simulated surface energy fluxes are also shown.

5 km. Their model runs were driven by radiosonde data from Egedesminde, 200 km north of Kangerlussuaq, and they present data for sites S4, S6 and S9 in terms of daily

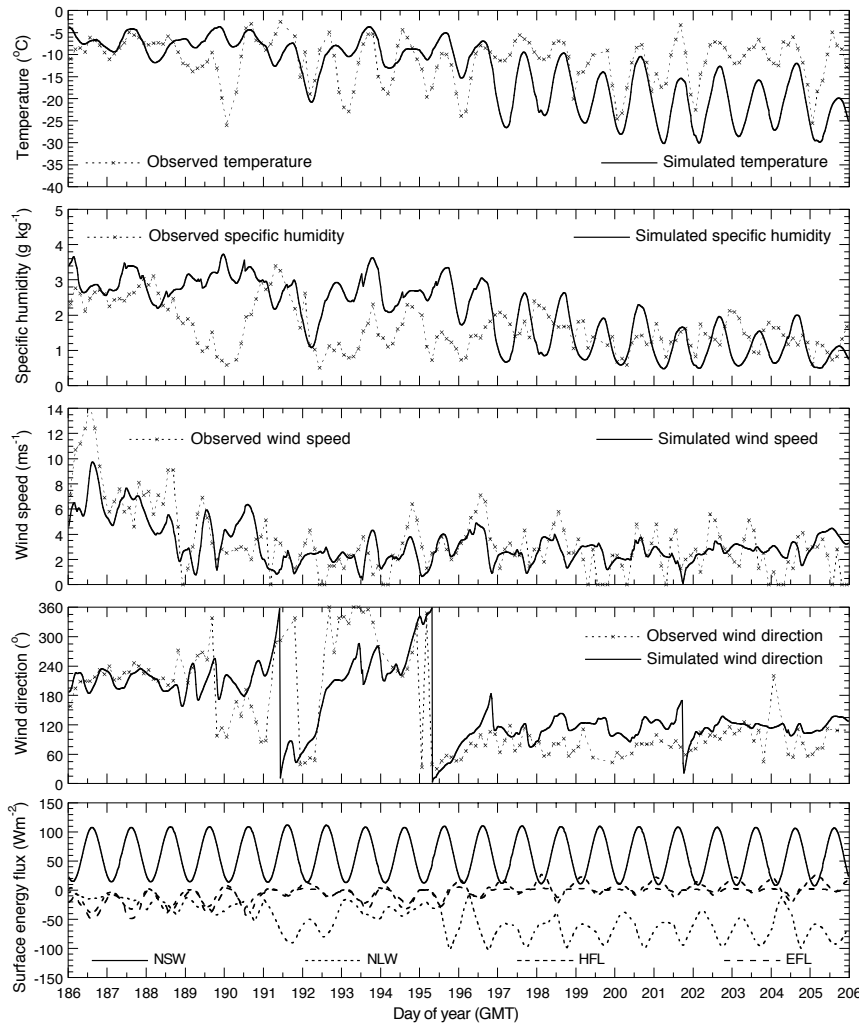


Figure 6.10: Comparison of observed and simulated 2 m temperature, specific humidity, wind speed and wind direction at site AWS for the period 5 to 24 July (Day 186 to 205) 1991. The simulated surface energy fluxes are also shown.

average cycles and average surface energy fluxes over the entire period. Though radiation fluxes differ significantly due to differences in surface albedo and cloud cover description it is worth noting that for sites S6 and S9 there is good agreement between their results and the simulation presented here. Average temperatures agree to within 0.6°C and wind speeds to within 1 ms^{-1} . Average turbulent heat fluxes over the same period also agree to within 5 Wm^{-2} at these two sites.

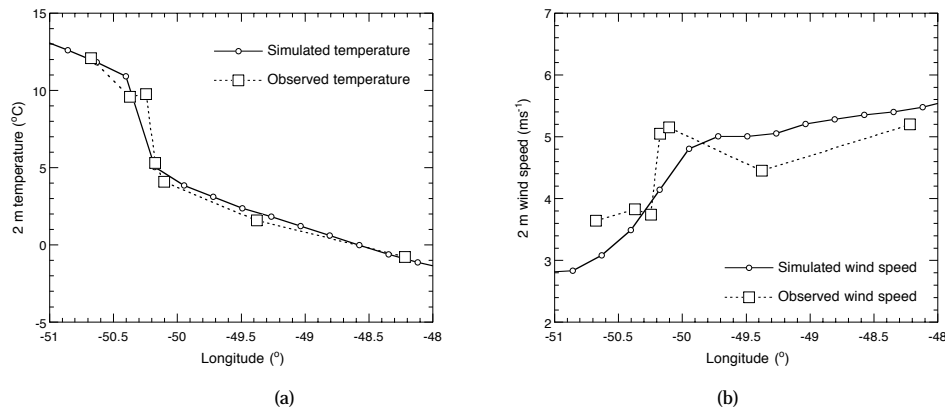


Figure 6.11: Comparison of simulated and observed average 2 m temperature (a) and wind speed (b) for the 20 day GIMEX period from 5 to 24 July. The ice margin is situated at a longitude of 50.2 °.

6.4 Sensitivity tests

Since the primary aim of the model is to improve estimates of the surface energy budget in the ablation region, particularly the turbulent heat fluxes and longwave radiation, the following sensitivity tests are analysed in terms of the four energy balance components described in Section 6.2.7. For this a reference run is used. The input fields of geo-potential height, synoptic temperature, relative humidity and total cloud cover are averaged over the 20 day GIMEX period described in the previous section. The resulting average fields are then used for a four day simulation where the model is spun up for 3 days and the results from the fourth day are used for the sensitivity tests. The 20 km resolution model with 10 vertical levels is used for all of these tests unless otherwise specified.

The sensitivity of each energy budget component to model resolution, model parameterisations, dynamics and input fields are areally averaged over the ice sheet in a region where summer ablation can take place. This is defined in all sensitivity studies as a fixed region where the predefined surface albedo is less than 0.85, equal to a yearly average isotherm of -19 °C (Section 6.2.6.1). For the reference run, 94% of all melt takes place in this region, which covers approximately 25% of the ice sheet or 4.5×10^5 km². The defined ablation region is shown in Figure 6.12 as well as the calculated melt for the reference run.

The resulting spatially and temporally averaged surface energy balance in the defined ablation region is shown for both the reference run and for the 20 day run from Section 6.3 in Figure 6.13. Differences between the reference run and the 20 day run are expected, particularly in the turbulent flux components since these are driven in the 20 day run by continually varying synoptic pressure and temperature fields. However, the differences are not large and are considered unimportant for the sensitivity runs being conducted here.

As can be seen, the net shortwave radiation component (NSW) dominates the energy budget and strongly determines the distribution and quantity of melt that takes place. However, the net longwave radiation (NLW), which continually cools

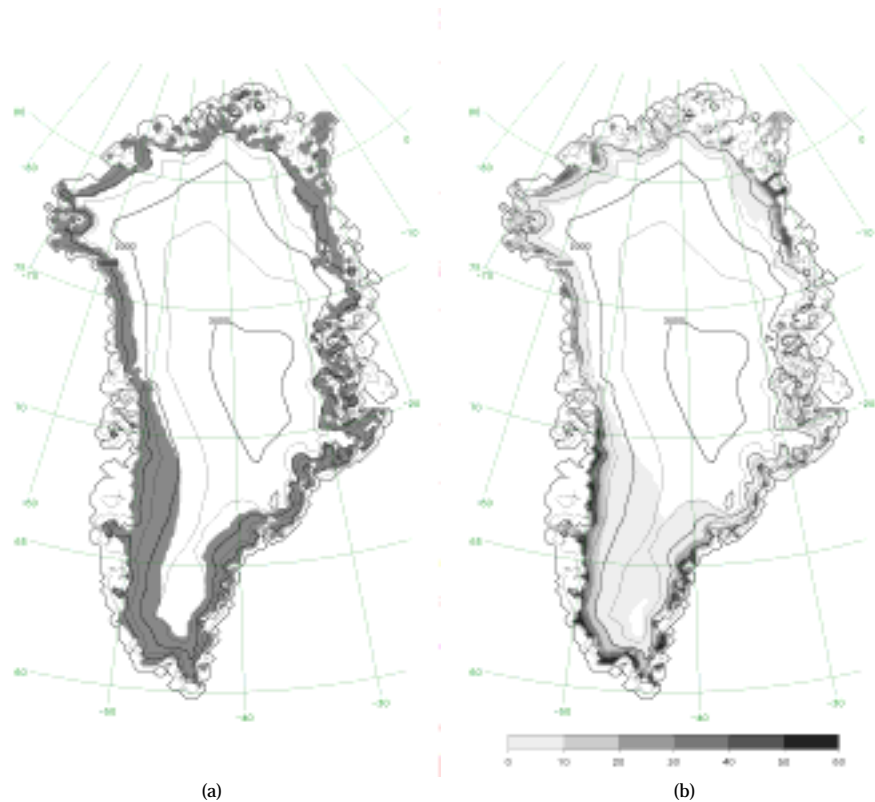


Figure 6.12: (a) Defined ablation region used in the sensitivity tests. Surface energy fluxes are areally and temporally averaged over the shaded region. (b) Simulated melt for the one day reference run in mm w.e..

the surface, partially balances the total radiative flux component of the surface energy budget. As a result, the turbulent sensible heat flux (HFL) and turbulent latent heat flux (EFL) account for around one third of the total surface energy flux (GFL) indicating the importance of these terms in the energy budget.

The surface energy flux components are plotted in Figure 6.14a as a function of longitude along the K-transect using the 10 km resolution model run (Section 6.4.1). The NSW radiation flux reaches a maximum near the ice edge where albedo, as prescribed in the model, reaches a minimum. The downward longwave radiation flux ($L \downarrow_s$) is to a large extent determined by cloud cover. In the ablation region, where surface temperature is fixed at the melting point, $L \downarrow_s$ will determine the net longwave radiation flux.

Sensible heat flux also reaches a maximum at the ice edge. Along the K-transect this is due chiefly to the increased temperature difference between ice and air and not due to higher wind speeds since these increase only slightly towards the ice margin. The latent heat flux is small in magnitude, $< 5 \text{ Wm}^{-2}$, and on average slightly negative over most of the ice sheet, indicating evaporation. In general increased evaporation will occur in areas where wind speeds are higher and directed downs-

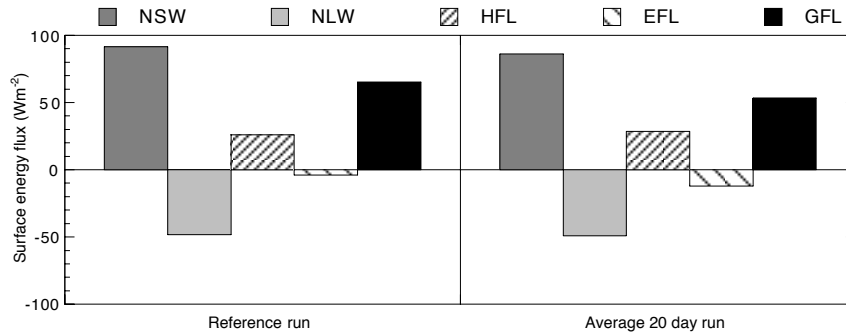


Figure 6.13: Average surface energy flux components over the defined ablation region for the reference run and the 20 day period described in the previous section. *NSW* is the net shortwave radiation, *NLW* the net longwave radiation, *HFL* the turbulent sensible heat flux, *EFL* the turbulent latent heat flux and *GFL* the total net surface heat flux.

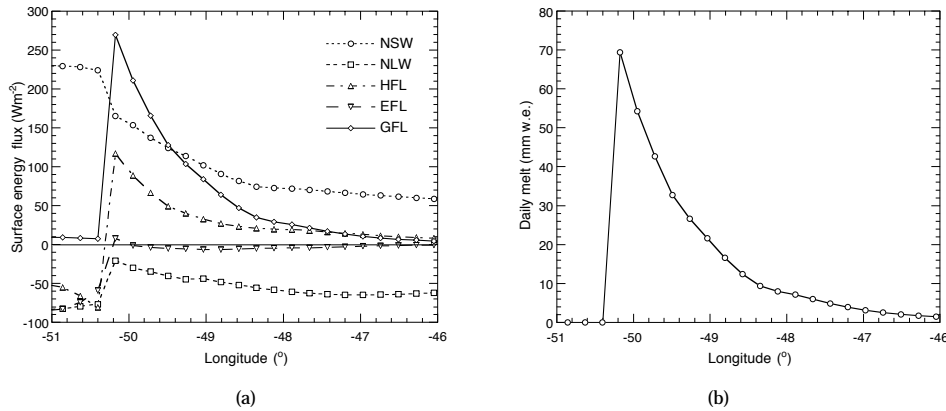


Figure 6.14: (a) Average surface energy flux components over the defined ablation region for the 10 km resolution reference run (Section 6.4.1) along the K-transect. *NSW* is the net shortwave radiation, *NLW* the net longwave radiation, *HFL* the turbulent sensible heat flux, *EFL* the turbulent latent heat flux and *GFL* the total net surface heat flux. (b) Calculated daily melt for the 10 km resolution reference run along the K-transect.

lope due to the advection of drier air from higher elevations.

The total surface energy balance, *GFL*, represents the average daily energy available for melt of the ice and snow pack, shown in Figure 6.14b along the K-transect. In regions where *GFL* approaches zero, as on the tundra and at higher elevations on the ice sheet, little or no melt takes place.

6.4.1 Model resolution

The horizontal and vertical resolution of the model is varied in order to access model sensitivity to resolution. In these tests horizontal resolutions of 40 and 10 km, com-

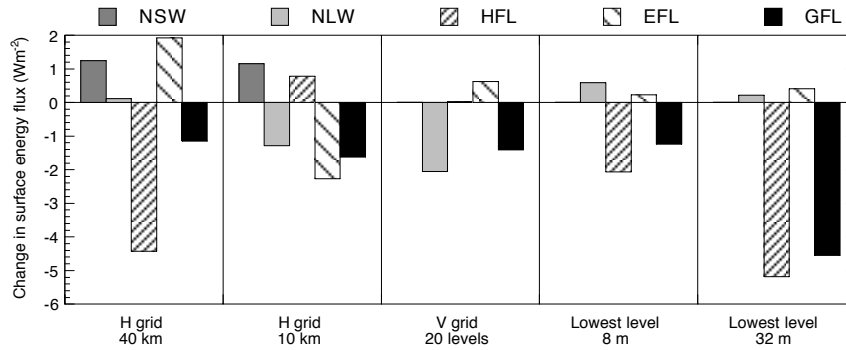


Figure 6.15: Difference between the average surface energy flux components over the defined ablation region for the various model resolution sensitivity runs compared to the reference run. **H grid** indicates horizontal grid resolution, **V grid** the number of vertical levels and **lowest level** the lowest model grid level above the surface. **NSW** is the net shortwave radiation, **NLW** the net longwave radiation, **HFL** the turbulent sensible heat flux, **EFL** the turbulent latent heat flux and **GFL** the total surface energy flux.

pared to the reference resolution of 20 km, are used. The number of vertical levels in the model is also increased from 10 to 20 and the height of the lowest vertical level is varied from 2 to 8 and 32 m. The results are summarised in Figure 6.15 where the difference between the reference run, Figure 6.13, and the sensitivity runs are shown. Small changes in the NSW radiation are seen in the two horizontal resolution runs as a result of changes in the sampling area.

The largest differences occur in the turbulent flux components where the magnitude of both turbulent fluxes increases with increasing resolution. With a horizontal resolution of 40 km HFL decreases by almost 20% compared to the reference run. With 10 km resolution the increase is just 3%. The latent heat flux, small compared to the sensible heat flux, alters in both cases by a factor of 50%. In total GFL changes by less than 3% for both horizontal resolutions.

Increasing the horizontal resolution is expected to lead to increasing magnitudes in the turbulent heat fluxes. This is because the ice sheet margin, where turbulent heat fluxes are largest, is better resolved. The improved resolution near the ice margin has a distinct effect on the wind speed. Since katabatic forcing is the dominant driving force in these regions the ability to resolve surface slope is an important factor in modelling wind speeds. This can be seen in Figure 6.16a where the 2 m wind speed and surface slope is shown for the three different horizontal resolutions. In Figure 6.16b the sensible heat fluxes for the three different horizontal resolutions are also shown. As can be seen the wind speed and sensible heat flux near the ice margin is significantly less with the 40 km grid, corresponding to more poorly resolved slopes in this area.

Increasing the vertical resolution of the model from 10 to 20 levels has a very limited effect on the results. The major contribution comes from a change in incoming longwave radiation which results from a shift in model levels and thus a change in the height at which clouds are introduced in the model.

Increasing the lowest model level from 2 m to 32 m has an interesting effect on

HFL. In Figure 6.16 it can be seen that HFL is only affected near the ice margin. In this region the height of the wind speed maximum decreases to around 70 m as slope and katabatic forcing increase. Since the second model level is also at this height, when the lowest level is at 32 m, it becomes impossible for the model to resolve the structure of the boundary layer and the bulk method used to calculate the turbulent heat fluxes at the surface will no longer be valid.

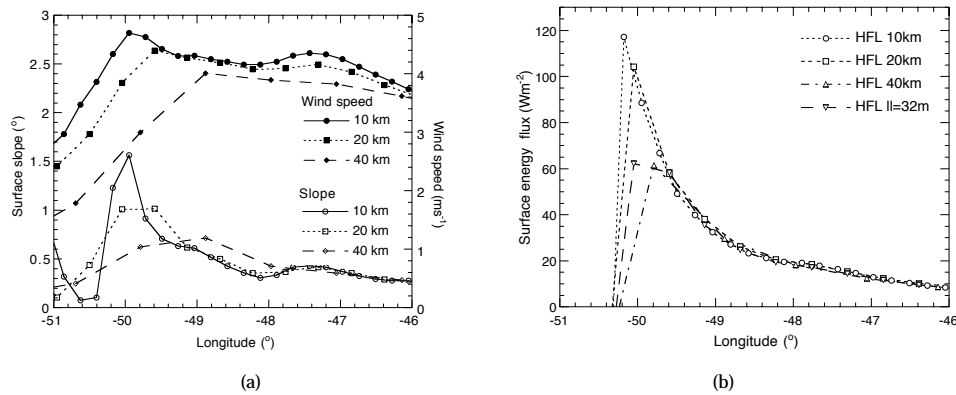


Figure 6.16: (a) Model surface slope and simulated wind speeds for the 3 different horizontal model resolutions (b) Calculated sensible turbulent heat flux (HFL) for the three different horizontal resolutions and with a lowest model level (ll) of 32 m. Results are shown for the K-transect where the ice margin is at a longitude of 50.25°.

6.4.2 Albedo parameterisation

As already shown in Figure 6.13 the major contributor to melt on the Greenland ice sheet is the shortwave radiation flux. Since albedo is prescribed in the model it is important to know how sensitive the other surface energy fluxes are to changes in surface albedo.

In Figure 6.17 the change in surface energy fluxes are shown for three different ice albedo scenarios. In the first two, the slush-line albedo is altered by +0.1 and -0.1, limited by the maximum value of 0.85. In the third case, surface albedo is set to its lowest ice value up to a height corresponding to the annual isotherm of -13 °C, see Section 6.2.6.2, to imitate the dark zone found on the West Greenland ablation zone. The three different albedo scenarios are shown as a function of longitude along the K-transect in Figure 6.18.

Clearly the NSW radiation is strongly affected by the change in albedo however the other fluxes are not sensitive to this change. Since the surface temperature is limited by the melting point in areas where ablation already occurs, the ABL will not be affected by changes in albedo.

Also shown in Figure 6.17 are three different tundra albedo scenarios. In the first two, which have little effect on the surface energy flux in the ablation zone, the tundra albedo is altered by ± 0.1 . In the third the effect of a warm tundra is

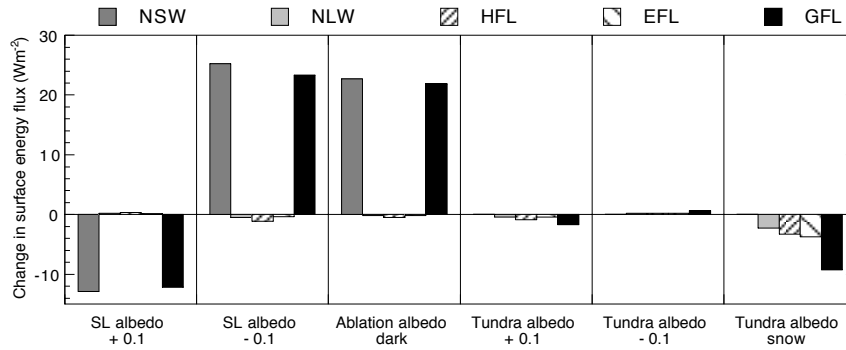


Figure 6.17: As in Figure 6.15 but showing the differences between the average surface energy flux components of six differing albedo scenarios compared to the reference run. **SL albedo** refers to changes in the slush line albedo described in the text, **Ablation albedo dark** to the dark zone simulation and **Tundra albedo** to changes in tundra albedo.

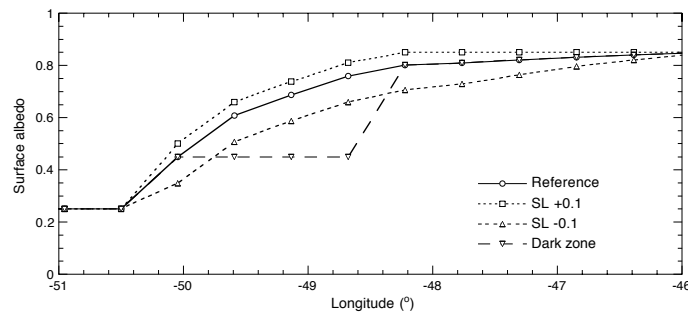


Figure 6.18: The four different ice sheet albedo scenarios used in the model sensitivity runs shown along the K-transect. See text for details.

removed by applying a snow albedo to the tundra region. Gallée *et al.* (1995) carried out a similar sensitivity experiment with a 2-D model along the K-transect by setting the tundra temperature to water but found little influence on the ice sheet energy balance. In this model both wind speeds and temperatures near the ice margin are reduced by the existence of a cool tundra since the land-ice circulation is removed.

6.4.3 Surface roughness

One of the prescribed surface parameters necessary to calculate turbulent heat fluxes at the surface are the roughness lengths for momentum, temperature and water vapour. Roughness lengths on the Greenland ice sheet are generally unknown and so the parameterisation used here makes the simple assumption that momentum roughness lengths increase from smooth snow covered areas to rough ice areas near the margin. Measurements made during GIMEX indicate large variations in roughness lengths (Duynkerke and van den Broeke, 1994) however these are quite locally

determined and are not likely to be representative of the region as a whole.

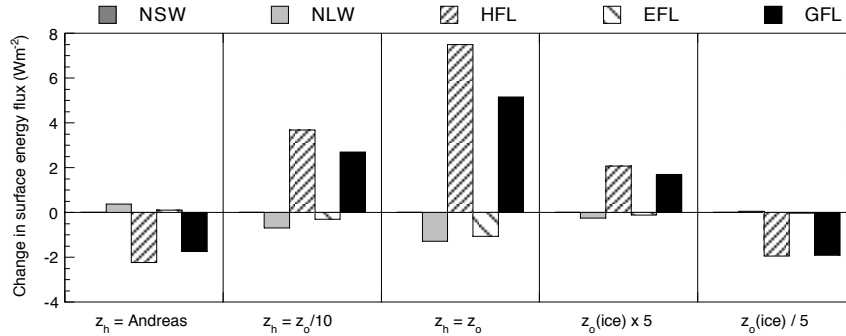


Figure 6.19: As in Figure 6.15 but showing the differences between the average surface energy flux components for three different temperature roughness length formulations and two different ice momentum roughness lengths compared to the reference run. See text for details.

The model sensitivity to changes in momentum roughness length and scalar roughness length formulations is tested in this section. Firstly, the maximum roughness length of ice near the margin is altered by a factor of five from the reference value of 5 cm to 1 and 25 cm whilst retaining the modified formulation suggested by Smeets and Vugts (2000) for the scalar roughness lengths. Secondly, the momentum roughness lengths are kept at their reference values and the scalar roughness length formulation is altered. Three different formulations are used: The unmodified form from Andreas (1987), a typical form used by other authors such as Gallée *et al.* (1995) where $z_{h,q} = z_o/10$ and the extreme case where $z_{h,q} = z_o$.

The results for these runs are shown in Figure 6.19. The turbulent heat fluxes are mildly sensitive to changes in momentum roughness length, changing on average by approximately 10% in the ablation region. Close to the ice margin this difference can be up to 20%. This is shown in Figure 6.20b where the sensible heat flux is set out along the K-transect for the six different roughness length runs. Wind speeds are also sensitive to changes in momentum roughness length, altering by $\pm 1 \text{ ms}^{-1}$ near the margin for corresponding decreases/increases in roughness length.

Turbulent heat fluxes are more sensitive to the different formulations used to prescribe the scalar roughness lengths, particularly in the extreme case of $z_{h,q} = z_o$, where an average increase of 27% in HFL is found. Maximum increases in HFL of more than 50% occur near the ice margin when using this formulation.

It is worth noting that turbulent fluxes are not as sensitive to changes in roughness lengths as Equation 6.15 would imply. For instance, use of the unmodified Andreas formulation (Equation 6.25) for surface roughness leads to a decrease in $\ln(z_h)$ by a factor of 60% near the ice margin, however the simulated sensible heat flux in this region only decreases by 20%. Because decreasing turbulent heat exchange will also decrease the amount of cooling in the ABL above the surface, temperatures will be higher for smaller temperature roughness lengths. This compensates to a large degree for the decreased turbulent exchange which results from the smaller temper-

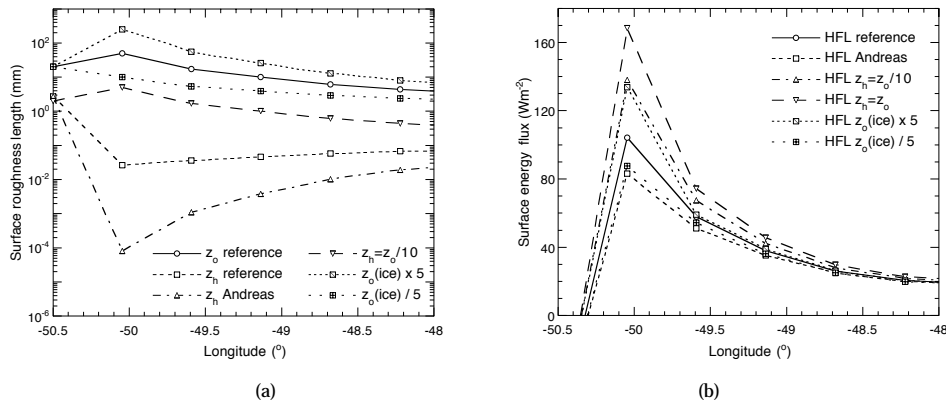


Figure 6.20: (a) Prescribed surface roughness lengths for the roughness length sensitivity tests described in the text (b) Calculated sensible turbulent heat flux (HFL) for the 6 different roughness length sensitivity tests. Results are shown along the K-transect.

ature roughness lengths. The consequence is that 2 m temperatures calculated with the model are more dependent on surface roughness formulations for temperature, than are the turbulent heat fluxes themselves.

Similar sensitivity runs were carried out by van den Broeke (1997a) using a bulk model along the K-transect with similar results. However, in his model the temperature roughness length was calculated using the unmodified formulation from Andreas and as a result turbulent heat fluxes decreased with increasing momentum roughness length.

6.4.4 Subsurface parameterisation

The model sensitivity to the subsurface parameterisations is also tested (Figure 6.21). In two runs the initial subsurface temperatures are varied by $\pm 2^\circ C$. The model is quite insensitive to the initial soil and snow temperatures, with a change in total surface flux of less than 1%.

In two other runs the subsurface parameters of density, thermal conductivity and specific heat over the entire ice sheet are set to either the snow values or the ice values listed in Table 6.1. When the entire ice sheet takes on the thermal properties of an ice surface, temperatures decrease and so turbulent fluxes will increase in magnitude. This is because the thermal diffusivity of ice is roughly twice as large as that for snow so temperature is conducted more efficiently into the surface, reducing the surface temperature. Since most of the non-melt region where surface temperatures depend on the energy balance is prescribed as snow, setting the subsurface parameters to their snow values has little effect.

6.4.5 Turbulence parameterisations

The turbulent closure scheme used in the model (Denby, 1999) was developed chiefly for use under stable conditions and in katabatic flows. It is interesting to

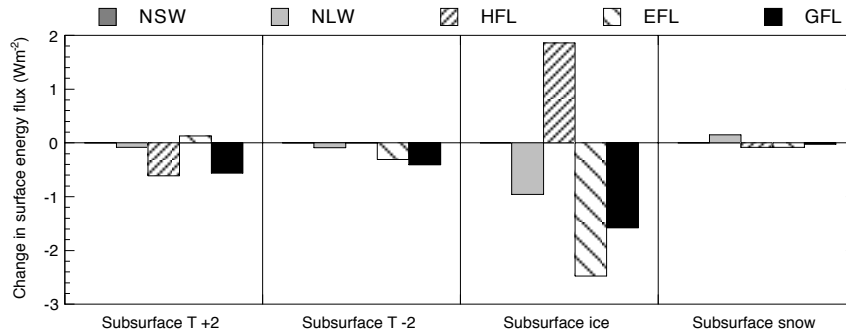


Figure 6.21: As in Figure 6.15 but showing the differences between the average surface energy flux components for four different subsurface sensitivity tests compared to the reference run. See text for details.

look at the effect that variations in the closure assumptions will have on the energy balance. Six of these sensitivity tests are listed in Figure 6.22 where three constants, the near surface Prandtl number Pr , the turbulent transport coefficient c_s and the turbulent length scale parameter C_B are altered from their reference value, see Appendix 6.A.

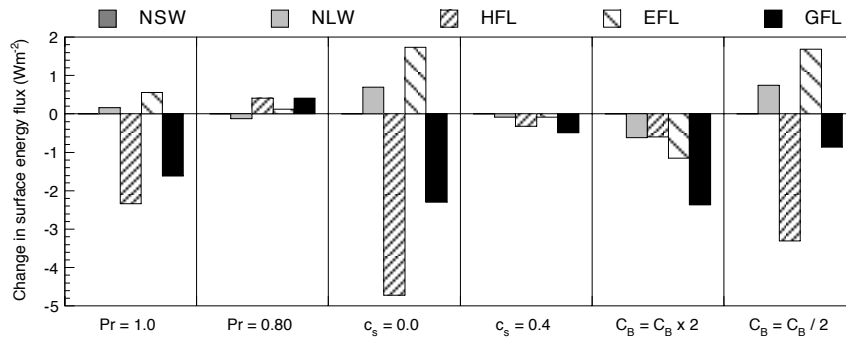


Figure 6.22: As in Figure 6.15 but showing the differences between the average surface energy flux components for six different turbulent parameterisation sensitivity tests compared to the reference run. See text for details.

Increasing the turbulent Prandtl number from the reference value of 0.92 to 1.0 has a similar effect to a decrease in temperature roughness length since Pr defines the turbulent exchange at the surface (Equation 6.15) as well as within the boundary layer itself. This results in a decrease in magnitude for HFL and GFL of 10% and 2.5% respectively. Decreasing the Prandtl number to a value of 0.8 has little effect.

Setting the turbulent transport coefficient c_s to zero is equivalent to the removal of the transport term in the TKE budget, Equation 6.A.2. The reduction in turbulent heat fluxes is significant (20%) and is the result of boundary layer thinning, reducing

the transport of heat and water vapour towards the surface. Doubling this coefficient has little effect on the boundary layer in general. This reflects the results previously found in Denby (1999).

The turbulent length scale l used in the model under stable conditions is asymptotically limited, Equation 6.A.7, by the buoyant length scale l_b which is determined using Equation 6.A.8. In this sensitivity run C_B is varied by a factor of two, doubling and halving the buoyant length scale. As a result, the turbulent length scale in the ABL is also changed by roughly this amount since l_b is the limiting length scale throughout most of the stable boundary layer. The most significant change in the turbulent heat fluxes occurs when C_B is halved, reducing the depth of the boundary layer and decreasing the magnitude of the turbulent fluxes at the surface.

6.4.6 Dynamics

The dynamic equations governing the boundary layer model (Equations 6.3, 6.4, 6.10 and 6.11) determine the budgets for momentum, temperature and water vapour in the ABL. In this section some of the terms in the dynamic equations are omitted in order to gauge their importance in determining surface energy fluxes. Results from these sensitivity tests are shown in Figure 6.23.

Two terms in the thermodynamic equation are removed independently, namely longwave radiative cooling and advection of the perturbation potential temperature (Θ). Other terms such as ambient temperature advection and turbulent flux divergence are too important to be omitted from the equations in this fashion.

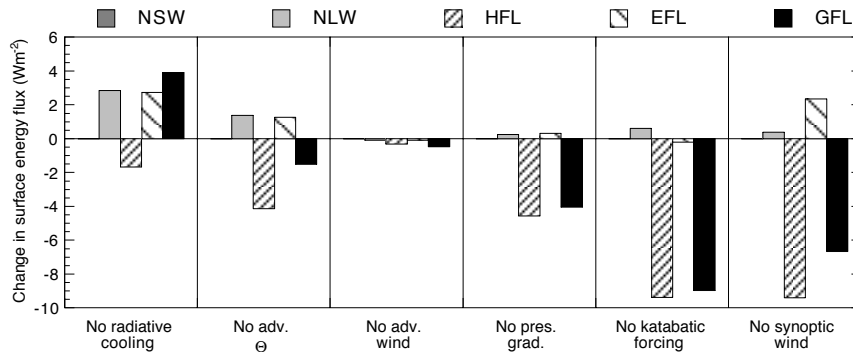


Figure 6.23: As in Figure 6.15 but showing the differences between the average surface energy flux components for omissions of various terms in the dynamic equations compared to the reference run. See text for details.

When radiative cooling is omitted the boundary layer warms slightly, causing an increase in NLW radiation at the surface. Since the ABL is slightly warmer, $0.5\text{ }^{\circ}\text{C}$ on average over the ablation region at 2 m, katabatic forcing will decrease and wind speeds will lessen. The net effect is a slight reduction in HFL. The decrease in wind speeds also affects water vapour content in the ABL and thus EFL. The specific humidity budget is a balance between advection and flux divergence, Equation 6.11.

Any decrease in wind speeds will reduce the advection of drier upslope air down to the ablation zone which will in turn increase the water vapour content of the boundary layer, thus reducing evaporation at the surface.

The perturbation temperature advection term has a complex effect. In general, this term is smaller than the advection of ambient temperature (Θ_o) and can vary in sign depending on the local conditions. Near the margin, advection of warm air over the ice sheet from the tundra will warm the ABL but because temperature inversion strengths are higher upslope this term can also cool the ABL. The net effect of its omission is a cooling of the ABL near the margin, leading to a decrease in HFL.

Also shown in Figure 6.23 are the results of omissions in the momentum budget. The advection of momentum is not an important term for the average surface energy budget. To a larger degree the horizontal pressure gradient, or thermal wind, does affect the turbulent heat fluxes. This is due to changes in circulation at the ice margin where thermal wind effects are strongest, resulting from the temperature gradient at the tundra/ice interface and the horizontal temperature gradient on the ice sheet itself.

The largest influence however, on the turbulent heat fluxes, is the effect of katabatic forcing and synoptic pressure gradients. Both these terms are essential in determining wind speeds on the ice sheet and hence turbulent fluxes.

6.4.7 Input fields

As a final sensitivity test the input fields of temperature, humidity, total cloud cover and sea surface temperature taken from ECMWF re-analysis data are altered to gauge the model sensitivity to these quantities. Though variation of these quantities can be seen as a form of climate sensitivity test, which will be discussed in more detail in Chapter 7, we are primarily interested at this point in a comparison with the other sensitivity tests described in the previous sections.

The results are shown in Figure 6.24. Changes in ambient atmospheric temperatures of ± 1 K have a direct effect on all three atmospheric components of the energy balance and the total change in surface energy flux is 16%.

Increasing total cloud cover (TCC) by 0.1 leads to a slight decrease in NSW via the parameterisation used in the model, Equation 6.20, and a large increase in downward radiative flux. This subsequently warms the ice and snow pack resulting in increased surface temperatures, a weakened temperature inversion and thus a decrease in turbulent heat flux. The resulting surface heat flux (GFL) increase is slightly less than that for a 1 K increase in atmospheric temperature. The opposite argument is true for a reduction in TCC.

Normally cloud height is fixed at an elevation of around 3500 m a.s.l.. As an alternative formulation the cloud base is set to 1500 m above the surface everywhere. The model is quite insensitive to this change.

The initial relative humidity field is altered by $\pm 20\%$. Once more the model is fairly insensitive to this value resulting in slight changes in the downward radiation flux and hence NLW radiation. Latent heat fluxes vary by up to 50% but still remain small.

Lastly, the sea surface temperature (SST) is set overall to 0 °C. This has little effect on the energy budget of the ice sheet indicating that advection of air from the sea

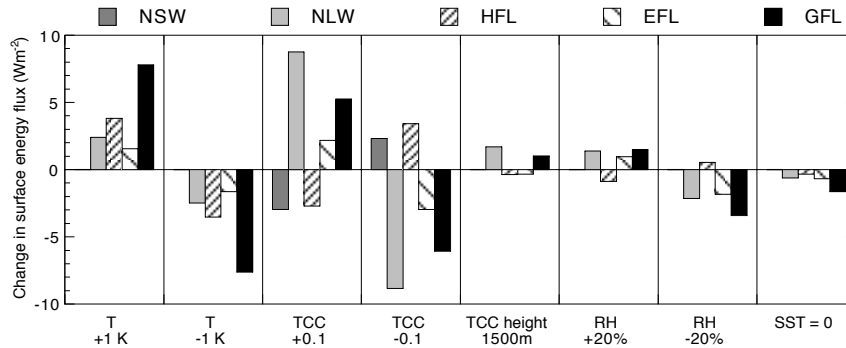


Figure 6.24: As in Figure 6.15 but showing the differences between the average surface energy flux components, for changes in the various input fields, when compared to the reference run. *T* indicates changes in temperature, *TCC* total cloud cover, *RH* relative humidity and *SST* sea surface temperature. See text for details.

onto the ice sheet is not an important factor. This is primarily due to the local forcing by ECMWF temperature fields used in the model.

6.5 Discussion

The aim of this study is to verify and test a boundary layer model of the Greenland ice sheet with particular emphasis on the model's ability to correctly represent the surface energy balance components associated with the atmospheric boundary layer, principally the turbulent heat fluxes and secondly the longwave radiation flux. The model is tested in two ways, firstly by comparison with observations during a 20 day summer period and secondly by testing the sensitivity of the model to its internal parameterisations.

No attempt is made to model surface albedo in spite of its importance in the energy budget of the ice sheet. Instead this is prescribed as a function of surface temperature and the sensitivity of the model is tested to variations in this albedo scheme. For the scenarios tested here, albedo has a very small influence on the ABL in regions where surfaces are already melting.

Though turbulent fluxes were not measured directly during the observational period it is assumed that if the model can reproduce faithfully the near surface variables of wind, temperature and specific humidity then it will also be able to reproduce the turbulent fluxes. Given the limited observational data available, the model does seem to be able to reproduce these variables when forced by ECMWF re-analysis data.

It is worth summarising the most important aspects of the model in regard to the sensitivity of the energy budget components. In Figure 6.25 the various sensitivity studies carried out in Section 6.4 are sorted in decreasing order of sensitivity to the sum of the three non-shortwave energy budget components, i.e. net longwave radiation, sensible heat flux and latent heat flux. The sensitivity of each of these three components, in absolute terms, is shown in each column. Though the absolute mag-

nitude of each of these sensitivity tests is to some extent arbitrarily determined by the type and size of the perturbation applied, Figure 6.25 does give an overall indication of the importance of the various parameterisations, dynamic terms and input fields.

Perhaps surprisingly the model is most strongly influenced by the warm tundra. Each of the three energy components are negatively affected when the tundra albedo is set to that of snow. Though this scenario is unrealistic for a summer period it does indicate that any modelling attempt should include the thermal and circulatory influence of a warm tundra.

Dynamics are of great importance when modelling the atmospheric boundary layer. Both synoptic forcing and katabatic forcing appear to be of equal importance when determining the turbulent heat fluxes and as such need to be accounted for properly in the simulations. Radiative cooling of the boundary layer also has a significant influence on ABL temperature and subsequently on the turbulent and long-wave radiation fluxes.

The parameterisation for surface roughness length, particularly for temperature, is also a significant contributor to uncertainty in the turbulent sensible heat flux. This is slightly unfortunate since there is still some uncertainty in the correct relationship between scalar roughness lengths and momentum roughness lengths. The formulation used here, the modified version from Andreas (Smeets and Vugts, 2000), is possibly the best estimate available. The extreme case where $z_h = z_o$ is not a reasonable estimate for z_h . The reality most likely lies somewhere between the unmodified Andreas formulation and the estimate $z_h = z_o/10$. Well determined roughness lengths for momentum unfortunately do not exist for the ablation region of the Greenland ice sheet. The range used here in the sensitivity runs is indicative of the uncertainty in this parameter. In this regard it is encouraging that the sensitivity of the turbulent heat fluxes to z_o is only of the order of 10%.

The model sensitivity to vertical resolution shows that it is necessary to resolve the vertical structure of the ABL to sufficient accuracy, at least to be able to resolve the boundary layer up to the height of the wind speed maximum. This requires lowest grid levels of less than 15 m under most conditions. Even so, increasing the height of the lowest level in the model from 2 to 8 m results in a reduction of turbulent heat fluxes by a factor of 10%.

As for horizontal resolution, intuition suggests that improved horizontal resolution, particularly near the ice margin, will lead to improved estimates in turbulent fluxes. In the three resolutions tested here the increase in sensible heat flux from 40 to 20 km is approximately 20%. From 20 to 10 km this is only 3% indicating that the asymptotic limit for improving sensible heat flux estimates has almost been reached at 20 km resolution. The decrease in latent heat flux shows no such asymptotic trend. In both reductions of resolution the latent heat flux decreases by 50% though it still remains small, approximately 14% of the sensible heat flux. This is why both the 10 and 40 km resolution models give lower estimates of the total turbulent heat flux. All in all it would appear that a 20 km resolution model of 10 levels has sufficient resolution to determine the turbulent heat fluxes to the necessary degree of accuracy.

Of the three turbulent closure parameters tested, turbulent heat fluxes are most sensitive to the turbulent transport closure. When there is no transport of TKE then turbulent transfer of heat and water vapour through the boundary layer is reduced.

It is thus recommended that ABL modelling of the stable boundary layer include this transport term.

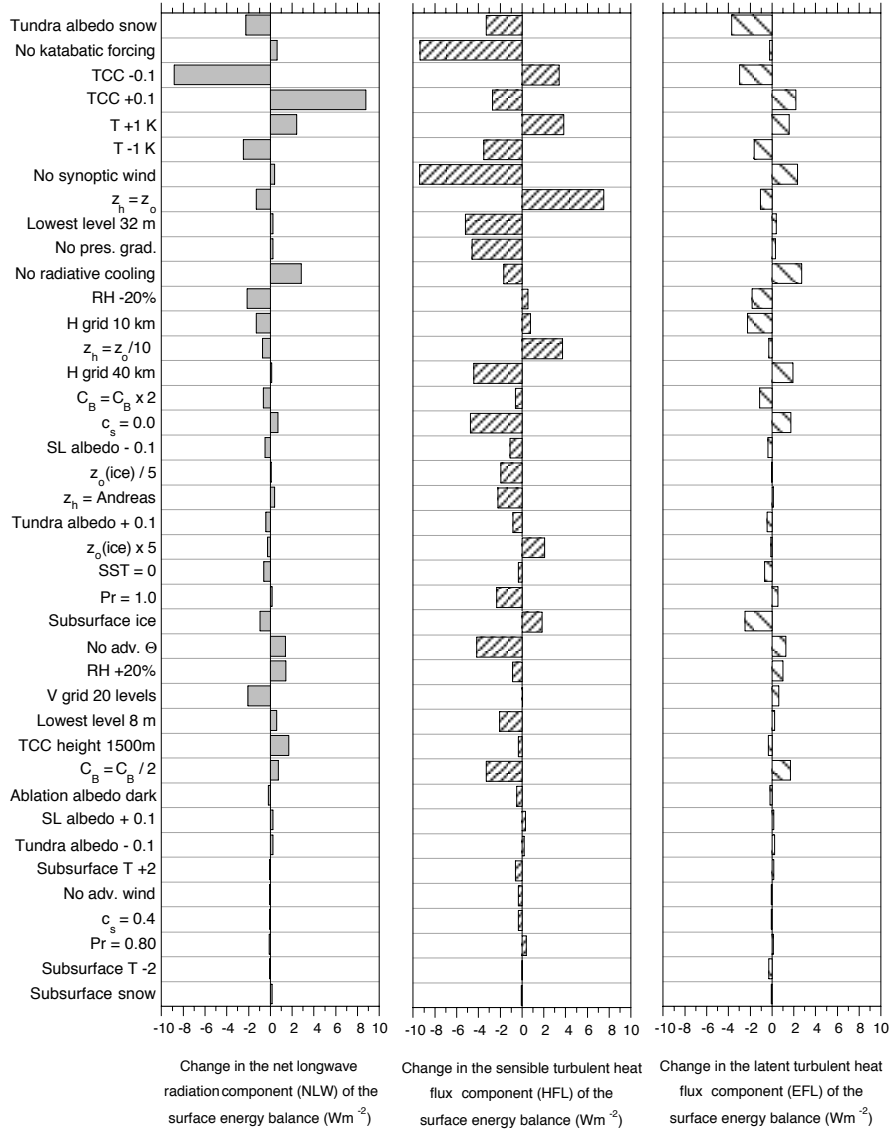


Figure 6.25: Change in net longwave radiation (NLW), and turbulent sensible (HFL) and latent (EFL) heat fluxes arealy averaged over the defined ablation region for all the sensitivity studies carried out in Section 6.4. These are sorted in decreasing order of sensitivity to the sum of the three components (NLW+HFL+EFL). Values are given in Wm^{-2} .

Appendix

6.A Turbulence scheme

The two prognostic equations used to describe the model turbulence are E , turbulent kinetic energy, and $\overline{w\overline{w}}$ the vertical momentum variance.

$$\frac{dE}{dt} = MP_E + BP_E - \epsilon + J_{zz} \frac{\partial}{\partial \tilde{z}} \left(c_s \frac{E}{\epsilon} \overline{w\overline{w}} J_{zz} \frac{\partial E}{\partial \tilde{z}} \right) \quad (6.A.1)$$

$$\begin{aligned} \frac{d\overline{w\overline{w}}}{dt} &= \frac{2}{3} c_2 (1 - 2c_2' F) MP_E + 2 \left(1 - \frac{2}{3} c_3 \right) BP_E - \frac{2}{3} (1 - c_1) \epsilon \\ &\quad - \frac{\overline{w\overline{w}}}{E} (c_1 + 2c_1' F) \epsilon + J_{zz} \frac{\partial}{\partial \tilde{z}} \left(3c_s \frac{E}{\epsilon} \overline{w\overline{w}} J_{zz} \frac{\partial \overline{w\overline{w}}}{\partial \tilde{z}} \right) \end{aligned} \quad (6.A.2)$$

where

$$MP_E = -J_{zz} \left(\overline{uw} \frac{\partial U}{\partial \tilde{z}} + \overline{vw} \frac{\partial V}{\partial \tilde{z}} \right) \quad (6.A.3)$$

$$BP_E = \frac{g}{\Theta_o} \overline{w\theta} \quad (6.A.4)$$

$$\epsilon = c_\epsilon \frac{E^{3/2}}{l} \quad (6.A.5)$$

$$\frac{1}{l^2} = \frac{1}{(\kappa z)^2} + \frac{1}{l_a^2} \quad (6.A.6)$$

$$F = \frac{l}{\kappa z} \quad (6.A.7)$$

The asymptotic length scale l_a is equal to the buoyant length scale l_b under stable conditions as follows

$$l_b = \kappa C_B \left(\frac{\overline{w^2}}{N^2} \right)^{1/2} \quad (6.A.8)$$

where N is the Brunt Väisällä frequency and C_B a constant. Under unstable conditions it is given by the boundary layer length scale proposed by Mellor and Yamada (1974)

$$l_a = 0.2 \frac{\int_0^{z_d} z E dz}{\int_0^{z_d} E dz} \quad (6.A.9)$$

where z_d is the height of the model domain.

Using these equations and the second-order closure scheme derived in Denby (1999) the vertical turbulent diffusion coefficients K_Φ , which relate vertical fluxes to their mean gradients via

$$K_\Phi = -\frac{1}{\overline{w\Phi}} \frac{\partial \Phi}{\partial z} \quad (6.A.10)$$

are calculated in the following way

$$K_{m,h,q} = C_{m,h,q} \frac{E^{1/2} l}{c_\epsilon} \quad (6.A.11)$$

The coefficients $C_{m,h,q}$ are dependent on stability and are given as follows:

$$C_m = \frac{A_7 \overline{w\overline{w}}/E - A_8(1 - d_2)/d_1 N_R C_h}{1 + A_8/d_1 N_R} \quad (6.A.12)$$

$$C_h = \frac{\overline{w\overline{w}}/E}{d_1 + d'_1 F + A_9 N_R} \quad (6.A.13)$$

$$C_q = \frac{\overline{w\overline{w}}/E - 0.5 A_9 N_R C_h}{d_1 + d'_1 F + 0.5 A_9 N_R} \quad (6.A.14)$$

where

$$N_R = \frac{g}{\Theta_o} \frac{l^2}{E c_\epsilon^2} \frac{\partial \overline{\Theta}}{\partial z} \quad (6.A.15)$$

$$A_7 = \frac{1 - c_2 + 1.5 c_2 c'_2 F}{c_1 + 1.5 c'_1 F} \quad (6.A.16)$$

$$A_8 = \frac{1 - c_3}{c_1 + 1.5 c'_1 F} \quad (6.A.17)$$

$$A_9 = \frac{1 - d_3}{d_\epsilon} \quad (6.A.18)$$

For a complete description of the constants and the derivation of the equations mentioned in this section see Denby (1999).

Simulating the Greenland Atmospheric Boundary Layer: Energy Balance and Climate Sensitivity

A three-dimensional boundary layer model, with a horizontal resolution of 20 km, is used to simulate the 1998 summer ablation season of the Greenland ice sheet. The model is forced by the ECMWF analysis data fields of synoptic pressure, free atmospheric temperature, cloud cover, humidity and sea surface temperature. Results from the simulation are compared with six automatic weather stations on the ice sheet and with ECMWF 2 m temperature and wind data. The simulations indicate that the increased spatial resolution of the boundary layer model improves estimates of near surface meteorological quantities and surface energy fluxes near the margin of the ice sheet where surface melt takes place. The sensitivity of the surface energy balance to a 2 K increase in free atmospheric temperature is also investigated. It is found that the increase in turbulent heat flux accounts for 41% of the total increase in melt in the ablation region, net longwave radiation for 17% and the albedo feedback mechanism for 42%. Parameterisations based on free atmospheric temperature and suitable for use in energy balance models are developed for the turbulent heat and incoming longwave radiation fluxes.

7.1 Introduction

In the previous chapter the Greenland atmospheric boundary layer model (GABLM) is described and tested for a 20 day period in 1991. In this Chapter the model is used to calculate the energy budget for the entire Greenland ice sheet during the summer ablation season of 1998. The aim of this experiment is to determine the energy budget of the ice sheet and the spatial dependency of that budget. In particular the sensible and latent heat fluxes in the ablation region of the ice sheet are investigated. In so doing the dynamics of the flow are discussed and a comparison made with observations at six different sites on the ice sheet, three in the ablation zone and three in the accumulation zone.

In addition, the climate sensitivity of the model to a change in free atmospheric temperature is investigated by increasing the input temperature field by 2 K and re-running the model. The sensitivity of 2 m temperature, wind and the surface energy budget is investigated and a simplified parameterisation for the turbulent heat fluxes and the incoming longwave radiation, based on free atmospheric temperatures, is suggested. This may be applied in energy balance models used for mass balance calculations and will avoid the use of 2 m temperatures, which are influenced by the thermal regime of the glacier, in calculating these energy flux components.

7.2 Model description and methodology

The model used for this study is described in detail in Chapter 6, though some changes have been made. These changes are in general minor except for the albedo parameterisation which now generates the albedo internally.

As stated in the previous chapter, the GABLM is a dynamic downscaling model that takes meteorological fields from an already existing model, in this case ECMWF analysis data, and forces an atmospheric boundary layer model with these fields. The prescribed fields used are:

1. Geopotential height at 700 hPa to determine geostrophic winds. These are assumed to be barotropic and thus constant with height.
2. Free atmospheric temperature specified as a linear function of height taken by fitting ECMWF data from above the boundary layer up to a height of approximately 4 km.
3. Relative humidity field taken from ECMWF data at a height of approximately 1200 m above the surface.
4. Cloud cover from ECMWF total cloud cover analysis. Low, medium or high cloud covers are not distinguished and cloud height is set at approximately 3500 m above the surface.
5. Monthly mean sea surface temperatures from ECMWF analysis.

With the exception of sea surface temperatures these fields are updated every 12 hours, 00 and 12 GMT, and linearly interpolated in time. The specific humidity field is prescribed only at the horizontal and top boundaries of the model whilst the free atmospheric temperature field and synoptic pressure gradient field is prescribed directly in the model field itself.

Attenuation of the incoming shortwave radiation by atmosphere and clouds is parameterised using schemes from van de Wal (1994) and Konzelmann *et al.* (1994) whilst an emissivity scheme from Garratt and Brost (1982) is used to calculate the longwave radiation. Subsurface temperatures are initialised on the basis of the 2 m temperature parameterisation from Ohmura (1987) and the subsurface temperature is calculated using a temperature diffusion model. Surface roughness lengths and subsurface parameters are also specified on the basis of the temperature parameterisation from Ohmura (1987). These parameterisation schemes and initialisations are described in detail in Chapter 6.

The boundary layer simulation is carried out using a 20 km horizontal grid resolution, chosen on the basis of sensitivity tests carried out in Chapter 6 and on computation convenience. 20 vertical layers, up to a maximum height of 5 km, are used with a lowest level height of 2 m. In the previous chapter, 10 vertical levels were deemed to be sufficient for calculating the surface energy fluxes. However, in this chapter we are also interested in the dynamics of the flow which are better represented with a 20 layer model. The number of vertical levels in the subsurface temperature diffusion model has been increased from 10 to 15 and the lowest level is placed at 10 m below the surface, with an upper level depth of 5 mm.

The year 1998 has been chosen for the current study because during this period several automatic weather stations (AWS) were operational on the ice sheet. These will be used for a comparative study in Section 7.3.2.

7.2.1 Albedo scheme

The most important change to the model is in the albedo scheme. In the previous study albedo was directly prescribed using a temperature based parameterisation because the duration of the simulation was just 20 days. Since the entire ablation season is now simulated albedo can be internally generated. This is done using a two layer snow model, with ice beneath, where the upper snow layer has an initial depth of zero and the lower layer a snow depth equal to 2/3 of the annual precipitation, taken from Ohmura and Reeh (1991). The top layer is a fresh snow layer where snow is deposited once every 6 days for 6 hours at a rate commensurate with the mean annual precipitation rate. The snow albedo is determined as a function of melt for both layers as follows

$$\alpha_{snow} = \alpha_{firn} + (\alpha_{f\ snow} - \alpha_{firn}) \exp\left(\frac{-M}{M^*}\right) \quad (7.1)$$

with the maximum value of fresh snow $\alpha_{f\ snow} = 0.85$, and of firn $\alpha_{firn} = 0.6$. M is the accumulated melt and M^* is a characteristic melt scale with a value of 600 mm w.e.. This equation describes the effect of metamorphosis in the snow pack and the associated change in albedo. Both snow layers are allowed to melt, the lower layer melting only once the top layer has disappeared.

As the depth of a snow layer decreases the transition from the overlaying layer with albedo α_1 and depth d_1 to the underlying ice or snow layer α_2 is described by the following equation

$$\alpha = \alpha_1 + (\alpha_2 - \alpha_1) \exp\left(\frac{-d_1}{d^*}\right) \quad (7.2)$$

which describes the patchiness of the snow cover (Oerlemans and Knap, 1998) and is parameterised so that surface albedo α varies exponentially with the depth of the snow layer d_1 . The characteristic snow depth d^* used in this model is 1.6 cm.

The background ice albedo is prescribed using a similar parameterisation to Zuo and Oerlemans (1996) which allows the ice albedo to increase towards and above the equilibrium line in the following way:

$$\alpha_{ice} = \frac{(\alpha_{min} + \alpha_{max})}{2} + \frac{(\alpha_{max} - \alpha_{min})}{\pi} \arctan\left[c_{ice}\left(\frac{h}{ELA} - 1\right)\right] \quad (7.3)$$

where $\alpha_{min} = 0.5$, $\alpha_{max} = \alpha_{firn}$, $c_{ice} = 10$, h is the elevation and ELA is the equilibrium line altitude taken from Reeh (1989) and parameterised as a function of latitude. The ELA in this parameterisation is held fixed during the simulation.

7.3 The 1998 simulation

The model is run using ECMWF input fields taken from the 1998 ECMWF analysis data starting on 20 May 1998, day 140, and ending on 28 August 1998, day 240. Hourly and daily means of model variables are saved for several positions on the ice sheet and tundra during the run. These correspond to positions of known observations and six of these sites, positioned on the ice sheet and shown in Figure 7.1, are used for a direct comparison with the model simulation.

Results from the model are shown as daily average means for a number of observational sites and also in terms of the summer seasonal mean. This is taken as the 90 day period starting on day 150 and finishing at the end of the model run, day 240, which allows a 10 day spin up period at the beginning of the simulation. The ice sheet is also divided into two regions for comparative studies. These two regions are chosen to be representative of the accumulation and ablation zones and are demarked by free atmospheric isotherms. The ablation region is defined as the region where the summer average surface-extrapolated free atmospheric temperature is greater than 2 °C and the accumulation, or plateau, region is defined by free atmospheric temperatures being lower than -2 °C. These regions correspond roughly to elevations of 1500 and 2400 m respectively.

7.3.1 General characteristics

The simulated summer average 2 m temperature field for the Greenland ice sheet is shown in Figure 7.2. Summer temperatures on the ice sheet plateau reach -10 °C whilst the maximum average temperature near the ice margin is around +7 °C. The average 2 m temperature lapse rate over the entire ice sheet is -5.0 K km⁻¹.

In Figure 7.2 the simulated summer average 2 m wind field and ECMWF 700 hPa pressure level height are also shown. A high pressure region can be seen above the

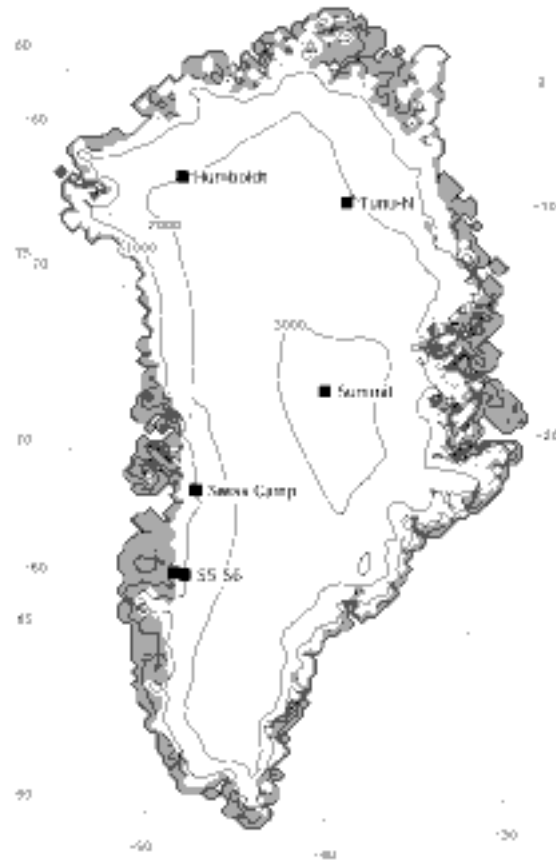


Figure 7.1: Positions of the 6 AWS sites used in the comparison. Elevation is shown in meters with contours separated by 500 m. The tundra is shown as the shaded region.

Greenland plateau as the result of atmospheric cooling above the ice sheet. This high pressure synoptic field introduces a general anticyclonic circulation which enhances the downslope katabatic forcing. Wind speeds can be seen to increase towards the ice margin and this is chiefly the result of increased katabatic forcing. However, wind speeds are also retarded by the prescribed surface roughness length, which increases towards the ice edge.

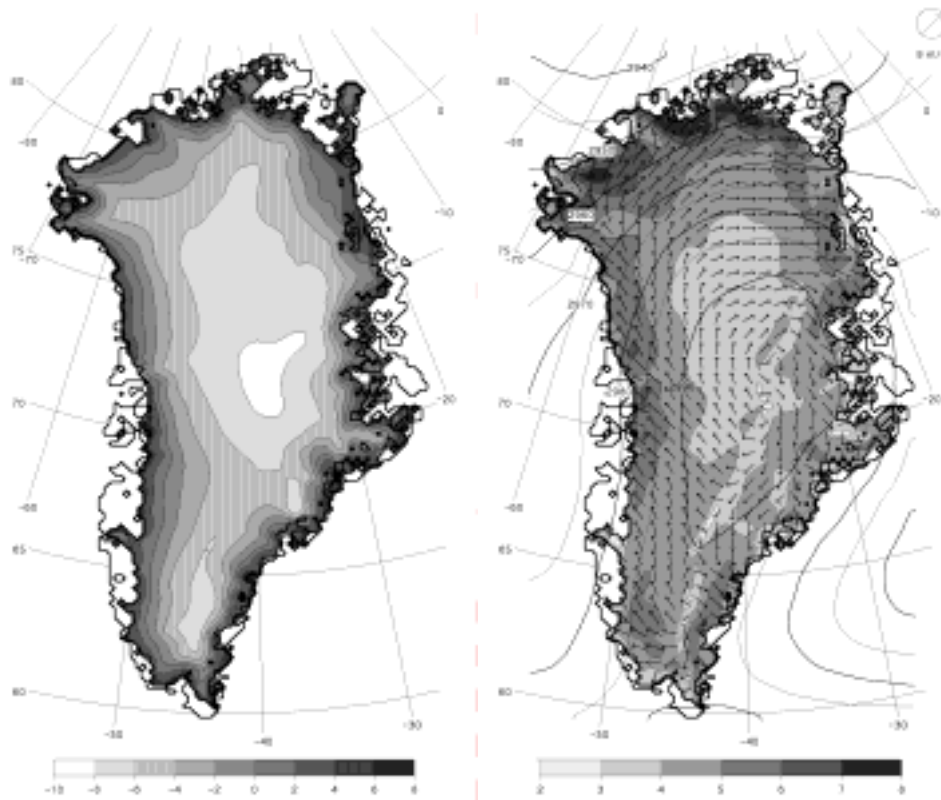


Figure 7.2: Left: Simulated average summer 2 m temperatures in $^{\circ}\text{C}$. Right: Simulated average summer 2 m wind and synoptic pressure fields over the Greenland ice sheet. The shading indicates the magnitude of the wind vector in ms^{-1} and the contours indicate the height, in meters, of the 700 hPa pressure level taken from ECMWF analysis data. Arrows showing wind vectors are placed at every third grid point.

7.3.2 Comparison with observations

A number of meteorological stations are available for a comparative study with the 1998 GABLM simulation. Six of these stations, positioned on the ice sheet (Table 7.1 and Figure 7.1), are selected for verification. Unfortunately only three of these stations are situated in the ablation region, S5 and S6 from the Utrecht University K-transect and Swiss Camp, now part of the PARCA network. The stations Humboldt, Tunu-N and Summit from the PARCA network in the accumulation zone are also used (Steffen *et al.*, 1996).

A comparison is made of 2 m daily average values for temperature, wind speed and specific humidity which are the three meteorological components important in defining turbulent fluxes. The results are shown in Figures 7.3 to 7.5 as a function of time. Included in the comparison are ECMWF analysis data of the same 2 m vari-

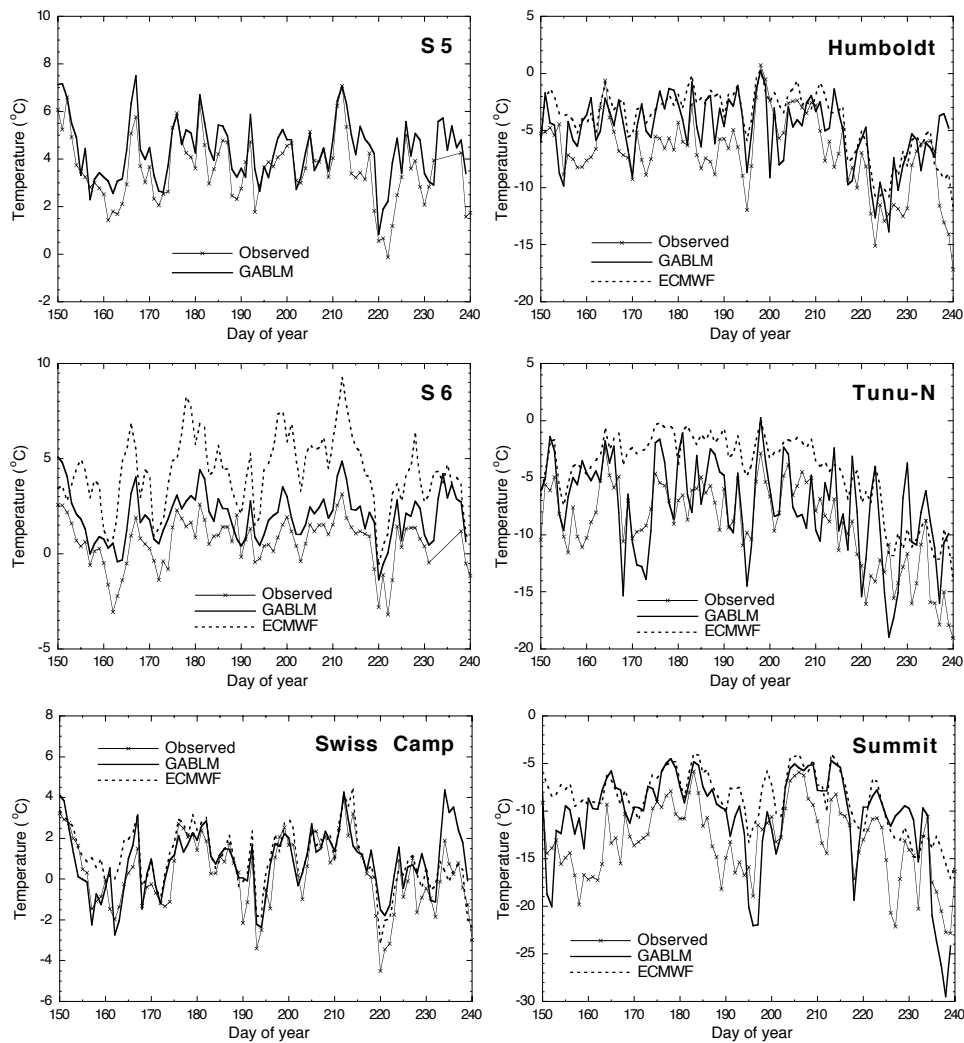


Figure 7.3: Observed, simulated (GABLM) and ECMWF analysis data for 2 m temperature from day 150 to 240. The positions of the six sites shown are listed in Table 7.1.

ables. ECMWF analysis data is produced with a spectral resolution of T213, roughly equivalent to a horizontal resolution of 70 km. Interpolated data can be obtained from ECMWF down to a resolution of 0.5° in both latitude and longitude. This means that interpolated data obtained near the ice margin may be a combination of both tundra and ice sheet points.

For the three ablation zone sites the boundary layer model reproduces quite well the observed daily average temperatures, as does the ECMWF analysis for Swiss Camp. In contrast, ECMWF analysis temperatures are far too high at site S6, on average 3.2°C . S6 is located a similar distance from the ice edge as Swiss Camp,

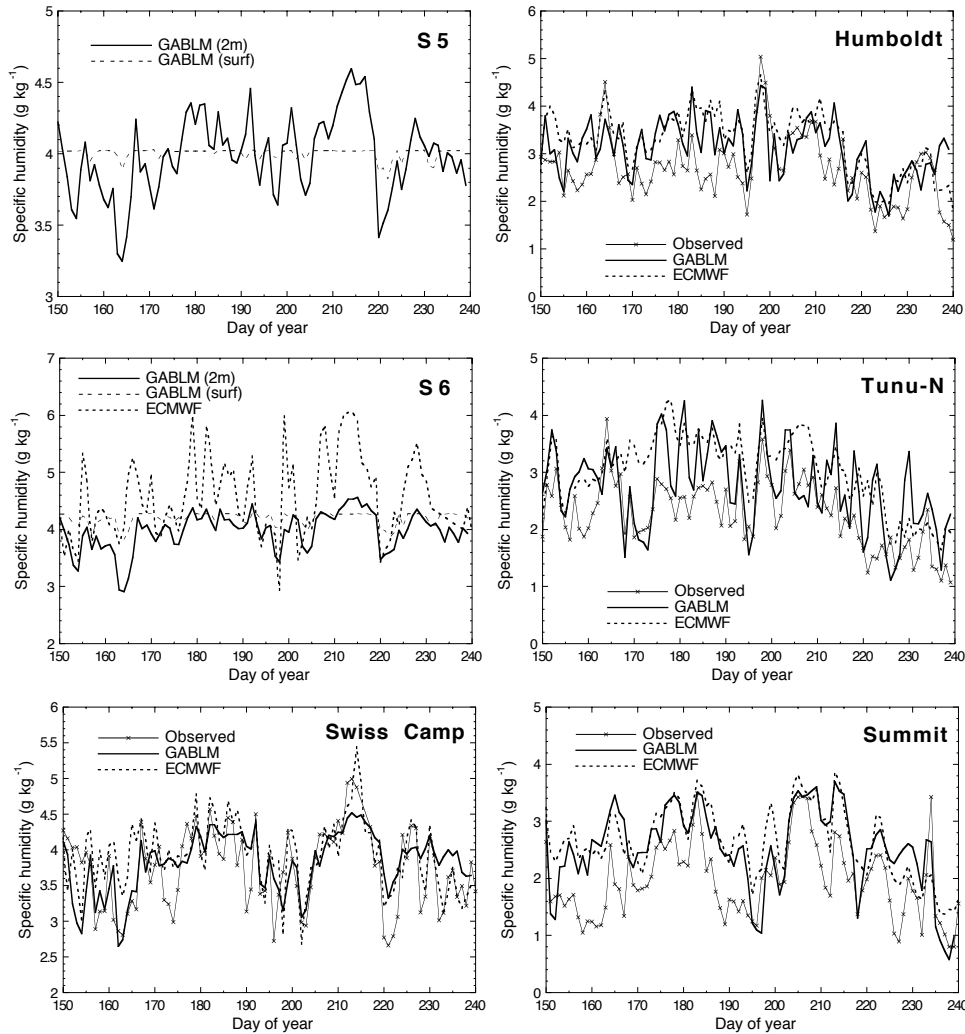


Figure 7.4: Observed, simulated (GABLM) and ECMWF analysis data for 2 m specific humidity from day 150 to 240. The positions of the six sites shown are listed in Table 7.1.

approximately 35 km, but in this case the interpolated data obtained from ECMWF consists of both ice sheet and tundra values. The nearest available ECMWF data point for S5 is situated on the tundra and so has not been used in the comparison.

Temperatures at the three accumulation sites are also reasonably well simulated during the summer period with GABLM though all sites are slightly too warm, the average temperature difference being from 1.5 to 2.5 °C. ECMWF analysis data also tends to be too warm at all these sites, by up to 4.4 °C, which is most likely due to the lower snow albedo value of 0.7 used in the ECMWF model.

Specific humidity will in general follow the same trend as temperature since the

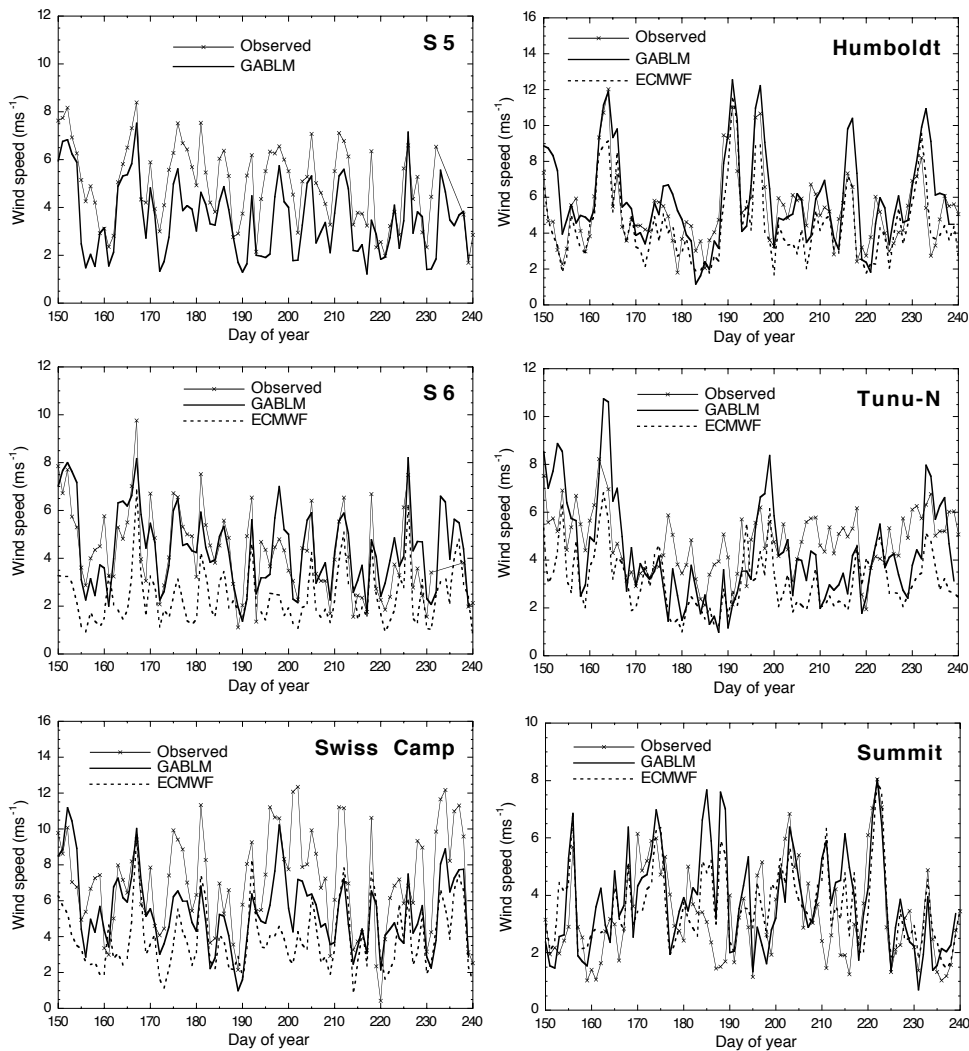


Figure 7.5: Observed, simulated (GABLM) and ECMWF analysis data for 2 m wind speed from day 150 to 240. The positions of the six sites shown are listed in Table 7.1.

surface vapour pressure above snow and ice is directly determined by the temperature of the surface. Humidity is not measured at sites S5 and S6 and so no observational data is included in Figure 7.4 for these sites. Instead the GABLM determined surface specific humidity has been included as reference.

In Figure 7.5 the observed and simulated wind speeds are shown. Considering the inherent variability of winds the GABLM is capable of reproducing wind speeds in the ablation region quite well. In this area katabatic forcing plays an important role in the determination of wind speed and direction. The lower resolution ECMWF model cannot accurately simulate this effect and so ECMWF wind speeds will be

too low in the ablation region. The higher resolution of the GABLM allows wind speeds to be more accurately determined. For the ice sheet plateau sites GABLM wind speeds are similar to ECMWF estimates and both agree reasonably well with observations.

In Table 7.2 the average difference between simulated and observed meteorological variables for this period are given for each of the sites. Also included in Table 7.2 are the mean differences for the net shortwave radiation (NSW) and the net longwave radiation (NLW). At all sites NSW is overestimated, particularly at Swiss Camp where the mean difference is 38 Wm^{-2} . This has a two fold cause. Firstly, the observed albedo at Swiss Camp is higher than the simulated albedo and secondly the parameterisation for shortwave radiation cloud transmission, see Chapter 6, appears to underestimate the influence of clouds. This last discrepancy is common to all sites with the exception of S5, which is the lowest site.

The NLW is also overestimated at most sites, with the exception of Tunu-N. Possible explanations for these discrepancies come from incorrect cloud cover, incorrect cloud height, or inaccuracies in the emissivity scheme itself. ECMWF cloud cover near the ice margin is the result of physical processes on the tundra since the model resolution is not sufficient to resolve this area. It is perhaps not surprising that cloud cover could be overestimated in this region. Cloud cover in the Summit region is also quite high, with a mean value of 0.8 for the summer period. This may also help to explain the higher simulated temperatures found in this region.

Since GABLM is driven by simplified ECMWF analysis data and ECMWF model resolution is sufficiently good to resolve processes on the ice sheet plateau it is not expected that the GABLM will improve the simulations in this region. However, daily average temperatures on the ice sheet are in general better represented after downscaling with the GABLM. This is most likely due to differences in surface parameters, such as albedo, but it does indicate that such a downscaling model can be used to improve near surface variables such as temperature even when surface parameters are not correctly represented in the forcing model.

Table 7.1: Positions and elevations of the observational sites used in the comparison.

Site	Latitude	Longitude	Elevation (m)	Model elevation (m)	Model slope (°)
S5	N 67°05' 56"	W 50°06' 25"	484	456	1.00
S6	N 67°04' 35"	W 49°22' 44"	1021	958	1.01
Swiss Camp	N 69°34' 06"	W 49°18' 57"	1149	1126	0.91
Humboldt	N 78°31' 36"	W 56°49' 50"	1995	1988	0.21
Tunu-N	N 78°01' 00"	W 33°59' 38"	2113	2096	0.21
Summit	N 72°34' 47"	W 38°30' 16"	3254	3242	0.07

Table 7.2: Mean difference between daily average simulations and observations for the 90 day summer period shown in Figures 7.3 to 7.5 for both ECMWF analysis and GABLM simulations. The standard deviation around the mean is also given in brackets.

SITE	Temperature (°C)	Specific humidity (g kg ⁻¹)	Wind speed (ms ⁻¹)	NSW (Wm ⁻²)	NLW (Wm ⁻²)
GABLM – Observed					
S5	+0.7 (0.7)	-	-1.4 (1.1)	+1.1 (28)	+15 (18)
S6	+1.1 (0.7)	-	+0.1 (1.1)	+17 (35)	+22 (23)
Swiss Camp	+0.5 (1.0)	+0.1 (0.4)	-1.6 (1.9)	+38 (26)	+10 (15)
Humboldt	+1.8 (2.7)	+0.4 (0.6)	+0.7 (1.8)	+18 (9)	+5.6 (20)
Tunu-N	+1.5 (3.3)	+0.4 (0.5)	-0.5 (1.6)	+21 (5)	-6.4 (15)
Summit	+2.5 (3.8)	+0.6 (0.5)	+0.5 (1.7)	+23 (9)	13 (18)
ECMWF – Observed					
S5	-	-	-	-	-
S6	+3.2 (1.6)	-	-2.0 (0.6)	-	-
Swiss Camp	+0.6 (0.8)	+0.1 (0.4)	-2.8 (2.2)	-	-
Humboldt	+2.8 (1.9)	+0.5 (0.5)	-0.8 (1.2)	-	-
Tunu-N	+4.4 (2.3)	+0.6 (0.5)	-1.7 (1.3)	-	-
Summit	+4.1 (2.5)	+0.6 (0.5)	+0.2 (1.4)	-	-

7.3.3 Katabatic and pressure gradient forcing

Since turbulent fluxes are to a large extent determined by near surface wind speeds, it is worth looking at the forcing mechanisms that drive the ABL winds on the ice sheet. In Figure 7.2 wind speeds can be seen to increase towards the ice margin and this is the result of both katabatic forcing and horizontal perturbation pressure gradients. The strength of the katabatic forcing is determined by slope and temperature inversion strength. Since hydrostatic equilibrium is assumed for the perturbation pressure field, see Chapter 6, the perturbation pressure is determined by the vertically integrated temperature inversion. Both these forcing mechanisms are thus dependent on inversion strength. In non-melt regions inversion strength is dependent on the surface energy balance, particularly the radiative fluxes, and in melt regions on the limiting surface temperature. In melt regions boundary layer dynamics and turbulent exchange with the surface will determine the temperature inversion strength, in particular the advection of potentially warmer stratified air from the plateau down to the margins is an important source of heating for the boundary layer.

In Figure 7.6 the strength of the temperature inversion, or temperature perturbation Θ , at 2 m is shown for the average summer period on the ice sheet. The inversion strength on the plateau is at its highest in regions with low cloud cover, as in Northern Greenland where average cloud cover is around 0.4. In the Summit region average cloud cover is 0.8 and so inversion strengths are not particularly large here. A typical inversion strength of -5 °C can be seen along the Western ice margin compared to the Eastern margin where inversion strengths are noticeably less. Any gradient in inversion strength will result in a perturbation pressure gradient.

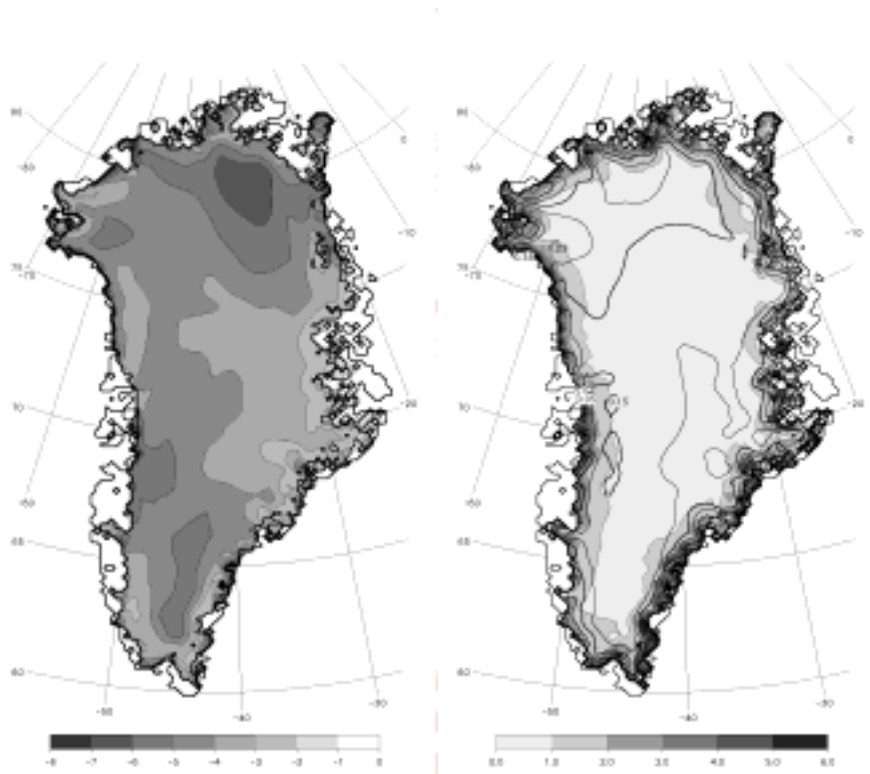


Figure 7.6: Left: Average summer 2 m temperature perturbation indicating the inversion strength of the ABL in $^{\circ}\text{C}$. Right: 2 m average summer katabatic forcing in $\text{ms}^{-2} \times 10^3$ (shading) and perturbation pressure field in hPa (contours).

To clarify these forcing mechanisms the summer time average katabatic forcing term and the perturbation pressure field, converted to hPa, at 2 m are also shown in Figure 7.6. Regions where katabatic forcing and/or pressure perturbation gradients are strongest correspond to areas where wind speeds are highest, see Figure 7.2. In most regions katabatic forcing is the largest of the two forcing mechanisms but in Northern Greenland, near the ice margin, enhanced wind speeds are also a result of perturbation pressure gradient forcing.

7.3.4 Momentum and temperature budgets

The dynamic structure of the ABL can best be seen in the vertical profiles of wind and temperature and in the momentum and temperature budgets. In Figure 7.7 the summer average along-slope (U), cross slope (V) and absolute wind speed ($|U|$) are shown at site S6 where downslope flow at this site is negative. Clearly visible is the wind speed maximum at around 90 m, compared to the depth of the ABL of around 650 m. The wind turns from a South-Eastern direction of 134° near the surface to a Southern direction of 180° , perpendicular to the slope, at a height of

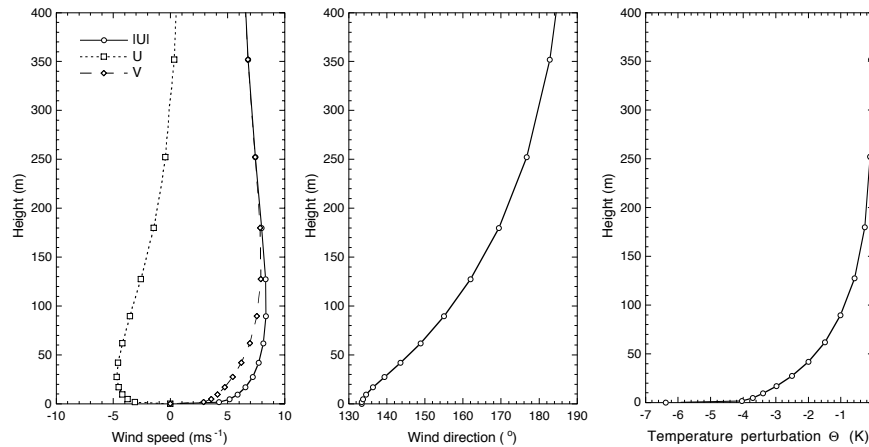


Figure 7.7: Summer average vertical profiles of wind, wind direction and perturbation temperature at site S6. Left: Along-slope (U), cross-slope (V) and absolute ($|U|$) wind speeds where the downslope component U is negative. Middle: Wind direction where the downslope direction is 90° at this site. Right: Temperature perturbation Θ or temperature inversion strength.

300 m. The downslope angle is Eastern at 90° in this case. This is fairly typical of the wind profiles along the Western margin of the ice sheet where katabatic forcing in the lower part of the ABL drives the wind downslope and Coriolis forcing turns the wind clockwise away from the downslope direction. The average geostrophic wind speed for this period is 5.3 ms^{-1} at 190° which explains the large cross-slope component (V) in the upper boundary layer.

The momentum budget components in the ABL are shown, for the same site, in Figure 7.8. In the lower part of the ABL, below 50 m, katabatic forcing (KAT) dominates and accelerates the wind in the downslope direction which is retarded by the flux divergence (FLU) of horizontal momentum. Above 50 m both katabatic forcing and horizontal perturbation pressure gradient (PGR) are important terms. At this height, flux divergence becomes small and so the downslope acceleration is balanced almost completely by Coriolis forcing. Horizontal perturbation pressure gradients directed downslope will thus lead to cross-slope winds, as seen in Figure 7.7.

The strength of the katabatic forcing is determined by the slope and the temperature perturbation, shown in Figure 7.7. This in turn depends on the temperature budget of the ABL which is shown for site S6 in Figure 7.8. The ABL is warmed chiefly by the downslope advection of positively stratified ambient potential temperature (ADV0). The vertical temperature flux divergence (FLU) in general cools the ABL except in the lowest few meters where radiation divergence (RDIV) becomes important. The ABL is also cooled by the advection of perturbation temperature as a result of the horizontal inversion gradient.

The water vapour budget, not shown here, can be looked at in a simpler manner. Drier air is both entrained and advected downslope which is replenished by evaporation from the surface. This means that increasing wind speeds will not just increase the turbulent exchange of water vapour with the ABL but will also enhance

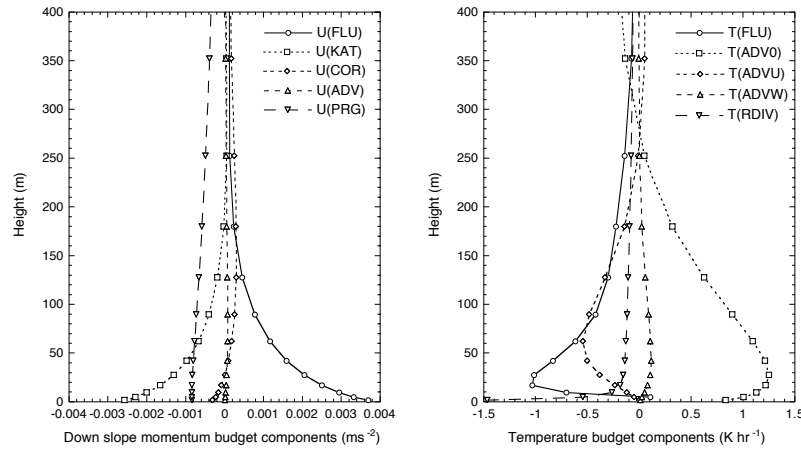


Figure 7.8: Left: Summer average vertical profiles of the along-slope component of the momentum budget at site S6. KAT is the katabatic forcing, COR the Coriolis forcing, ADV advection, PGR the horizontal perturbation pressure gradient and FLU the turbulent flux divergence of horizontal momentum. Right: Components of the temperature budget given in K hr^{-1} . ADVU is the horizontal advection of perturbation temperature Θ parallel to the surface, ADVW the vertical entrainment of perturbation temperature perpendicular to the surface, RDIV is the radiative divergence, ADV0 is the horizontal advection of ambient stratified temperature Θ_0 and FLU is the turbulent flux divergence of temperature.

the advection terms drying the ABL.

The rather complicated nature of the katabatic ABL with several forcing mechanisms of similar magnitude make it difficult to describe in a simplified manner. Values for near surface parameters such as wind and temperature are dependent on a complex budget, especially for the case of temperature where advection plays an important role.

7.3.5 Surface energy balance

The four energy balance components of the Greenland ice sheet, averaged over the summer season for the ablation and plateau regions, are summarised in Figure 7.9. The areal distribution of these four components is also shown in Figure 7.10. In the plateau region warming by shortwave and incoming longwave radiation fluxes is balanced chiefly by radiative cooling of the surface and partially by evaporative cooling giving a total surface energy flux of just 1.5 Wm^{-2} . Sensible heat flux makes up only a small component of the surface energy budget in this region. In the ablation region the excess energy flux of 65 Wm^{-2} is used almost entirely for melt of the ice and snow surface.

In the ablation region, lower albedo accounts for the strong increase in NSW radiation near the ice margin. Over most of the ice sheet surface albedo is at the pre-defined snow value of 0.85 since no melt takes place. In general the NLW radiation reflects the cloud cover distribution on the ice sheet plateau. As the margin is approached, incoming longwave radiation increases with increasing temperatures but

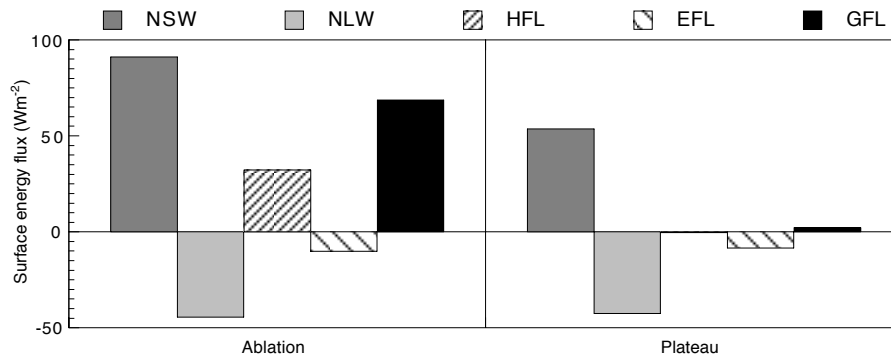


Figure 7.9: Areally averaged surface energy budget for the ablation and plateau region during the summer season. NSW is the net shortwave radiation, NLW the net longwave radiation, HFL the sensible heat flux, EFL the latent heat flux and GFL the total heat flux, all in Wm^{-2} .

unless the surface is melting this is largely compensated for by the outgoing radiation.

Near the ice margin both the sensible and latent heat fluxes can be seen to increase. The increase in sensible heat flux is the direct result of increasing temperature difference between ice and ABL as well as increasing wind speeds. Latent heat flux is negative over almost all of the ice sheet except in small regions at the ice margin where ABL temperatures are high.

The resulting melt from the calculations can be compared to measurements made at S5 and S6 in the ablation region. At S5 the total observed melt is 4.1 m w.e. and the simulated melt is 4.0 m w.e.. At S6 the observed melt is 1.7 m w.e. and the simulated melt is 3.0 m w.e.. The discrepancy between the simulated and observed values at S6 can be largely accounted for by the radiation budget. On average the simulated net radiation budget at S6 is 39 Wm^{-2} too high. If this were to be converted to melt during the melt season then this would account for 1.1 m w.e. of the excess melt, leaving a difference of just 0.2 m w.e..

7.4 Climate sensitivity

In this section a climate sensitivity experiment is carried out in order to determine the models sensitivity to an increase in free atmospheric temperature. The aim of this experiment is to quantify sensitivities of the surface energy budget and 2 m meteorological values as the result of an atmospheric temperature change. This is done simply by increasing the ECMWF atmospheric temperatures by a constant 2 K over the entire model domain. The initial subsurface temperatures are also increased by the same amount. This run is known as the T+2 run and is carried out over the same time period as the reference run described in the previous section.

In the following discussion the climate sensitivity of some quantity Φ to a change in surface-extrapolated atmospheric temperature T_a is defined as

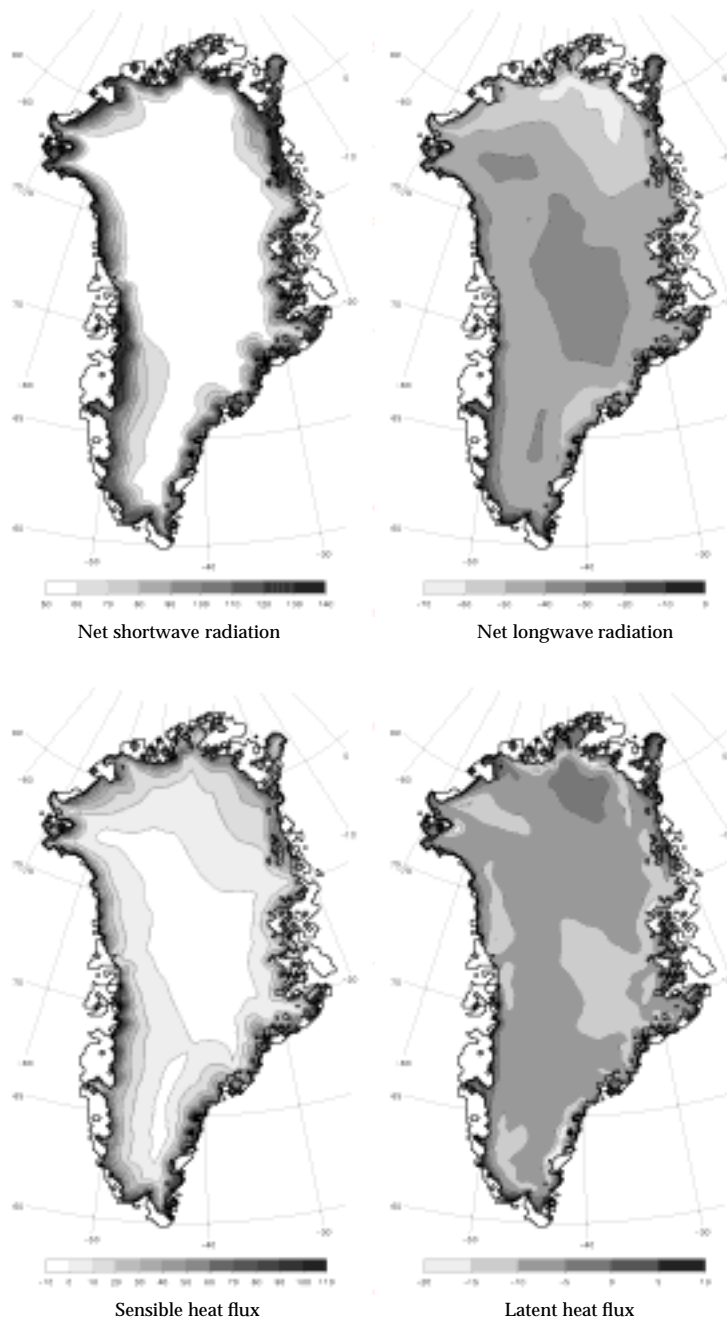


Figure 7.10: Summer average energy balance components in Wm^{-2} .

$$d\Phi = \frac{\partial\Phi}{\partial T_a} \quad (7.4)$$

This quantity is calculated from the model results by dividing the difference between the T+2 and the reference run by a factor of 2, resulting in a climate sensitivity per Kelvin (K^{-1}).

Before discussing the climate sensitivity of 2 m meteorological variables and surface energy fluxes from model results, it is informative to discuss the surface energy balance and its climate sensitivity in an analytical sense. The surface energy balance components can be written in the following form:

$$\text{NSW} = S_s(1 - \alpha) \quad (7.5)$$

$$L \downarrow_s = \varepsilon_a \sigma T_a^4 \quad (7.6)$$

$$L \uparrow_s = \sigma T_s^4 \quad (7.7)$$

$$\text{HFL} = \rho c_p C_H U_{2m} \Delta T_{2m} \quad (7.8)$$

$$\text{EFL} = \rho L_e C_E U_{2m} \Delta Q_{2m} \quad (7.9)$$

where the energy fluxes are described in terms of the surface extrapolated free atmospheric temperature (T_a), the ABL temperature and specific humidity at 2 m (T_{2m} and Q_{2m}), and the surface temperatures and humidity (T_s and Q_s). The difference between the 2 m and surface levels is written as ΔT_{2m} and ΔQ_{2m} . In the above equation $L \downarrow_s$ and $L \uparrow_s$ are the incoming and outgoing longwave radiation fluxes, ε_a is the effective emissivity of the atmosphere for the surface-extrapolated atmospheric temperature and the surface emissivity is assumed to be unity. The sensible (HFL) and latent (EFL) heat fluxes are described using the exchange coefficients C_H and C_E which are a function of surface roughness lengths, height and stability. These coefficients are described in Chapter 6.

Differentiating the above equations w.r.t. a change in free atmospheric temperature T_a , with the assumption of no change in cloud cover or wind speed and a constant relative humidity, R_{2m} , gives the following sensitivities for the surface energy flux components.

$$d\text{NSW} = S_s (1 - d\alpha) \quad (7.10)$$

$$dL \downarrow_s = L \downarrow_s \left(\frac{4}{T_a} + \frac{d\varepsilon_a}{\varepsilon_a} \right) \quad (7.11)$$

$$dL \uparrow_s = L \uparrow_s \frac{4}{T_s} dT_s \quad (7.12)$$

$$d\text{HFL} = \rho c_p C_H U_{2m} d\Delta T_{2m} \quad (7.13)$$

$$d\text{EFL} = \frac{L_e}{R_v T_s^2} \left(\text{EFL} dT_s + R_{2m} Q_s \frac{L_e}{c_p} d\text{HFL} \right) \quad (7.14)$$

Use is made of the Clausius-Clapeyron equation in deriving Equation 7.14 with the assumption that $\Delta T_{2m} \ll T_{2m}$ where T_{2m} is in Kelvin.

In non-melt regions the total sum of the above changes will approach a steady state and so the climate sensitivity of the energy budget will be close to zero.

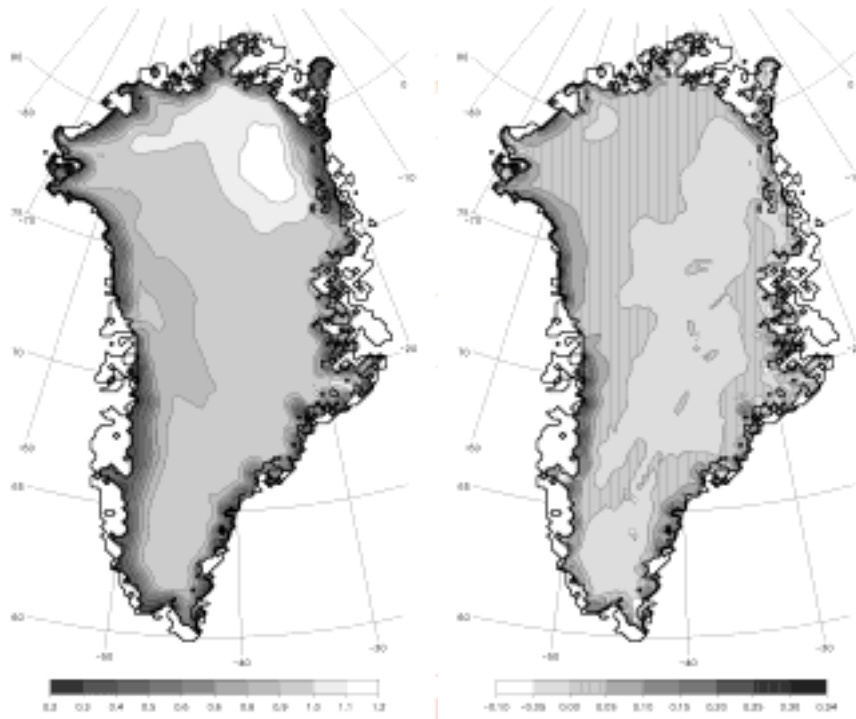


Figure 7.11: Left: Summer average climate sensitivity of 2 m temperature. Right: Summer average climate sensitivity of 2 m wind speed in $\text{ms}^{-1} \text{K}^{-1}$.

7.4.1 Temperature sensitivity

In many energy balance and degree day models used to calculate ablation, climate sensitivity experiments are carried out by increasing a predefined near surface temperature field, usually at 2 m, by a fixed value. However air temperatures in the boundary layer are affected by both surface and free atmospheric conditions and the change in 2 m temperature will not correspond directly to a change in free atmospheric temperature. The calculated average climate sensitivity of 2 m temperature, dT_{2m} , for the summer season is shown in Figure 7.11 for the entire Greenland ice sheet.

Let us firstly look at dT_{2m} in the non-melt region of the ice sheet. Over most of the plateau area $dT_{2m}=0.93$ but in Northern Greenland, where cloud cover is lowest, this can be greater than 1. The 2 m climate sensitivity in the non-melt region will be determined by the climate sensitivity of the surface energy flux components.

If we look at the surface energy budget sensitivities for longwave radiation, Equation 7.11, then an increase in atmospheric temperature will lead to an increase in $L \downarrow_s$ due to the change in atmospheric temperature and due to an increase in effective emissivity. The change in effective emissivity, $d\varepsilon_a$, is dependent on the increased

water vapour content, cloud cover, and any change in the ABL profiles of temperature and specific humidity. Since cloud cover is unchanged in the T+2 run this will not affect $d\varepsilon_a$. However, $d\varepsilon_a$ does depend on the amount of cloud cover, as does ε_a . We will return to this point in Section 7.4.3.

If a purely radiative change in energy balance is assumed, i.e. that changes in incoming longwave radiation are balanced by changes in outgoing radiation, then the surface temperature sensitivity will be given by $dT_s = \varepsilon_a (T_s/T_{2m})^3$ if $d\varepsilon_a = 0$. Typical values for ε_a in the non-melt region would then give $dT_s = 0.80$. The sensitivity of ε_a to an increase in water vapour content, as the result of a change in temperature, can not be so easily defined. In the model, average sensitivities of 0.002 K^{-1} are found in the plateau region which would result in an added sensitivity of 0.15, leading to a surface temperature sensitivity of 0.95.

In addition, the latent heat flux, which is significant during summer on the Greenland ice sheet at around -8 Wm^{-2} on the plateau, will to a first approximation increase by a relative factor of $(L_e dT_s)/(R_v T_s^2)$, if the second term in Equation 7.14 is ignored. This leads to a roughly $8\% \text{ K}^{-1}$ decrease in EFL. This decrease in latent heat flux works as a negative feedback mechanism on the surface temperature, reducing the total sensitivity. If the 2 m temperature difference ΔT_{2m} also increases, which it must do to close the climate sensitivity energy budget when evaporative cooling is greater than net radiative heating, then the change in latent heat flux will be reduced via the second term in Equation 7.14. Exactly how these terms interact is dependent on the ABL dynamics but the major determining factor for the climate sensitivity of the surface temperature in non-melt regions is the longwave radiation flux.

In regions where melt does take place, energy is transferred to the surface and the surface temperature is limited for all or part of the ablation season by the melting point. Analysis of the surface energy budget in this region will not give insight into temperature sensitivities since this is the result of boundary layer dynamics. The consequence of a fixed surface temperature is that 2 m temperatures will increase only fractionally as a result of a free atmospheric temperature increase. For the results presented here the minimum sensitivity, in regions where melt prevails for most of the summer season, is around 0.3.

This value for the climate sensitivity of 2 m temperature can also be determined directly from the reference run at any particular site. In Figure 7.12, T_{2m} is plotted as a function of T_a at site S5 and Swiss Camp. There is a clear relationship between these two temperatures and a linear fit to the data gives climate sensitivities at S5 of 0.32 and at Swiss Camp of 0.34. This can be compared to the summer average climate sensitivities determined with the T+2 model run of 0.33 and 0.46 respectively. When climate sensitivity is calculated by fitting daily average temperature data it is assumed that dT_{2m} is independent of T_a . This is not the case, as is shown in Section 7.5, and so linear fits do not always give the correct sensitivity.

The dominant processes controlling ABL temperature are the advection of potentially warmer air from upslope regions and the cooling by turbulent flux divergence (Figure 7.8). Greuell and Böhm (1998) have found similar climate sensitivities to those simulated here, on the Pasterze glacier, Austria. They also showed, with a simple analytical glacier-wind model, that the climate sensitivity of a continually melting glacier surface decreases exponentially with distance down the glacier, when

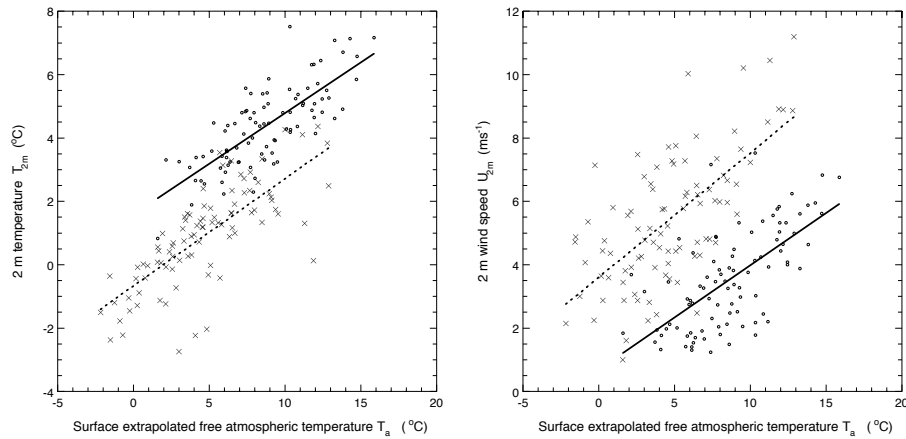


Figure 7.12: Left: Daily average simulated 2 m temperature (T_{2m}) as a function of surface-extrapolated free atmospheric temperature (T_a) for site S5 (circles) and Swiss Camp (crosses). The linear fit to each site gives a gradient of 0.32 and 0.34 for S5 and Swiss Camp respectively. Right: Daily average simulated 2 m wind speeds (U_{2m}) as a function of surface-extrapolated free atmospheric temperature (T_a) for site S5 (circles) and Swiss Camp (crosses). The linear fit to each site gives a gradient of 0.33 and $0.39 \text{ ms}^{-1} \text{ K}^{-1}$ for S5 and Swiss Camp respectively.

advection and flux divergence are the only two terms affecting the temperature budget. A similar effect, though complicated by the other budget terms, occurs here as well.

7.4.2 Wind sensitivity

With increasing atmospheric temperatures above melting ice surfaces katabatic forcing will enhance wind speeds in the marginal regions of the ice sheet due to an increase in inversion strength. Using a bulk model of the Greenland ABL with little synoptic forcing, van den Broeke (1997a) simulated a 6 m wind speed sensitivity near the margin of $0.35 \text{ ms}^{-1} \text{ K}^{-1}$. Measurements made during the GIMEX experiment clearly indicate a strong correlation between summer time 2 m wind speeds and 2 m temperatures in the ablation region along the K-transect. This increase in wind speed can be seen in Figure 7.11 where maximum climate sensitivities for wind speed of approximately $0.3 \text{ ms}^{-1} \text{ K}^{-1}$ are simulated at the ice margin.

In Figure 7.13, the simulated vertical profiles showing the climate sensitivity of along-slope (U), cross-slope (V) and absolute wind speed ($|U|$) at site S6 for the summer period are shown. Wind speeds in the lower boundary layer increase by up to 0.35 ms^{-1} but by just 0.16 ms^{-1} at the 2 m level. With the increase in downslope forcing the wind turns by 1.5° towards the downslope direction.

The climate sensitivity of the along-slope momentum budget at site S6 is shown in Figure 7.14. Throughout the boundary layer the only major change in forcing with increased temperature comes from the katabatic term which is compensated for by the flux divergence of horizontal momentum.

In Figure 7.12, simulated 2 m wind speed is plotted as a function of T_a for the sites

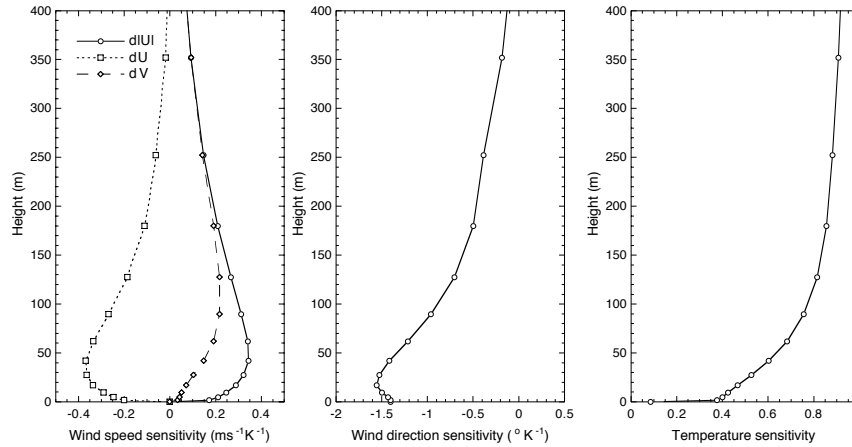


Figure 7.13: Average summer vertical profiles showing the climate sensitivity of wind, wind direction and temperature at site S6. Left: Along-slope (U), cross-slope (V) and absolute ($|U|$) wind speeds where the downslope component U is negative. Middle: Wind direction where a negative change in direction indicates winds directed in the downslope direction. Right: Temperature sensitivity.

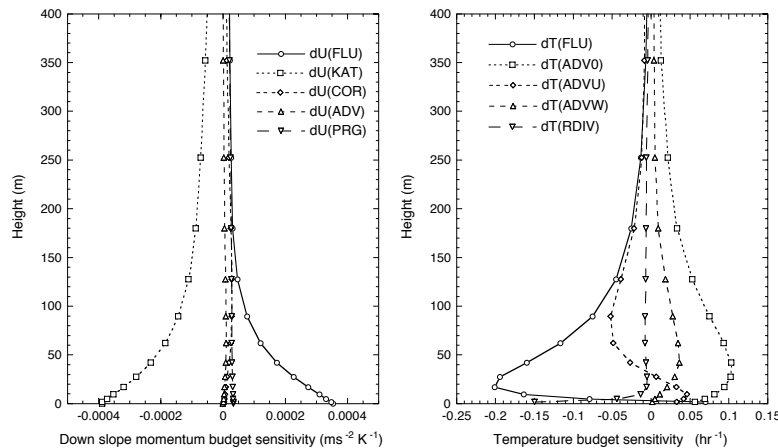


Figure 7.14: As in Figure 7.8 but showing the climate sensitivity of the along-slope momentum and temperature budgets.

S5 and Swiss Camp using the daily average results from the reference run. There is a clear correlation between wind speed and atmospheric temperature and a linear fit to the data indicates a gradient for S5 of $0.33 \text{ ms}^{-1} \text{ K}^{-1}$ and for Swiss Camp of $0.39 \text{ ms}^{-1} \text{ K}^{-1}$. This is in contrast to the climate sensitivity test which indicates that $dU_{2m}=0.18$ and $0.13 \text{ ms}^{-1} \text{ K}^{-1}$ for both sites respectively. The relationship between wind and temperature in Figure 7.12 would not appear to be purely the result of katabatic forcing. When synoptic winds are Southerly at these sites, then synoptic scale forcing will enhance the katabatic flow. At the same time, Southern flows cor-

respond to the advection of warmer atmospheric air and this combination increases the apparent sensitivity of ABL wind speeds to free atmospheric temperatures.

7.4.3 Energy balance sensitivity

The climate sensitivity of the four surface energy balance components, averaged over the summer period, are summarised in Figure 7.15 and the areal distribution of these four components is shown in Figure 7.16.

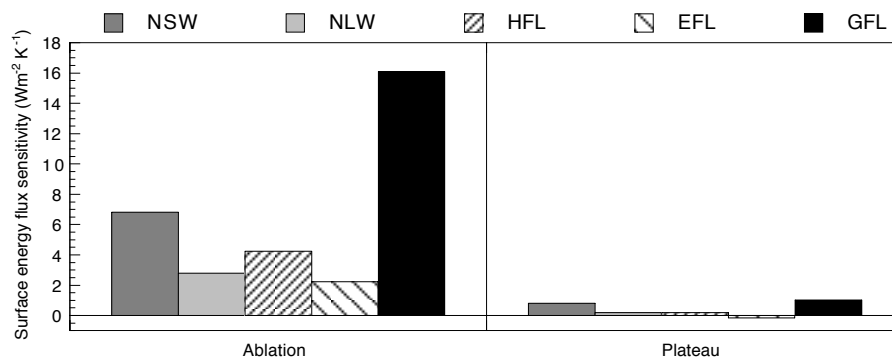


Figure 7.15: Areal averaged surface energy budget climate sensitivities for the ablation and plateau regions during the summer season. NSW is the net shortwave radiation, NLW the net longwave radiation, HFL the sensible heat flux, EFL the latent heat flux and GFL the total heat flux. All climate sensitivities are given in $\text{Wm}^{-2}\text{K}^{-1}$.

Net shortwave radiation sensitivity

The climate sensitivity of NSW radiation in non-melt regions will be zero when factors such as cloud cover and atmospheric extinction do not change. In Figure 7.15 a slight increase in NSW in the plateau region can be seen because a small amount of melt takes place in this region as a result of the 2 K increase.

In the ablation zone NSW radiation is the largest single contributor to the increase in surface energy flux. This is the result of the albedo feedback mechanism whereby increased melt, due to increases in turbulent heat and longwave radiation fluxes, reduces the snow albedo and leads to enhanced melting through shortwave radiation absorption. In regions where the surface is bare ice for most of the melt season, i.e. close to the margin, this feedback mechanism will not play a strong roll. The albedo feedback mechanism has thus a maximum effect in the region of the snow line where melt is generally low to begin with. The strength of the feedback will depend on the albedo parameterisation used (Section 7.2.1) particularly the depth of snow cover and the characteristic melt scale M^* . Caution should be aired when attaching a quantitative value to the increase in surface energy flux as a result of albedo feedback but the results from this study show that it can strongly enhance, by a factor of 1.6, the effect of the other energy flux components. This is in line with

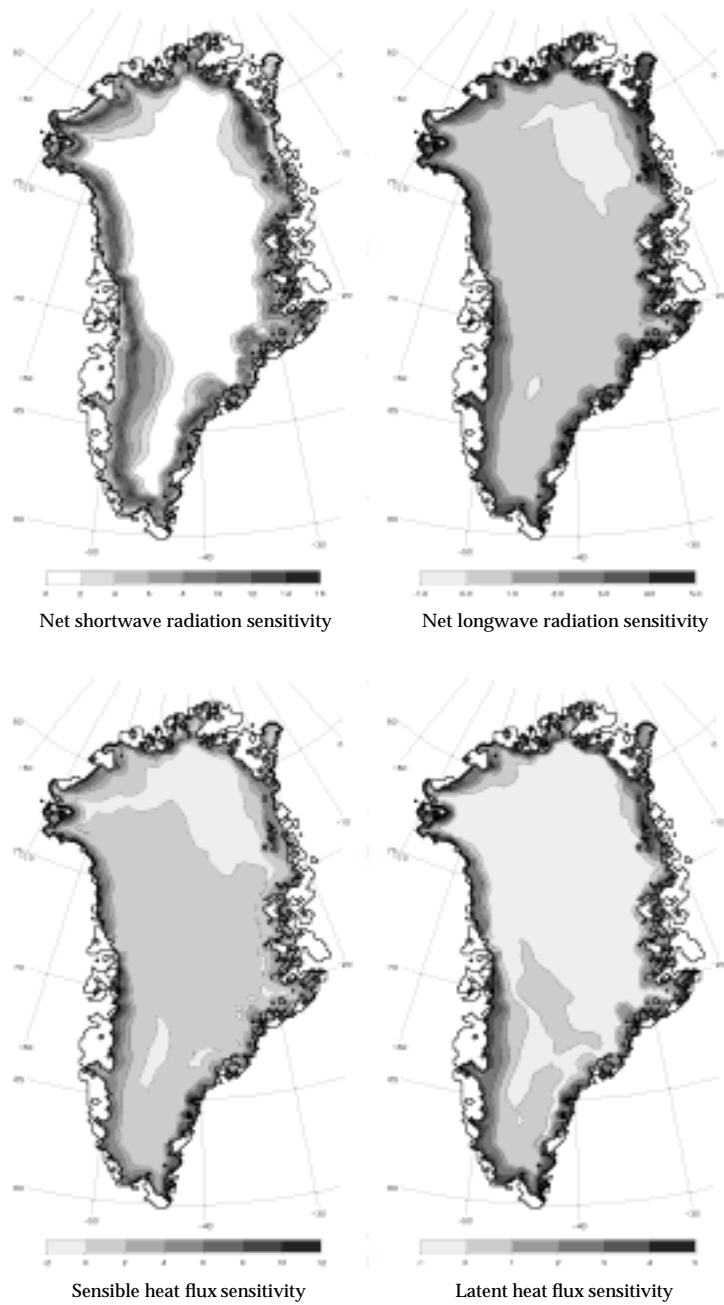


Figure 7.16: Summer time average climate sensitivity of the four energy balance components given in $Wm^{-2}K^{-1}$. Note that the scales are different for each component.

the results from van de Wal (1996) who found that the albedo feedback could double the total simulated melt.

Net longwave radiation sensitivity

The climate sensitivity of the incoming longwave radiation flux ($dL \downarrow_s$) is given by Equation 7.11, and is dependent on $L \downarrow_s$, T_a and on the sensitivity of the effective emissivity ($d\varepsilon_a$). $d\varepsilon_a$ is determined by the change in water vapour content, on the cloud cover and height, and on any variation in the ABL temperature profile as a result of a temperature change. One of the most important factors affecting $d\varepsilon_a$ is the cloud cover. With a totally overcast sky, the emitted longwave radiation from clouds can be approximated by a black body with a temperature equal to the cloud temperature. Because of this $d\varepsilon_a$ will be small when clouds are present. The effect of cloud cover on $d\varepsilon_a$ can be seen in the temperature sensitivity in Figure 7.11. In Northern Greenland cloud cover is at a minimum of around 0.4 and it is in this region that $d\varepsilon_a$ and thus also dT_s are greatest.

The other factor that will affect $d\varepsilon_a$ is the alteration of the temperature profile. Because the climate sensitivity of ABL temperature in melt regions is less than unity, the effective emissivity will change as a result of the change in temperature profiles. To a first approximation $dL \downarrow_s$ can be expressed in terms of Equation 7.11, assuming $d\varepsilon_a$ to be zero. This results in an underestimation of $dL \downarrow_s$ by, on average, 1.0 Wm^{-2} when compared with the simulated values.

Turbulent heat flux sensitivity

In non-melt regions, the climate sensitivity of the total turbulent heat flux is dependent on the sensitivity of the radiative flux components, as discussed in Section 7.4.1, since the turbulent fluxes will try to balance the energy budget.

In the ablation zone sensible heat flux is enhanced by an increase in both temperature and wind speed. However, the climate sensitivity of temperature is at least twice as large as that for wind and will dominate the change in HFL. This increase is reflected in the climate sensitivity of the near surface temperature difference $d\Delta T_{2m}$ which, near the margin, is a function of ABL dynamics.

As discussed in Section 7.4.1 evaporation will be enhanced in the non-melt regions as a result of temperature increases. This is not the case in the ablation zone due to the fixed surface temperature. When the climate sensitivity of the surface temperature (dT_s) is small or zero, i.e. melting, then $d\text{EFL}$ will be directly proportional to the sensitivity of $d\text{HFL}$, if R_{2m} is unchanged (Equation 7.14). $d\text{EFL}$ is thus directly related to $d\text{HFL}$ under these conditions by:

$$d\text{EFL} = \frac{R_{2m} Q_s L_e^2}{c_p R_v T_s^2} d\text{HFL} \quad (7.15)$$

which means that the ratio $d\text{EFL}/d\text{HFL} \cong 0.7 R_{2m}$ for conditions near the margin. Given an average relative humidity of 70% this is very close to the values found in the current study and in Chapter 6 for the relative sensitivities of $d\text{EFL}$ and $d\text{HFL}$.

The climate sensitivity of the total energy flux (GFL) in the ablation region is thus the result of only positive effects, all components leading to an increase in surface energy fluxes. This, in combination with the albedo feedback, leads to a 35% increase

in melt over the entire ablation region for a 1 K increase in atmospheric temperature. This is almost exactly the same value as arrived at by van de Wal (1994).

At site S5, where melt has been measured, the average increase in GFL is 16 Wm^{-2} which results in a melt increase of 430 mm w.e.. This is an 11% increase in melt as a result of a 1 K atmospheric warming at this site. Are these sorts of variations observed in the mass balance measurements? From the 10 year mass balance record obtained from the K-transect, the inter-annual variability from 1991 to 2000 is of the order of $\pm 0.5 \text{ m w.e. melt}$ at S5. The inter-annual variability in temperature at Kangerlussuaq during this period is approximately $\pm 1.2 \text{ }^\circ\text{C}$ which would agree with the result obtained here.

The summer average surface energy flux sensitivities for NLW, HFL and EFL, calculated here for the ablation region in 1998, agree well with the results from Chapter 6 where the sensitivity of the model to a 1 K change in temperature is calculated for an average summer day in 1991. This is in spite of the fact that the individual energy balance components in that study differed to the averages calculated here and that in the previous chapter albedo feedback was not included. This confirms that the sensitivities of these components are not strongly affected by albedo nor by the specific synoptic conditions present in the free atmosphere.

7.5 Simplified parameterisations for energy balance modelling

The physics of the atmospheric boundary layer, surface processes and the interaction of tundra and ice margins are a complicated system. Energy balance models used for mass balance calculations over decadal or centennial time scales cannot hope to describe the ABL processes included in this model in order to calculate surface ablation. For this reason it is useful to describe the surface energy balance components and their climate sensitivity in parameterised terms. The energy balance components we are concerned with in this section are the turbulent heat fluxes and the incoming longwave radiation flux.

There are several approaches possible when considering parameterisations for turbulent heat and longwave radiation fluxes. The simplest is to choose one or two external variables, such as the free atmospheric temperature, and develop a parameterisation for the total turbulent heat flux on the basis of this quantity. A second approach, and the type often used, is to express the turbulent heat and longwave radiation fluxes as a function of the 2 m variables. A third approach, and the most physical, is to develop dynamic parameterisations based on the dynamic equations governing the ABL and to calculate fluxes from these.

The last of these schemes is, and would be, the most complete and satisfying approach however this proves to be difficult considering the complexity of the dynamic system. Nonlocal effects such as advection or pressure gradients complicate any analysis and even if these can be ignored, several different forcing mechanisms of equal magnitude will not allow a simplified analysis. As such a dynamic description of the ABL, which can be used to determine the turbulent heat fluxes, will require a dynamic model to describe them.

The second approach will also not be considered here. This method is most useful when observational data is available and these data can be used to drive an energy balance model with measured variables of wind, temperature and water vapour, e.g. Greuell and Konzelmann (1994). The most important point when using this approach is that any alteration of input temperature, e.g. for climate sensitivity runs, must take into account the climate sensitivity of 2 m temperature when forcing the energy balance model.

This last point, the climate sensitivity of 2 m temperature, will be briefly discussed in Section 7.5.3. However, we will start with the first, and most pragmatic, approach whereby the total turbulent heat and incoming longwave radiation fluxes are parameterised in terms of the surface-extrapolated free atmospheric temperature (T_a) and, for the case of longwave radiation, also as a function of total cloud cover.

7.5.1 Parameterisation of turbulent heat fluxes based on free atmospheric temperature

The turbulent heat fluxes on the Greenland ice sheet are a function of both energy balance and boundary layer dynamics. Any parameterisation based on just one single variable cannot include all the processes that occur. To begin, the ice sheet is divided into melt, $T_a > 0^\circ\text{C}$, and non-melt regions, $T_a < 2^\circ\text{C}$. The major reason for this distinction is that turbulent fluxes are strongly determined by the energy balance in the non-melt region but in the ablation region they are more directly dependent on the limiting melt temperature of ice. We will concentrate mainly on the melt region in this section.

In Figure 7.17a the summer average total turbulent heat flux (TFL=HFL+EFL) is plotted as a function of T_a for the entire ice sheet. High on the plateau turbulent fluxes must compensate for the net warming by radiation and so in this region turbulent fluxes are negative. In the region around $T_a = 0^\circ\text{C}$ there is a large amount of scatter, as might be expected considering the possible variation over the ice sheet, but in general the turbulent fluxes have a magnitude of no more than 10 Wm^{-2} . In the ablation region the turbulent fluxes increase dramatically as the temperature difference between surface and air increases.

Insight into the dependence of TFL on the free atmospheric temperature can be gained by investigating the climate sensitivity of TFL determined from the T+2 run. This is shown in Figure 7.17b where it is also plotted as a function of T_a . In non-melt regions the turbulent fluxes have a climate sensitivity which is directly determined by the radiation fluxes, see Section 7.4.3, and these terms are very small. In the region around $T_a = 0^\circ\text{C}$ negative sensitivities are the result of changes in albedo since turbulent fluxes will compensate for the increase in net shortwave radiation. For $T_a > 0^\circ\text{C}$ there is a clear increase in $d\text{TFL}$ with increasing T_a .

In Figure 7.17b a linear fit to the data for $T_a > 0^\circ\text{C}$ is shown, which parameterises the climate sensitivity of the total turbulent heat flux as a function of T_a . This is written as:

$$d\text{TFL} = \begin{cases} 0 & T_a < 0 \\ 1.4 T_a & 0 < T_a \end{cases} \quad (7.16)$$

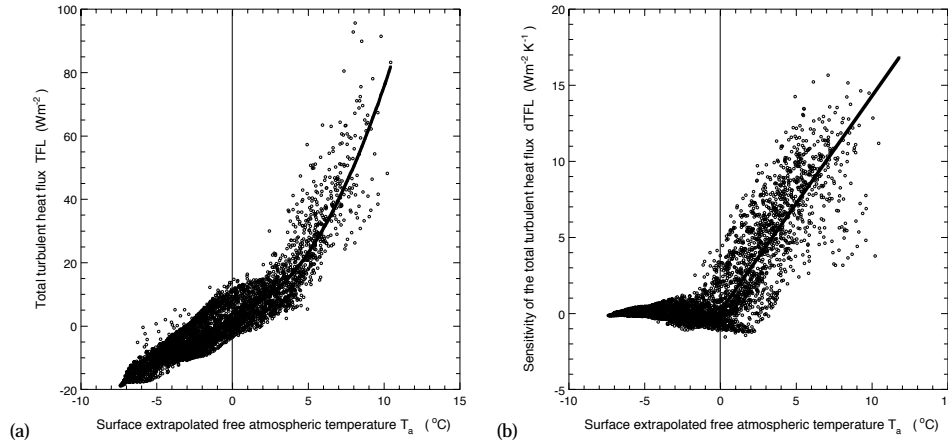


Figure 7.17: (a) Summer average total turbulent heat flux (TFL) as a function of T_a for the entire ice sheet. Also shown is the parameterisation given in Equation 7.17. (b) The summer average climate sensitivity of the total turbulent heat flux ($dTFL$) as a function of T_a . Also shown is the parameterisation given in Equation 7.16.

Integrating this equation when $T_a > 0$ °C will give a quadratic relationship for TFL shown in Figure 7.16a and given as:

$$\text{TFL} = \begin{cases} 5.6 - 2.5 T_a & T_a < 0 \\ 5.6 + 0.7 T_a^2 & 0 < T_a \end{cases} \quad (7.17)$$

The parameterisation in Equation 7.17 for $T_a < 0$ °C only reflects the radiation component of the energy budget and this will depend on such factors as albedo and cloud cover, however it has been included here for completeness.

The apparent non-linear relationship between turbulent heat flux and atmospheric temperature is the result of the combined effect of temperature difference and wind speed. The surface-extrapolated free atmospheric temperature is correlated with surface topography and thus slope. As a result wind speeds, which are largely driven by katabatic and pressure gradient forcing, will increase with increasing atmospheric temperatures leading to the quadratic relationship deduced in Equation 7.17.

7.5.2 Parameterisation of the incoming longwave radiation flux based on free atmospheric temperature

In spite of the simplicity by which clouds are introduced in the longwave radiation scheme of the GABLM, we present here a parameterisation for the incoming longwave radiation ($L \downarrow_s$) and its sensitivity ($dL \downarrow_s$), based on three variables. The first is the surface-extrapolated free atmospheric temperature (T_a) the second is cloud cover (n) and the third is the climate sensitivity of 2 m temperature (dT_{2m}) which is described in the following section as a function of T_a .

The major factors controlling $L \downarrow_s$ are air temperature, cloud cover and water

vapour content. Most parameterisations, e.g. Konzelmann *et al.* (1994) and Brutsaert (1975a), attempt to parameterise clear sky $L \downarrow_s$ in terms of screen level temperature and water vapour pressure assuming these to be representative of the entire atmospheric column. A simple parameterisation based on the free atmospheric temperature and cloud cover is presented here and is deduced from the summer average reference run over the entire Greenland ice sheet. The incoming longwave radiation is parameterised with the following equation

$$L \downarrow_s = \varepsilon_a(n) \sigma T_a^4 \quad (7.18)$$

where

$$\varepsilon_a(n) = 0.62 + 0.3 n \quad (7.19)$$

ε_a is thus described as a linear function of cloud cover determined from a least-squares fit to the summer average data.

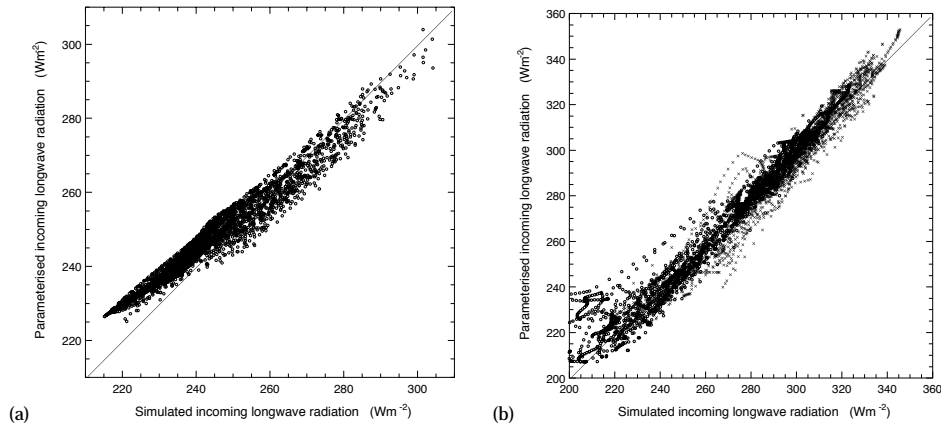


Figure 7.18: Comparison of simulated and parameterised (Equation 7.18) incoming longwave radiation. (a) for the entire Greenland ice sheet averaged over the summer season. (b) for hourly averages at site S5 (crosses) and Swiss Camp (circles).

The comparison of parameterised and simulated $L \downarrow_s$ is shown in Figure 7.18 where both summer average values and hourly average values from two ablation sites, S5 and Swiss Camp, are shown. The parameterised form tends to overestimate $L \downarrow_s$ when fluxes are low but agrees well in the ablation region.

In other parameterisations, based on observations, the dependence of ε_a on n is usually non-linear and given as n^3 (Konzelmann *et al.*, 1994). This non-linearity is intended to reflect a relationship between cloud cover and cloud type. A linear relationship would be expected if clouds are all of the same type and height, as they are assumed to be in the longwave radiation scheme used here.

From the climate sensitivity run a parameterisation for $d\varepsilon_a$ can also be made. As mentioned in Section 7.4.3, $d\varepsilon_a$ is a strong function of cloud cover since $d\varepsilon_a$ is small-

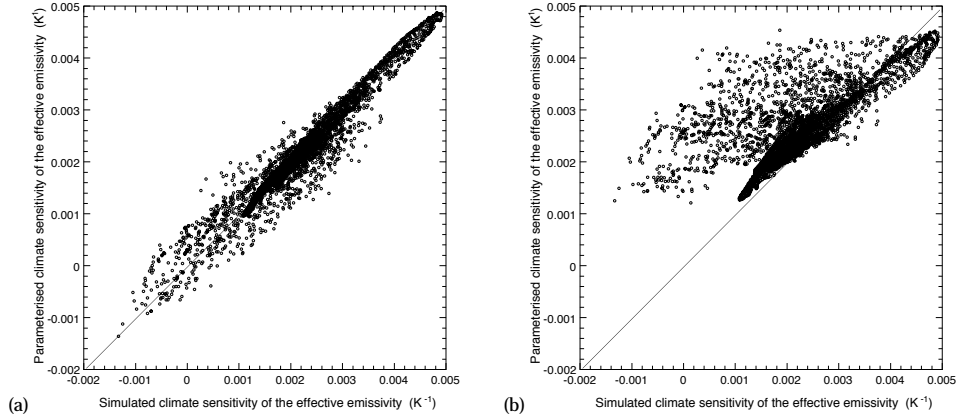


Figure 7.19: Comparison of simulated and parameterised climate sensitivity of the effective emissivity $d\varepsilon_a$ for the entire Greenland ice sheet averaged over the summer season. (a) the full parameterisation as given in Equation 7.20. (b) Equation 7.20 without the temperature correction term dT_{2m} .

est when clouds are present. Fitting $d\varepsilon_a$ as a linear function of n gives a reasonable fit to the simulated data with a large scatter in the melt zone. A better representation is obtained by including the climate sensitivity of the 2 m temperature, since this reflects the change in vertical temperature profile in the ABL as the result of an increase in free atmospheric temperature. This gives the following relationship

$$d\varepsilon_a = 0.0068 (1 - 0.55 (1 - dT_{2m}) - 1.04 n) \quad (7.20)$$

which is shown in Figure 7.19. The dependence on dT_{2m} indicates that $d\varepsilon_a$ decreases when the 2 m temperature is limited by the melting point, i.e. $dT_{2m} < 1$, and reflects the contribution of the ABL to ε_a .

7.5.3 Parameterisation for the climate sensitivity of 2 m temperature

As previously mentioned, most energy balance models use 2 m temperatures to drive the energy balance parameterisations. In such models, climate sensitivity experiments are carried out by increasing 2 m temperature by an amount assumed to correspond directly to temperature changes in the free atmosphere. As shown in Section 7.4.1, 2 m temperatures are influenced by both atmospheric and surface temperatures and have climate sensitivities much less than unity in the ablation region.

To quantify this, the climate sensitivity of 2 m temperature (dT_{2m}) is shown in Figure 7.20 as a function of both T_a and T_{2m} . This shows a sensitivity in the non-melt region, as discussed in Section 7.4.1, of around 0.94 during summer. For $T_a > 0$ or $T_{2m} > -3.5$ °C the 2 m temperature sensitivity decreases steadily as the result of the limiting surface temperature. dT_{2m} does not seem to decrease below a value of around 0.3 so this value is selected as the minimum sensitivity. A linear fit made to

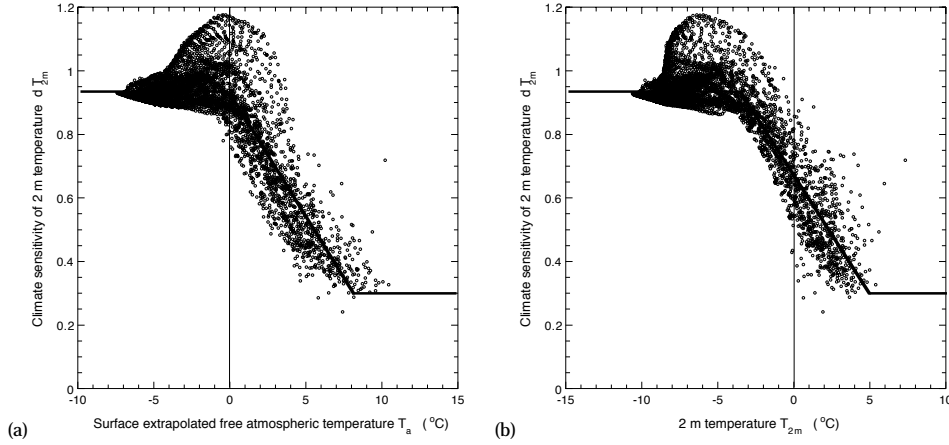


Figure 7.20: (a) Climate sensitivity of 2 m temperature as a function of T_a for the simulated summer period. Also shown is the parameterisation given in Equation 7.21. (b) Climate sensitivity of 2 m temperature as a function of T_{2m} for the simulated summer period. Also shown is the parameterisation given in Equation 7.22.

the data for $T_a > 0$ and $T_{2m} > -3.5$ °C gives the following parameterisation for the summer time 2 m temperature climate sensitivity as a function of T_a

$$dT_{2m} = \begin{cases} 0.94 & T_a < 0 \\ 0.94 - 0.08 T_a & 0 < T_a < 8.0 \\ 0.3 & 8.0 < T_a \end{cases} \quad (7.21)$$

and as a function of T_{2m}

$$dT_{2m} = \begin{cases} 0.94 & T_{2m} < -3.5 \\ 0.94 - 0.075 (T_{2m} + 3.5) & -3.5 < T_{2m} < 5.0 \\ 0.3 & 5.0 < T_{2m} \end{cases} \quad (7.22)$$

The decrease in dT_{2m} for $T_{2m} > -3.5$ °C reflects the period of time, during the summer season, that melt occurs. This is due largely to the daily amplitude of 2 m temperature but also to the length of the ablation season. When the surface is not melting the surface temperature is free to adjust to the 2 m temperature. When the surface is melting, for part or all of the averaging period, then changes in 2 m temperature will be dampened. For $T_{2m} > 5.0$ °C the surface will be continuously limited by the melt point and dT_{2m} reaches a minimum value of 0.3.

7.6 Summary

The major aim of this paper is to quantify the surface energy budget of the Greenland ice sheet during the ablation season. This is done by applying a boundary layer model (GABLM) to ECMWF analysis data. The simulation is compared to observa-

tional data from six AWS on the ice sheet and is found to give reasonable estimates of the near surface meteorological variables of wind, temperature and humidity.

In general, 2 m wind speeds are well simulated but 2 m temperatures tend to be too high at almost all sites. This may indicate that the model does not correctly simulate the temperature inversion of the boundary layer. Incoming longwave radiation fluxes also tend to be too high, by 10 to 20 Wm^{-2} , and this may also reflect on the simplistic manner in which cloud cover is introduced in the longwave radiation scheme.

The question may arise: Why not just use ECMWF output data to derive the surface energy budget? The reason lies in the ability of the ECMWF model to resolve the ablation zone of the ice sheet which in many regions is less than 100 km wide. The coarser resolution of ECMWF, approximately 70 km, does not give sufficient accuracy to investigate this region. The 20 km resolution of the GABLM assists in determining the processes which occur in the ablation zone.

One of the areas of interest is the dynamics of the ABL, particularly the role of katabatic forcing in determining wind speeds and their sensitivity to changes in atmospheric temperature. Enhanced wind speeds do occur near the margin of the ice sheet as a result of increased atmospheric temperature but this increase is generally of lesser importance than the increase in temperature in determining turbulent fluxes.

Particular emphasis is given to the turbulent heat fluxes and their climate sensitivity in the ablation zone since it is these fluxes, along with incoming longwave radiation, that directly determine the atmospheric input to the surface energy balance. However, as shown in Section 7.4.3, the albedo feedback mechanism can enhance melt as a result of changes in the atmospheric components of the surface energy budget.

An attempt is made to parameterise the total turbulent heat flux in terms of free atmospheric temperature. The resulting parameterisation is simplistic in its nature but would appear to reflect the general conditions found on the ice sheet. Included in such a parameterisation are the relationships between atmospheric temperature and height, slope, surface roughness lengths, wind speeds, etc.. Some of these are dependent on changes in atmospheric temperature whilst others are not.

A parameterisation for the incoming longwave radiation is also described, based on atmospheric temperature and cloud cover. This uses the simplest possible formulation that includes both cloud cover and free atmospheric temperature. The advantage of developing parameterisations of this type directly from simulations is that changes in vertical profiles can be incorporated. The disadvantage is that cloud type and height is poorly represented in the model. In this regard, improvements to the model will certainly help in developing a better parameterisation for the longwave radiation flux.

One important point, at least in regard to the use of 2 m temperatures to run energy balance models, is that the limiting temperature of the melting surface strongly influences the climate sensitivity. In melt regions this means that climate sensitivity tests, made with energy balance models, can overestimate the increase in 2 m temperature, and hence turbulent fluxes, by a factor of 3. This is also true for degree day models when they are run using locally determined values for 2 m temperature.

8

Some final words

Every chapter in this thesis contains its own conclusion and discussion. However, it is worth touching upon some of the major points and possible future developments of each of these.

The 1-D second-order model developed in Chapter 2 has proved to be useful for both modelling studies and for the interpretation of turbulence in katabatic flows. The essential conclusion from this work is that the turbulent structure of katabatic flows is sufficiently different to the classical stable boundary layer to necessitate the inclusion of turbulent transport terms in its description. Modelling attempts that disregard these terms or apply concepts based on local-scaling laws, such as the gradient Richardson number, to determine stability parameterisations will require ad-hoc numerical fixes to get the model to work at all.

The closure model makes use of present and past ideas concerning near-wall and atmospheric turbulence. Any closure model can be criticised for the approximations that must be made in order to close the Reynolds equations, however, it is the authors belief that the closures used here are adequate for the purposes for which it is applied. The results of turbulence measurements made in katabatic flows, such as those conducted by Smeets *et al.* (1998, 2000) and van der Avoird and Duynkerke (1999) are extremely useful for testing any turbulence model. Some of these data have been used to verify the closure model developed in Chapter 2 and some have come to light since that work was completed. Unfortunately, field measurements of the third-order moments in the Reynolds equations are not of sufficient quality to test higher-order closures in katabatic flows, as has been done in the laboratory (Irwin, 1974), so any higher-order refinement can not be supported by observation. One possible direction is the use of large eddy simulations (LES) to simulate the turbulent structure of katabatic flow. Unfortunately, current LES models are not capable of simulating the stable ABL, and spatial resolutions of less than 1 m, essential for capturing the turbulent structure of the katabatic flow, are computationally prohibitive. Perhaps this situation will change in the future.

When the Pasterze experiment (PASTEX) was being planned for 1994, less was

known about the structure of the ABL of this or similar glaciers. Five of the observational sites deployed were energy balance stations with measurement heights for temperature and wind at 0.5 and 2 m. The intention at the time was to deduce turbulent heat fluxes using the profile method described in Chapter 3. This method was discarded because use of the profile method, and the assumptions of Monin-Obukhov similarity, lead to severe underestimates of the expected fluxes, as is illustrated in Chapter 3. The method eventually adopted was to use profile measurements under near-neutral conditions to estimate the surface roughness length for momentum and then apply these roughness lengths using the bulk method to determine turbulent fluxes (Greuell and Smeets, 2000). The results presented in Chapter 3 of this thesis have helped illustrate why such a methodology needs to be employed and may help in planning future experimental campaigns.

The results presented in Chapter 4 are an interesting case of how our understanding of the dynamics of katabatic flows can be applied to develop alternative methods for determining the surface roughness lengths of glaciers. This approach is limited to glaciers with strong katabatic forcing, i.e. steep slopes and strong temperature inversions, and requires the use of high resolution profile masts for wind and temperature. However, as shown for the Pasterze glacier where katabatic flows dominate, the number of usable profiles for determining roughness lengths is considerably enhanced, by a factor of 30, when the katabatic method is employed.

Despite its brevity, Chapter 5 presents an important result: conformation of surface renewal theories for the surface roughness length of temperature on a melting ice surface. The observations used to confirm this are selected, contrary to much of the other work presented here, on the basis of the absence of the katabatic wind speed maximum. It is only through increased understanding of the turbulent structure of katabatic flows that a suitable selection criteria could be applied.

There are still several questions yet to be answered in regard to scalar roughness lengths. The applicability of surface renewal theories to the surface roughness length for water vapour has yet to be confirmed on ice or snow surfaces. Its measurement is difficult due to the inherent errors associated with humidity measurements. However, a well planned strategy for determining its value is not beyond the current state of sensor technology and an observational experiment to test these theories would be very useful for both glaciologists and atmospheric modellers alike. Another problem is addressed by Smeets and Vugts (2000) where they suggest that scalar roughness lengths should be calculated on the basis of momentum roughness lengths determined by the micro-structure of the ice surface, i.e. ice crystal size. This point needs to be clarified and it is perhaps preferable to carry out laboratory experiments to cast more light on both these problems.

In Chapters 6 and 7 the second-order closure scheme developed in Chapter 2 is applied to the Greenland ice sheet using a 3-D boundary layer model. The aim of this study is to determine the contribution, as well as the climate sensitivity, of the turbulent heat and longwave radiation fluxes to the surface energy budget. The eventual aim of the study is the development of parameterisations for these fluxes that can be used to improve energy balance models of the Greenland ice sheet (van de Wal, 1996). The resulting parameterisation for turbulent heat flux, which is based on the single external variable of surface extrapolated free atmospheric temperature, indicates a quadratic relationship between atmospheric temperature and turbulent

heat flux. This non-linear dependence is due to katabatic forcing of the boundary layer winds, leading to a temperature dependence of wind speeds in the ablation zone.

Much effort has been put into a suitable turbulent scheme for the boundary layer model but less has been expended on the other parameterisations used to create a complete energy balance model. There are many possible changes to the model that would improve its performance. These include: an improved method for introducing clouds in the longwave radiation scheme, improved parameterisations for the transmission of shortwave radiation through clouds and atmosphere, a subsurface model that allows processes such as refreezing and densification to be described and an improved albedo parameterisation.

However, coupled to many of these changes are increased computational costs as well as implementation time. These are major factors in model development, and research in general, and should not be underestimated when initiating such a project. As the complexity of the model grows, it slowly approaches the quality of other limited area models that describe more completely the physical processes of the atmosphere. The question remains, whether it is more efficient to adapt already existing atmospheric models to the Greenland situation or to add improvements to the boundary layer model presented here.

One of the advantages of such a boundary layer model, and perhaps not exploited to its fullest extent in this thesis, is that more fundamental studies can be carried out to bring insight into particular processes in the boundary layer. More attention should be paid to this aspect of the modelling work.

The importance of observational data has been emphasized on several occasions throughout the thesis. However, it must also be emphasized that these observations are most useful when an appropriate theoretical and conceptual framework is also available. It is hoped that the work presented here has helped improve this framework and that future observational and theoretical studies will benefit from the results.

Acknowledgments

In every chapter of this thesis there are official acknowledgments for work done in direct connection to the particular studies. Most of these concern the people responsible for the processing and acquisition of observational data. I would like to reiterate these thanks, in particular to Ernst van der Avoird and Paul Smeets from whom most of this data originates. Apart from these two, many people have been involved in acquiring the observational data. The technical staff at the IMAU, Wim Boot, Marcel Porthanger and Henk Snellen have designed and maintained all of the instruments used by the IMAU during the various measurement campaigns. Also thanks to Jason Box, University of Colorado, for making the PARCA observational data available.

No thesis is completed without the support of supervisors and colleagues. I would firstly like to thank my co-promoter Wouter Greuell for the time he has spent in discussing and correcting much of the work presented here and his solid support in the Greenland project. Secondly, Hans Oerlemans for his non-demanding critique and for originating the West Greenland mass balance project in which I have been involved. Constructive criticism has also come from my other colleagues within the 'Ice and Climate' group at the IMAU for which I am indebted. Particularly Michiel van den Broeke, Roderik van de Wal and Andrew Mackintosh. In this vain I would also like to thank Peter Duynkerke for many discussions in the field of turbulence.

I am also happy to have participated in several field trips. To Iceland with Jan de Wolde and to Greenland with Henk, Wim and Andrew. The experience of 'being there' has made the thousands of hours spent before the screen far less abstract than they otherwise would have been.

Having said this, there is more to life than science and some colleagues are simply a pleasure to be with. I am happy to have shared my office with both Wouter Knap and Carleen Reijmer. In fact if it were not for Carleens support and her refusal to get annoyed at me for asking far too many silly, and dare I say, lazy questions this thesis would have taken significantly longer to finish. To Carina van de Veen for a bright light down the corridor and to Andrew Mackintosh for reminding me of my English origins. Also to Dan Zwartz who, whether he knows it or not, brought back the antipodean sunshine I'd been so dearly missing in the sometimes gloomy halls surrounding me. Finally, I would dearly like to thank Cecilie Rolstad for her many varied support during what can only be called a somewhat trying period.

Curriculum Vitae

Bruce was born on the 11th of December, 1963, at the now defunct Ryde Memorial Soldiers Hospital in the sun swept suburbs of Sydney. He spent his entire youth playing in the bush behind his house, feeding his ducks and butting his goat. In 1981 he completed his tertiary education at James Ruse Agricultural High School where he obtained sufficient marks to attend the University of N.S.W., studying physics as had his father before him. Bruce completed his bachelors degree with honours (IIa) in 1985, which was insufficient to obtain a scholarship for a Ph.D.. For the next two years he worked part time at both the University of N.S.W. and at Sydney Observatory, as tutor and guide lecturer respectively before spending a year on the Powerhouse museum train, taking science and social commentary to outback New South Wales. Having decided academia and museum life was threatening his humanity, Bruce embarked on a number of bicycle trips. Firstly New Zealand, then China and finally to Europe. After the theft of his bicycle in Den Haag he decided to stay in The Netherlands a while, moving first to sea side Heemskerk in 1991, and eventually to Amsterdam. During his first few years in Holland he worked as a bicycle mechanic. This work led him to the brilliant idea of restarting his academic career, which he did, by studying meteorology and physical oceanography at Utrecht University where he completed his second undergraduate degree (cum laude) in 1997. Giving himself no time to think Bruce launched himself immediately into a Ph.D. which you now see before you, completed almost on time, on the 7th of December 2000, and celebrated with a fine bottle of bubbly.

References

- Albrecht, B., Fairall, C., Thomson, D., and White, A. (1990). Surface-based remote sensing of the observed and the adiabatic liquid water content of stratocumulus clouds. *Geophys.Res.Lett.*, **17**, 89–92.
- Ambach, W. (1979). Zum wärmehaushalt des Grönländischen inlandeises: Vergleichende studie im akkumulations- und ablationsgebiet. *Polarforschung*, **49**, 44–54.
- Anderson, D., Tannehill, J., and Pletcher, R. (1984). *Computational Fluid Mechanics and Heat Transfer*, page 252. Hemisphere Publishing.
- Andreas, E. (1987). A theory for the scalar roughness and the scalar transfer coefficients over snow and sea ice. *Boundary-Layer Meteorol.*, **38**, 159–184.
- Andrén, A. (1990). Evaluation of a turbulence closure scheme suitable for air-pollution applications. *J.Appl.Meteorol.*, **29**, 224–239.
- Arritt, R. and Pielke, R. (1986). Interactions of nocturnal slope flows with ambient winds. *Boundary-Layer Meteorol.*, **37**, 183–195.
- Brost, R. and Wyngaard, J. (1978). A model study of the stably stratified planetary boundary layer. *J.Atmos.Sci.*, **35**, 1427–1440.
- Brost, R., Wyngaard, J., and Lenschow, D. (1982). Marine stratocumulus layers. Part II: Turbulence budgets. *J.Atmos.Sci.*, **39**, 818–836.
- Brutsaert, W. (1975a). On a derivable formula for longwave radiation from clear skies. *Water Resour.Res.*, **11**, 742–744.
- Brutsaert, W. (1975b). A theory of local evaporation (or heat transfer) from rough and smooth surfaces at ground level. *Water Resour.Res.*, **11**, 543–550.
- Crow, S. (1968). Viscoelastic properties of fine grained incompressible turbulence. *J.Fluid.Mech.*, **41**, 81.
- Davies, T., Palutikof, J., Guo, X., Berkofsky, L., and Halliday, J. (1995). Development and testing of a two-dimensional downslope wind model. *Boundary-Layer Meteorol.*, **73**, 279–297.
- de Ruyter de Wildt, M., Oerlemans, J., and Björnsson, H. (2000). A calibrated mass balance model for Vatnaökull, Iceland. Submitted, *J.Geophys.Res.*
- Delage, Y. (1974). A numerical study of the nocturnal atmospheric boundary layer. *Quart.J.Roy.Meteorol.Soc.*, **100**, 351–364.
- Denby, B. (1999). Second-order modelling of turbulence in katabatic flows. *Boundary-Layer Meteorol.*, **92**, 67–100.

- Denby, B. and Greuell, W. (2000). The use of bulk and profile methods for determining the surface heat fluxes in the presence of glacier winds. *J.Glaciol.*, **46**, 445–452.
- Denby, B. and Smeets, P. (2000). Derivation of turbulent flux profiles and roughness lengths from katabatic flow dynamics. *J.Appl.Meteorol.*, **39**, 1601–1612.
- Detering, H. and Etling, D. (1985). Application of the E- ϵ turbulence model to the atmospheric boundary layer. *Boundary-Layer Meteorol.*, **33**, 113–133.
- Doran, J. and Horst, T. (1983). Observations and models of simple nocturnal slope flows. *J.Atmos.Sci.*, **40**, 708–717.
- Duynkerke, P. (1988). Application of the E- ϵ turbulence closure model to the neutral and stable atmospheric boundary layer. *J.Atmos.Sci.*, **45**, 865–880.
- Duynkerke, P. and Nieuwstadt, F. (1989). The solution of the E- ϵ model for nearly homogenous turbulence with a mean shear. *Boundary-Layer Meteorol.*, **46**, 25–43.
- Duynkerke, P. and van den Broeke, M. (1994). Surface energy balance and katabatic flow over glacier and tundra during GIMEX-91. *Global Planet. Change*, **9**, 17–28.
- Ekhholm, S. (1996). A full coverage, high-resolution, topographic model of Greenland computed from a variety of digital elevation data. *J.Geophys.Res.*, **21**, 21961–21972.
- Forrer, J. and Rotach, M. (1997). On the turbulence in the stable boundary layer over the Greenland ice sheet. *Boundary-Layer Meteorol.*, **85**, 111–136.
- Gal-Chen, T. and Somerville, R. (1975). On the use of coordinate transformation for the solution of the Navier-Stokes equations. *J.Comp.Phys.*, **17**, 209–228.
- Gallée, H. and Duynkerke, P. (1997). Air-snow interactions and the surface energy and mass balance over the melting zone of West Greenland during the Greenland Ice Margin Experiment. *J.Geophys.Res.*, **102**, 13813–13824.
- Gallée, H., de Ghelin, O., and van den Broeke, M. (1995). Simulation of atmospheric circulation during the GIMEX 91 experiment using a meso- γ primitive equation model. *J.Clim.*, **8**, 2843–2859.
- Garratt, J. (1977). Review of drag coefficients over oceans and continents. *Mon.Wea.Rev.*, **105**, 915–929.
- Garratt, J. (1992). *The Atmospheric Boundary Layer*. Cambridge University Press, Cambridge.
- Garratt, J. and Brost, R. (1982). Radiative cooling effects within and above the nocturnal boundary layer. *J.Atmos.Sci.*, **38**, 2730–2746.
- Gibson, M. and Launder, B. (1978). Ground effects on pressure fluctuations in the atmospheric boundary layer. *J.Fluid.Mech.*, **86**, 491–511.
- Glover, R. (1999). Influence of spatial resolution and treatment of orography on GCM estimates of the surface mass balance of the Greenland ice sheet. *J.Clim.*, **12**, 551–563.

- Grant, A. (1990). The structure of turbulence in the mean atmospheric boundary layer. *J.Atmos.Sci.*, **49**, 226–239.
- Greuell, W. and Böhm, R. (1998). 2 m temperatures along melting mid-latitude glaciers, and implications for the sensitivity of the mass balance to variations in temperature. *J.Glaciol.*, **44**, 9–20.
- Greuell, W. and Knap, W. (2000). Remote sensing of the albedo and detection of the slush line on the Greenland ice sheet. *J.Geophys.Res.*, **105**, 15567–15576.
- Greuell, W. and Konzelmann, T. (1994). Numerical modelling of the energy balance and the englacial temperature of the Greenland ice sheet. Calculations for the ETH camp location (West Greenland, 1155 m a.s.l.). *Global Planet. Change*, **9**, 79–90.
- Greuell, W. and Smeets, C. (2000). Elevation variations in the surface energy balance on the Pasterze (Austria). Submitted to *J.Geophys.Res.*
- Greuell, W., Knap, W., and Smeets, P. (1997). Elevational changes in meteorological variables along a midlatitude glacier during summer. *J.Geophys.Res.*, **102**, 941–954.
- Hanjalić, K. and Launder, B. (1972). A Reynolds stress model of turbulence and its application to thin shear flows. *J.Fluid.Mech.*, **52**, 609–638.
- Horst, T. and Doran, J. (1986). Nocturnal drainage flow on simple slopes. *Boundary-Layer Meteorol.*, **34**, 263–286.
- Horst, T. and Doran, J. (1988). The turbulence structure of nocturnal slope flow. *J.Atmos.Sci.*, **45**, 605–616.
- Huybrechts, P. and de Wolde, J. (1999). The dynamic response of the Greenland and Antarctic ice sheets to multiple-century climatic warming. *J.Clim.*, **12**, 2169–2188.
- Iqbal, M. (1983). *An Introduction to Solar Radiation*. Academic Press, Toronto.
- Irwin, H. (1974). Measurements in a self-preserving plane wall jet in a positive pressure gradient. *J.Fluid.Mech.*, **61**, 33–63.
- Joffre, S. (1982). Momentum and heat transfers in the surface layer over frozen sea. *Boundary-Layer Meteorol.*, **24**, 211–229.
- King, J. (1990). Some measurements of turbulence over an Antarctic ice shelf. *Quart.J.Roy.Meteorol.Soc.*, **116**, 379–400.
- King, J. (1994). Heat and water vapour fluxes and scalar roughness lengths over an Antarctic ice shelf. *Boundary-Layer Meteorol.*, **69**, 101–121.
- Knap, W. and Oerlemans, J. (1996). The surface albedo of the Greenland ice sheet: satellite-derived and in situ measurements in the Søndre Strømfjord area during the 1991 melt season. *J.Glaciol.*, **42**, 364–374.
- Kolmogorov, A. (1941). The local structure of turbulence in incompressible viscous fluid for very large Reynolds number. *Dokl.Akad.Nauk.SSSR*, **30**, 301.

- Kondo, J. and Yamazawa, H. (1986). Bulk transfer coefficient over a snow surface. *Boundary-Layer Meteorol.*, **34**, 123–135.
- Konzelmann, T., van de Wal, R., Greuell, W., Bintanja, R., Henneken, E., and Abe-Ouchi, A. (1994). Parameterization of global and longwave incoming radiation for the Greenland ice sheet. *Global Planet. Change*, **9**, 143–164.
- Koo, Y. and Reible, D. (1995). Flow and transport modelling in the sea-breeze. Part I: A modified E- ϵ model with a non-equilibrium level 2.5 closure. *Boundary-Layer Meteorol.*, **75**, 109–140.
- Kuhn, M. (1979). On the computation of heat transfer coefficients from energy-balance gradients on a glacier. *J.Glaciol.*, **22**, 263–271.
- Larsson, L. (1997). Measurements and modelling of turbulence characteristics in stable boundary layers. *Internal report, IMAU, University of Utrecht*, **97-25**.
- Launder, B. (1975). On the effects of a gravitational field on the turbulent transport of heat and momentum. *J.Fluid.Mech.*, **67**, 569–581.
- Lettau, H. (1969). Note on aerodynamic roughness-parameter estimation on the basis of roughness-element description. *J.Appl.Meteorol.*, **8**, 828–832.
- Mahrt, L. (1982). Momentum balance of gravity flows. *J.Atmos.Sci.*, **39**, 2701–2711.
- Meesters, A., Henneken, E., Bink, N., Vugts, H., and Cannemeijer, F. (1994). Simulation of the atmospheric circulation near the Greenland ice sheet margin. *Global Planet. Change*, **9**, 53–67.
- Meesters, A., Bink, N., Henneken, E., Vugts, H., and Cannemeijer, F. (1997a). Katabatic wind profiles over the Greenland ice sheet: Observation and modelling. *Boundary-Layer Meteorol.*, **85**, 475–496.
- Meesters, A., Bink, N., Vugts, H., Cannemeijer, F., and Henneken, E. (1997b). Turbulence observations above a smooth melting surface on the Greenland ice sheet. *Boundary-Layer Meteorol.*, **85**, 81–110.
- Mellor, G. and Yamada, T. (1974). A hierarchy of turbulence closure models for planetary boundary layers. *J.Atmos.Sci.*, **31**, 1791–1806.
- Mellor, G. and Yamada, T. (1982). Development of a turbulence closure model for geophysical fluid problems. *Rev.Geophys.*, **20**, 851–875.
- Monin, A. and Obukhov, A. (1954). Basic laws of turbulent mixing in the atmosphere near the ground. *Tr.Akad.Nauk SSSR Geofiz.Inst.*, **24**, 163–187.
- Munro, D. (1989). Surface roughness and bulk heat transfer on a glacier: Comparison with eddy correlation. *J.Glaciol.*, **35**, 343–348.
- Munro, D. and Davies, J. (1978). On fitting the log-linear model to wind speed and temperature profiles over a melting glacier. *Boundary-Layer Meteorol.*, **15**, 423–437.

- Nappo, C. and Shankar Rao, K. (1987). A model study of pure katabatic flows. *Tellus*, **39A**, 61–71.
- Nieuwstadt, F. (1984). The turbulent structure of the stable nocturnal boundary layer. *J.Atmos.Sci.*, **41**, 2202–2216.
- Nieuwstadt, F. and van Dop, H., editors (1981). *Atmospheric Turbulence and Air Pollution modelling*, page 81. D. Reidel Publishing Company, Dordrecht. Article from J.C.Wyngaard.
- Oerlemans, J. (2000). Analysis of a three-year meteorological record from the ablation zone of the Morteratschgletscher, Switzerland: energy and mass balance. In press, *J.Glaciol.*
- Oerlemans, J. and Knap, W. (1998). A 1 year record of global radiation and albedo in the ablation zone of the Morteratschgletscher, Switzerland. *J.Geophys.Res.*, **44**, 231–238.
- Oerlemans, J. and Vugts, H. (1993). A meteorological experiment in the ablation zone of the Greenland ice sheet. *Bull.Am.Meteorol.Soc.*, **74**, 355–365.
- Oerlemans, J., Björnsson, H., Kuhn, M., Obleitner, F., Pálsson, F., Smeets, P., Vugts, H., and Wolde, J. (1999). Glacio-meteorological investigations on Vatnajökull, Iceland, summer 1996: An overview. *Boundary-Layer Meteorol.*, **92**, 3–26.
- Ohata, T. (1989). Heat balance study on Glacier no.1 at head of Urumqi river, Tianshan Mountains, China. *Journal of Glaciology and Geocryology*, **11**, 298–309.
- Ohmura, A. (1987). New temperature distribution maps for Greenland. *Z.Gletscherkd.Glazialgeol.*, **23**, 1–45.
- Ohmura, A. and Reeh, N. (1991). New precipitation and accumulation maps for Greenland. *J.Glaciol.*, **37**, 140–148.
- Ohmura, A., Wild, M., and Bengtsson, L. (1996). Present and future mass balance of the ice sheets simulated with GCM. *Ann.Glaciol.*, **23**, 187–193.
- Økland, H., Engedahl, H., and Sannes, O. (1988). Model simulations of katabatic wind in a simplified valley topography. *Z.Meteorol.*, **38**, 293–298.
- Pielke, R. (1984). *Mesoscale Meteorological Modelling*. Academic Pres, Orlando.
- Press, W., Teukolsky, S., Vettering, W., and Flannery, B. (1992). *Numerical Recipes*, page 657. Cambridge University Press, Cambridge.
- Rao, K. and Snodgrass, H. (1981). A nonstationary nocturnal drainage flow model. *Boundary-Layer Meteorol.*, **20**, 309–320.
- Reeh, N. (1989). Parameterization of melt rate and surface temperature on the Greenland ice sheet. *Polarforschung*, **59**, 113–128.

- Reeh, N., Mayer, C., Miller, H., Thomsen, H., and Weidick, A. (1999). Present and past climate control on fjord glaciations in Greenland: Implications for IRD-deposition in the sea. *Geophys.Res.Lett.*, **26**, 1039–1042.
- Rodgers, C. (1967). The use of emissivity in atmospheric radiation calculations. *Quart.J.Roy.Meteorol.Soc.*, **73**, 67–92.
- Rotta, J. (1951). Statistische theorie nichthomogener turbulenz. *Z.Phys.*, **129**, 547–572.
- Shir, C. (1973). A preliminary numerical study of atmospheric turbulent flows in the idealized planetary boundary layer. *J.Atmos.Sci.*, **30**, 1327–1339.
- Smeets, C. and Vugts, H. (2000). A comparison of surface energy balance calculations and measured ablation at an Alpine and sea-based glacier. Submitted to *J.Glaciol.*
- Smeets, C., Duynkerke, P., and Vugts, H. (1998). Turbulence characteristics of the stable boundary layer over a mid-latitude glacier. Part I: A combination of katabatic and large scale forcing. *Boundary-Layer Meteorol.*, **87**, 117–145.
- Smeets, C., Duynkerke, P., and Vugts, H. (1999). Observed wind profiles and turbulence fluxes over an ice surface with changing surface roughness. *Boundary-Layer Meteorol.*, **92**, 101–123.
- Smeets, C., Duynkerke, P., and Vugts, H. (2000). Turbulence characteristics of the stable boundary layer over a mid-latitude glacier. Part II: Pure katabatic forcing conditions. *Boundary-Layer Meteorol.*, **97**, 73–107.
- Steffen, K., Box, J., and Abdalati, W. (1996). Greenland climate network: GC-Net. in Colbeck, S. C. Ed. *CRREL 96-27 Special report on glaciers, ice sheets and volcanoes, trib. to M. Meier*, pages 101–123.
- Thompson, S. and Pollard, D. (1997). Greenland and Antarctic mass balances for present and doubled atmospheric CO₂ from the GENESIS version-2 global climate model. *J.Clim.*, **10**, 871–900.
- van de Wal, R. (1994). An energy balance model for the Greenland ice sheet. *Global Planet. Change*, **9**, 115–131.
- van de Wal, R. (1996). Mass balance modelling of the Greenland ice sheet: a comparison of an energy-balance and degree-day model. *Ann.Glaciol.*, **23**, 36–45.
- van den Broeke, M. (1994). The observed katabatic flow at the edge of the Greenland ice sheet during GIMEX-91. *Global Planet. Change*, **9**, 3–15.
- van den Broeke, M. (1996). Characteristics of the lower ablation zone of the West Greenland ice sheet for energy-balance modelling. *Ann.Glaciol.*, **23**, 160–166.
- van den Broeke, M. (1997a). A bulk model of the atmospheric boundary layer for inclusion in mass balance models of the Greenland ice sheet. *Z.Gletscherkd.Glazialgeol.*, **33**, 73–94.
- van den Broeke, M. (1997b). Momentum, heat, and moisture budgets of the katabatic wind layer over a midlatitude glacier in summer. *J.Appl.Meteorol.*, **36**, 763–774.

- van den Broeke, M. (1997c). Structure and diurnal variations of the atmospheric boundary layer over a mid-latitude glacier in the summer. *Boundary-Layer Meteorol.*, **83**, 183–205.
- van der Avoird, E. and Duynkerke, P. (1999). Turbulence in a katabatic flow. Does it resemble turbulence in stable boundary layers over flat surfaces? *Boundary-Layer Meteorol.*, **92**, 39–66.
- Wagnon, P., Ribstein, P., Francou, B., and Pouyaud, B. (1999). Annual cycle of energy balance of Zongo glacier, Cordillera Real, Bolivia. *J.Geophys.Res.*, **104**, 3907–3923.
- Warren, S. (1982). Optical properties of snow. *Reviews of Geophysics and Space Physics*, **20**, 67–89.
- Warrick, R., Provost, C. L., Meier, M., Oerlemans, J., and Woodworth, P. (1996). *Changes in sea level*, pages 359–405. in *Climate change 1995*, J.T. Houghton et al., Eds. Cambridge University Press.
- Welch, R. and Zdunkowski, W. (1976). A radiation model of the polluted atmospheric boundary layer. *J.Atmos.Sci.*, **33**, 2170–2184.
- Wong, R., Hage, K., and Philips, L. (1987). The numerical simulation of drainage winds in a small urban valley under conditions with supercritical Richardson numbers. *J.Climate Appl.Meteor.*, **26**, 1447–1463.
- Yamada, T. (1983). Simulations of nocturnal drainage flows by a q^2l turbulence closure model. *J.Atmos.Sci.*, **40**, 91–106.
- Zuo, Z. and Oerlemans, J. (1996). Modelling albedo and specific balance of the Greenland ice sheet: calculations for the Søndre Sstrømfjord transect. *J.Glaciol.*, **42**, 305–317.

